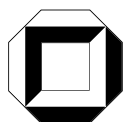


Dissertationsreihe am Institut für Hydromechanik  
der Universität Karlsruhe (TH)  
Heft 2005/3

Investigation of Flow and Pressure  
Characteristics around Pyramidal  
Buildings

Muhammad Ikhwan





Muhammad Ikhwan

**Investigation of Flow and Pressure Characteristics  
around Pyramidal Buildings**

Dissertationsreihe am Institut für Hydromechanik  
der Universität Karlsruhe (TH)  
Heft 2005/3

# Investigation of Flow and Pressure Characteristics around Pyramidal Buildings

von  
Muhammad Ikhwan



---

universitätsverlag karlsruhe

Dissertation, genehmigt von der  
Fakultät für Bauingenieur-, Geo- und Umweltwissenschaften  
der Universität Fridericiana zu Karlsruhe (TH), 2005  
Referenten: Prof. Dr.-Ing. habil. Dr.h.c. Bodo Ruck,  
Prof. Dr.-Ing. Christoph Egbers

## **Impressum**

Universitätsverlag Karlsruhe  
c/o Universitätsbibliothek  
Straße am Forum 2  
D-76131 Karlsruhe  
www.uvka.de



Dieses Werk ist unter folgender Creative Commons-Lizenz  
lizenziert: <http://creativecommons.org/licenses/by-nc-nd/2.0/de/>

Universitätsverlag Karlsruhe 2005  
Print on Demand

ISSN 1439-4111  
ISBN 3-937300-72-4

# Investigation of Flow and Pressure Characteristics around Pyramidal Buildings

Zur Erlangung des akademischen Grades eines

DOKTOR-INGENIEURS

der Fakultät für

Bauingenieur-, Geo- und Umweltwissenschaften  
der Universität Fridericiana zu Karlsruhe (TH)

genehmigte

DISSERTATION

von

Muhammad Ikhwan, M.Sc.

aus Jakarta, Indonesien

Tag der mündlichen Prüfung: 17. Juni 2005

Hauptreferent: Prof. Dr.-Ing. habil. Dr.h.c. Bodo Ruck

Korreferent: Prof. Dr.-Ing. Christoph Egbers

Karlsruhe 2005





# **Erklärung**

Hiermit versichere ich, die vorliegende Arbeit selbständig verfasst und keine weiteren als die angegebenen Hilfsmittel und Quellen benutzt zu haben.

Karlsruhe, dem 18 April 2005

Muhammad Ikhwan

# Investigation of Flow and Pressure Characteristics around Pyramidal Buildings

## Abstract

Pyramidal buildings are undergoing a renaissance in today's architectural design due to their attractive mystery that has fascinated many architects. From an aerodynamic engineering point of view, structural buildings with the shape of a pyramid have their own interesting and particular aerodynamic characteristics as compared to other 'usual' structural buildings (i.e. cuboidal). However, despite its distinct aerodynamic characteristics compared to other 'usual' structural buildings, the flow and pressure characteristics around pyramidal structures have not yet been investigated completely. Very limited studies about pyramidal buildings can be found in the literature. Consequently, the technical layout with respect to wind load assumption of pyramidal buildings are usually not listed in standard tables which underlines the need of systematic investigations for pyramidal structures.

In this study, pyramids with a wide range of base angle variation ( $\theta = 30^\circ, 40^\circ, 45^\circ, 50^\circ, 55^\circ, 60^\circ, 70^\circ$ ) have been investigated intensively through a detailed and accurate laboratory experiments at the Laboratory of Building- and Environmental Aerodynamics, Institute for Hydromechanics, at the University of Karlsruhe. The flow measurements were performed using a 2-D Laser Doppler anemometry (LDA) and The pressure measurements were carried out using a standard pressure tapping technique. The present study focuses on the most important parameters affecting the flow and pressure characteristics that include the influence of base angles, the influence of wind directions and the influence of the pyramid heights with respect to a characteristic length. Besides the experimental investigations, numerical investigations with the aid of a software package called FLOVENT were also additionally performed in order to prove, whether experimental and numerical studies deliver the same results.

Based on the flow measurement results, this study was able to distinguish the general characteristics of flow around pyramid building when compared to other type of structures (i.e. cuboidal structure). A set of equations to calculate the reattachment length at the leeward side of the pyramid was generated. In addition, an equation to estimate the zero streamline and an area below line as a function of the reattachment length and base angle, respectively, are proposed. These equations will illustrate the recirculation zone at the leeward side of the pyramid.

The pressure measurement results show that the three investigated parameters (base angle, wind direction and pyramid height) have an important influence to the pressure characteristics (magnitude of pressure, suction and fluctuation) in the surfaces of the pyramids. For practical purposes, this study was able to provide the typical values of pressure and aerodynamic coefficients for pyramidal buildings that can be used for structural calculations. The values that are given in this study can be used to fill in the gap of the unavailable design values for pyramidal buildings in standard tables.

# Untersuchungen des Strömungs- und Druckfeldes um pyramidenförmige Gebäude

## Kurzfassung

Heutzutage erlebt die Pyramidenform im architektonischen Bereich aufgrund ihres attraktiven Geheimnisses, das viele Architekten fasziniert hat, eine Renaissance. Vom aerodynamischen Standpunkt hat ein pyramidenförmiges Gebäude im Vergleich zu konventionell rechteckigen Gebäuden eine wesentlich veränderte Charakteristik (z.B. kürzeres Wiederanlegegebiet). Trotz seiner eigenen aerodynamischen Eigenschaften ist das Strömungs- und Druckfeld um pyramidenartige Strukturen noch nicht im Detail untersucht worden. Es existieren nur sehr wenige Studien in der Literatur zur Problematik der Pyramidenumströmung. Demgegenüber existiert eine Vielzahl von Studien über rechteckige Gebäude, die jedoch nicht so einfach auf pyramidenförmige Bauwerke übertragen werden können. Pyramidenförmige Bauwerke sind weder in den nationalen noch in den internationalen Normenwerken aufgeführt, was den Bedarf an systematischen Untersuchungen für pyramidenartige Strukturen unterstreicht.

In diese Studie sind Pyramiden mit variierten Basiswinkeln ( $\theta = 30^\circ, 40^\circ, 45^\circ, 50^\circ, 55^\circ, 60^\circ, 70^\circ$ ) in einem detaillierten und genauen Laborexperiment am Laboratorium für Gebäude- und Umweltaerodynamik, Institut für Hydromechanik, an der Universität Karlsruhe untersucht worden. Die Strömungsgeschwindigkeiten um die pyramidenförmigen Strukturen wurden mit Hilfe eines 2D-Laser-Doppler-Anemometers (LDA) gemessen. Die Druckverteilungen auf den Pyramidenoberflächen wurden mittels der gebräuchlichen Druckaufnehmertechnik („taps“) erfasst. Diese Studie konzentriert sich auf die wichtigsten Parameter, welche die Strömungs- und Druckmerkmale beeinflussen. Der Einfluss von dem Basiswinkel, der Windrichtung und der Pyramidenhöhe bezogen auf eine charakteristische Länge wurde erfasst. Zusätzlich zu den experimentellen Untersuchungen wurden auch noch numerische Untersuchungen mit Hilfe des Software-Paketes FLOVENT durchgeführt, um zu zeigen, ob die experimentellen und numerischen Studien die gleichen Ergebnisse liefern.

Aus den Strömungsmessergebnissen können die allgemeinen Merkmale der Strömung um Pyramidengebäude im Vergleich zu andersartigen Strukturen wie z.B rechteckigen Gebäuden unterschieden werden. Verschiedene Parameter, die die Strömung um die Pyramide charakterisieren, werden besprochen. Eine Gruppe von Gleichungen wurde erstellt, um die Wiederanlegelänge an der Lee-Seite der Pyramide zu berechnen. Außerdem werden Gleichungen vorgeschlagen, um die Nullstromlinien und die Flächen unter diesen Linien als eine Funktion der Wiederanlegelänge und der Basiswinkel abzuschätzen. Diese Gleichungen veranschaulichen den Umlauf an der Lee-Seite der Pyramide.

Die Druckmessergebnisse zeigen, dass die drei untersuchten Parameter (der Basiswinkel, die Windrichtung und die Höhe der Pyramide) einen großen Einfluss auf die Druckeigenschaften an den Pyramidenoberflächen (die Größe des Drucks, des Sogs und der Schwankungen) besitzen. Diese Studie konnte die typischen Werte des Drucks und der aerodynamischen Koeffizienten für pyramidenartige Gebäude liefern, die in der Praxis für Kalkulationen benutzt werden können. Die Werte, die in dieser Studie gegeben werden, können benutzt werden, um die Lücke der nicht verfügbaren Designwerte für pyramidenartige Gebäude in standardmäßigen Tabellen auszufüllen.

*To my father and the memory of my mother*

*Teruntuk papa dan kenangan bersama mama*

# Acknowledgements

I would like to express my sincere gratitude and appreciation to my advisor, Prof. Bodo Ruck for his constant guidance, encouragement and support during my research. I wish to thank my co-referee Prof. Christoph Egbers. I'm also grateful to the director of the Institute for Hydromechanics, Prof. Gerhard H. Jirka, for his support to me and my family especially during the final stage of my research.

I would also like to express my gratitude to all my colleagues at the Institute for Hydromechanics for their support during my work, especially to the member of the Laboratory of Building and Environmental Aerodynamics. In particular, I am very grateful to Harald Deutsch and Armin Reinsch for their help in the establishment of the experimental setup and a nice atmosphere they created during the coffee break, Dr.-Ing. Boris Pavlovski for his help in laser measurement technique, Patrick Heneka and Cornelia Frank for all the blue mark they put on my work, Chistof Gromke and Wilken Agster for their support and also my appreciation to all of them for the constructive discussion. I'm very grateful for their friendship that has made my study in Karlsruhe a lot more cheerful and enjoyable. I also wish to thank Dr-Ing. Cornelia Lang, Dr-Ing. Volker Weitbrecht and Gregor Kühn for all their support during my time in Karlsruhe.

I am deeply grateful to my parents, my wife Herlina, my son and my daughter for their loving support and constant encouragement throughout the time that this work was in progress. Last but not least I would like to thank the support from my friends in Karlsruhe, especially to Arifah and her family to look after my son during his first and second year of life.

Finally, the financial support from the "Deutsche Forschungsgemeinschaft"(DFG) for funding this project through project grant No. Ru 345/25 is gratefully acknowledged.

Karlsruhe, July 2005

# Contents

- 1. Introduction ..... 1**
  - 1.1. Background ..... 1
  - 1.2. Objective ..... 4
  - 1.3. Methodology ..... 5
  
- 2. Literature Review..... 6**
  - 2.1. Characteristics of Turbulent Flow ..... 6
  - 2.2. Governing Equations..... 7
  - 2.3. Atmospheric Boundary Layer ..... 10
  - 2.4. Flow around Buildings ..... 13
  - 2.5. Wind Action on Buildings..... 15
    - 2.5.1. Pressure Coefficient on Buildings..... 16
    - 2.5.2. Aerodynamic Coefficients on Buildings ..... 20
  - 2.6. Previous Investigations on Pyramidal Buildings ..... 22
  
- 3. Wind Tunnel Technique ..... 25**
  - 3.1. Similarity Criteria..... 26
    - 3.1.1. Similarity of Incoming Flow ..... 26
    - 3.1.2. Similarity of Flow Around Building ..... 28
    - 3.1.3. Similarity of Wind Load ..... 28
  - 3.2. Atmospheric Boundary Layer Wind Tunnel ..... 29
  - 3.3. Simulation of Atmospheric Boundary Layer Flow ..... 30
  
- 4. Experimental Setup and Measurement Techniques ..... 39**
  - 4.1. Pyramid Models and Measurement Programs ..... 39
  - 4.2. Flow Measurement Technique (LDA) ..... 42
    - 4.2.1. Basic Principle of LDA ..... 42
    - 4.2.2. LDA Configuration in the Wind Tunnel ..... 45
  - 4.3. Pressure Measurement Technique..... 47

<b>5. Experimental Results.....</b>	<b>50</b>
5.1. Flow Characteristics of Pyramids .....	50
5.1.1. Mean Velocity Profile .....	52
5.1.2. Vector Fields .....	56
5.1.3. Recirculation Zone .....	60
5.1.4. Turbulence Intensity .....	68
5.1.5. Reynolds Shear Stress .....	72
5.1.6. Turbulent Kinetic Energy.....	75
5.2. Pressure Characteristics of Pyramids.....	79
5.2.1. Influence of the Pyramid Base Angle on the Surface Pressure Distribution .....	79
5.2.2. Influence of the Wind Direction on the Surface Pressure Distribution .....	86
5.2.3. Influence of the Pyramid Height on the Surface Pressure Distribution.....	93
5.3. Aerodynamic Coefficients of Pyramids.....	98
5.3.1. Drag Coefficient.....	99
5.3.2. Lift Coefficient.....	101
5.3.3. Moment coefficient.....	103
5.4. Summary of Experimental Results .....	105
<b>6. Additional Numerical Investigations.....</b>	<b>107</b>
6.1. Mathematical Background .....	107
6.2. Boundary Conditions .....	111
6.3. Numerical Results .....	114
6.3.1. Mean Velocity Profiles .....	116
6.3.2. Velocity Fields .....	123
6.3.3. Reattachment Lengths.....	126
<b>7. Conclusions.....</b>	<b>128</b>



# List of Figures

Fig. 1.1.	Cheops pyramid in Giza, Egypt [Schüssler, 1983] .....	1
Fig. 1.2	Pyramidal structure in today’s architectural design (online sources listed at the end of reference list).....	3
Fig. 1.3	Sketches of typical 2-D flow structure around bluff body .....	4
Fig. 2.1.	Schematic of the vertical structure of the lower atmosphere and its various layers during neutral and stable conditions.....	11
Fig. 2.2.	The power law profiles for the velocity distributions in a boundary layer over homogeneous area [Plate, 1982]. .....	12
Fig. 2.3.	Typical flow profiles in the centre plane of cuboidal buildings.....	13
Fig. 2.4.	Three-dimensional flow structure around cuboidal building [Woo et.al, 1977].....	14
Fig. 2.5.	Pressure coefficient at the centre plane of cuboidal building [Cook, 1990]. .....	17
Fig. 2.6.	Mean pressure distribution on the cuboidal building [Sachs, 1972].....	18
Fig. 2.7.	“Delta-wing” vortices and the contour of pressure coefficient ( $c_p$ ) on the top of cuboidal building [Sockel, H., 1984] .....	19
Fig. 2.8.	Representation of coordinate axes convention for the present study, where the axes are aligned with the incoming wind and cross wind directions and the illustration of the projected area for the pyramids. ....	21
Fig. 2.9	Oil film visualization of the mean flow patterns on floor of pyramid faces ( $\zeta = 60^\circ$ , $\alpha' = 0^\circ$ ) [Abuomar et.al, 2000].....	23
Fig. 2.10.	(a) Design values of the pressure coefficient ( $c_p$ ) at different wind directions for the case of pyramid base angle $45^\circ$ [Cook, 1990], (b) Wind direction for pyramidal structure, (c) Wind direction for A-Frame structure .....	24
Fig. 3.1.	The closed-loop low speed wind tunnel at the Institute for Hydromechanics .....	29
Fig. 3.2.	Wind tunnel set up for atmospheric boundary layer flow .....	30
Fig. 3.3.	Roughness elements arrangement in the wind tunnel .....	31
Fig. 3.4.	The variation of mean wind velocities with height (exponential law).....	32
Fig. 3.5.	The variation of mean wind velocities with height (logarithmic law).....	33
Fig. 3.6.	The variation of turbulence intensities with height .....	35
Fig. 3.7.	The variation of integral length scale with height.....	36
Fig. 3.8.	Power spectral density of longitudinal velocity fluctuations .....	38

Fig. 4.1.	Pyramid geometry and coordinate arrangement .....	39
Fig. 4.2.	Parallel measuring planes.....	40
Fig. 4.3.	The measurement points for flow measurement with Laser-Doppler-Anemometer ..	41
Fig. 4.4.	Wind direction arrangements ( $u_0 = 12$ m/s).....	42
Fig. 4.5.	Principle of a LDA two beam anemometry [Ruck, 1987] .....	44
Fig. 4.6.	Derivation of the fringe model in laser Doppler anemometry – superposition of two laser beams [Ruck, 1987].....	45
Fig. 4.7.	Schematic illustration of the experimental set-up, data acquisition and data processing for the flow measurements.....	46
Fig. 4.8.	Schematic illustration of the experimental set-up, data acquisition and data processing for the pressure measurements.....	48
Fig. 4.9.	Example of pressure taps distribution on the pyramid surface (Pyramid P45, 57 pressure taps).....	49
Fig. 5.1.	A schematic illustration of the 3-D flow structures around a single pyramid building and the flow visualization using laser sheet at the near the bottom of the pyramid with base angle $\theta = 70^\circ$ . .....	51
Fig. 5.2.	Longitudinal mean velocity profiles at $y/l = 0.0$ ( $\alpha' = 0^\circ$ , $u_0 = 5$ m/s) .....	53
Fig. 5.3.	Longitudinal mean velocity profiles at $y/l = 0.25$ ( $\alpha' = 0^\circ$ , $u_0 = 5$ m/s). .....	54
Fig. 5.4.	Longitudinal mean velocity profiles at $y/l = 0.50$ plane ( $\alpha' = 0^\circ$ , $u_0 = 5$ m/s) .....	55
Fig. 5.5.	Vector field in a 2D-plane at $y/l = 0.0$ for investigated pyramids ( $\alpha' = 0^\circ$ , $u_0 = 5$ m/s, $h_{70} = 274.7$ mm) .....	57
Fig. 5.6.	Vector field in a 2D-plane at $y/l = 0.25$ for investigated pyramids ( $\alpha' = 0^\circ$ , $u_0 = 5$ m/s, $h_{70} = 274.7$ mm) .....	58
Fig. 5.7.	Vector field in a 2D-plane at $y/l = 0.50$ for investigated pyramids ( $\alpha' = 0^\circ$ , $u_0 = 5$ m/s, $h_{70} = 274.7$ mm) .....	59
Fig. 5.8.	Presentation of zero streamlines which illustrate the recirculation zone in the windward side and leeward side of the pyramids at $y/l = 0.0$ ( $\alpha' = 0^\circ$ , $u_0 = 5$ m/s)...	60
Fig. 5.9.	Presentation of non-dimensional zero streamline diagram at the leeward side of the pyramids.....	61
Fig. 5.10.	Area of the recirculation zone at $y/l = 0.0$ in non-dimensional form as a function of base angle for investigated pyramids.....	62
Fig. 5.11.	Sketch of reattachment length ( $x_r$ ) .....	62
Fig. 5.12.	Reattachment length ( $x_r$ ) for different pyramids at different lateral position ( $y$ ) in dimensional form, with wind direction $\alpha' = 0^\circ$ . .....	63
Fig. 5.13.	Reattachment length for different pyramids at different lateral position in non-dimensional form ( $x_r/h$ and $y/h$ ), measured from the pyramid edges with wind direction $\alpha' = 0^\circ$ .....	64
Fig. 5.14.	Comparison of the reattachment lengths ( $x_r$ ) between pyramidal and cuboidal buildings ( $w = 1$ ) as a function of length to height ratio.....	65

Fig. 5.15. Zero streamline at the leeward side of the centre pyramid ( $y/l = 0$ ), normalized with the height and the reattachment length.....	68
Fig. 5.16. Longitudinal turbulent intensity at $y/l = 0.0$ for investigated pyramids ( $\alpha' = 0^\circ$ , $u_0 = 5$ m/s, $h_{70} = 274.7$ mm) .....	69
Fig. 5.17. Turbulence intensity profiles for the pyramids at $y/l = 0.0$ and $x/l = 0.15$ ( $\alpha' = 0^\circ$ , $u_0 = 5$ m/s) .....	70
Fig. 5.18. Vertical turbulent intensity at $y/l = 0$ for investigated pyramids ( $\alpha' = 0^\circ$ , $u_0 = 5$ m/s, $h_{70} = 274.7$ mm).....	71
Fig. 5.19. Reynolds shear stress at $y/l = 0.0$ for investigated pyramids, normalized by the free stream mean velocity ( $\alpha' = 0^\circ$ , $u_0 = 5$ m/s, $h_{70} = 274.7$ mm).....	73
Fig. 5.20. Reynolds shear stress at $y/l = 0.25$ for investigated pyramids, normalized by the free stream mean velocity ( $\alpha' = 0^\circ$ , $u_0 = 5$ m/s, $h_{70} = 274.7$ mm).....	74
Fig. 5.21. Turbulent kinetic energy at $y/l = 0$ for investigated pyramids, normalized by free stream velocity ( $\alpha' = 0^\circ$ , $u_0 = 5$ m/s, $h_{70} = 274.7$ mm) .....	76
Fig. 5.22. Turbulent kinetic energy at $y/l = 0.25$ for investigated pyramids, normalized by free stream velocity ( $\alpha' = 0^\circ$ , $u_0 = 5$ m/s, $h_{70} = 274.7$ mm) .....	77
Fig. 5.23. Turbulent kinetic energy at $y/l = 0.50$ for investigated pyramids, normalized by free stream velocity ( $\alpha' = 0^\circ$ , $u_0 = 5$ m/s, $h_{70} = 274.7$ mm) .....	78
Fig. 5.24. Distribution of mean pressure coefficient ( $c_p$ mean) in the surfaces of the investigated pyramids ( $\alpha' = 0^\circ$ , $u_0 = 12$ m/s).....	81
Fig. 5.25. Mean pressure coefficient on surface A as a function of base angle for investigated wind directions.....	83
Fig. 5.26. Distribution of standard deviation of pressure coefficient fluctuations ( $c_p'$ ) on the surfaces of the investigated pyramids ( $\alpha' = 0^\circ$ , $u_0 = 12$ m/s).....	85
Fig. 5.27. Location of the maximum and the minimum values of mean pressure coefficients ( $c_{p-max.}$ and $c_{p-min.}$ ), and the maximum fluctuations as a function of pyramid base angles ( $\alpha' = 0^\circ$ , $u_0 = 12$ m/s).....	86
Fig. 5.28. Distribution of mean pressure coefficient on the surface of the pyramid P70 at different wind directions ( $\alpha' = 0^\circ$ to $\alpha' = 90^\circ$ ) .....	89
Fig. 5.29. Distribution of standard deviation of pressure coefficient fluctuations on the surface of the pyramid P70 at different wind directions ( $\alpha' = 0^\circ$ to $\alpha' = 90^\circ$ ).....	91
Fig. 5.30. Mean pressure coefficients and standard deviation of pressure coefficient fluctuations in surface A of the investigated pyramids as a function of wind directions .....	93
Fig. 5.31. Pressure distribution on the surfaces of pyramid P70 ( $h = 274.75$ mm), P70a ( $h = 142.81$ mm) and P70b ( $h = 100$ mm), at wind direction $\alpha' = 0^\circ$ .....	94
Fig. 5.32. Maximum pressure coefficient (time-mean) in the surface A as a function of wind direction and Jensen-number for pyramid P70 ( $h = 274.75$ mm), P70a ( $h = 142.81$ mm) and P70b ( $h = 100$ mm). .....	95

Fig. 5.33.	Minimum pressure coefficient (time-mean) in surface A as a function of wind direction and Jensen-number for pyramid P70 ( $h = 274.75$ mm), P70a ( $h = 142.81$ mm) and P70b ( $h = 100$ mm).....	96
Fig. 5.34.	Distribution of the standard deviation of pressure coefficient fluctuations in the surfaces of pyramid P70 ( $h = 274.75$ mm), P70a ( $h = 142.81$ mm) and P70b ( $h = 100$ mm), at wind direction $\alpha' = 0$ .....	97
Fig. 5.35.	Maximum standard deviation of pressure coefficient fluctuations in surface A as a function of wind direction for pyramid P70 ( $h = 274.75$ mm), P70a ( $h = 142.81$ mm) and P70b ( $h = 100$ mm).....	97
Fig. 5.36.	Drag coefficients of pyramids as a function of pyramid base angle.....	99
Fig. 5.37.	Drag coefficient of pyramids as a function of wind direction .....	100
Fig. 5.38.	Drag coefficient of pyramids as a function of Jensen-number, P70 ( $h/z_0 = 110$ ), P70a ( $h/z_0 = 57$ ) and P70b ( $h/z_0 = 40$ ) .....	100
Fig. 5.39.	Lift coefficient of pyramids as a function of pyramid base angle .....	101
Fig. 5.40.	Lift coefficient of pyramids as a function of wind direction .....	102
Fig. 5.41.	Lift coefficient of pyramids as a function of Jensen-number, P70 ( $h/z_0 = 110$ ), P70a ( $h/z_0 = 57$ ) and P70b ( $h/z_0 = 40$ ) .....	103
Fig. 5.42.	Moment coefficient as a function of pyramid base angle.....	104
Fig. 5.43.	Moment coefficient as a function of wind direction.....	104
Fig. 5.44.	Moment coefficient as a function of Jensen-number, P70 ( $h/z_0 = 110$ ), P70a ( $h/z_0 = 57$ ) and P70b ( $h/z_0 = 40$ ).....	105
Fig. 6.1.	Solution domain for the numerical computation representing the simulated wind tunnel (“numerical wind tunnel”).....	111
Fig. 6.2.	Comparison of experimental and numerical simulation of the atmospheric boundary layer flow in the wind tunnel, .....	113
Fig. 6.3.	Representation of the pyramid geometry in the numerical model.....	113
Fig. 6.4.	Visualization of flow structure in the lee of the pyramid P60, from FLOVENT visualization program.....	114
Fig. 6.5.	Vector plots at $y/l = 0$ for pyramid P70n, from FLOVENT visualization program .	115
Fig. 6.6.	Vector velocity field at the near bottom of pyramid P70n ( $u/u_0$ ).....	115
Fig. 6.7.	Cavity at the lee of the pyramid P70n, depicted from FLOVENT visualization program.....	116
Fig. 6.8.	Longitudinal mean velocity profiles at $y/l=0$ .....	118
Fig. 6.9.	Longitudinal mean velocity profiles at $y/l=0.25$ .....	120
Fig. 6.10.	Longitudinal mean velocity profiles at $y/l=0.50$ .....	122
Fig. 6.11.	Vector velocity fields at the $y/l = 0$ for different pyramids .....	123
Fig. 6.12.	Comparison of recirculation zone between numerical and experimental results, in the windward and leeward side of the pyramid .....	124
Fig. 6.13.	Comparison of the recirculation zone area at $y/l = 0$ for numerical and experimental results. ....	125

Fig. 6.14 Comparison of experimental and numerical results for the reattachment length ( $x_r/h$ ) at the lee of the pyramids as a function of the pyramid length and height ratio.....	126
---	-----

# List of Tables

Table 3.1. Atmospheric Boundary Layer Wind Tunnel at University of Karlsruhe.....	30
Table 3.2. $Lu_x$ in the nature compared to the simulated flow .....	36
Table 4.1. Geometry of the pyramids.....	40
Table 4.2. Characteristics of the LDA system .....	46
Table 5.1. Comparison of reattachment length to height ratio ( $x_r/h$ ) at the leeward side of the pyramid between the experimental results and calculation. ....	67
Table 5.2. Aerodynamic coefficients .....	98
Table 5.3. Qualitative summary of the effects of the investigated parameters to the pressure characteristics.....	106
Table 5.4. Typical value of mean pressure coefficient ( $c_p$ ) on the pyramid surfaces and aerodynamic coefficients (drag, lift and moment coefficient) in minimum and maximum range.....	106

# List of Symbols

$\vec{u}$	Velocity vector
$\Delta f$	Doppler beat frequency (signal)
$A_{\text{mean}}$	Mean area for the influence of the pressure taps
$A_{\text{proj}}$	Projected area of the pyramids
$c$	Velocity of light
$c_d$	Drag coefficient
$c_{\text{dyn}}$	Dynamic coefficient
$c_e$	Exposure factor
$c_f$	Force coefficient
$c_g$	Gust factor
$c_l$	Lift coefficient
$c_{m-z}$	Moment coefficient working at the z-axes
$c_p$	Mean pressure coefficient
$c_p'$	Pressure coefficient fluctuation (rms)
$c_{pi}$	Internal pressure coefficient
$d$	Displacement thickness
$F$	Force
$f$	Frequency
$f'$	Doppler shifted light frequency, emitter
$f_0$	Laser light frequency
$f_D$	Doppler shifted light frequency, detector
$f_E$	Driver frequency for bragg cells
$G$	Production of turbulence kinetic energy due to buoyancy
$h$	Pyramid height
$I_u, I_v, I_w$	Turbulence intensity of u, v, w- vector velocity component
$k$	von Karmàn constant
$L_c$	Length scale characteristic
$L_{ux}$	Integral length scale
$M$	Model scale
$N$	Nature scale
$p$	Pressure
$P$	Shear production
P30 to P70	Pyramid with base angle 30° to 70°
$p_{\text{stat.}}$	Static pressure at the reference
$p_{\text{surface}}$	Total pressure on the surface of the pyramid
$q$	Dynamic velocity pressure
$q$	Dissipation energy of turbulent kinetic energy
$q_h$	Dynamic velocity pressure at mean roof height
$q_{\text{ref}}$	Dynamic pressure at the reference (pyramid height)

## List of Symbols

Re	Reynolds number
Re <sub>R</sub>	Roughness Reynolds number
R	Auto correlation function
S	Spectral density
t	Time
U	Velocity of undisturbed stream
u <sub>⊥</sub>	Velocity component perpendicular to bisector of crossing beams
u*	Velocity friction
u', v', w'	Fluctuation rate in x, y, z directions
u <sub>0</sub>	Mean velocity at the boundary
u <sub>c</sub>	Velocity characteristics
u <sub>ref</sub>	Mean velocity at the reference (pyramid height)
u <sub>surface</sub>	Velocity where p <sub>surface</sub> is measured
u <sub>z</sub>	Mean velocity at height z
x, y, z	Cartesian spatial coordinates
z <sub>0</sub>	Roughness length
z <sub>ref.</sub>	Reference height of 0.10 m

## Greek Symbol

α	Profile exponent of mean wind velocity profile for exponential velocity law
σ <sub>u</sub> , σ <sub>v</sub> , σ <sub>w</sub>	Standard deviation of u, v, w- vector velocity component
α'	Wind direction
θ	Base angle
φ	Semi angle of crossing beams
ψ	Streamline function
φ	Angle between direction of velocity vector and bisector of crossing beams
ρ	Air density
δ	Atmospheric boundary layer depth
ν	Kinematic viscosity
λ	Wave length
μ	Eddy viscosity
τ	Shear stress
ζ	Apex angle



# 1. Introduction

## 1.1. Background

Pyramids are often associated with historical buildings or tombs. Many historical buildings or monuments have been built in the shape of a pyramid (e.g. Pyramids in Egypt, Pyramid of Teotihuacan in Mexico built in the 6th century, Pyramid Spain in Canary Island built in the 15th Century). The most famous pyramids are the three Great Pyramids of Giza in Egypt. One of them is the Great Pyramid of Khufu (Cheops), which is the largest among the three and therefore known as one of the Seven Wonders of the World (see Fig. 1.1). It is the highest pyramid ever built, belongs to the fourth dynasty in Egypt and is dated 2606-2583 B.C. The size of the project is gigantic, around 2.3 million granite blocks of stone were used. Each stone is approximately 2.6 cubic meters in volume resulting in a total mass of around 6 million tons. The base area and the height of the pyramid are 230.40 m x 230.40 m and 146.60 m, respectively and the base angle is  $51^{\circ} 52'$  (see e.g. Schüssler, 1983 for detail description of the pyramid).

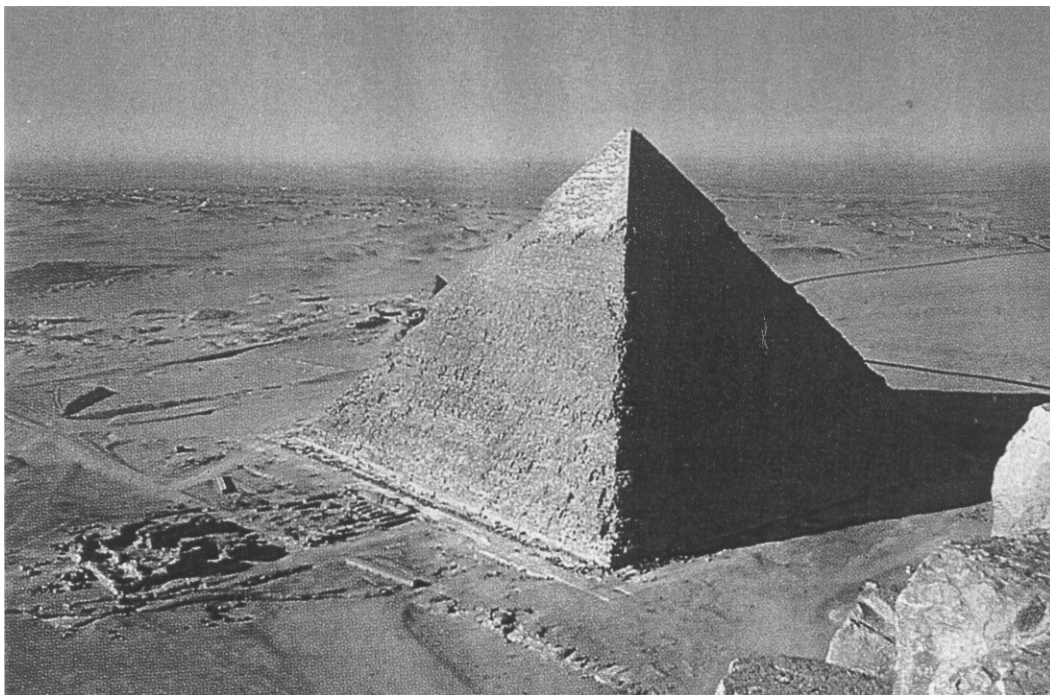


Fig. 1.1. Cheops pyramid in Giza, Egypt [Schüssler, 1983]

For millennia, the shape of the four-sided pyramid has been the subject of pondering for the curious-minded. Nevertheless, until today, no one can give an exhaustive account of the reasons why a tomb was constructed as such a giant regularly shaped monument. Questions such as why and how was it built?, what techniques did the builders use?, what kinds of instruments did they apply?, are still the subjects that interest many historical pyramid researchers.

The term pyramid comes from the Greek words *Pyramidos* and *Pyramis* which originated from the word *Pyre*. The word *Pyre* means fire and *Pyramidos* has been translated as "Fire in the Middle" [Mehler, 1997]. The meaning of the word *Pyramis* is obscure and it may relate to the shape of a pyramid. One description of pyramid at Merriam-Webster online dictionary is "*an ancient massive structure found especially in Egypt having typically a square ground plan, outside walls in the form of four triangles that meet in a point at the top, and inner sepulchral chambers*". Nowadays, many definitions of the term pyramid can be found that are not always related to the ancient structural buildings in Egypt. For example, agriculturists use the term pyramid to introduce a food pyramid concept and economics use it as transitive or intransitive senses to cost and profit. Pyramid scheme and pyramid selling are common terms in nowadays business. In the present study, the term pyramid refers to the shape of a structural building as described in the Cambridge dictionary, "*a solid object with a flat, often square, base and four flat triangular sides which slope inwards and meet to form a point at the top*".

Pyramid buildings are undergoing a renaissance in today's architectural design due to their attractive mystery that has fascinated many architects. Buildings as a whole such as hotels, offices, houses, museums, halls as well as building components like roofs, or entrance halls are constructed in a pyramid shape. For example, the museum entrance in Louvre, Paris has the shape of a pyramid. The pyramid is made of glass and consists of 666 glass elements with a total mass of 170 tons. The base length and the height of the pyramid are 35.4 m and 21.65 m, respectively. Knoll [1989] discussed the development of the construction principal and wind tunnel experiments for the wind load investigations of this pyramidal glass structure. However, the typical design values for wind load were not presented. Another example is the Luxor hotel in Las Vegas, which was built in 1994. The building has 30 storeys with a total height of 105 m and a base length of 183 m. Discussion regarding the construction and design principal have been reported by Tuchmann [1993] and Schilling [1994]. However, discussions with respect to the flow mechanisms were not covered. Other examples of today's pyramid buildings include the Pyramid Arena in Memphis, the Pyramid Hotel in Australia, the Pyramid House in Phoenix, the Hotelpyramide with Euromed Clinic in Fürth Germany, etc, see Fig. 1.2.



Fig. 1.2. Pyramidal structure in today's architectural design (online sources listed at the end of reference list).

From an aerodynamic engineering point of view, structural buildings with the shape of a pyramid have their own interesting and particular aerodynamic characteristics as compared to other 'usual' structural buildings (i.e. cuboidal). The pyramid geometry is different from other geometries mainly due to the modifying effect of the vertical wall taper that introduces important implications to environmental and industrial aerodynamics. For example, Fig. 1.3 shows sketches of the typical 2-D flow structures around cuboidal bluff bodies and pyramidal bluff bodies. The sketches show that the size and length of the recirculation zone decreases significantly for pyramidal buildings as compared to cuboidal buildings of the same height. The specific flow characteristics around pyramid will be discussed in more detail in Chapter 5.

However, despite its distinct aerodynamic characteristics compared to other 'usual' structural buildings, the flow and pressure characteristics around pyramidal structures have not yet been investigated completely. Very limited studies about pyramidal buildings can be found in the literature. A summary of the previous studies (e.g. Chyu et.al [1996], Ruck et.al [1997 ] ) will be given in Chapter 2.4. Consequently, the technical layout with respect to wind load assumption of pyramidal buildings are usually not listed in standard tables which underlines the need of systematic investigations for pyramidal structures. Therefore, detailed and accurate investigations of

the flow and pressure characteristics around pyramidal structural buildings are needed in order to understand the aerodynamics involved. The improved and detailed understanding of the aerodynamic characteristics around pyramidal buildings will be an important contribution for providing a reliable database for further development of aerodynamic standards as well as for further development of prediction tools.

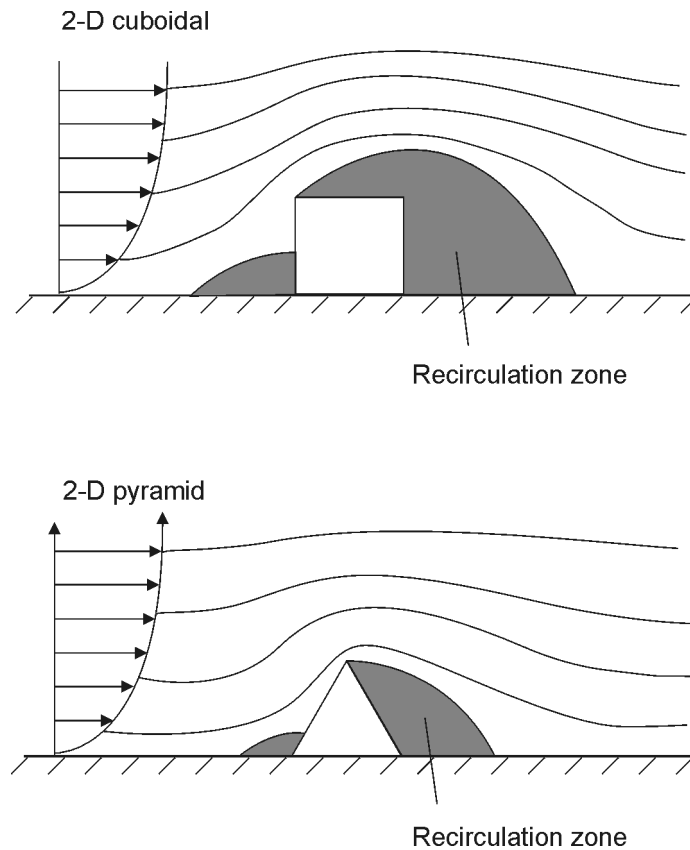


Fig. 1.3 Sketches of typical 2-D flow structure around bluff body

## 1.2. Objective

The objective of this study is to investigate the aerodynamic characteristics of pyramidal structures in order to gain an improved and detailed understanding of the flow around a pyramidal building. The flow characteristics around pyramidal buildings and the pressure distributions on the pyramid surfaces are therefore investigated in this study through detailed and accurate laboratory experiments. The present study focuses on the most important parameters affecting the flow and pressure characteristics that include the influence of base angles, the influence of wind directions and the influence of the pyramid heights with respect to a characteristic length.

As stated above, the technical layout with respect to wind load assumption of pyramidal buildings is usually not listed in standard tables. Normally, the standard tables for wind loads will provide typical design values of aerodynamic loading coefficients for different types of

buildings. With these values, civil engineers can calculate the loading on the structures caused by the wind. Typical design values for pyramidal buildings rarely exist. Therefore, the ultimate objective of this study is to provide typical values of pressure and aerodynamic coefficients specifically for pyramidal buildings. For practical purposes, this study is expected to fill in the gap of standard tables for wind load design.

### **1.3. Methodology**

The flow and pressure characteristics around pyramidal structures were investigated experimentally. The experiments were conducted in a closed-loop 29 m long atmospheric boundary layer wind tunnel of the Laboratory of Building- and Environmental Aerodynamics, Institute for Hydromechanics, University of Karlsruhe. Two measurement systems were installed in the wind tunnel, namely a flow measurement system with a 2D Laser Doppler anemometry (LDA) and a pressure measurement system with standard tappings.

Besides experimental investigations in the laboratory, numerical investigations were also conducted. They were performed with the aid of the software package FLOVENT version 3.2 from Flomerics Ltd., which is a specific software for numerical calculations in the area of building- and environmental aerodynamics.

## 2. Literature Review

### 2.1. Characteristics of Turbulent Flow

Most flows in nature are typically turbulent including the flow in the atmospheric boundary layer. Giving a precise definition of turbulent flow is difficult. One characteristic of turbulence is the irregularity or randomness. The velocity, pressure, and other flow quantities fluctuate irregularly in time and space. Turbulent flows are also characterized by three-dimensional and rotational motions. The three-dimensional irregular movements of the fluid parcels create a swirling or chaotic motion with high levels of fluctuating vorticity.

Due to its chaotic movements and high irregularity, a deterministic approach to turbulence problems is impossible. In order to describe and to analyse turbulent flows, one has to rely on statistical methods. The mathematical equations of turbulent flows correspond to non-linear differential equations. This has the consequence that the mathematical equations can only be solved for flows with well-known and well-defined initial conditions. In practice, the same turbulent flow condition can only be reproduced with a certain level of accuracy. Thus, the simulation of turbulence flows in experimental studies should be carried out carefully since small deviations in the initial conditions can lead to completely different results.

An important characteristic of turbulence is its ability to transport and mix fluid much more effectively than a laminar flow. This is well demonstrated by an experiment first reported by Osborne Reynolds in 1883 which is described by Pope [2000]. With his experiment, Reynolds established that the flow is characterized by a single non-dimensional parameter, now known as the Reynolds number  $Re$ . In general, it is defined by:

$$R_e = \frac{u_c \cdot L_c}{\nu} \quad (2.1)$$

where  $u_c$  and  $L_c$  are characteristics velocity and length scales of the flow, respectively, and  $\nu$  is the kinematic viscosity of the fluid. The Reynolds number is therefore a ratio between the perturbations introduced into the flow with the viscosity of the fluid which provides dissipative mechanism that tries to damp out perturbations. If the perturbations are sufficiently large so that the viscous forces of the fluid are no longer able to damp out these perturbations, the flow be-

comes unstable and enters the turbulent flow regime. Different types of flows are characterized by different critical Reynolds number. For instance, in Reynolds' pipe-flow experiment, the flow becomes unstable as soon as the critical Reynolds number of 2000 is exceeded and becomes fully turbulent when Re exceeds about 4000. Between these two critical Reynolds numbers, the flow is said to be in a transition zone between laminar and turbulent. In the atmosphere, turbulence can be induced by wind-shear or thermal convections. Reynolds numbers for atmospheric boundary layer flows can reach as high as  $10^8$  or  $10^9$ .

## 2.2. Governing Equations

The governing equations for the turbulent flow in an atmospheric boundary layer are presented in the following.

In tensor notation, the continuity equation is given as

$$\frac{\partial \rho}{\partial t} + \frac{\partial}{\partial x_k} (\rho u_k) = 0 \quad (2.2)$$

where  $\rho$  is the density at any location,  $x_k$  and  $u_k$  ( $k=1,2,3$ ) are the coordinates and velocities along the x,y,z directions, respectively. For an incompressible fluid, we have

$$\frac{\partial \rho}{\partial t} = 0, \quad \frac{\partial u_k}{\partial x_k} = 0 \quad (2.3)$$

The Navier-Stokes equation describing the real velocity field of a flow at the lower atmospheric boundary layer is as follows

$$\frac{\partial u_i}{\partial t} + u_k \frac{\partial u_i}{\partial x_k} = -g\delta_{3i} - \frac{1}{\rho} \frac{\partial p}{\partial x_i} + \nu \frac{\partial^2 u_i}{\partial x_k \partial x_k} \quad (2.4)$$

with  $g$  denotes the gravitational force and  $p$  the pressure. In this lower layer of atmosphere, the Coriolis force due to the Earth's rotation is negligible and does not govern the flow structure. The viscous properties of the fluid are expressed by the kinematic viscosity,  $\nu$ , which is defined as the ratio of the viscosity,  $\mu$ , to the fluid density  $\rho$  ( $\nu = \mu/\rho$ ). The derivation of the Navier-Stokes equation can be found in many literatures such as Schlichting [2000] and Tennekes and Lumley [1972]. The Navier-Stokes equations is a non-linear partial differential equations in  $u$  that arises from the dual role of the velocity determining the acceleration of a fluid particle. A technique for dealing with this non-linearity is by dividing the instantaneous  $u$ ,  $p$  and  $\rho$  terms into two parts, the time average part and the turbulent part, known as Reynolds decomposition

## 2. Literature Review

$$\mathbf{u}(t) = \bar{\mathbf{u}} + \mathbf{u}'(t) \quad (2.5)$$

$$\mathbf{v}(t) = \bar{\mathbf{v}} + \mathbf{v}'(t) \quad (2.6)$$

$$\mathbf{w}(t) = \bar{\mathbf{w}} + \mathbf{w}'(t) \quad (2.7)$$

$$p(t) = \bar{p} + p'(t) \quad (2.8)$$

$$\rho(t) = \bar{\rho} + \rho'(t) \quad (2.9)$$

The terms written with overbars denote the time average components and the primed letters denote the fluctuating components. Averaging over a sufficiently long period comparable to the typical time constant of the system, the mean values are independent of the averaging time  $t$ . This leads to the conclusion that the mean values of the fluctuating components are zero.

$$\overline{\mathbf{u}'(t)} = \overline{\mathbf{v}'(t)} = \overline{\mathbf{w}'(t)} = 0 \quad (2.10)$$

$$\overline{p'(t)} = 0 \quad (2.11)$$

$$\overline{\rho'(t)} = 0 \quad (2.12)$$

Substituting Eq. 2.5 to 2.12 into Eq. 2.4 and then averaging over time yields

$$\frac{\partial \bar{\mathbf{u}}_i}{\partial t} + \bar{\mathbf{u}}_k \frac{\partial \bar{\mathbf{u}}_i}{\partial x_k} = -g\delta_{3i} - \frac{1}{\rho} \frac{\partial \bar{p}}{\partial x_i} + \nu \frac{\partial^2 \bar{\mathbf{u}}_i}{\partial x_k \partial x_k} - \frac{\partial}{\partial x_k} \overline{\mathbf{u}'_k \mathbf{u}'_i} \quad (2.13)$$

The last term on the right hand side is a new additional shear stress term that arises due to the fluctuation. These additional stresses are called “apparent stresses” of the turbulent flow or also called the “Reynolds shear stresses” and can be written in tensor form as

$$\begin{bmatrix} \sigma'_x & \tau'_{xy} & \tau'_{xz} \\ \tau'_{xy} & \sigma'_y & \tau'_{yz} \\ \tau'_{xz} & \tau'_{yz} & \sigma'_z \end{bmatrix} = -\rho \begin{bmatrix} \overline{\mathbf{u}'^2} & \overline{\mathbf{u}'\mathbf{v}'} & \overline{\mathbf{u}'\mathbf{w}'} \\ \overline{\mathbf{u}'\mathbf{v}'} & \overline{\mathbf{v}'^2} & \overline{\mathbf{v}'\mathbf{w}'} \\ \overline{\mathbf{u}'\mathbf{w}'} & \overline{\mathbf{v}'\mathbf{w}'} & \overline{\mathbf{w}'^2} \end{bmatrix} \quad (2.14)$$

A general description for the total shear stress is given as

$$\tau_{ki} = \bar{\rho} \nu \left[ \frac{\partial \bar{\mathbf{u}}_i}{\partial x_k} + \frac{\partial \bar{\mathbf{u}}_k}{\partial x_i} \right] - \bar{\rho} \cdot \overline{\mathbf{u}'_k \mathbf{u}'_i} \quad (2.15)$$

Equation 2.13 which describes the transport of a fluid mass can as well be applied to the transport of other substances such as contaminants. Thus, the equation can be extended to



$$\frac{\partial \bar{c}}{\partial t} + \bar{u}_i \frac{\partial \bar{c}}{\partial x_i} = D \frac{\partial^2 \bar{c}}{\partial x_i \partial x_i} - \frac{\partial}{\partial x_i} \overline{u'_i c'} \quad (2.16)$$

where  $c$  is the concentration of the substance and  $D$  the molecular diffusivity coefficient. The total mass flux density  $j$  of a substance is governed by Fick's law

$$j_i = D \frac{\partial \bar{c}}{\partial x_i} - \overline{u'_i c'} \quad (2.17)$$

The first term on the right hand side describes the molecular diffusion process and the second term the turbulent mass transport component.

Looking again at Eq. 2.13 and 2.14, it is necessary to develop model equations in order to produce a relation between the Reynolds shear stresses and the quantities of the mean motion. Therefore, one uses "turbulence models" or "turbulence modelling" which will contain empirical elements. Different turbulence models exist such as the eddy viscosity model (Boussinesq, 1872) and the mixing length model (Prandtl, 1925).

When studying turbulence, it is important to examine how fluctuations are distributed around the averaged values and how adjacent fluctuations relate to each other [Tennekes et.al., 1972]. One way is through spectral analysis. The spectra give an indication of the energy distribution over various length or time scales and also an indication in which way eddies of different sizes exchange energy with each other.

The power spectral density  $S_{ii}$  of the velocity fluctuations  $u'_i(t)$  is related to the Fourier transformation of its auto-correlation function  $R_{ii}(\tau)$ . The auto-correlation function  $R_{ii}(\tau)$  describes the relation or correlation between the velocity fluctuation at time  $t$  with the velocity fluctuation at time  $t + \tau$ , in mathematical form

$$R_{ii}(\tau) = \lim_{T \rightarrow \infty} \frac{1}{T} \int_0^T u'_i(t) \cdot u'_i(t + \tau) dt \quad (2.18)$$

The power spectral density  $S_{ii}$  is thus written as

$$S_{ii}(f) = 2 \int_{-\infty}^{\infty} R_{ii}(\tau) e^{-j2\pi f \tau} d\tau \quad (2.19)$$

The importance of the spectra analysis in order to describe the turbulence flow characteristics in the atmospheric boundary layer will be shown and discussed further in this study (see Chapter 3).

### 2.3. Atmospheric Boundary Layer

An atmospheric boundary layer (ABL), which is also referred to as the planetary boundary layer, can be defined as ‘the part of the troposphere that is directly influenced by the presence of the earth’s surface, and responds to surface forcing with a time scale of about an hour or less’ Stull [1988]. In other words, the atmospheric boundary layer is the lowest part of the atmosphere that forms as a consequence of the interactions between the atmosphere and the underlying surface (land or sea). The effects of this surface force upon the flow decreases as the height above the ground increases and become negligible above a height of  $\delta$  known as the height or depth of the boundary layer. The height of a neutrally stratified boundary layer ranges from a few hundred metres to several kilometres, depending on the wind intensity, the roughness of the terrain, the seasons, the latitude, and the time of the day. Within the boundary layer, the wind speed increases with elevation; its magnitude at the top of the boundary layer is often referred to as the gradient speed.

The atmospheric boundary layer (ABL) is a very well mixed layer, because the pollutants that originating from close to the surface are uniformly distributed both horizontally and vertically. In this layer, the effects of the surface roughness, temperature and other properties are directly transmitted through the mechanism of turbulent mixing. This has important applications in the field of air pollution and wind engineering, wherein a knowledge of how wind and turbulence characteristics are distributed vertically and horizontally can be extremely helpful in predicting both ambient concentrations of air pollutants as well as the wind forces on structures [Stull, 1988].

Fig. 2.1 presents a schematic illustration of a typical boundary layer flow profile together with the vertical structure of the lower atmosphere over an urban canopy and its various layers during neutral and stable conditions. The surface layer (sometimes referred as Prandtl layer) is the lowest 10% of the atmospheric boundary layer. This layer is characterized by the variations of wind speed, temperature and other meteorological parameters with height. It also encompasses small-scale turbulence produced by surface roughness or friction which is sometimes further intensified due to heating of the surface by thermal convection. The depth of this layer is around 50m. This layer is also referred to as constant flux layer owing to near constant vertical fluxes of mass, momentum and heat. The wind direction remains more or less constant with height and the mean flow may be assumed horizontally homogeneous. As stated in Section 2.2, in this lower layer of atmosphere, the Coriolis force due to the Earth’s rotation is negligible and does not govern the flow structure.

The surface layer includes an important layer namely the roughness layer which is also commonly referred to as the canopy layer. The depth of the roughness layer is still subject to debate but it is very close to the earth’s surface and in the range of 2 to 5 times of the average building height [Roth 2000]. Consequently, the mean flow in this layer is highly affected by the

individual roughness elements. The flow is very inhomogeneous, contains small-scale and time dependent eddies.

When the altitude moves to the outer layer, the flow shows little dependence on the nature of the surface and the Coriolis force becomes also important. This region is sometimes referred to as the Ekman layer since Ekman [1905] first dealt with the effects of earth's rotation on ocean currents. Above the boundary layer, the frictionless wind balance is established and the wind flows with the gradient wind velocity along the isobars.

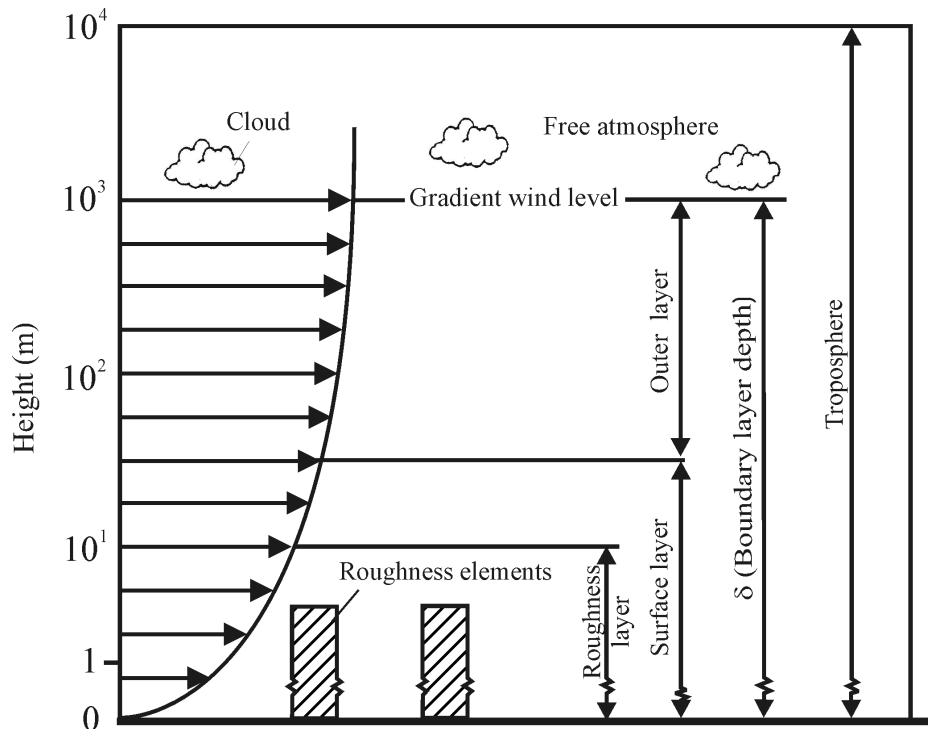


Fig. 2.1. Schematic of the vertical structure of the lower atmosphere and its various layers during neutral and stable conditions

In order to derive the mean wind profile of the atmospheric boundary layer, various methods have been developed (see e.g. Garrat [1994]). The earliest and most widely used method is the power law or exponential law. This method was first suggested by Archibald in 1886 and further elaborated by Davenport and others [Cermak, 1975]. This method represents the mean wind profile in horizontally homogeneous terrain. The power law is regarded by meteorologist as a superior representation of strong wind profiles in the lower atmosphere [e.g; Tennekes, 1973; Pasquill, 1972]. In the case of strong winds, thermal stratification is usually destroyed by intense mixing, thereby producing a neutral ABL. In such ABL, the mean wind velocity depends only on the height above the surface roughness (governed by topography). Thus, the vertical profile of velocity distribution can be conceived as a function dependent on a reference velocity at reference height. In mathematical form, the power law is described as:

$$\frac{u_z}{u_{ref}} = \left( \frac{z-d}{z_{ref}} \right)^\alpha \tag{2.20}$$

where  $z$  is the elevation,  $u_z$  is the longitudinal velocity at height  $z$ ,  $u_{ref}$  is the reference velocity in the height  $z_{ref}$ ,  $d$  is the displacement thickness and  $\alpha$  represents the power law exponent which depends upon the surface roughness (i.e. terrain types). Fig. 2.2 shows an example of different power law profiles for different types of terrain, obtained by Davenport in 1960. For design purposes, a classification of  $\alpha$  at different types of terrain has been recommended in many publications and standard codes, e.g. Wolfseher et.al. [1978], Plate [1995], EUROCODE 1 [1991].

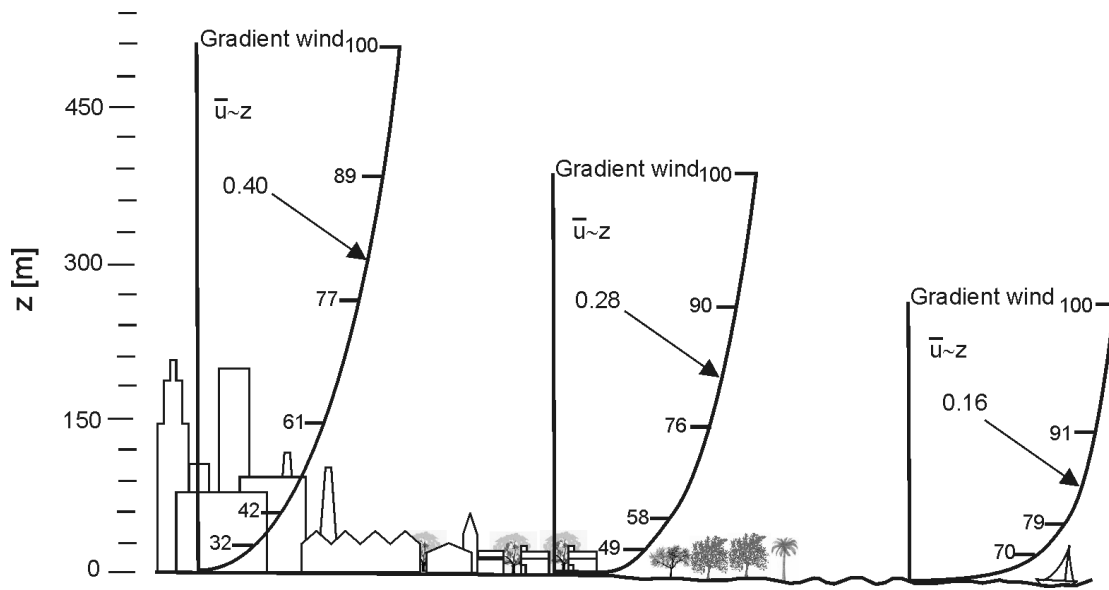


Fig. 2.2. The power law profiles for the velocity distributions in a boundary layer over homogeneous area [Plate, 1982].

Despite the superiority of the power law to represent strong wind profiles at the lower atmosphere, this method does not incorporate much of the turbulence effects. Another more elaborated law to describe the mean velocity profile and also the turbulence structures in the surface layer is the well-known logarithmic law. The logarithmic law is derived from an integration of the Boussinesq approximation (1877) whereby density is assumed to be constant except in the buoyancy term of the vertical velocity equation. The logarithmic law has been assumed that the wind shear and other flow characteristics in a neutral surface layer depend only on friction velocity  $u_*$  and roughness length  $z_0$  (see e.g. Plate [1995] and others). In mathematical form it may be written as:

$$\frac{u_z}{u_*} = \frac{1}{k} \ln \left( \frac{z-d}{z_0} \right) \tag{2.21}$$

with  $k = 0.4$  which denotes the von Karmàn constant

The friction velocity  $u_*$  is a measure of the strength of the turbulent variations in wind speed (the ‘gusts’) and the efficiency of the turbulence in mixing atmospheric constituents. The roughness length  $z_0$  characterizes the profile shape accounting for different surface properties. Many studies have suggested typical values of  $z_0$  for different terrains. However, there exist large scatter in these values, which has been discussed and summarized by Wieringa [1993]. He reviewed about fifty high-quality experiments on roughness of homogenous terrain types and published a table summarizing the various roughness lengths for different homogenous terrains.

Beside the mean wind profile, there are several other important parameters that characterize an atmospheric boundary layer, namely turbulence intensities, integral length scale and spectral distribution. A detailed description on these parameters will be given in Chapter 3, together with the discussion on the simulation of the atmospheric boundary layer flow in the wind tunnel.

## 2.4. Flow around Buildings

Many studies within the area of flow around obstacles can be found such as Hunt [1972], Meroney et.al [1982], Simiu [1996], Lawson, T. [2001]. Different studies might emphasise different areas of interest. From the results of these various studies, it is relatively difficult to draw a single conclusion since the building geometry and the characteristics of the incoming flow among these studies vary. However, despite the differences, some typical flow characteristics and phenomena of the flow around buildings can be addressed. In this section, the typical characteristics of the flow past buildings will be described.

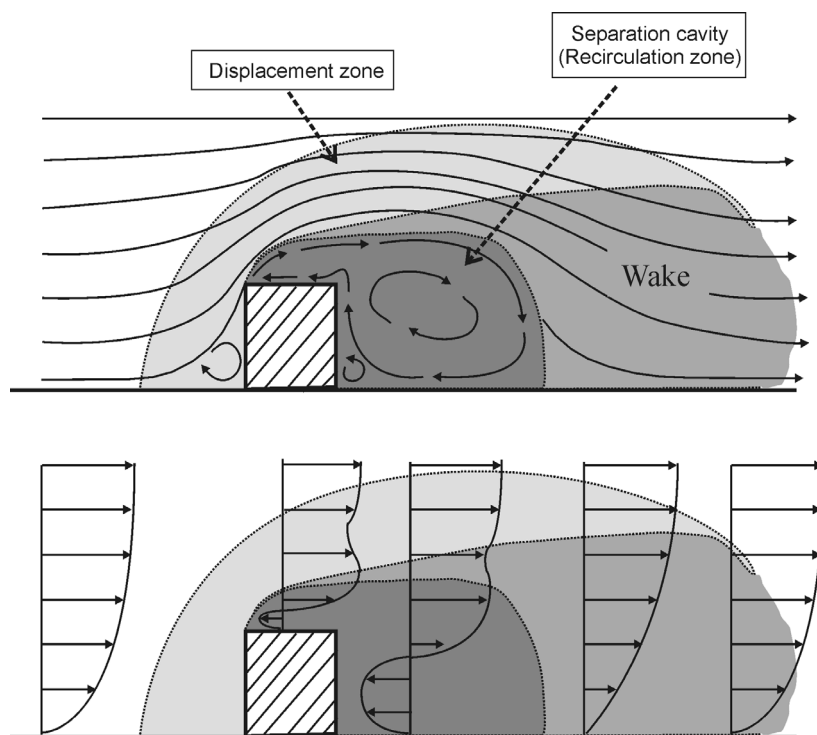


Fig. 2.3. Typical flow profiles in the centre plane of cuboidal buildings

Fig. 2.3 shows a typical two-dimensional flow structure around a cuboidal building. The area indicated by the dark colour near the building is known as the recirculation area, which is formed by the reversed flow. The recirculation zone is characterized by the flow separation and the reattachment around the bluff body. Flow separation is one of the most important phenomenon in aerodynamic problems involving flows past obstacles. Depending on the size of the Reynolds number, flow separation can take place in a steady or unsteady manner. The separation in the boundary layer occurs if fluid particles in the boundary layer are sufficiently decelerated by inertial forces so that the flow near the surface becomes reversed. These deceleration effects occur as a result of the presence of adverse pressure gradients in the flow. The recirculation zone in the lee of the building is characterized by the point where the flow reattaches again, known as the reattachment point.

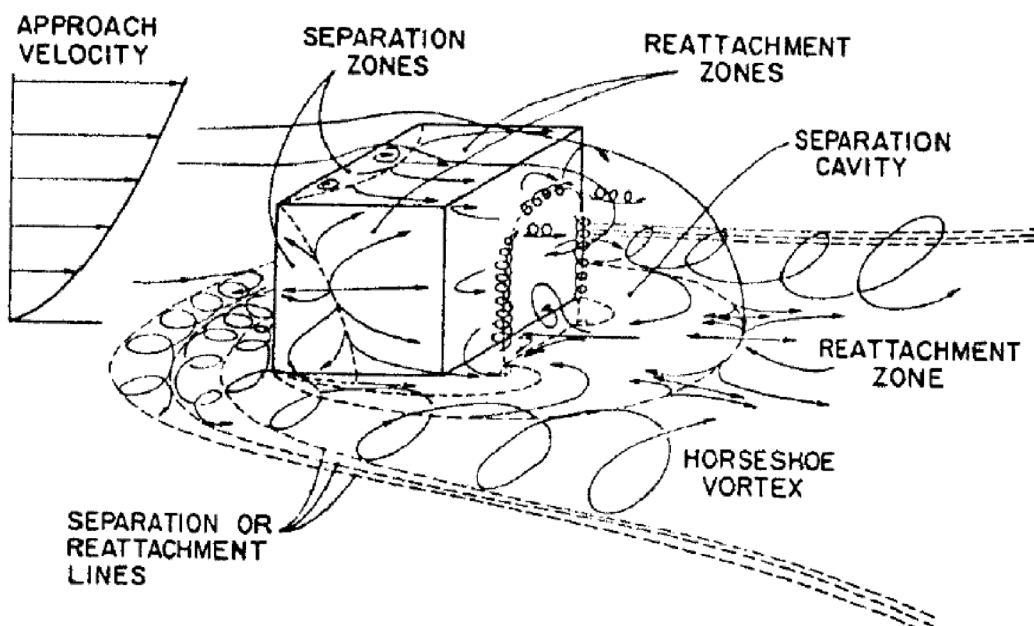


Fig. 2.4. Three-dimensional flow structure around cuboidal building [Woo et.al, 1977]

Fig. 2.4 shows a typical 3-D flow structure around a single cuboidal building which was described comprehensively by Woo et.al.[1977] and Peterka et.al., [1985]. The figure shows that the mean streamline forms a complex flow geometry. The flow approaching the building separates from the surface at a certain distance upstream of the building. This separation location is dependent, to the first order, on the building height-to-width ratio, the building height-to-boundary-layer-height ratio and the upstream surface roughness. The vorticity in this separated flow, in combination with the pressure distribution on the front of the building, results in a downward flow on the front of the building. This subsequently causes the separated flow to roll up into a vortex. The vortex is wrapped around the building by convection into a horseshoe shape. The horseshoe vortex can be identified in the flow at some distance downstream. The

flow structure where the vortices are identified or where the flow is still affected by the presence of the building is commonly called the wake.

The wind that blows on the front of the building forms a stagnation region between  $2/3$  and  $3/4$  of the building height depending on the building height-to-width ratio. From this region, the flow moves outward toward all front edges of the building. The flow separates at the front edge of the top and sides and may or may not reattach to the top or side before reaching the back edges. In

Fig. 2.4, a case of reattached flow is shown. The reattachment depends on the building height-to-width ratio, height-to-length ratio and upstream roughness (which determines the turbulence intensity of the approaching wind – a significant factor in distance of reattachment). Similar as the 2-D flow structure above, the point where the flow reattaches characterizes the recirculation zone and it will create a cavity in the lee of the building.

## 2.5. Wind Action on Buildings

Several types of loading are accounted when designing a building. Wind loading is one of the important types of loading, especially in areas with potential extreme wind conditions. The threats of climate changes and more frequent natural disasters caused by wind have put the wind loading as an important factor in designing a building. Damages and losses caused by wind had been reported in many articles and publications [e.g. Sacré, 2000; Heneka et.al., 2004]. Generally, damages caused by wind can be categorized into three scales. The first scale is for older structures that have deteriorated in strength through insufficient maintenance or for new structures that do not include wind load as a significant loading in their building construction specification. The second scale is due to occasional occurrence of extremely severe storms, which causes widespread damage to all classes of structure within the affected area. The third scale is damages caused by tornadoes, hurricanes, and possibility of dust devils through built-up areas [Cook, 1985].

In order to minimize damages caused by wind, it is necessary to include wind loading in the static planning of the building design. Hence, at least the first category of damages can be avoided. In modern definitions, wind loading actions and effects on the structures are reduced to the form of non-dimensional parameters, namely loading coefficients. There are two main loading coefficients, which are the pressure coefficient and the shear-stress coefficient. The pressure coefficient acts as a normal pressure on the building and the shear-stress acts due to the friction between the surface of a building structure and the local wind speed past the surface. However, in most cases of aerodynamically smooth surfaces, the shear-stress will be insignificant compared to the normal pressure because the viscosity of air is so small. Exception where shear-stresses may be significant are cases in which the area of the attached flow is particularly large, such as roofs of very long low building, large plate-like structures, canopies or dutch barns when wind is parallel to the surface [Cook, 1990]. Based on these reasons the shear- stress coefficient will not be further discussed in this study.

In addition, other important loading coefficients can be calculated from the normal pressure, namely the force coefficient and the moment coefficient. The force coefficient consists of action work in the horizontal and vertical direction, regarded as drag and lift coefficients, respectively. In some studies, these coefficients are sometimes called aerodynamic coefficients. More detail of the wind induced forces and moments will be described in Section 2.5.2.

### 2.5.1. Pressure Coefficient on Buildings

The pressure coefficients ( $c_p$ ) are calculated by dividing the differential pressures between the measured pressures on the buildings surfaces and the static pressure by the dynamic pressure at the reference. This is derived from Bernoulli's equations, which is a special form of the first Law of Thermodynamics. The first Law of Thermodynamics or the Law of Conservation of Energy, is often expressed as:

$$\text{Potential Energy} + \text{Kinetic Energy} = PE + \frac{1}{2} mU^2 = \text{Constant (K)} \quad (2.22)$$

where  $m$  is the mass of air and  $U$  is the velocity of the undisturbed flow. In case of a fluid or gas, the potential energy is represented by the static pressure and the kinetic energy is a function of the motion of the air and its mass. It is generally more convenient to use the density ( $\rho$ ) of the air as the mass representation. Thus, the special form of Bernoulli's equation can be expressed as:

$$\underbrace{p_{\text{stat.}}}_{\text{Static pressure}} + \underbrace{\frac{1}{2} \rho u_{\text{ref.}}^2}_{\text{Dynamic pressure}} = K \quad (2.23)$$

where  $p_{\text{stat.}}$  is the static pressure and  $u_{\text{ref.}}$  is the undisturbed velocity, both at a reference height, which in the present study is at the top of the building. Bernoulli's equation is usually stated as, "Static Pressure plus Dynamic Pressure is Constant." Based on Eq. 2.23, the total pressure at two different areas can be written as:

$$p_{\text{stat.}} + \frac{1}{2} \rho u_{\text{ref.}}^2 = p_{\text{surface}} + \frac{1}{2} \rho u_{\text{surface}}^2 \quad (2.24)$$

where  $p_{\text{surface}}$  is the static pressure at some point in the flow, which in the present study is the static pressure on the building surfaces, and  $u_{\text{surface}}$  is the velocity at the point where  $p_{\text{surface}}$  is measured. Thus, Eq. 2.24 can be arranged as:

$$p_{\text{surface}} - p_{\text{stat.}} = \frac{1}{2} \rho (u_{\text{ref.}}^2 - u_{\text{surface}}^2) = \frac{1}{2} \rho u_{\text{ref.}}^2 \left\{ 1 - \left( u_{\text{surface}} / u_{\text{ref.}} \right)^2 \right\} \quad (2.25)$$

and the pressure coefficient  $c_p$  can be formulated as:

$$c_p = 1 - \left( u_{\text{surface}} / u_{\text{ref.}} \right)^2 = \frac{p_{\text{surface}} - p_{\text{stat.}}}{\frac{1}{2} \rho u_{\text{ref.}}^2} = \frac{\Delta p}{q_{\text{ref.}}} \quad (2.26)$$



where  $q_{\text{ref}}$  is a dynamic pressure at the reference height. It is always more convenient to calculate the wind-induced pressure in a dimensionless form as stated above than as an absolute value. This is because the pressure fluctuations due to the wind are very small compared to the absolute atmospheric pressure ( $\rho_{\text{atm}} \approx 100 \text{ kPa}$ ).

For design purposes, most of the existing standard codes provide  $c_p$  – values for typical or basic types of buildings, building elements and components, such as free standing walls, circular cylinders, cuboids or sharp edge sections. In some cases, measurements using precise model scales are required in order to find the suitable  $c_p$  – values. Especially when the types of the building and the planned locations fail to be categorized as “typical” cases [e.g. Taylor, 1991; Uematsu et.al., 1997] or when parts of the structure require detail attention in order to avoid failure of the whole system [Cochran, 2004].

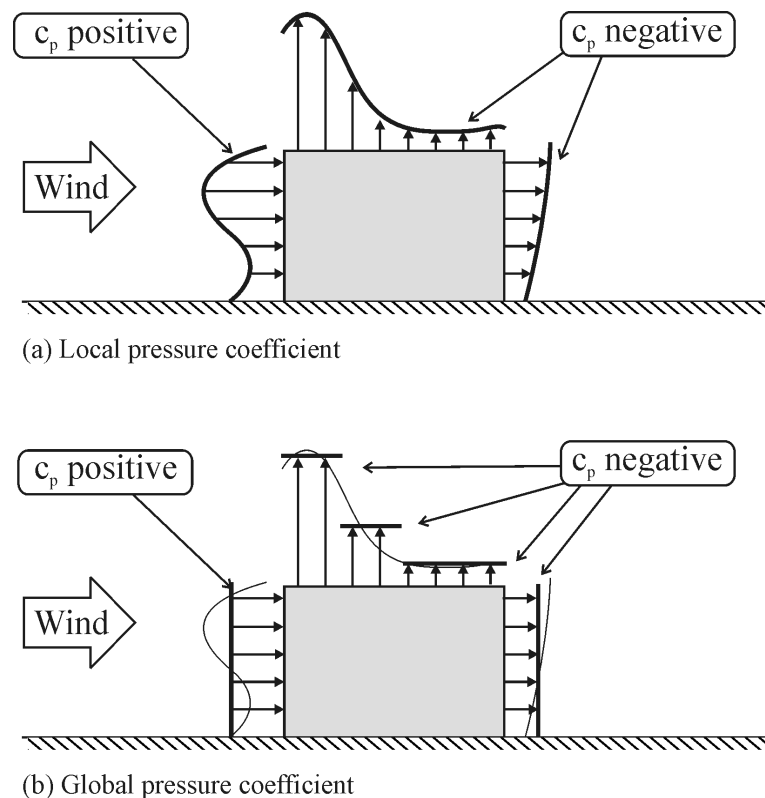


Fig. 2.5. Pressure coefficient at the centre plane of cuboidal building [Cook, 1990].

In order to have a general impression of pressure (i.e. wind action) on buildings, an example of pressure distributions on a cuboidal building is presented. Fig. 2.5 (a) and (b) represent a typical distribution of mean pressure coefficient ( $c_p$ ) in the middle of a cuboidal building induced by an atmospheric boundary layer wind flow. The arrows acting normally into the surface indicate positive pressures and arrows acting normally out from the surface indicate negative pressures (suctions). Fig. 2.5 (a) shows the distribution of the local mean  $c_p$ . Because pressure or

stress has the dimension of force per unit area, the global mean  $c_p$  for an area is equivalent to a uniformly distributed load. This is represented in Fig. 2.5 (b), for the same case. The roof can be divided into convenient areas. Because of these properties, the pressure coefficient is independent of any coordinate axis convention.

Fig. 2.5 represents only the mean pressure coefficient in the middle of a cuboidal building. Another way to represent the distribution of pressure coefficients on the building surfaces is by using contour plots. The contour plot of the pressure coefficients will give a better representation of how the pressures are distributed on the building surfaces. Fig. 2.6 shows an example of a pressure coefficients distribution on the surface of a cuboidal building when the wind blows in a direction of  $45^\circ$ . The figure shows that cuboidal buildings experience the maximum suction on the top surface near the upstream corner. The suction decreases as the wind goes further downstream of the building.

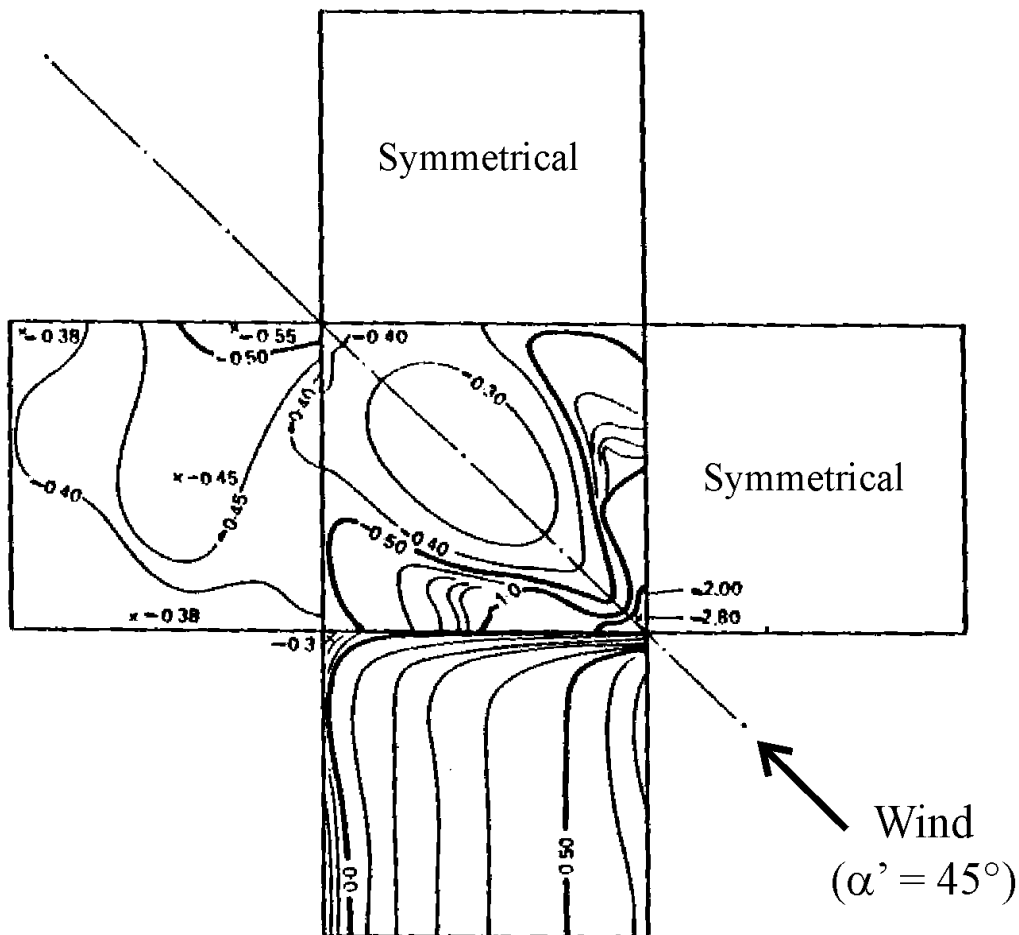


Fig. 2.6. Mean pressure distribution on the cuboidal building [Sachs, 1972]

The characteristics of pressure distribution shown in the example above are principally affected by the structure of the flow around the building. The maximum suction on the corner of the top surfaces is caused by strong vortices, which occur there. This is more clearly described by Sockel [1984] as presented in Fig. 2.7. The figure illustrates the “Delta-wing” vortices, which occur in the corner of the top surfaces when the wind blows in a direction of  $45^\circ$ . The centre of the vortices is the region with the highest negative pressure (suction) and an area characterized with high suction develops along the edges of the building. The figure suggests that the highest suction on the top of the cuboidal can reach  $-5$ . It is clear that if the appearance of delta wing vortices is not anticipated, it can cause serious damages to the building roof even at slow velocity conditions.

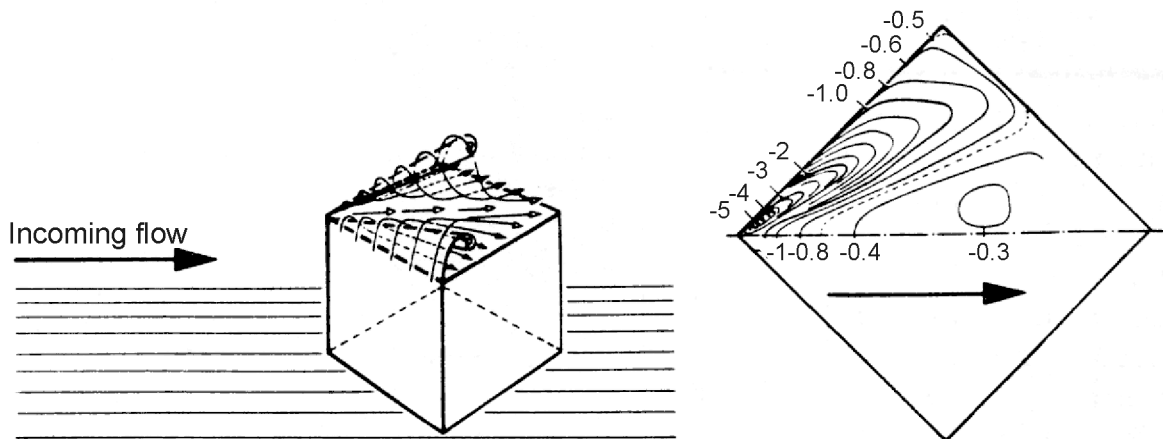


Fig. 2.7. “Delta-wing” vortices and the contour of pressure coefficient ( $c_p$ ) on the top of cuboidal building [Sockel, H., 1984]

For design purposes of low buildings, the wind pressure can be calculated in a general form by multiplying the pressure coefficient with the suitable dynamic pressure at the planned location. Most standards and codes of practices suggest some variations of the following general form for the calculation of the total wind pressure acting on low buildings [ASCE, 1987; EUROCODE 1991], such as:

$$p = q \cdot c_e \cdot c_g \cdot (c_p - c_{pi}) \quad \text{National Building Code of Canada} \quad (2.27)$$

$$p = q_{\text{ref.}} \cdot (c_g \cdot c_p) - q_{\text{ref.}} \cdot (c_g \cdot c_{pi}) \quad \text{American National Standard} \quad (2.28)$$

$$p = q_{\text{ref.}} \cdot c_e(z_e) \cdot c_{\text{dyn.}} \cdot c_f \quad \text{EUROCODE 1} \quad (2.29)$$

All the above equations have actually the same form only represented with different variables. For Eq. 2.27,  $q$  is the dynamic velocity pressure,  $c_e$  is an exposure factor accounting for the variation of the wind velocity with height and terrain exposure,  $c_g$  is the gust factor reflecting the gustiness of the wind and the fluctuating character of the pressure, and  $c_p$  and  $c_{pi}$  are the external

and internal pressure coefficients, respectively. In Eq. 2.28, the influence of exposure ( $c_e$ ) has been incorporated into  $c_g$  and  $q_{ref}$ .

The EUROCODE 1 [1991] gives the equation to calculate wind forces from pressure by multiplying the pressure ( $p$ ) with  $A_{ref}$  which is defined as the projected area of the structure, see Fig. 2.8. The calculation of the pressure is as presented in Eq. 2.29. Where  $z_e$  is the reference height for the local and internal pressure,  $c_{dyn}$  is the dynamic coefficient, and the external pressure is incorporated into the force coefficient ( $c_f$ ). The typical values of each coefficient for the design purpose with various conditions and standard building types are provided by this code.

### 2.5.2. Aerodynamic Coefficients on Buildings

As stated previously, there are two types of aerodynamic coefficients, the force coefficient and the moment coefficient. The force coefficient results from the effect of normal pressure integrated over all or part of the building and is defined as

$$c_f = F/q_{ref} A_{proj} \quad (2.30)$$

where  $F$  is the force and  $A_{proj}$  is a reference area which is required to make the coefficient non-dimensional.

The force acting on a small surface area  $A$ , over which a static pressure  $p$  is acting, is equal in magnitude to the product  $p$  times  $A$  and acts in a direction normal to the surface. On a flat surface, the net force acting on it due to the pressure will be the simple sum of the products of all the small areas and the local pressures acting on it [Houghton, 1976]. As illustrated in Fig. 2.8, the total force can be calculated as

$$F = p_1 A_1 + p_2 A_2 + p_3 A_3 \dots + p_n A_n. \quad (2.31)$$

In the present study, due to a symmetrical distribution of the pressure taps and its high spatial resolutions, the small area  $A$  can be generalized as  $A_{mean}$ , which is calculated from

$$A_{mean} = \frac{\text{Total surface area}}{\text{Number of taps on the surface}} \quad (2.32)$$

Mathematically, the total force  $F$  can be calculated as:

$$F = \int p dA_{mean} = q \int c_p dA_{mean} \quad (2.33)$$

Since force is a vector quantity, it is necessary to define a coordinate axes convention. There are two standard axes conventions, namely the body axes and the wind axes. In the body

axes, the axes are aligned relative to the building structure. The forces are the x-axis force ( $F_x$ ), the y-axis force ( $F_y$ ) and the z-axis force ( $F_z$ ). For the wind axes, the axes are aligned with the incoming wind and cross wind directions. The force induced by the incoming wind is called the drag force  $F_d$ , and the force induced by the cross wind is called the lift force,  $F_l$ . The lift force may act in either or both of the two orthogonal wind directions. In the present study,  $F_l$  is defined as the force working in the vertical direction (z-axes). Fig. 2.8 illustrates the coordinate axes convention of the force coefficients used in the present study.

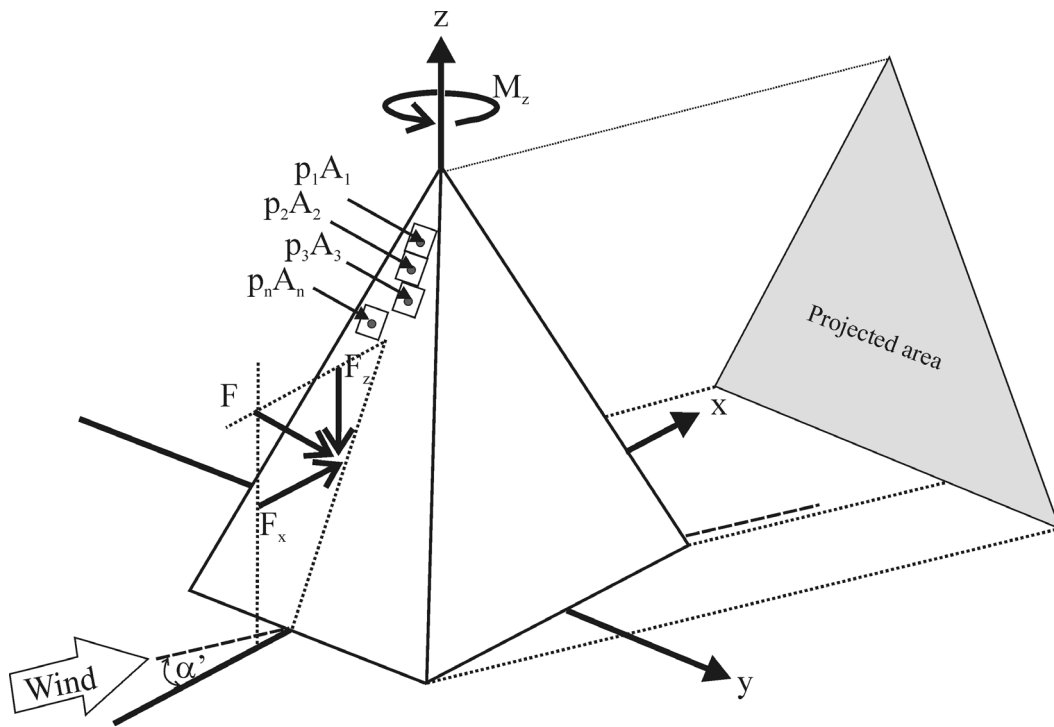


Fig. 2.8. Representation of coordinate axes convention for the present study, where the axes are aligned with the incoming wind and cross wind directions and the illustration of the projected area for the pyramids.

Several alternative definitions for the reference area can be used [Cook, 1990]. In this study, the reference area is defined as the projected area of the building in the wind direction (indicated as  $A_{proj}$ ). Consequently, the projected area changes in value with the wind direction which is calculated as follows:

$$A_{proj} = A_x \cos \alpha' + A_y \sin \alpha' \quad (2.34)$$

where  $\alpha'$  is the wind direction,  $A_x$  and  $A_y$  are the surface areas perpendicular to the x and y – axes, respectively. In the present study,  $A_x$  and  $A_y$  are equal.

The second aerodynamic coefficient is the moment coefficient. It is an action effect resulting from the normal pressure and shear-stress actions multiplied by their moment arms and integrated over all or part of the buildings structure. The moment coefficient is defined as

$$c_m = \text{Moment} / (q_{\text{ref}} A_{\text{proj.}} l_{\text{ref}}) \quad (2.35)$$

where  $M$  is the moment,  $A_{\text{proj.}}$  is the projected area and  $l_{\text{ref}}$  is a reference moment arm. There are three possibilities of moments, each of them works on different axes. Therefore, the reference moment arm depends on which axes the moment is working. In the present study, only the moment working along the  $z$ -axes is discussed ( $c_{m-z}$ ) whereby the  $l_{\text{ref}}$  can be defined as the pyramid base length.

## 2.6. Previous Investigations on Pyramidal Buildings

As stated before, very limited technical literature focusing on the aerodynamics of pyramidal buildings can be found. Most of the previous technical studies, which provide information such as the reliability of performance and the improvement of the economy of design, are related to conventional building shapes (i.e cuboidal or cylinder) and tall buildings [ASCE, 1996; Isyumov, 1999].

Chyu et.al [1996] studied the flow around surface-mounted pyramid, which concentrated mainly on qualitative observations drawn from mass and heat transfer measurements. The study showed that the mean flow structure around surface-mounted square-based pyramids shares some similarity with the flow around cubes and hemispheres. However, the influence of the wall taper gives rise to some distinctive vortical structure, which has been discussed in Section 1.1. They also concluded that different types of bluff bodies would create different reattachment length. Cubical structure with wind direction  $\alpha' = 45^\circ$  induces the longest reattachment length downstream, followed by, cubical structure, cylinder, pyramid and hemisphere with wind direction  $\alpha' = 0^\circ$ .

Ruck & Roth [1997] carried out experimental investigations, which involved 2 types of pyramids. They were able to show interesting phenomena of the flow and pressure characteristic around pyramids. Summarizing the results of the pressure measurements of all investigated models indicates that in contrast to flow around cuboidal bluff bodies where the upper edges are exposed to high suction, the highest suction values around pyramids occur in the baseline region [see also Ikhwan et.al., 2002, 2003].

Heist and Gouldin [1997] performed an experimental study of a surface-mounted triangular obstacle. They showed the special characteristics of flow around the triangular cylinder and presented a discussion on the mean velocity, the Reynolds shear stresses, the momentum, the turbulent kinetic energy, the auto-correlation functions and the spectra. They concluded that the flow over a surface mounted triangular obstacle differs from the flow over backward-facing step be-

cause of the acceleration of the flow as it passes over the obstacles and separates. The acceleration has an effect on the structure parameter in the free stream, causing a dramatic increase before separation. Also the acceleration of the flow over the obstacle causes the boundary layer at the separation to be thin relative to the obstacle height.

Abuomar and Martinuzzi [2000, 2003] investigated seven pyramids with different apex angle ( $\zeta$ ) in thin and thick boundary layers. As conclusions, they were able to classify the flow around pyramids based on the nature of the wake periodicity as slender pyramid ( $15^\circ < \zeta < 75^\circ$ ) and broad pyramid. For slender pyramids, the mean flow along the side faces is characterized by a double-vortex structure rooted behind the leading edge of the pyramid corner. This structure is present when vortex shedding is observed. These vortices form vorticity concentration nodes directly behind the pyramid corners (dark pigment accumulation marked F in Fig. 2.9). For broad pyramids at small wind direction, only a single vortex structure is observed along the side faces. The wake structure is similar to that found around hemispheres [Acarlar et.al 1987 and Savory et.al, 1988]. A single arch forms where the vortex tubes are rooted directly behind the leading edge corners. Their study also showed that the flow (i.e. separation and reattachment zone) and the pressure characteristics do not significantly depend on the base angle.

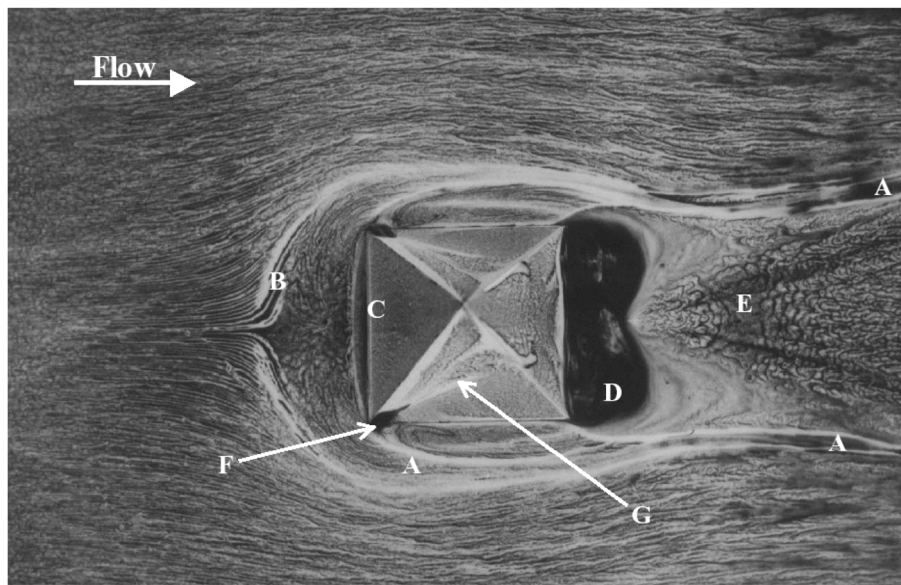


Fig. 2.9 Oil film visualization of the mean flow patterns on floor of pyramid faces ( $\zeta = 60^\circ$ ,  $\alpha' = 0^\circ$ ) [Abuomar et.al, 2000]

For design purposes, the Building Research Establishment (BRE) gives the distribution of the pressure coefficient ( $c_p$ ) on the pyramid surfaces for different wind directions ( $\alpha'$ ). However, the case is limited for a pyramid with a base angle  $45^\circ$  [Cook, 1990], as can be seen in Fig. 2.10. Fig. 2.10 (a) shows the distribution of pressure coefficient on surface A of the pyramid for different wind directions, Fig. 2.10 (b) and (c) shows a wind direction and surface notation for pyramid and A-Frame structure, respectively. Cook found that when the wind blow from  $0^\circ \leq \alpha'$

$\leq 60^\circ$ , the pressure coefficient contours are similar to surface A' of the A-Frame structure, except that the position of the maximum pressure is lower and moves into the bottom corner in skew winds. When the wind blow from  $60^\circ \leq \alpha' \leq 120^\circ$ , the contours are similar to surface B' of the A-Frame structure. However, the triangular shape of surface A and C of the pyramid create stronger conical vortex at the windward corner and the maximum suction of pyramidal structure occur at  $\alpha' = 90^\circ$ , where for A-Frame structure, the maximum suction occur at  $\alpha' = 120^\circ$ .

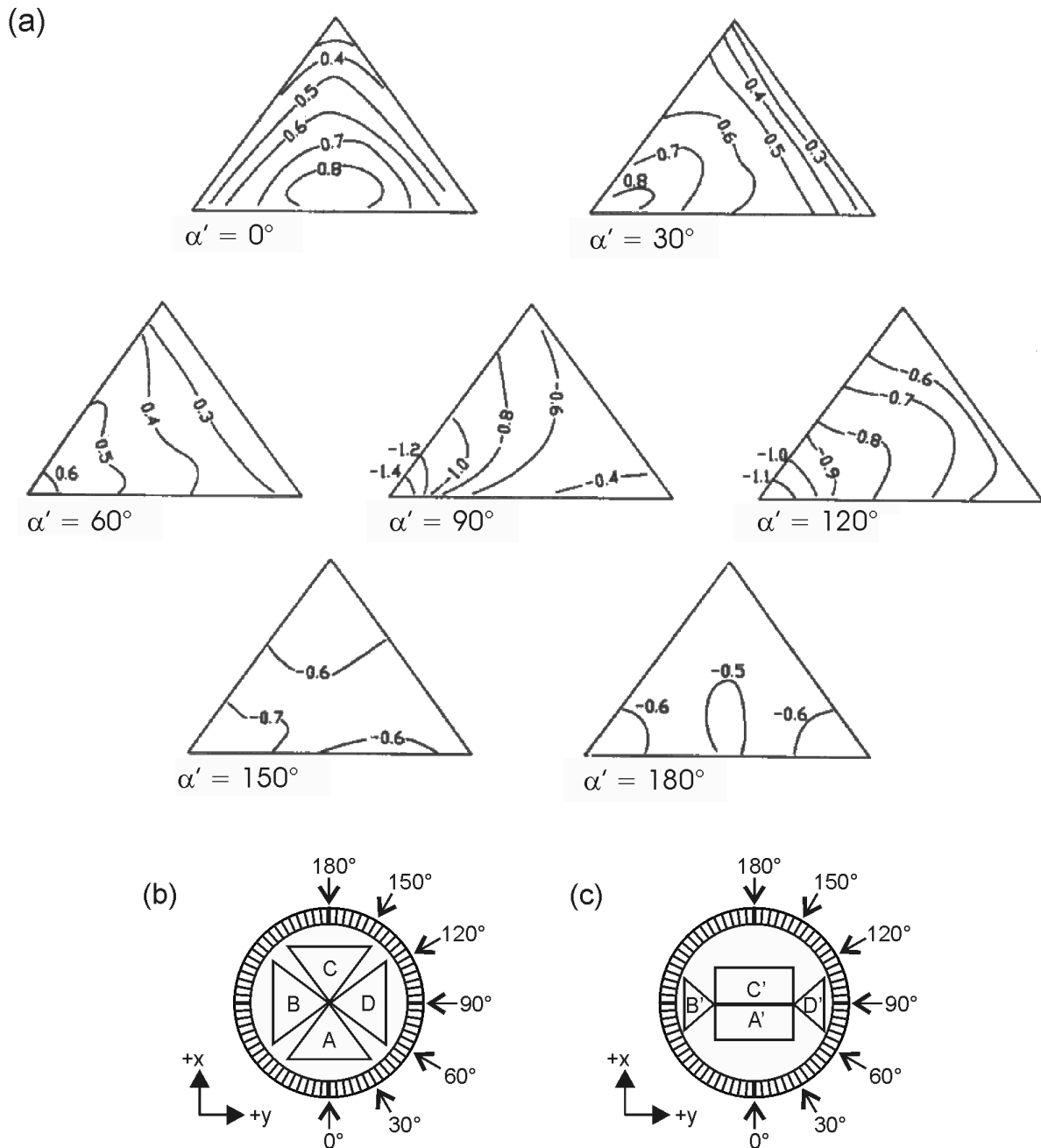


Fig. 2.10. (a) Design values of the pressure coefficient ( $c_p$ ) at different wind directions for the case of pyramid base angle  $45^\circ$  [Cook, 1990], (b) Wind direction for pyramidal structure, (c) Wind direction for A-Frame structure



### 3. Wind Tunnel Technique

Basically, there are two ways of measurement techniques in order to investigate the wind characteristic and its effect in the area of building aerodynamics. The first one is through field measurement with the original size of the buildings in natural wind conditions. Hereby, the measurements can only take place when the construction of the object under consideration has been completed. In some other cases, prototypes in full-scale or big-scale models are built. Another possibility of field measurement is by constructing a simple prototype, which consists of only some of the building's components. For example, Robertson et.al [1998] and Richards et.al. [2001] conducted field measurements of a free-standing wall and a 6 m cube, respectively. Obviously, field measurements will give results that come close to the real conditions but they are connected with a large financial expenditure especially if subsequent modifications at the object are required. Nevertheless, attempts at large-scale measurement are still important, because they permit conclusions on the reliability of small-scale measurements [Sullivan et.al., 1993].

The second way of measurement is through laboratory measurements at model scales in the wind tunnel. Frank H. Wenham constructed the first wind tunnel in 1871. He was a self-taught British engineer whose interests spanned a wide range of engineering applications. At that time, wind tunnel were primary used by airplane designers to have a better understanding of how air moved over aircraft surfaces. The idea was simply to blow air past a stationary aircraft and a wing model [Baals et.al, 1981]. For the application of wind tunnels in building aerodynamics, a so called boundary layer wind tunnel was required. The concept is to simulate the flow in the lower layers of the atmosphere down to the earth's surface. It goes back to the beginning of the 1940's when Wieghart in Göttingen used a boundary layer flow at the wind tunnel floor to investigate the spread of plumes. However, the length scale characteristics of the wind tunnel was too small to allow wider applications, especially for the application in building aerodynamics [Wieghart, 1948; Ermshaus et.al., 1997]. Jensen in Denmark (1958), Cermak in the USA (1958), and Davenport in Canada (1965) were considered as the pioneers in designing special boundary layers wind tunnels for wider applications in building aerodynamics [Neimann, 1993].

Before conducting measurements in a wind tunnel, ideally, the incoming flow should be simulated as similar as possible to the conditions in nature, which are determined as early as 1932 by Flachsbarth. He was the first who pointed out the differences between drag or pressure coefficients measured in a uniform flow and in a boundary layer flow [Simiu, 1996]. However, it

is almost impossible to achieve similarity for all flow characteristics. This is mostly due to the Reynolds number effects since it is almost impossible to achieve a Reynolds number similarity in the wind tunnel. As the kinematic viscosities between the model and nature ( $\nu_M = \nu_N$ ) are the same, the velocity in the wind tunnel has to be much higher than the wind velocity in nature in order to achieve the same order of Reynolds number. For example, a model in a wind tunnel having a scale of 1/200 would require a wind velocity that is 200 times greater than its velocity in nature, which is obviously unrealistic. As a consequence, one has to determine which flow characteristics are most important to be duplicated or simulated when performing wind tunnel measurements.

In the following section, the similarity criteria between nature (N) and model (M) are described, which consists of the similarity of incoming flow, the flow around buildings, and the wind load. Before presenting the characteristics of the simulated flow in the wind tunnel of the present study, general descriptions of the atmospheric boundary layer wind tunnel and the modelling technique in the wind tunnel are presented.

## 3.1. Similarity Criteria

A detailed description of wind tunnel modelling and the technical layout of atmospheric boundary layer flow simulation in wind tunnels is given by Plate [1982]. For standardisation of wind tunnel modelling, the Wind Technology Association (*Windtechnologische Gesellschaft, WTG*) published a guideline for wind tunnel experimentation in the area of building aerodynamics, which is covered in Plate [1995]. This guideline gives the similarity criteria in the wind tunnel for incoming flow, flow around building and wind loads. Before applying these criteria, it must be ensured that all models are geometrically similar.

### 3.1.1. Similarity of Incoming Flow

- Theoretically, the first criterion for the similarity of the incoming flow between nature and in the wind tunnel is determined by the Reynolds number similarity. However, as described before, it is unrealistic to apply Reynolds number similarity in order to simulate the atmospheric flows in wind tunnels. To overcome this problem, the concept of Reynolds number independence in fully developed turbulent flow has been widely accepted and hence the Reynolds number similarity criterion can be neglected.

In 1972, Snyder proposed the use of a roughness Reynolds number ( $Re_R$ ) to define the criterion for Reynolds number independence. He claims that if the modelled flow conditions satisfy the criterion of  $Re_R > 2.5$ , the whole flow-field around the model will change very little despite variation in the Reynolds number [Snyder. 1972]. On the other hand, Hoydysh et.al. [1974] argued that the roughness Reynolds number does not ensure Reynolds number independence between the roughness elements but only ensures a fully rough flow over the roughness elements.

However, in the guideline for wind tunnel experiments from WTG [Plate, 1995], the use of roughness Reynolds numbers for similarity of the incoming flow in wind tunnels is indicated and supported by a study of Uehara et.al [2003]. Uehara et al. [2003] concluded that the roughness Reynolds number was suitable to define the critical Reynolds number for Reynolds number independence. They used the following criterion

$$\text{Re}_{R,M} = \frac{u_{*,M} \cdot z_{0,M}}{\nu} > 5 \quad (3.1)$$

in which  $u_{*,M}$  is the friction velocity and  $z_{0,M}$  is the roughness length both for the model, and  $\nu$  is viscosity. The friction velocity could be defined as the velocity in a motion wherein it is assumed that the eddies and the motion are on a sufficiently large scale for the effects of the viscosity to be neglected. It is given by the term  $(\tau/\rho)^{1/2}$  where  $\tau$  refers to the shear stress.

- The next criterion is that the mean velocity profile of the atmospheric boundary layer flow in the wind tunnel must be similar to the one occurring in nature. The mean velocity profiles must be well fitted using the exponential velocity law,  $u_z/u_{\text{ref}} = (z - d/z_{\text{ref}})^\alpha$ , which means that the profile exponent  $\alpha$  in the wind tunnel and in nature must be similar:

$$\alpha_M = \alpha_N \quad (3.2)$$

As described in Chapter 2.3, the mean velocity profile can also be expressed by a logarithmic law,  $u_z/u_* = (1/k) \cdot \ln(z - d/z_0)$ . With this law, the roughness length ( $z_0$ ) for simulated flow can be achieved. Therefore, the ratio between the roughness length of the model and nature could represent the model scale M.

$$\frac{z_{0,M}}{z_{0,N}} = M \quad (3.3)$$

- Beside the mean velocity profile, the profile of turbulence intensities  $I_i = \sigma_i/u_i$  in the wind tunnel has to be similar to the turbulence intensities in nature. ( $\sigma$  = standard deviation,  $u$  = mean wind velocity and  $i$  denotes for the magnitude along  $x,y,z$ )

$$I_i \left( \frac{z}{L_c} \right)_M = I_i \left( \frac{z}{L_c} \right)_N \quad (3.4)$$

where  $L_c$  is a characteristic length scale.

### 3. Wind Tunnel Technique

- In order to assure that the spatial distribution of the turbulence is similar to the nature, the integral length scale  $L_{ux}$  between the model and nature must also be similar:

$$\left( \frac{L_{ux}}{L_c} \right)_M \approx \left( \frac{L_{ux}}{L_c} \right)_N \quad (3.5)$$

- Another criterion is that the distribution of the turbulence fluctuations with the frequency between the model and nature must be similar. In other words, the normalized power spectral density function must be congruent with an application over the normalized frequency  $f_n = f \cdot L_{ux} / u$ :

$$\left( \frac{f \cdot S_{uu}(f)}{\sigma_u^2} \right)_M \approx \left( \frac{f \cdot S_{uu}(f)}{\sigma_u^2} \right)_N \quad (3.6)$$

where  $S_{uu}$  is spectral density for longitudinal velocity.

#### 3.1.2. Similarity of Flow Around Building

Identical to the similarity of the incoming flow, ideally, the Reynolds number in the model must be similar to the Reynolds number in nature in order to guarantee a similarity of the flow around the modeled buildings. However, since it is almost impossible to achieve the Reynolds number similarity, the guideline of wind tunnel experiments from WTG stated that for building models with sharp edges, the situation of the flow separation is fixed and independent starting from a certain Reynolds number. In this case, the Reynolds number should not fall below 10.000. The requirement for a similar flow past the buildings can be formulated as

$$Re_M = \left( \frac{u_c \cdot L_c}{\nu} \right)_M > 10000 \quad (3.7)$$

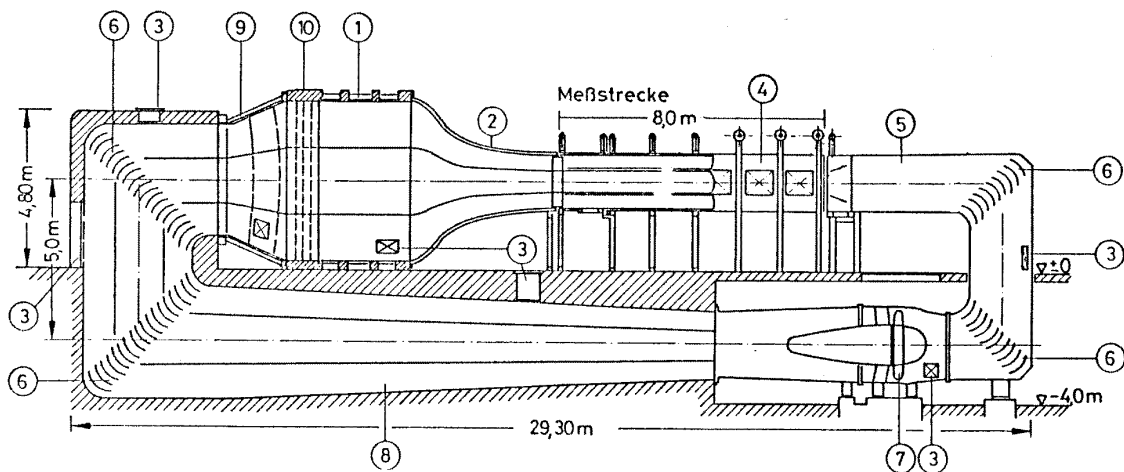
#### 3.1.3. Similarity of Wind Load

As stated in WTG, the similarity criteria for the wind loads between the wind tunnel and nature depends on the compliance of the similarity of incoming flow and flow around the building which is described in Section 3.1.1 and 3.1.2, respectively. In order to apply the results of pressure and loads measurements from the wind tunnel to nature, dimensionless values for pressure and force are used. As a reference, an undisturbed velocity pressure of incoming flow at the building height was used. This reference is the same reference for applications in nature, which is proposed by EUROCODE 1 [1991].

### 3.2. Atmospheric Boundary Layer Wind Tunnel

Wind tunnels may be classified according to their basic architecture (open-loop, closed-loop), according to their speed (subsonic or low speed, transonic, supersonic, hypersonic), according to the air pressure (atmospheric, variable-density), and their size (ordinary ones or full-scale). There are also numbers of wind tunnels such as meteorological tunnel, shock tunnel, plasma-jet tunnel, hotshot tunnel, that fall in a special category of their own [Garratt, 1994].

The experiments in this study were carried out in a closed-loop, low speed, atmospheric boundary layer wind tunnel at the Laboratory of Building- and Environmental Aerodynamics, Institute for Hydromechanics, University of Karlsruhe. Fig. 3.1 shows a schematic illustration of the wind tunnel used in the present study.



- (1) Pre-chamber (wood), 4.8 m clearance, (2) Nozzle (plastic), surface contraction 10:1, (3) Entering openings, (4) Measuring section cross section 2 x 2 m octagonal with 1.5 clearance (wood/steel), 6 side windows (acrylic glass), (5) Diffuser (steel), (6) Lattices (right-stell, left-concrete), (7) Blowers with direct current motor, impeller 2240 mm, (8) Large diffusor (concrete), (9) Wide angle diffuser with 2 textile filters, (10) 3 turbulence filters, 1.3 mm of mesh size.

Fig. 3.1. The closed-loop low speed wind tunnel at the Institute for Hydromechanics

The wind tunnel has a total length of 29.30 m. The actual measuring section is 8 m long and has a 1.5 m octagonal cross-section, capable of creating boundary layers with a depth of 0.5 m. The wind velocity in the measuring section can be varied within a range of 0 – 45 m/s. The typical properties of the wind tunnel are summarized in Table 3.1.

Table 3.1. Atmospheric Boundary Layer Wind Tunnel at University of Karlsruhe

<b>Location</b>	University of Karlsruhe, <i>Windkanalhalle</i> , Building 10.63.
<b>Begin to operate</b>	1974
<b>Short description of the facility</b>	Low-speed, closed-loop, close test section.
<b>Test section</b>	1.5 m octagonal cross-section, 8 m long
<b>Velocity</b>	Continuous velocity control from 0 to 45 m/s
<b>Turbulent degree</b>	0.1 %, no resonance places within the entire velocity range
<b>Pressure</b>	Atmospheric
<b>Fan speed</b>	90 kW (max. speed)
<b>Reynolds number based on 1 m</b>	$3.5 \times 10^6$ (maximum)
<b>Typical measured model</b>	Until $\pm 6$ m long, cross-section of building model until $\pm 0.2$ m
<b>Measurement facilities</b>	2-components laser Doppler anemometry forward scattering system and analogue pressure measurement system

### 3.3. Simulation of Atmospheric Boundary Layer Flow

A proper simulation of the atmospheric boundary layer in wind tunnels has been described by many researchers (e.g. Cermak [1971] and Counihan [1969], Davenport et.al [1967]). Recently, a review of the existing knowledge in this field including new suggestions for wind tunnel simulations was presented by Tieleman [1998, 2003], who studied wind loads on low-rise structures in the wind tunnel.

Fig. 3.2 shows the wind tunnel set up for the simulation of the atmospheric boundary layer (ABL) flow in the present study. The flow was developed along a 2.6 m section of roughness elements combined with two types of vortex generators (spires) 65 cm and 50 cm high, see Irwin [1981] for simple formulation for vortex generators. The roughness elements were produced by the Lego elements, which were arranged on the Lego base plates. This technique has the advantage that the arrangement and the height of the roughness elements could be easily changed. The arrangement of the Lego elements is shown in Fig. 3.3.

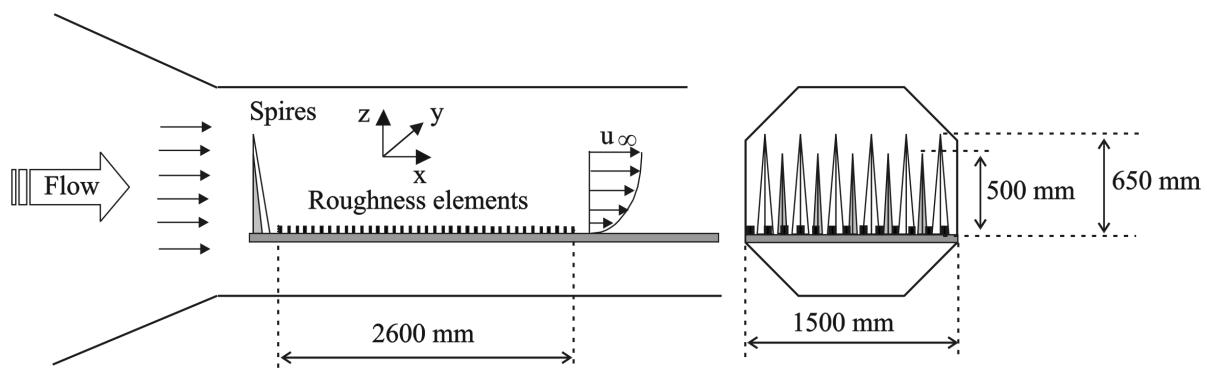


Fig. 3.2. Wind tunnel set up for atmospheric boundary layer flow

For the ABL flow simulation, the free stream velocity was fixed at  $u_\infty = 5$  m/s at  $z = 0.5$  m height and the corresponding Reynolds numbers (Re) based on the pyramid height (h) are varied from 12.000 to 90.000. According to the similarity criteria of the flow past buildings, these Reynolds numbers are sufficiently large (see Section 3.1.2).

In the present study, four main flow characteristics were simulated simultaneously, namely the mean wind velocity profile, the profile of turbulence intensities, the distribution of integral length scale with height and the power spectral density of longitudinal velocity fluctuations. By simulating these four main characteristics, the similarity laws of wind tunnel studies, which were described in Section 3.1, are expected to be fulfilled.

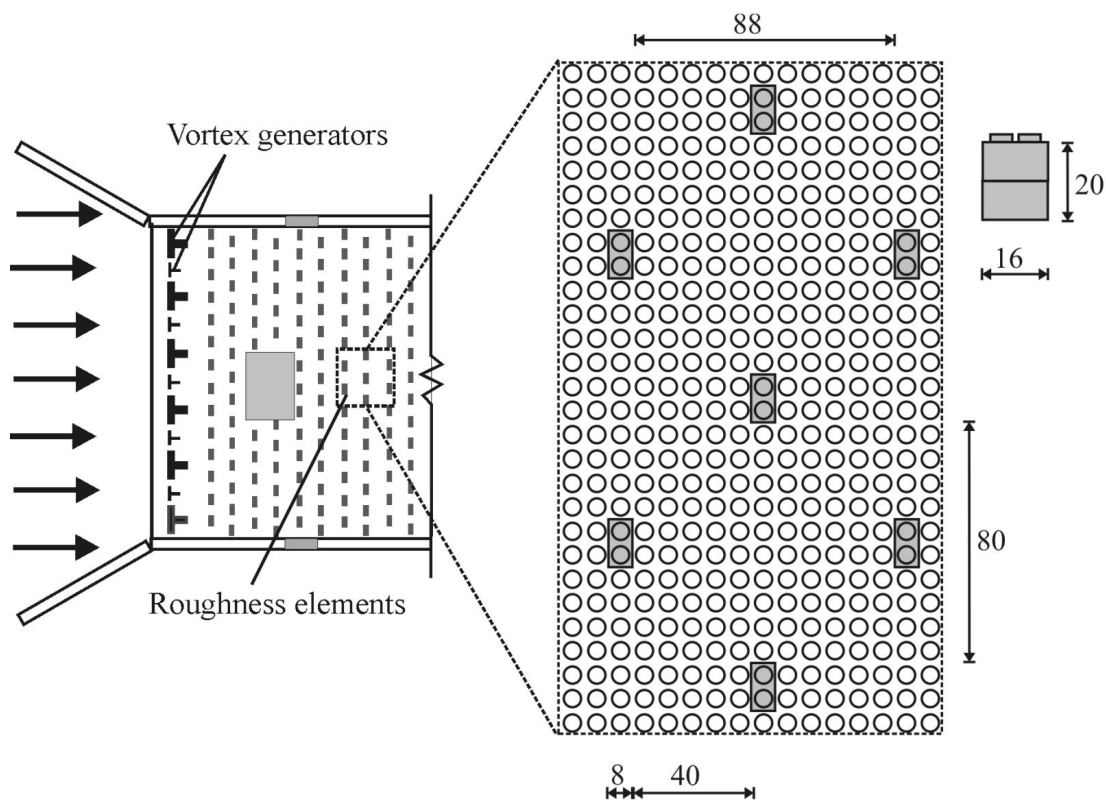


Fig. 3.3. Roughness elements arrangement in the wind tunnel

### **Mean Velocity Profile**

Fig. 3.4 shows the mean wind velocity profiles at two positions (upstream and downstream) of the test section in the wind tunnel. The profile indicated as ‘upstream flow’ is measured at 2.6 m after the roughness elements, which is the starting point of the investigating section (see Fig. 3.1). The end point of the investigating section is located 0.8 m downstream from the starting point and the measured profile is indicated in Fig. 3.4 as ‘downstream flow’. The results show that the velocity profiles are well fitted by the exponential profile with  $\alpha = 0.26$ , especially in the area below 300 mm ( $(z-d)/z_{\text{ref}} = 3.0$ ), which is equal to 60 m in nature. See Eq. 2.20 in

Chapter 2.3 for detail description of the exponential velocity law. The figure shows that the velocities above 300 mm are somewhat higher than the theoretical profile. However, the influence to the results is expected to be insignificant because this area is located sufficiently far enough from the model (pyramid).

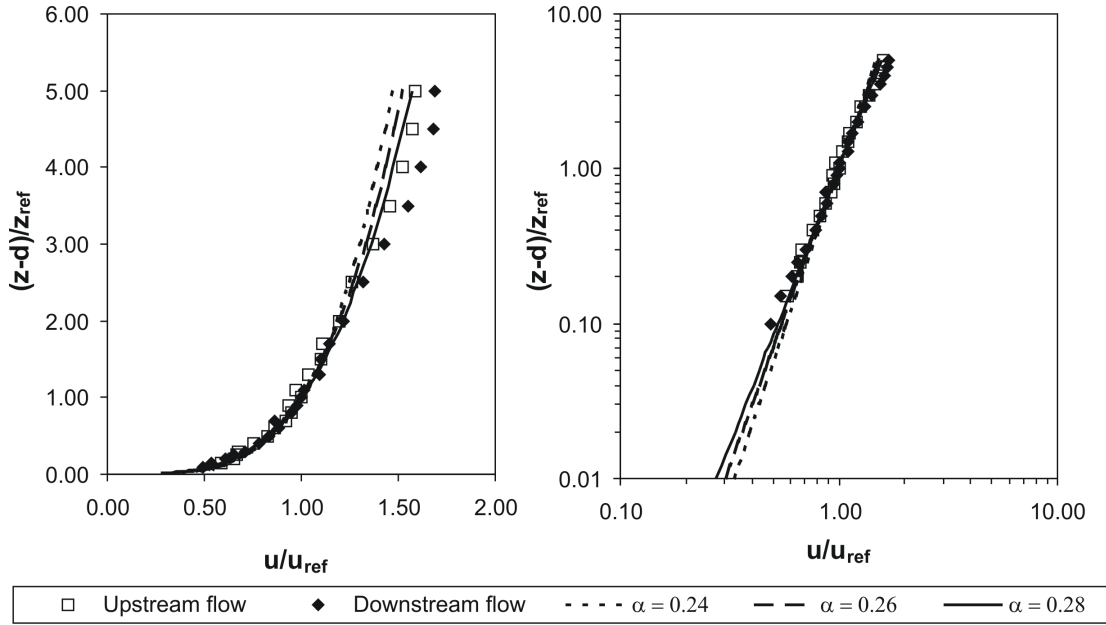


Fig. 3.4. The variation of mean wind velocities with height (exponential law)

Using the logarithmic law (Eq. 2.21), the experimental setup delivered a velocity profile with  $u_* = 0.422$  m/s and a roughness length of  $z_{0,M} = 2.49$  mm (Fig. 3.5). As shown in Fig. 3.5, the values below 30 mm (equal to 6 m in nature) are neglected. Theoretically, a boundary layer over an urban canopy could be subdivided into two layers, the surface layer and the roughness layer, see also Fig. 2.1. The depth of the roughness layer is still a subject of debate but it is in the range of 2 to 5 times the average building height. Roth [2000] stated that inside the roughness layer the turbulent fluxes and all other boundary layer properties are assumed to be influenced by individual elements. This means that the turbulent fluxes are neither spatially homogeneous nor is the logarithmic law fully applicable. Therefore, the value below 30 mm can be neglected. For the area above 300 mm (equal to 60 m in nature), the logarithmic law is no longer applicable since this law applied for surface layer (approximately 50 m above ground).

Based on the results of the simulated flow described above, the roughness Reynolds number (Eq. 3.1) can be calculated as follow:

$$Re_{R,M} = \frac{u_{*,M} \cdot z_{0,M}}{\nu} = \frac{0.422 \text{ m/s} \times 0.00249 \text{ m}}{1.5 \cdot 10^{-5} \text{ m}^2 / \text{s}} = 70$$



with the following experimental condition, temperature at 20° C and pressure at 10<sup>5</sup> Pa. The roughness Reynolds number is larger than 5. According to the similarity law, the simulated flow is considered to be independent of the Reynolds number.

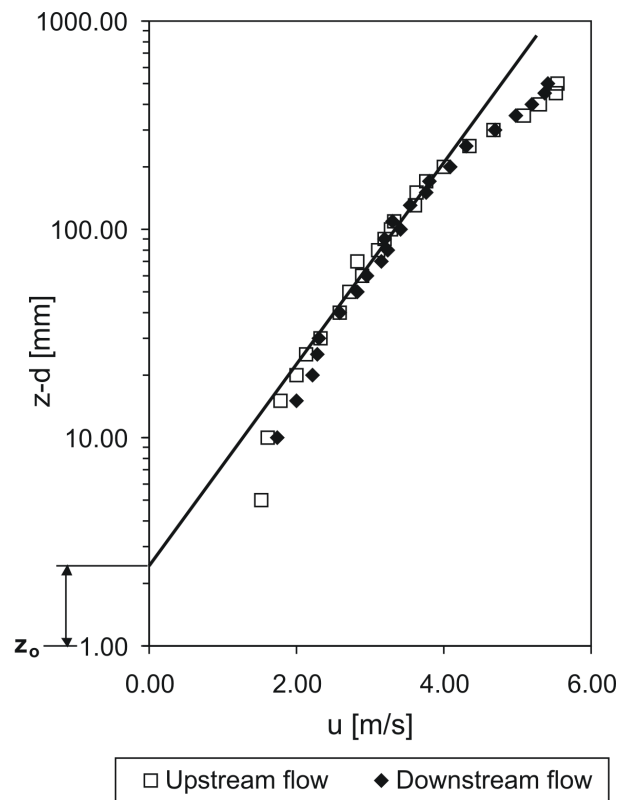


Fig. 3.5. The variation of mean wind velocities with height (logarithmic law)

According to the Plate [1995], when the exponential  $\alpha$  generated in the wind tunnel is comparable to the one in nature ( $\alpha_M = \alpha_N$ ), the simulated flow can be categorized between flow over suburbs ( $\alpha = 0.20 - 0.24$ ) and flow over city centres ( $\alpha = 0.28 - 0.40$ ). The typical value of  $z_{0,N}$  for flow over suburb ranges from 0.3 to 0.5 m [Plate, 1982], which is in a good agreement to the value of  $z_{0,N} = 0.3 - 1$  m suggested by EUROCODE 1: ENV 1991-2-4 [1991], and also to the value of  $z_{0,N} = 0.4 - 0.7$  m proposed by Wieringa [1993]. Using Eq. 3.3, the model scale can be calculated as follows:

$$\frac{z_{0,M}}{z_{0,N}} = \frac{2.49 \text{ mm}}{0.3 - 0.5 \text{ m}} \approx \frac{1}{200}$$

This means that the model in the wind tunnel corresponds to a model scale of 1:200. Based on the results, the mean velocity profile of the simulated flow in the wind tunnel is similar to the mean velocity profile in nature and can be categorized as a flow between suburb and city center area.

### **Turbulence Intensities**

According to the similarity criteria, the turbulence intensities in the model have to be similar to the turbulence intensities in nature, as stated in Eq. 3.4. In order to obtain reliable results (e.g. reliable pressure coefficients results), the turbulence intensities have to be reproduced carefully in the simulated model [Tieleman, 1999]. Therefore, the longitudinal and vertical turbulence intensities were measured in the present study and then compared to the theoretical profiles. The turbulent intensities are defined as:

$$I_u(z) = \frac{\sigma_u(z)}{u(z)} \quad (3.8)$$

$$I_w(z) = \frac{\sigma_w(z)}{u(z)} \quad (3.9)$$

where  $\sigma_u$  and  $\sigma_w$  are the standard deviations of the longitudinal and vertical velocities, respectively. The turbulence intensities can also be expressed in the following form [see Plate, 1995]

$$I_u(z) = \frac{1}{\ln\left(\frac{z - d_0}{z_0}\right)} \quad (3.10)$$

$$I_w(z) = \frac{0.5}{\ln\left(\frac{z - d_0}{z_0}\right)} \quad (3.11)$$

The vertical profiles of the turbulence intensities of the simulated boundary layer are presented in Fig. 3.6. This figure shows the comparison of the turbulence intensities in the wind tunnel with the turbulence intensities occurring in nature for the roughness lengths  $z_0$  between 0.3 m – 3 m. The value of  $z_0$  between 0.30 – 1.00 m is the typical value of flow over suburb and  $z_0$  between 1 – 4 m is typical for the flow over city center.

Below 40 cm of the modeled boundary layer height ( $z_M$ ) or 80 m in nature ( $z/z_{ref} = 4$ ), the profile of the longitudinal turbulence intensities  $I_u$  is fitted within the range of  $z_0 = 0.30 - 1.00$  m. Above 40 cm of the modeled boundary layer height, the turbulence intensities of the model are lower than the turbulence intensities in nature. However, the area above 40 cm does not cover the area of interest anymore since the highest pyramid model is only 27.47 cm high. Therefore, the height above 40cm is not significantly affected by the presence of the pyramid and the longitudinal turbulence intensity profile is expected to be similar to nature.

For the vertical turbulence intensity profile, the simulated values are higher than those given by the theoretical profile for flow over suburb area. However, the profile is still in the range of typical flow over city centres area with a roughness length  $z_0$  ranging between 1.00 and 3.00.

Based on the results and discussions presented above, the measured profiles show good agreement with the theoretical profiles. Therefore, the similarity criteria of the turbulence intensities are fulfilled. The longitudinal and vertical turbulence intensities ( $I_u$  and  $I_w$ ) of the incoming flow in the wind tunnel are similar to the  $I_u$  and  $I_w$  in nature and can be categorized as the flow between suburb and city centre areas.

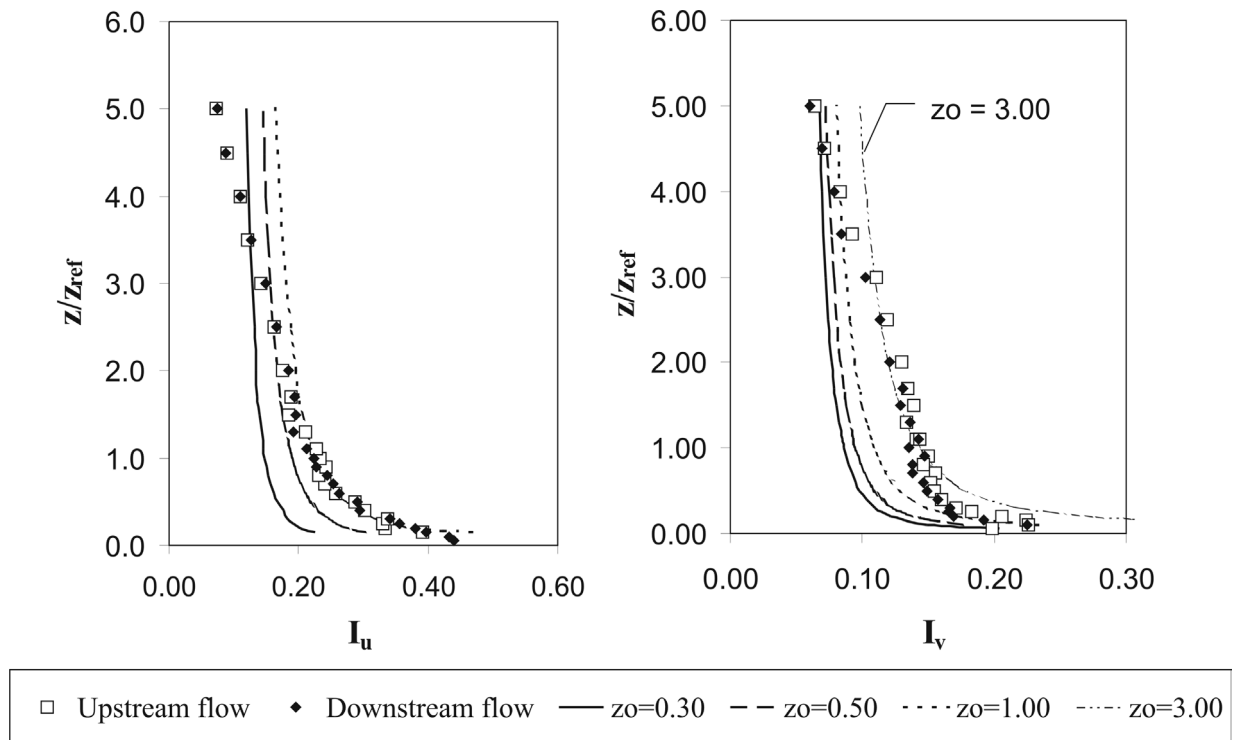


Fig. 3.6. The variation of turbulence intensities with height

### Integral Length Scale

Taylor (1920) introduced the concept of “frozen turbulence” allowing to determine the (spatial) integral length scale of a flow by temporal correlation measurements. Thus, the integral turbulent length scale can be determined from:

$$Lu_x = \frac{u}{\sigma_u^2} \int_0^{\infty} R_{uu}(\tau) d(\tau) \tag{3.12}$$

where  $Lu_x$  is the length scale of the turbulence and  $R_{uu}(\tau)$  is the temporal autocorrelation-function (Eq. 2.18). This integral length scale is a measure for the longitudinal length of vortices.

According to EUROCODE 1 [1991],  $Lu_x$  increases with height and remains constant when the height is above 300 m. In other words,  $Lu_x$  is independent of the surface roughness at elevations higher than 300m.

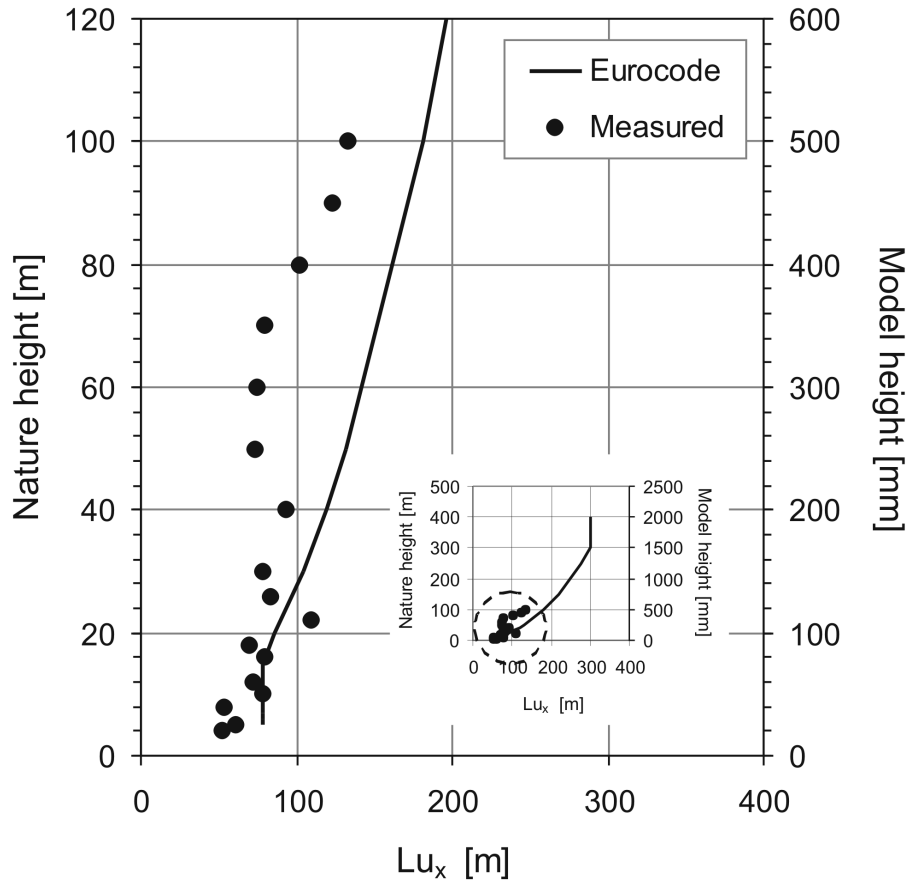


Fig. 3.7. The variation of integral length scale with height

Fig. 3.7 shows the simulated turbulent length scale compared with the values in nature given in EUROCODE 1 for flows above urban areas. The overall trend shows good agreement except in the region above 40 m (200 mm in model) where the  $Lu_x$  values in the model are found to be smaller than in nature. The latter seems to be due to the fact that the upper wall of the wind tunnel acts as a boundary which inhibits the growth of the eddies and thus restrain the size of the developing vortex. Plate [1995] also categorized different  $Lu_x$  values for different areas. The values of  $Lu_x$  above suburbs and city centres compared to the simulated boundary layer flow of this study are shown in Table 1. The comparison reveals that the simulated boundary layer flow is still acceptable to be categorized as a flow between suburban and city center areas.

Table 3.2.  $Lu_x$  in the nature compared to the simulated flow

	<b>Forrest and suburb area*</b>	<b>City centre area*</b>	<b>Simulated flow in this study</b>
<b><math>Lu_x(d_0 + 10m)</math></b>	65 – 85 m	48 – 60 m	78 m
<b><math>Lu_x(d_0 + 30m)</math></b>	130 – 360 m	100 – 190 m	94 m

\* Plate [1995]

### **Power Spectral Density**

The theoretical work by Taylor in 1938 provided a relationship between power spectra and the correlation coefficients [Counihan, 1975]. In practice, the measurement of spatial correlation and spectra as a function of wave numbers is difficult to perform. Likewise, measurements of the covariances as spatial averages are equally difficult. Taylor's hypothesis states that if the turbulence intensity is low and the turbulence is approximately steady and homogenous then the turbulent field is unchanged over the atmospheric boundary layer time scales of interest and advected with the mean wind [Garratt, 1994].

The spectral distributions of the fluctuations of velocity are given in the form of a logarithmic frequency spectra, which is usually obtained by using a Fast-Fourier Transform, see Kainam et.al. [1994], Simiu [1996], Tieleman [1995] for detail discussions on velocity spectral analysis. The one-dimensional spectral density is represented by  $S_{uu}(f)$  and is given by

$$\sigma_u^2 = \int_0^{\infty} S_{uu}(f) df \quad (3.13)$$

The spectra is usually given in logarithmic form and the Karmàn's function for the spectral distribution reads:

$$\frac{f \cdot S_{uu}(f)}{\sigma_u^2} = 4 \cdot \frac{f \cdot Lu_x}{\bar{u}} \left/ \left[ 1 + 70.8 \left( \frac{f \cdot Lu_x}{\bar{u}} \right)^2 \right]^{5/6} \right. \quad (3.14)$$

Fig. 3.8 shows the power spectral density of the longitudinal velocity fluctuations of the simulated flow at the height of  $z = 450$  and  $500$  mm. The power spectra measured are well fitted with the von Karmàn spectrum. After the maximum, the power spectrum declines with a gradient proportional to  $f^{2/3}$ . However, due to a finite measuring resolution, the power spectral density distribution is oscillating and increasing again – a typical shortcoming of the measuring technique used. Nevertheless, the comparisons show that the simulated atmospheric flow in the wind tunnel is kinematically similar to the conditions in nature.

### 3. Wind Tunnel Technique

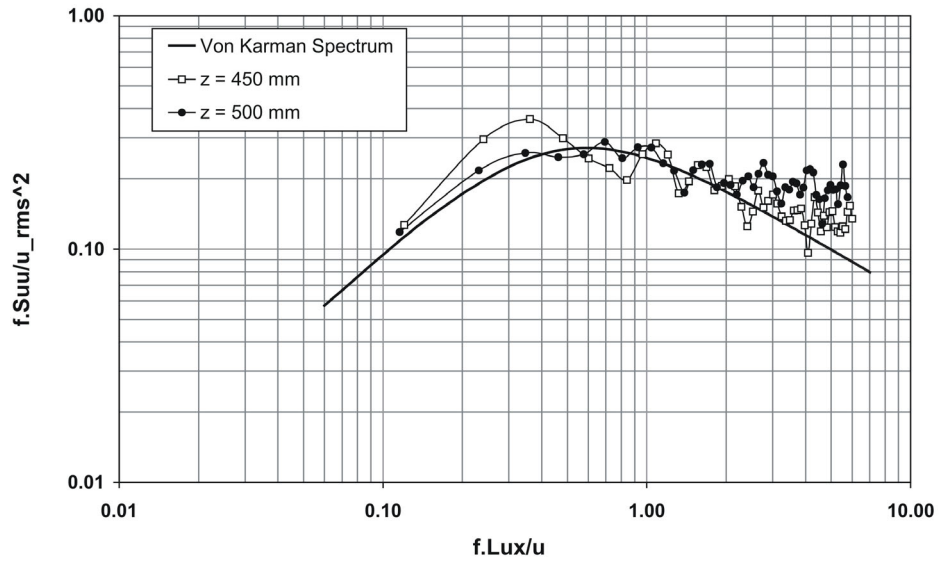


Fig. 3.8. Power spectral density of longitudinal velocity fluctuations

## 4. Experimental Setup and Measurement Techniques

### 4.1. Pyramid Models and Measurement Programs

The pyramid models are constructed using Plexiglas with a thickness of 4 mm. The intersection of the pyramidal surfaces are sharp edges. Nine different geometries of pyramids are investigated. Seven pyramids have a square base of  $1 \times 1 = 200 \text{ mm} \times 200 \text{ mm}$  with varying base angles  $\theta$ , which is the angle of surface declination of the pyramid. The other two pyramids have the same base angle,  $\theta = 70^\circ$ , with variation in height. Fig. 4.1 depicts the arrangement of the pyramid geometry and the coordinate system.

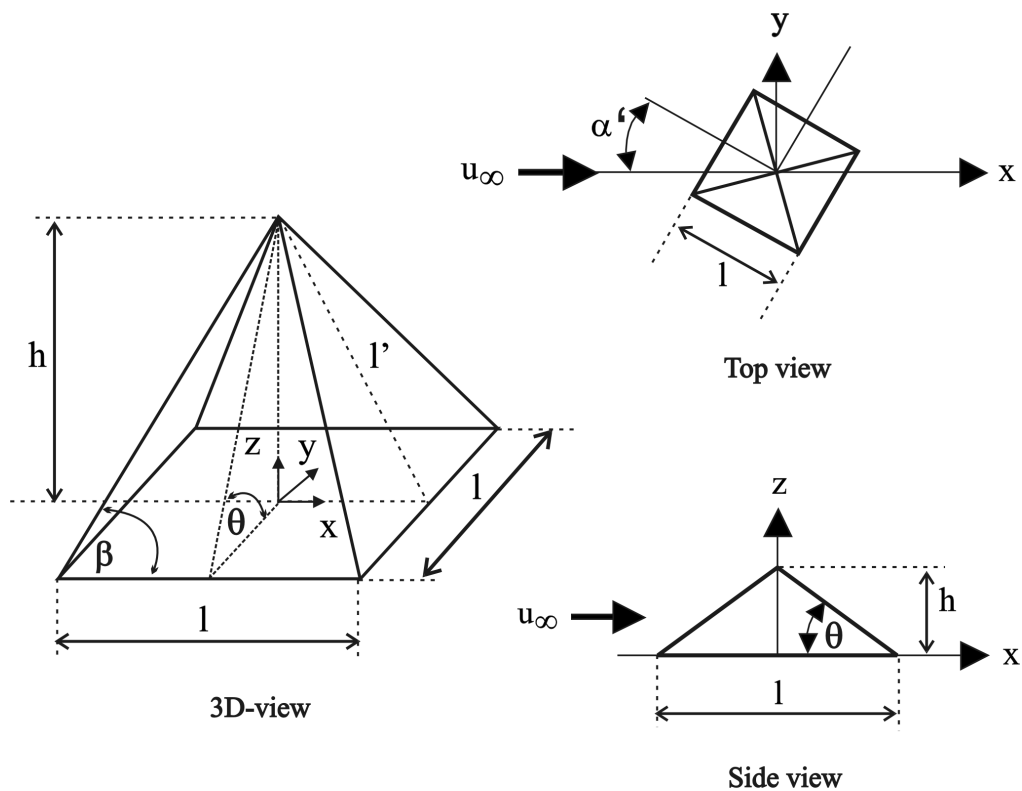


Fig. 4.1. Pyramid geometry and coordinate arrangement

The intention of this study is to cover the variation of the pyramid base angle and height as wide as possible. In order to determine the shallowest base angle, the Jensen number ( $Je$ ) and Jensen scaling law were used. The Jensen number expresses the height of the model (pyramid)

#### 4. Experimental Setup and Measurement Techniques

divided by the roughness length ( $z_0=2.49$  mm) of the surface,  $h/z_0$ , and the scaling law stated that this dimensionless parameter in the model should be similar to nature [Cook, 1986]. A typical Jensen number is between 50~500. For real buildings, Building Research Establishment (BRE) suggests that the Jensen number is in the range of 20~1000 [Cook, 1990]. This criterion eliminates the possibility that a model is undersized, which means that the height of the model is blending with the roughness elements. Based on this criterion, pyramid P30 was chosen as the shallowest pyramid with  $Je = 23.19$  and pyramid P70 with  $Je = 110.27$  as the steepest pyramid. The geometries of the investigated pyramids are summarized in Table 4.1.

Table 4.1. Geometry of the pyramids

No.	Pyramid	Base angle	Base length	Height	Flow field	$l'$	$\beta$
		( $\theta$ ) °	( $l$ ) mm	( $h$ ) mm	( $1.5 \times h$ ) mm		
1	Pyramid P30	30	200	57.74	86.60	115.47	49.11
2	Pyramid P40	40	200	83.91	125.86	130.54	52.55
3	Pyramid P45	45	200	100.00	150.00	141.42	54.74
4	Pyramid P50	50	200	119.81	178.76	155.57	57.27
5	Pyramid P55	55	200	142.81	214.22	174.34	60.16
6	Pyramid P60	60	200	173.21	259.81	200.00	63.43
7	Pyramid P70	70	200	274.75	421.12	292.38	71.12
8	Pyramid P70a	70	103.96	142.81	214.22	151.98	71.12
9	Pyramid P70b	70	72.79	100.00	150.00	106.42	71.12

The flow fields were investigated with a wind direction of  $\alpha' = 0^\circ$  (normal to the windward surface). The boundary layer was characterized by Reynolds numbers ranging from 12,000 to 90,000 based on the pyramid height ( $h$ ) and a free stream velocity,  $u_\infty = 5$  m/s. For pyramid P30 to pyramid P50, the flow field measurement planes ranged from  $1 \times l$  upstream to  $2 \times l$  downstream ( $l$ : pyramid length) and from a height of  $z=0$  to  $z=1.5 \times h_{70}$  ( $h_{70}$  = height of pyramid P70). For Pyramid P60 and P70 the measured flow fields were expanded to  $1.5 \times l$  upstream and  $2.5 \times l$  downstream, due to the geometry enlargement. The flow characteristics are presented in three parallel planes in the  $y$ -direction, each spaced by  $1/4 \times l$ , as shown in Fig. 4.2.

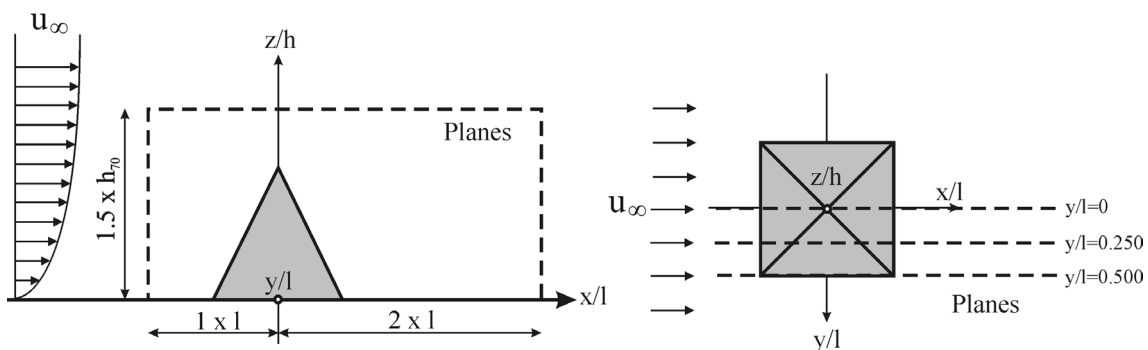


Fig. 4.2. Parallel measuring planes



Seven different flow characteristics, namely the mean velocity profiles, the vector fields, the reattachment lengths, the recirculation zone, the turbulent intensity, the Reynolds shear stresses and the turbulent kinetic energy, can be obtained from the flow measurements. The results will be presented and discussed in Chapter 5.

In each plane, within the measurement range, measurement points are distributed systematically in horizontal and vertical directions. These points are the points where the measurement volume from the LDA system will be aligned (see Section 4.2 for the flow measurement technique of LDA). Fig. 4.3 shows the distribution of the measurement points in the measuring planes. For pyramid P30 to pyramid P55, there are 13 measurement locations and basically, in each locations 25 measurement points are distributed vertically. For pyramid P60 and P70, two measurement locations at  $-300$  and  $500$  mm are added, same like the others, both have 25 measurement points in vertical direction. At certain locations ( $x = -75, 0, 30$  and  $60$  mm), due to the presence of the pyramids, some measurement points can not be measured since the measurement point will be located within the pyramids. Therefore, at these locations, the 25 vertical measurement points are reduced with the points within the pyramid, and depends on their base angle and height, the number of the measurements points are different for each pyramids. In order to maintain the accuracy of the results, at these locations, one measurement point which is located as near as possible to the pyramid surfaces are added.

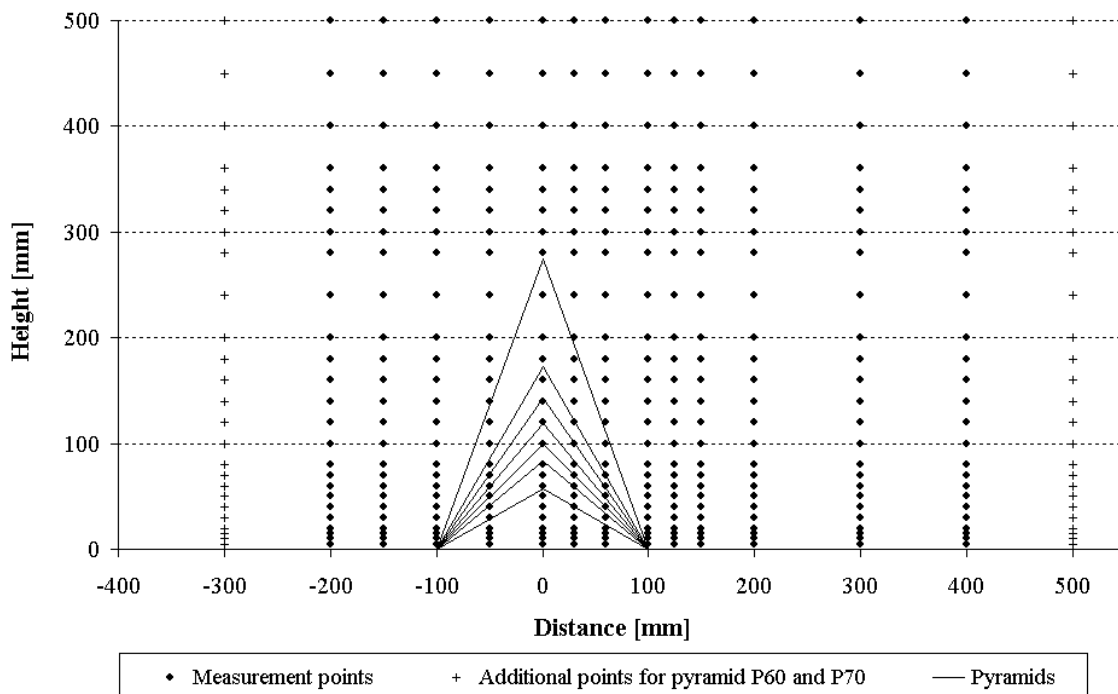


Fig. 4.3. The measurement points for flow measurement with Laser-Doppler-Anemometer

The pressure measurements were carried out with a velocity of 12 m/s in order to obtain a measurable and reliable pressure differences. Four different wind directions ( $\alpha' = 0^\circ, 15^\circ, 30^\circ$  and  $45^\circ$ ) for each pyramid were measured. Based on these results, the pressure distribution for further wind direction  $\alpha'$  with  $15^\circ$  step can be generated due to the symmetrical geometry of the pyramid, see Fig. 4.4. The capital letters A, B, C and D indicated in the figure are used to refer to the particular pyramid surfaces for further discussion in this study.

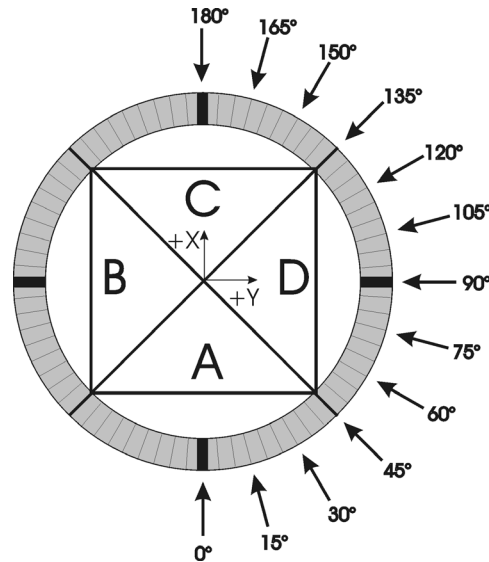


Fig. 4.4. Wind direction arrangements ( $u_0 = 12$  m/s)

## 4.2. Flow Measurement Technique (LDA)

The longitudinal and vertical velocities were measured with the aid of a 2D laser Doppler anemometry (2D-LDA). The basic principle of the LDA measurement technique is briefly explained in this section. Subsequently, a description of the flow measurement setup that is used in this study is also given.

### 4.2.1. Basic Principle of LDA

The Laser Doppler Anemometry (LDA) technique is a non-intrusive point-based measurement technique. This technique is considered as a technique with very high accuracy in terms of mean and turbulent flow properties. It consists of an optical measuring system for local non-intrusive velocity measurements in fluids, which is normally divided into three parts, the light source, the emission optics and the detection optics. Fundamental information about the LDA – measuring technique can be found in Rudd [1969], Farmer [1972], Elliason et.al. [1974], Drain [1980], Durst et.al [1981] and Ruck [1986, 1987, 1990], Albrecht [2003]. In this section, only the basic principles of the LDA are described.

The basic principle of LDA is based on the famous principle in physics – the Doppler effect. It determines velocities with help of the Doppler effect that is evoked by the light scattering

of small particles that travel through a measurement volume within the crossing point of two laser beams. The Doppler effect is evoked twice, first when the incident laser beam of the transmitter system reaches the moving target (particle tracers) and second when the coherent light is scattered from the moving target.

The first Doppler effect is characterized by the wavelength  $\lambda$  and the light frequency  $f_0$ , that have an effect on the moving target. This can be described by the Doppler formula

$$f' = f_0 \left[ 1 - \frac{\vec{u} \cdot \vec{l}}{c} \right] \quad (4.1)$$

where  $\vec{u} \cdot \vec{l}$  represents the scalar product of the particle velocity vector and the vector indicating the direction of propagation of the illuminating laser beam and  $c$  is the velocity of light.

The second Doppler effect is evoked when the coherent light with frequency  $f'$  is scattered from the moving target particle and received by a stationary detector with frequency  $f_D$  (subscript D denotes for detector), in mathematical form

$$f_D = f' \frac{1}{1 - \frac{\vec{u} \cdot \vec{l}_D}{c}} = f_0 \frac{\left[ 1 - \frac{\vec{u} \cdot \vec{l}}{c} \right]}{\left[ 1 - \frac{\vec{u} \cdot \vec{l}_D}{c} \right]} \quad (4.2)$$

which can also be written in series form

$$f_D \approx f_0 \left[ 1 - \frac{\vec{u} \cdot \vec{l}}{c} + \frac{\vec{u} \cdot \vec{l}_D}{c} \right] \quad (4.3)$$

As can be seen, Eq. 4.3 contains the Doppler shift of the incident wave frequency and hence contains velocity information. For typical flow systems the Doppler shift is of the order 1 – 100 MHz, which is very small compared to the frequency of light of approximately  $10^{14}$  -  $10^{15}$  Hz and thus it is virtually impossible to resolve the signal frequencies of this order with sufficient accuracy. In laser Doppler anemometry, the light beam of the laser is divided into two partial beams, as depicted in Fig. 4.5.

#### 4. Experimental Setup and Measurement Techniques

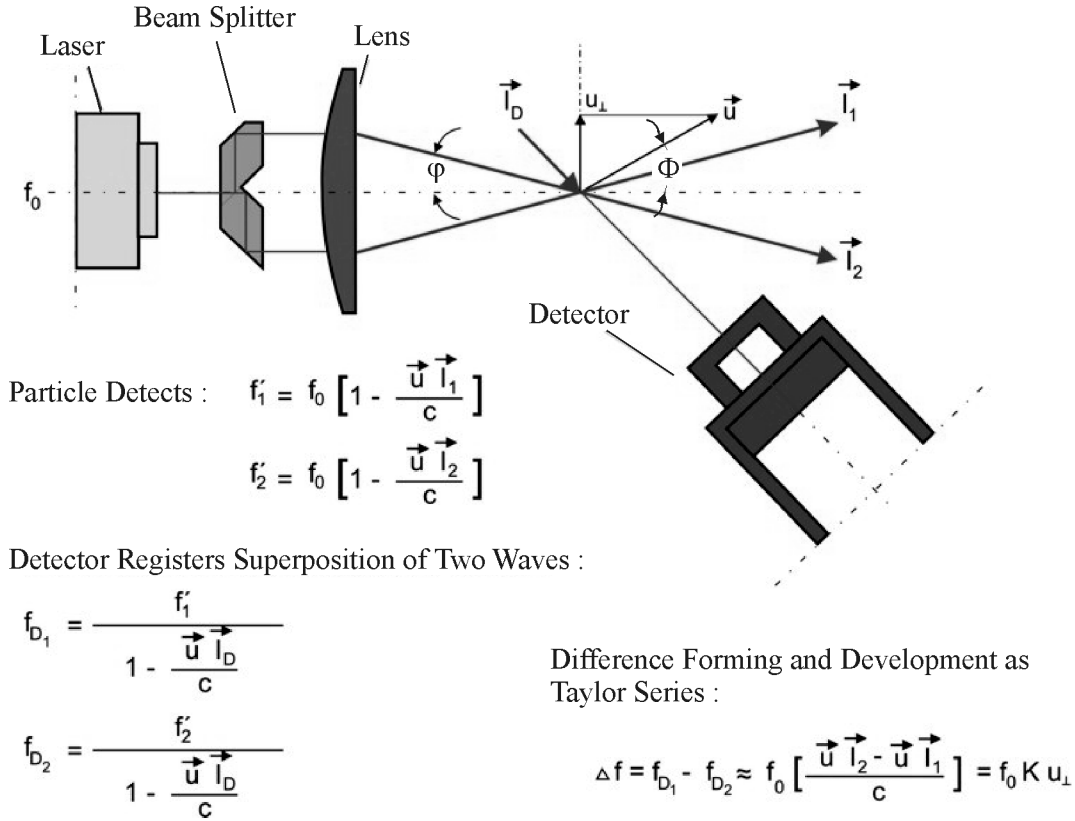


Fig. 4.5. Principle of a LDA two beam anemometry [Ruck, 1987]

The two partial beams are focused by means of the convex lens and form the measuring volume at their intersection. When using two laser beams, the detector registers the superposition of two separate Doppler effects,  $f_{D1}$  and  $f_{D2}$ , which are easy to resolve (frequency range  $10^6$  Hz). With trigonometrical transformation and taking  $f_0/c = 1/\lambda$ , the superposition of these frequency yields the relation between the detection frequency and the measured velocity component known as the Doppler beat frequency.

$$\Delta f = |\vec{u}| \sin \phi \frac{2 \sin \phi}{\lambda} \quad (4.4)$$

Another descriptive model to derive the relation between the detection signal and the measured velocity is the fringe model, which is often used in engineering. The model postulates the existence of interference fringes at the intersection point. Fig. 4.6 illustrates the detail of the measurement volume showing the formation of fringes. The concept of the fringe model is that a particle suspended in a fluid moves through the measuring volume and consecutively scatters the bright and dark sections of the interference pattern. A detector located in space detects these frequencies. Since the fringes are a distance  $\Delta x$  apart and if the velocity component perpendicular to the fringe system is  $u_{\perp}$  then the frequencies that are generated by the particles are

$$\Delta f = \frac{u_{\perp}}{\Delta x} = u_n \frac{2 \sin \varphi}{\lambda} \quad (4.5)$$

It can be seen that Eq.4.4 and Eq. 4.5 are identical. Furthermore, all existing description models in laser Doppler anemometry finally lead to the same formula. If the semi-angle between the crossing laser beams and the wave length of the laser light is fixed, it is easy to determine for Eq. 4.5 the beat frequency corresponding to unit fluid velocity. The linear proportionality between velocity and frequency distinguishes the LDA method from other existing fluid velocity measuring method [Ruck, 1987].

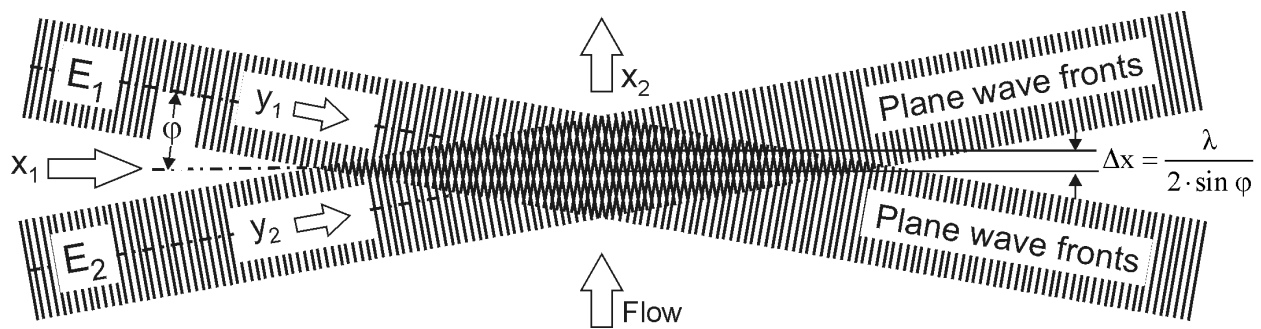


Fig. 4.6. Derivation of the fringe model in laser Doppler anemometry – superposition of two laser beams [Ruck, 1987]

#### 4.2.2. LDA Configuration in the Wind Tunnel

As mentioned before, for the experiments, a two-component laser Doppler anemometry system (2D-LDA) was installed in the wind tunnel. The LDA system was operated in a forward light scattering mode. Fig. 4.7 shows a schematic illustration of the experimental set-up, data acquisition and data processing for the flow measurements performed in the present study.

On the transmitter side, an argon-ion laser with maximum light power output of 4 W operates in a continuous wave operation mode. In the present study, an output power of 1.5 W was used. After a double diversion of the beam with successive mirrors, the beams enter an assembly of Bragg cells with colour beam splitter and beam splitter. Basically, the Bragg cells were used for frequency shifting to eliminate the directional ambiguity of the velocity measurements. The colour beam splitter divides the incident laser beam into two colours, a green beam with a wavelength 514.5 nm and a blue beam with a wavelength 488.0 nm. The beam splitter then divides the laser beam into two further parallel single beams thereby forming two planes, the green beams forming the horizontal plane and the blue beams forming the vertical plane. Table 4.2 shows the characteristics of the LDA system for the present study.

#### 4. Experimental Setup and Measurement Techniques

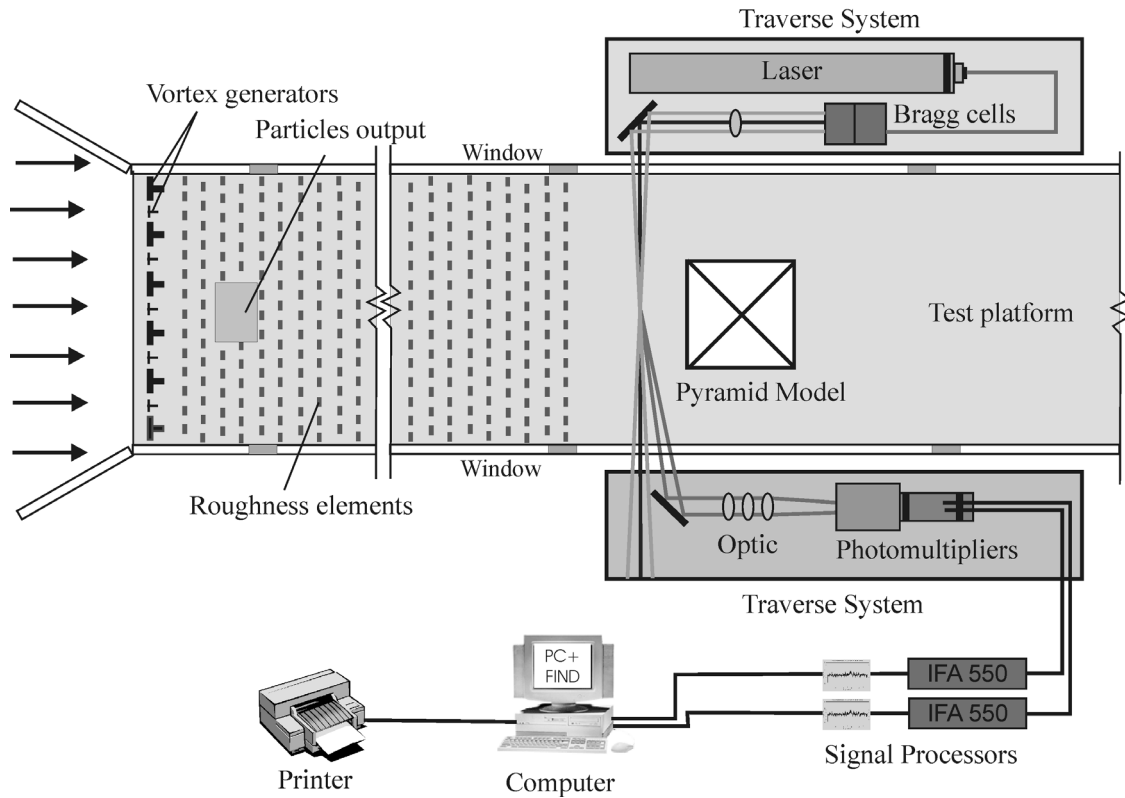


Fig. 4.7. Schematic illustration of the experimental set-up, data acquisition and data processing for the flow measurements

As tracer, 1,2-propandiol droplets were generated with an evaporation-/condensation-type particle generator, producing seeding particles of about  $1.5 \mu\text{m}$  mean diameter. The scattered light signals were detected by photomultipliers. These signals were processed using two counter-based signal processor TSI model IFA 550. The received signal is first sent to a filter system where it is filtered in through a band pass from 300 KHz to 1 MHz. It is possible to run signal evaluations in two different modes, one is the coincidence principle (random adjustment) and second the even time adjustment method. The latter has the advantage that the biasing effect can be excluded and a connection between two signals from different coordinates can also be determined [Elsäßer, 1999]. For the present study, the even time adjustment was used.

Table 4.2. Characteristics of the LDA system

	u-component	w-component
Laser light wave length $\lambda$	514.5 nm (green)	488 (blue)
Frequenz shift $\Delta f$	0.60 MHz	0.55 MHz
Focal length	1500 mm	1500 mm
Beam spacing	50 mm	50 mm
Semi-angle of crossing beams $\varphi$	$0.955^\circ$	$0.955^\circ$
Fringe spacing $\Delta x$	$14.642 \mu\text{m}$	$14.642 \mu\text{m}$
Number of fringes	51	52

### 4.3. Pressure Measurement Technique

A standard pressure tapping system was applied in the present study. Dimensionless mean pressure coefficients ( $c_p$ ) and root-mean-square (rms) values on the surfaces of the pyramids were deduced from a continuous sampling (clock rate 1024 Hz) over a period of 30 s. The pressure coefficients ( $c_p$ ) were calculated by dividing the differential pressures (surface pressure  $p_{\text{surface}}$  minus the static reference pressure  $p_{\text{stat.}}$ ) by the dynamic pressure at the reference. In this study, the reference height is the height of the pyramid, which means that the reference velocity ( $u_{\text{ref}}$ ) is the undisturbed velocity at the pyramid height. This was chosen based on the similarity criteria of wind loads from Plate [1995] and the practical design purpose as suggested by the EUROCODE 1 [1991]. The pressure coefficient  $c_p$ , is expressed as: (see also Eq. 2.26)

$$c_p = \frac{\Delta p}{q} = \frac{p_{\text{surface}} - p_{\text{stat.}}}{(\rho/2)u_{\text{ref}}^2} \quad (4.6)$$

where  $\rho$  is the air density,  $u_{\text{ref}}$  and  $(\rho/2)u_{\text{ref}}^2$  is the velocity and dynamic pressure at the pyramid height, respectively. The static reference pressure was measured at  $y = 0.75$  m, a location where the free stream turbulence intensity was low and no interaction of the flow with the model itself was observed.

Fig. 4.8 shows a schematic illustration of the configuration of the pressure measurement technique applied at the wind tunnel. In order to investigate the different wind directions, the pyramids were placed on a rotatable platform that adjusts the pyramid to the particular wind direction. On one half of a pyramid surface, 1.5 mm diameter pressure taps were distributed systematically. The distribution on half of the pyramid surface is considered to be sufficient since the geometry of the pyramid is symmetric [Roth, 1997]. Taking an example of pressure measurement when the wind blows from a direction of  $30^\circ$ . First, the model was rotated  $30^\circ$  clockwise direction. Afterwards, the model was rotated  $30^\circ$  anti-clockwise from the normal position. The pressure taps of the second measurement will be mirrored and become another half of the pyramid surface. In some cases, the pressure taps remain at the symmetric axes. In such cases, the mean value of the two measurements was taken. With this arrangement, a more accurate pressure distribution with the same number of pressure taps can be obtained since the pressure taps are distributed in a smaller area (i.e. only half surface). In order to achieve pressure coefficient values as close as possible to the edge of the pyramids, a distance of 6.5 mm between the pressure taps and the pyramid edges was not exceeded. The pyramid models investigated had different numbers of pressure taps ranging from 46 to 60 due to different sizes of surface area. Fig. 4.9 presents an example of the pressure taps distribution.

#### 4. Experimental Setup and Measurement Techniques

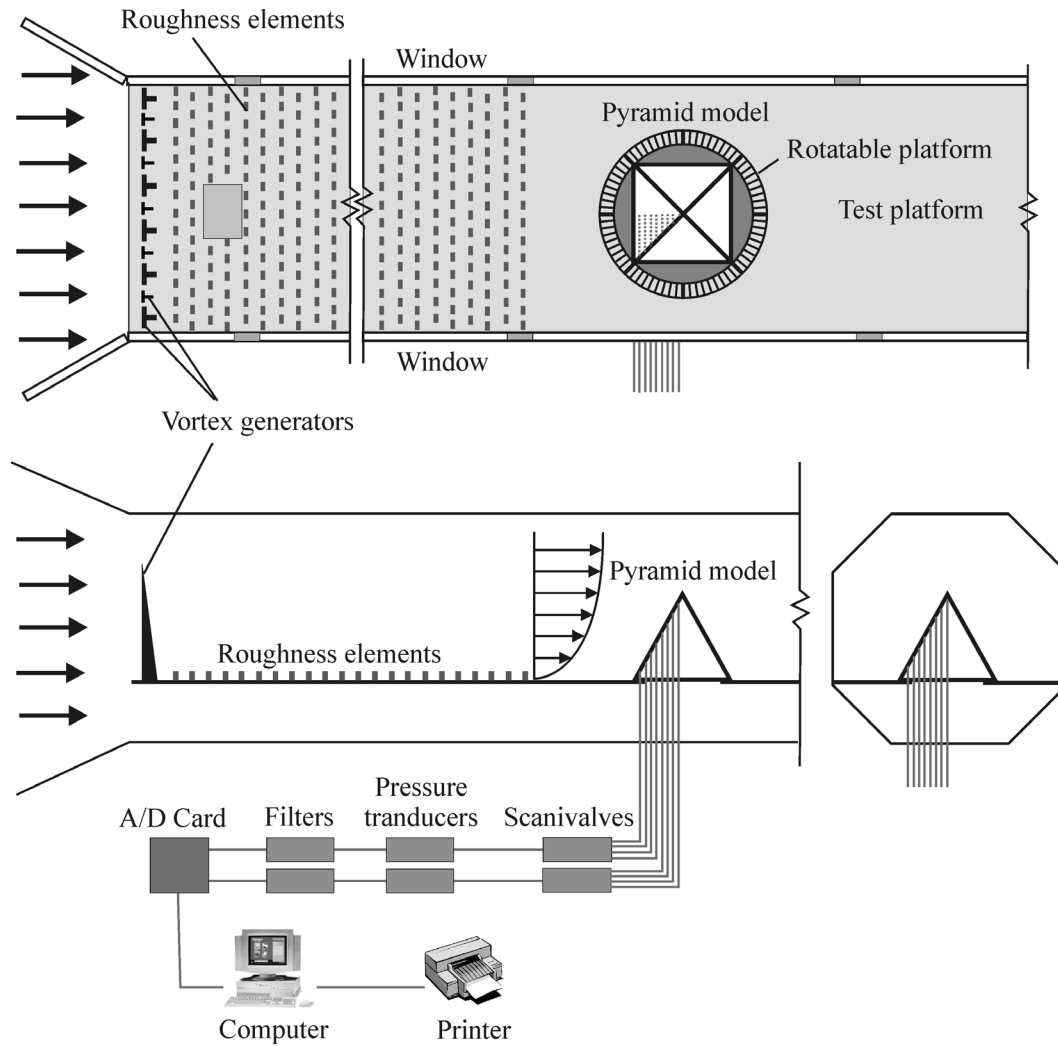


Fig. 4.8. Schematic illustration of the experimental set-up, data acquisition and data processing for the pressure measurements

The pressure taps were connected to the pressure transducers with vinyl tubes via metal connectors to a scanivalve unit. Usually, the connectors and tubes cause a certain pressure loss, which limits the frequency response of the pressure measuring system. However, this systematic error was negligible for the frequency range encountered here. The scanivalve unit switched the tubes connected to the pressure transducers i.e. the measurements were carried out one after another in a temporally stable boundary layer flow. The pressure transducers respond to the applied pressures and generate voltage signals. The signals were filtered with a low pass filter in order to remove noises before digitised into a computer for further analysis. According to Becker [1993] and Roth [1997], the total systematic and statistic errors for this measurement system are 5 %.



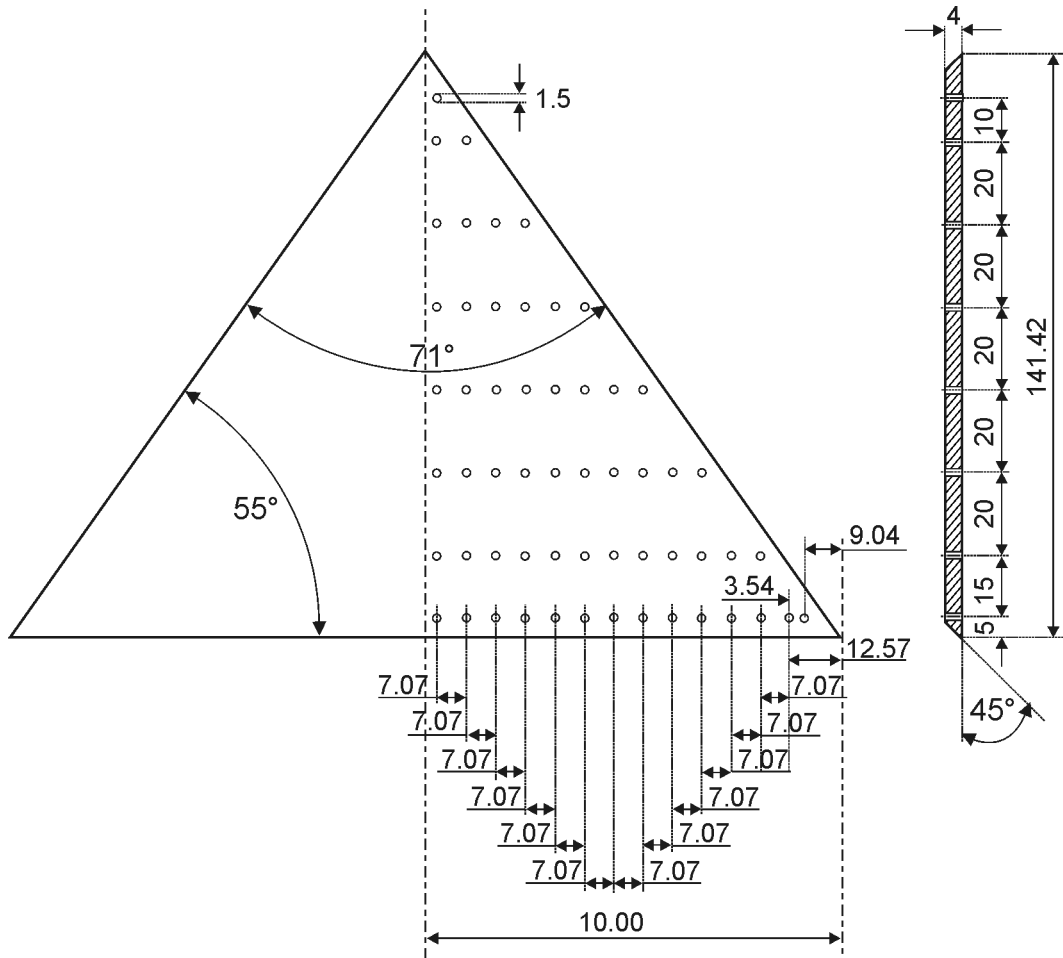


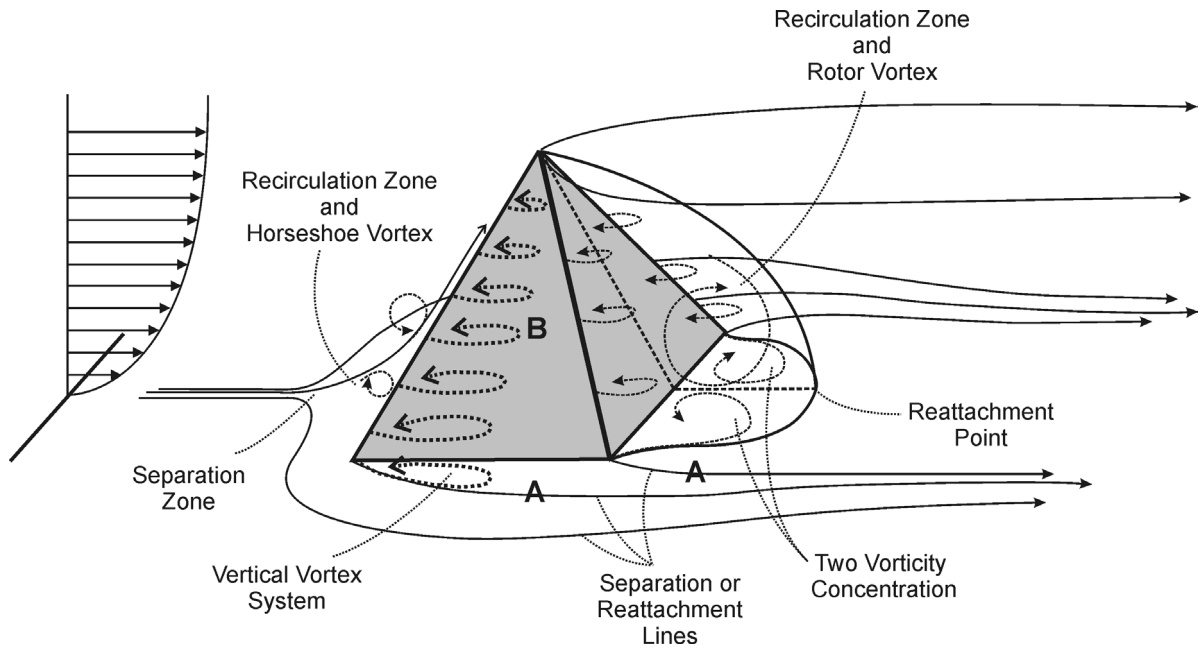
Fig. 4.9. Example of pressure taps distribution on the pyramid surface (Pyramid P45, 57 pressure taps)

## 5. Experimental Results

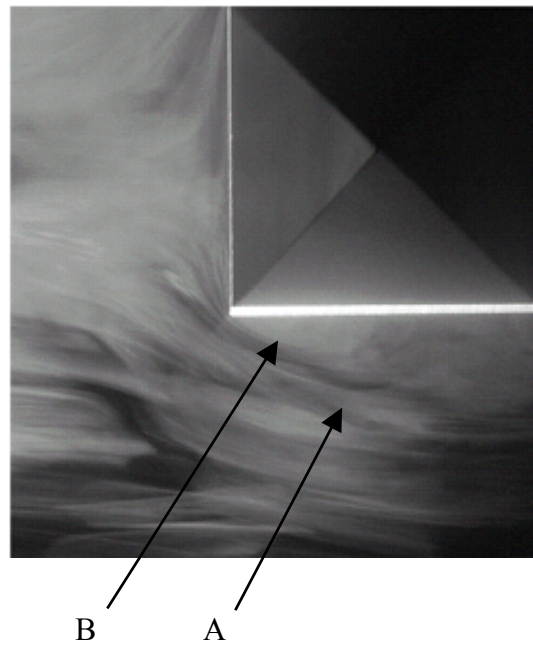
### 5.1. Flow Characteristics of Pyramids

Before conducting quantitative flow measurements with the Laser Doppler Anemometry, visual observations of the flow structures around the pyramidal building were carried out in the wind tunnel. The observations were conducted with the aid of a thin laser sheet and tracer particles to visualize the flow structures. The aim of the visual observation is to have a general impression of the flow structures around a pyramid, which helps to identify the distinct flow characteristics. Based on this visual observations and previous studies such as Abuomar and Martinuzzi [2000, 2003], qualitative conclusions can thus be made. Moreover, a schematic illustration of the 3-D flow structures around a single pyramid building can be generated as shown in Fig. 5.1.

Fig. 5.1 (a) shows that the flow around the pyramid gives rise to a discrete horseshoe vortex system, which is similar for almost all bluff bodies flows, see also e.g. Acarlar et.al. [1987], Hunt et.al. [1978], Sakamoto et.al. [1983]. However, the vortex system attached to the pyramids is not so uniform as the system of e.g. cuboidal bluff bodies, see Peterka et.al [1985]. When the wind blows from a direction of  $0^\circ$ , the wall taper induces a vortex system consisting of two conical vortices rotating near the outer edges of the leeward side and a rotor vortex in the vertical middle plane. The diameters of the two outer vortices depend on the local pressure and the height  $z$ . Thus, the aerodynamic loading of the structures is rather specific, which will be described further in detail in this study. Other distinct flow structures around the pyramids are identified at the side surfaces. Two separation lines are identified near the bottom at the side surface and in the leeward side of the pyramid (indicated with A in Fig. 5.1 (a)). This observation is in good agreement with the visualization conducted by Abuomar et.al [2000]. These separation lines are suggested to come from the resulting horseshoe vortex that occurs at the upstream side and extends to the sides of the pyramid. Besides these lines, a vertical vortex system at the side of the pyramid (indicated with B in Fig. 5.1 (a)) is also identified. These vortices are similar to those formed in the flow over delta wings [Donohoe et.al, 1997; Martinuzzi, 2003]. However, for cuboidal bluff bodies such vortex pairs occur rather at the free corner, i.e. roof, than at the wall-body junction [Martinuzzi, 1993; Tielman, 1994]. Fig. 5.1(b) shows the flow visualization at the upstream edge near the bottom of the pyramid. The figure illustrates the flow separation “A” and the vortices “B”.



(a) Sketch of the flow structures around a pyramid



(b) Flow visualization

Fig. 5.1. A schematic illustration of the 3-D flow structures around a single pyramid building and the flow visualization using laser sheet at the near the bottom of the pyramid with base angle  $\theta = 70^\circ$ .

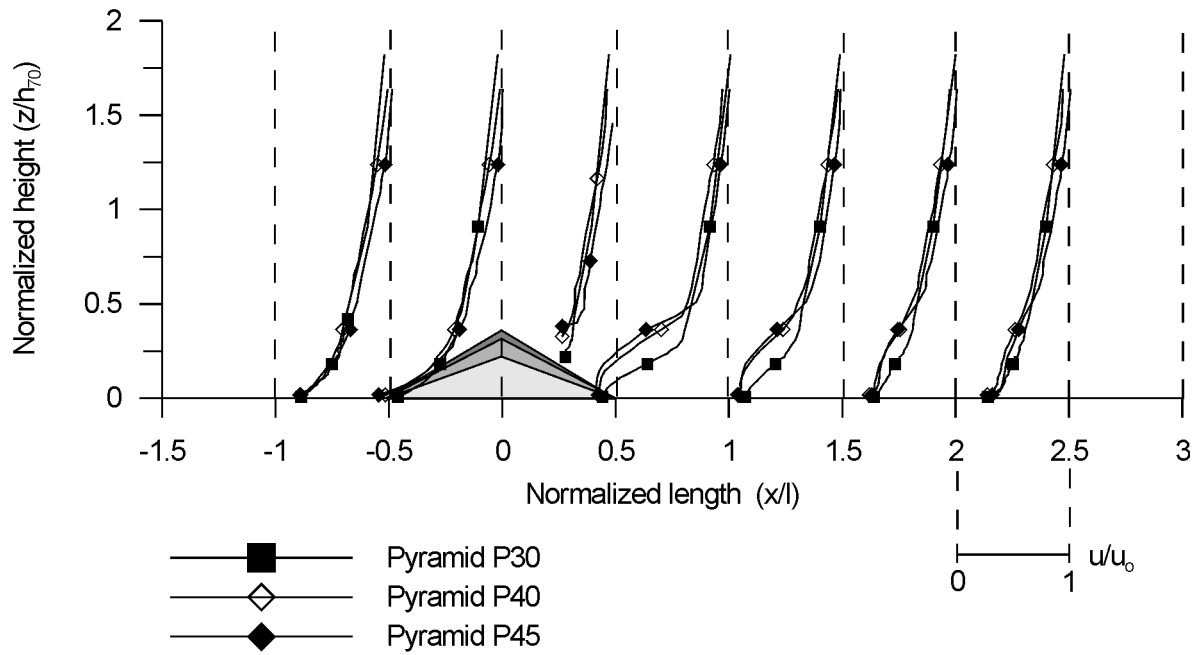
### 5.1.1. Mean Velocity Profile

Fig. 5.2 shows the longitudinal velocity profiles at  $y/l=0$ . The velocities are normalized by the free stream velocity  $u_0 = 5$  m/s. The  $x$ -axes are normalized by the pyramid lengths and the heights are normalized by the height of pyramid P70 ( $h_{70}=274.75$  mm). Fig. 5.2 (a) shows the profiles for pyramid P30 to P45. At the upstream side of the pyramids at a distance of  $x/l = -1$ , the velocity profile still follows the characteristics of the incoming velocity profile. Negative velocities are detected at a distance of  $x/l = -0.5$  at the bottom of the pyramid. The figure shows that the negative velocities increase when base angle increases from pyramid P30 to pyramid P45. At windward side, a negative velocities are detected at  $x/l = 0.5$ . These negative velocities will characterize the recirculation zone at this area. For pyramid P30, at a distance of  $x/l = 1.0$  the velocity profile is no longer effected by the presence of the pyramid. For pyramid P40 and P45, the presence of the pyramid still effected the velocity profiles until a distance of  $x/l = 2$ .

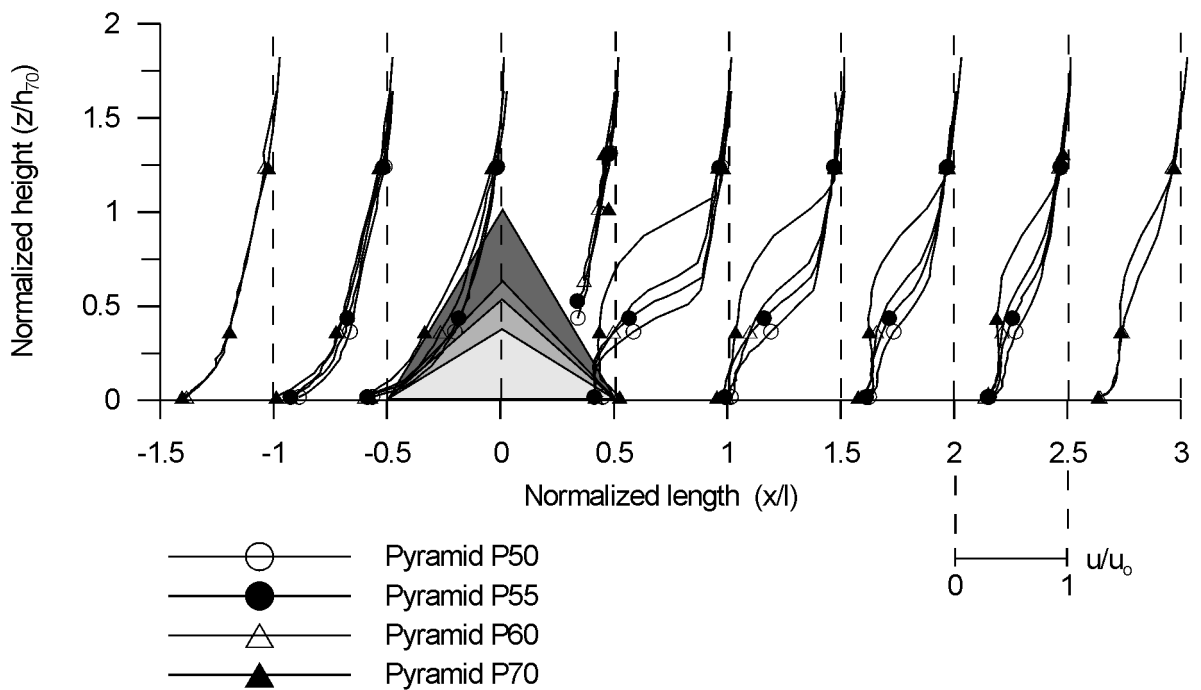
The mean longitudinal velocity profiles for the next investigated pyramids (pyramid P50 to pyramid P70) are presented in Fig. 5.2 (b). At a distance of  $x/l = -1.5$  the incoming velocity profiles are observed. When the distance becomes closer to the pyramids ( $x/l = -1$ ), the incoming velocity profile is still established for pyramid P50 whereas for the other pyramids, the velocity decreases. Negative velocities are identified when the distance reaches  $x/l = -0.5$ , which occur near the bottom of the pyramids. The zero velocities for each pyramid are observed at  $0.15 h$  ( $h$ : height of the pyramids). In the leeward side of the pyramid, a point of inflection of velocities are identified at the height of the pyramids. The zero velocities near the leeward side of the pyramids edge ( $x/l = 0.5$ ) are found at  $2/3 h$ . For pyramids P50 and P55, the incoming flow profiles at a distance of  $x/l = 2$  are still effected by the presence of the pyramid. However, the differences of the profiles compared to the incoming profiles are not significant. For pyramid P60 and P70, the velocity profiles at  $x/l = 2$  are still effected by the presence of the pyramids. The figure shows at  $x/l = 2.5$  point of inflections are still detected at the height of the pyramids.

The longitudinal mean velocity profiles at  $y/l = 0.25$  for pyramid P30 – P45 and pyramid P50 – P70 are presented in Fig. 5.3 (a) and (b), respectively. Similar to the profiles at  $y/l = 0.0$ , for pyramid P45, negative velocities are detected near the bottom at  $x/l = -0.5$ , which indicates small recirculation zone were formed. For the shallower pyramid, the velocities decrease but no negative velocities are yet detected. In the leeward side of the pyramid, negative velocities are detected at  $x/l = 0.5$ . Fig. 5.3 (b) shows that a similar behaviour is also found for the steeper pyramids (P50 to P60). In the windward side of the pyramid, negative velocities are found  $x/l = -0.5$ . In the leeward side of the pyramids negative velocities are also identified at  $x/l = 0.5$ , which shows small recirculation zone occurs and disappear before they reach  $x/l = 1$ . For pyramid P70, the velocity profile at  $x/l = 0.5$  shows different behaviour with the other pyramids. The negative velocities are detected near the bottom. It is likely that the measurement captured the secondary recirculation zone in the leeward side of the pyramid which increases as the base angle and the height of the pyramids increase. Despite this possibility, in general, based on the point of inflections of the profiles, it is clear that the recirculation zone at the leeward side of the pyramid at  $y/l$

$= 0.25$  is not as large as the recirculation zone  $y/l = 0.0$ . It decreases in size both in the vertical and horizontal directions.



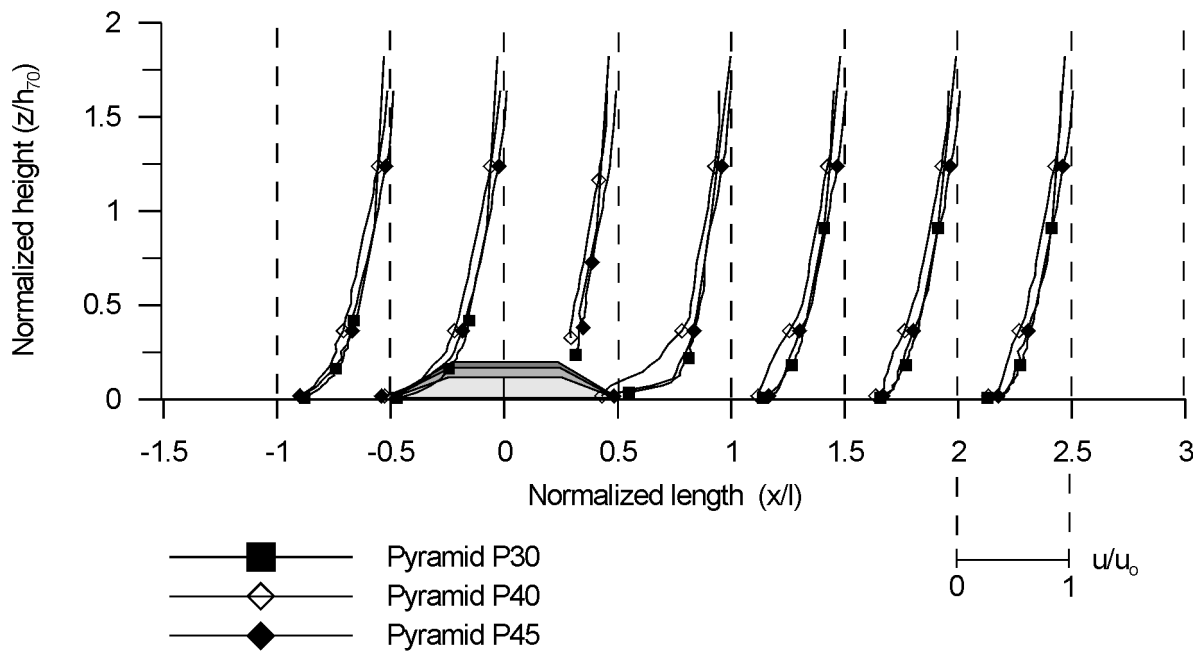
(a) Pyramids P30 – P45



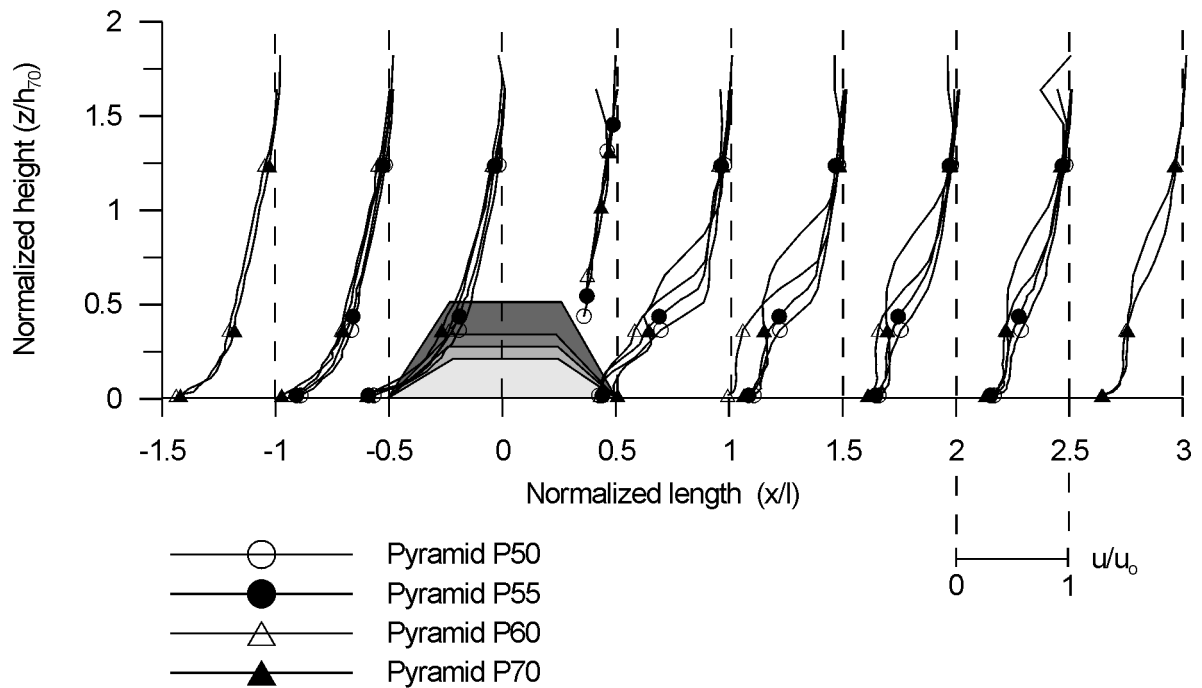
(b) Pyramids P50 – P70

Fig. 5.2. Longitudinal mean velocity profiles at  $y/l = 0.0$  ( $\alpha' = 0^\circ$ ,  $u_0 = 5$  m/s)

5. Experimental Results



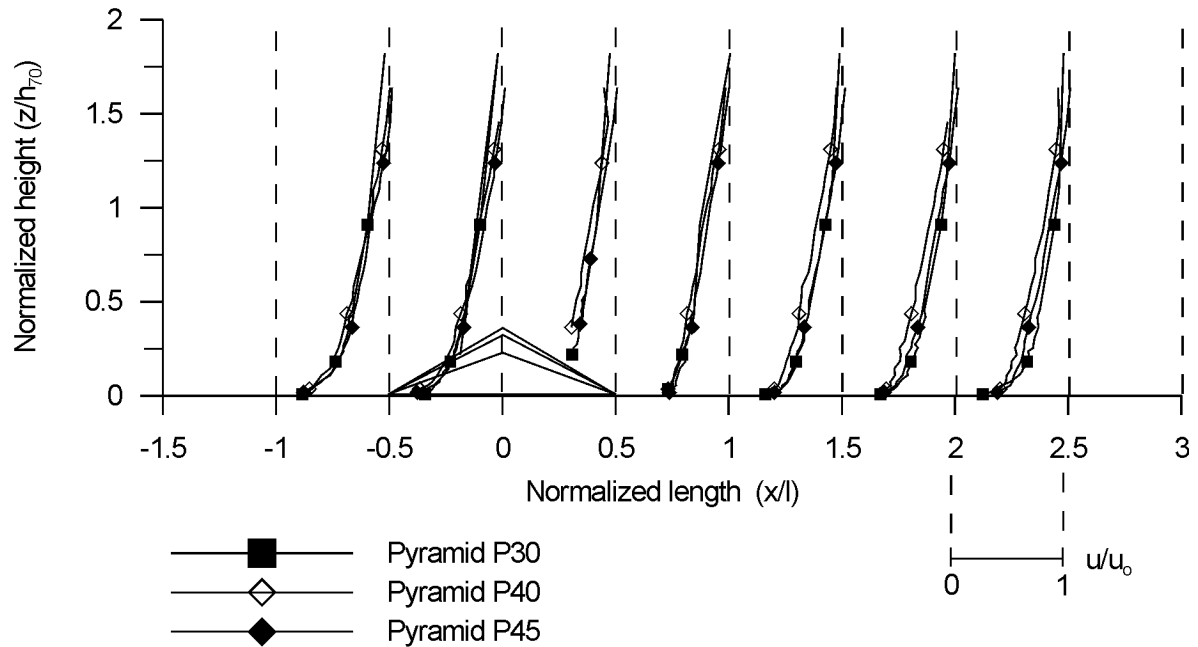
(a) Pyramids P30 – P45



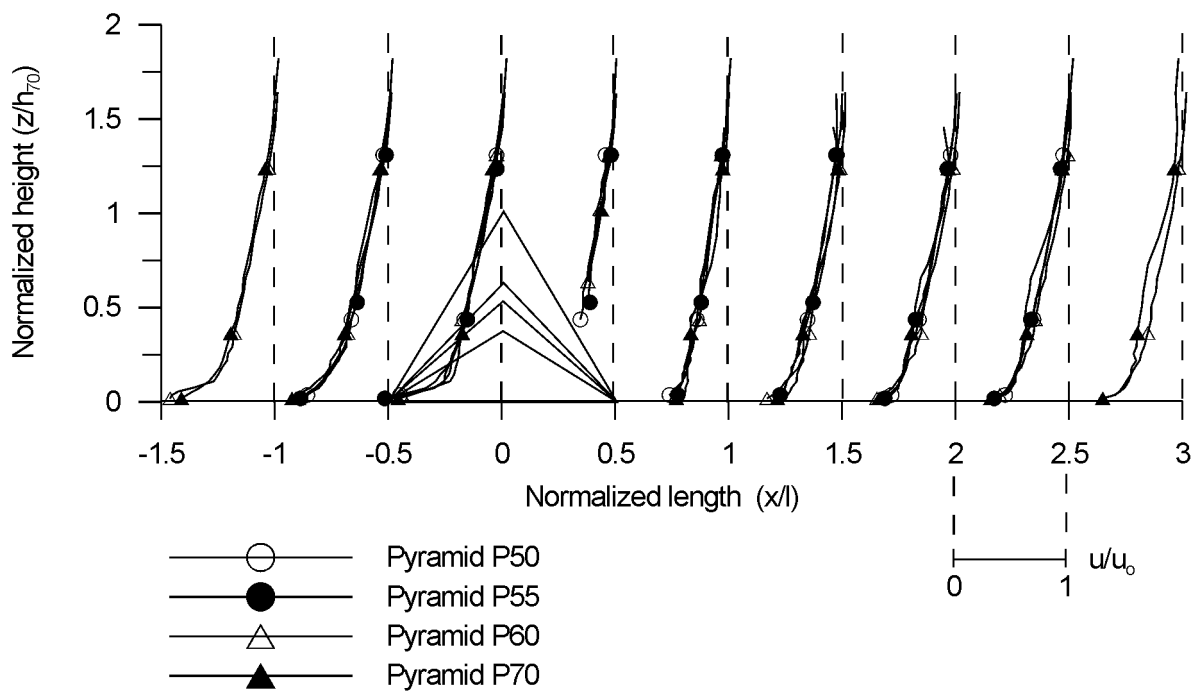
(b) Pyramids P50 – P70

Fig. 5.3. Longitudinal mean velocity profiles at  $y/l = 0.25$  ( $\alpha' = 0^\circ$ ,  $u_0 = 5$  m/s).

When the measurement plane moves to the 3<sup>rd</sup> plane, which is the side plane at  $y/l = 0.5$ , the mean velocity profiles show no significant disturbance, see Fig. 5.4. However, for the pyramids with base angles greater than  $50^\circ$ , negative velocities are still detected near the bottom at  $x/l = -0.5$ . Otherwise, the profiles are almost coinciding into one profile and the profile follows the incoming flow profile.



(a) Pyramids P30 – P45



(b) Pyramids P50 – P70

Fig. 5.4. Longitudinal mean velocity profiles at  $y/l = 0.50$  plane ( $\alpha' = 0^\circ$ ,  $u_0 = 5$  m/s)

### 5.1.2. Vector Fields

The longitudinal mean velocity combined with the vertical mean velocity generate the mean vector velocity field for each pyramid in a 2D-plane. The velocity vector fields at  $y/l = 0$  are shown in Fig. 5.5. From the plots given, the formation of the recirculation zones in the leeward side of the pyramids can be observed. Small recirculation zones can be observed in the leeward side of pyramid P30 and P40 (Fig. 5.5. (a) and (b)). The recirculation zones are attached to the backward facing the pyramid surfaces. For the pyramids with base angles greater than  $45^\circ$ , which can be categorized as tall buildings ( $2h/l > 1$ ), the recirculation zone can be visualized more clearly as presented in Fig. 5.5. (c) – (g).

The size of the recirculation zone increases with increasing base angle and height. In this zone, the vector plots of the flow velocity reveal a large-scale fluid rotation. This large scale vortex is considered to be very stable in comparison to recirculation bubbles behind cuboidal bluff bodies where the flapping of the shear layer intermittently causes the recirculation bubble to be convected downstream [Abuomar et al 2000]. Due to a smaller gradient between the ambient pressure and the back pressure of the pyramid, the rotating velocity within the recirculation zone decreases. The stability of the vortex system might come from the two very stable side vortices on the side walls and of the two very stable vortices at the corners of the backside of the pyramids. All of these vortices are found to have varying size and rotating velocity with height.

The next results are the mean velocity vector fields at  $y/l = 0.25$  and  $y/l = 0.50$  that can be seen in Fig. 5.6 and Fig. 5.7, respectively. Compared to the vector fields at  $y/l = 0$ , it is clear that the recirculation area in the upstream side and in the leeward side of the pyramids are decreasing. At  $y/l = 0.25$ , for pyramid P30, the presence of the pyramids has no significant effect to the flow structures. When the base angle increases to  $40^\circ$ , a small recirculation zone is identified in the leeward side of the pyramids and it increases as the base angle increases. At the upstream side, the recirculation zone is identified when the base angle reaches  $50^\circ$  and also increases with increasing base angles.

For the plane at  $y/l = 0.5$ , the presence of the pyramids does not introduce any significant disturbance to the flow structures. Only small disturbances can be identified near the bottom at  $x/l = -0.5$  for the pyramids with base angle greater than  $50^\circ$ . Based on the longitudinal velocity profiles shown in Fig. 5.4 (b), negative velocities are detected at  $x/l = -0.5$ . This means small recirculation zones are also expected to be formed at the side surface near the edges of the pyramids even though it could not be visualized in the Fig. 5.7. It seems that the density of the data points at this plane is not high enough to reveal the small recirculation zones at the side area. It should also be noted that the plots at the side area of the pyramids ( $x/l = -0.5$  to  $x/l = 0.5$ ) are not obtained from direct measurements but from an interpolation of results from measurements around the front and the back surface.



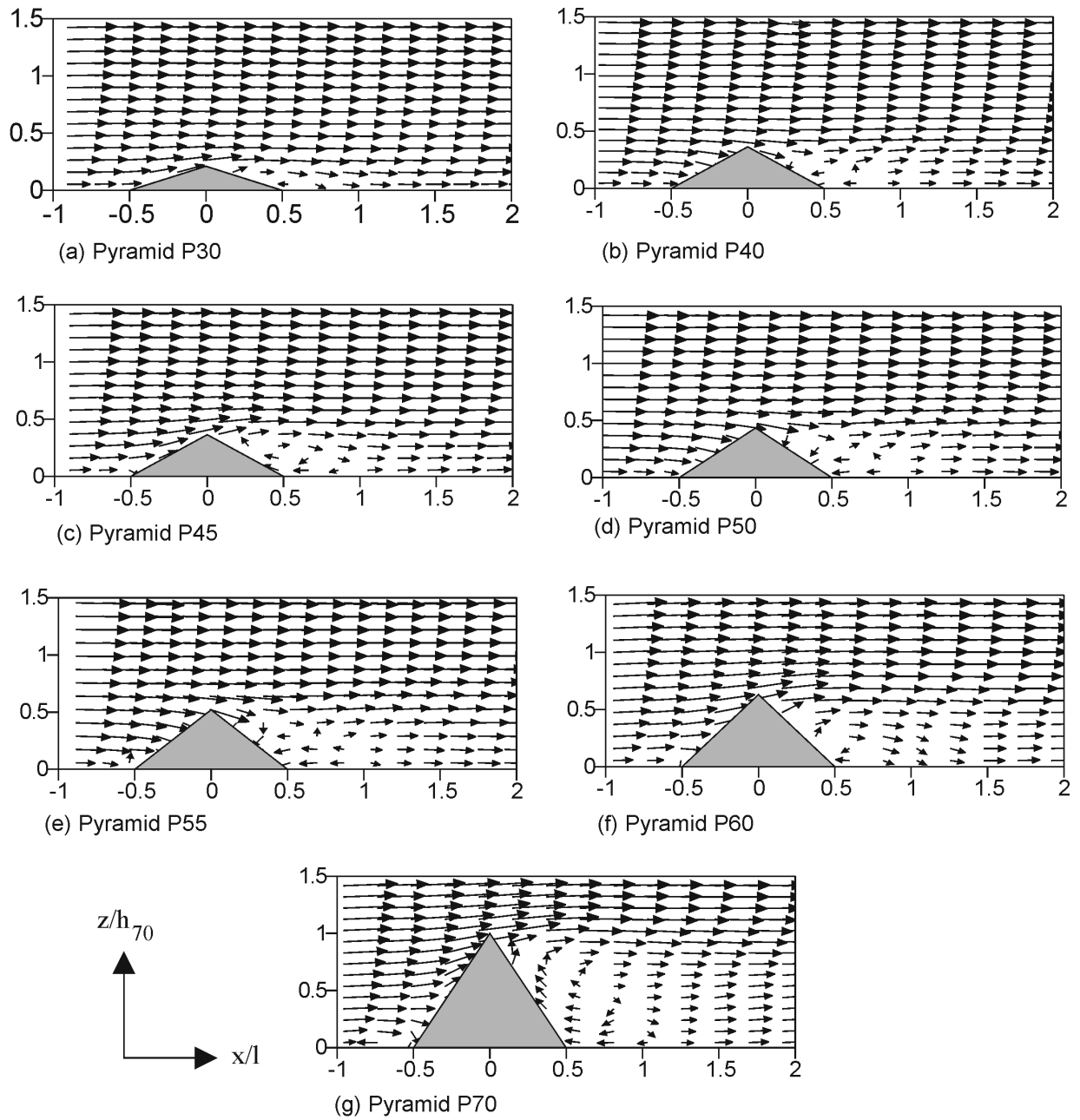


Fig. 5.5. Vector field in a 2D-plane at  $y/l = 0.0$  for investigated pyramids ( $\alpha' = 0^\circ$ ,  $u_0 = 5$  m/s,  $h_{70} = 274.7$  mm)

5. Experimental Results

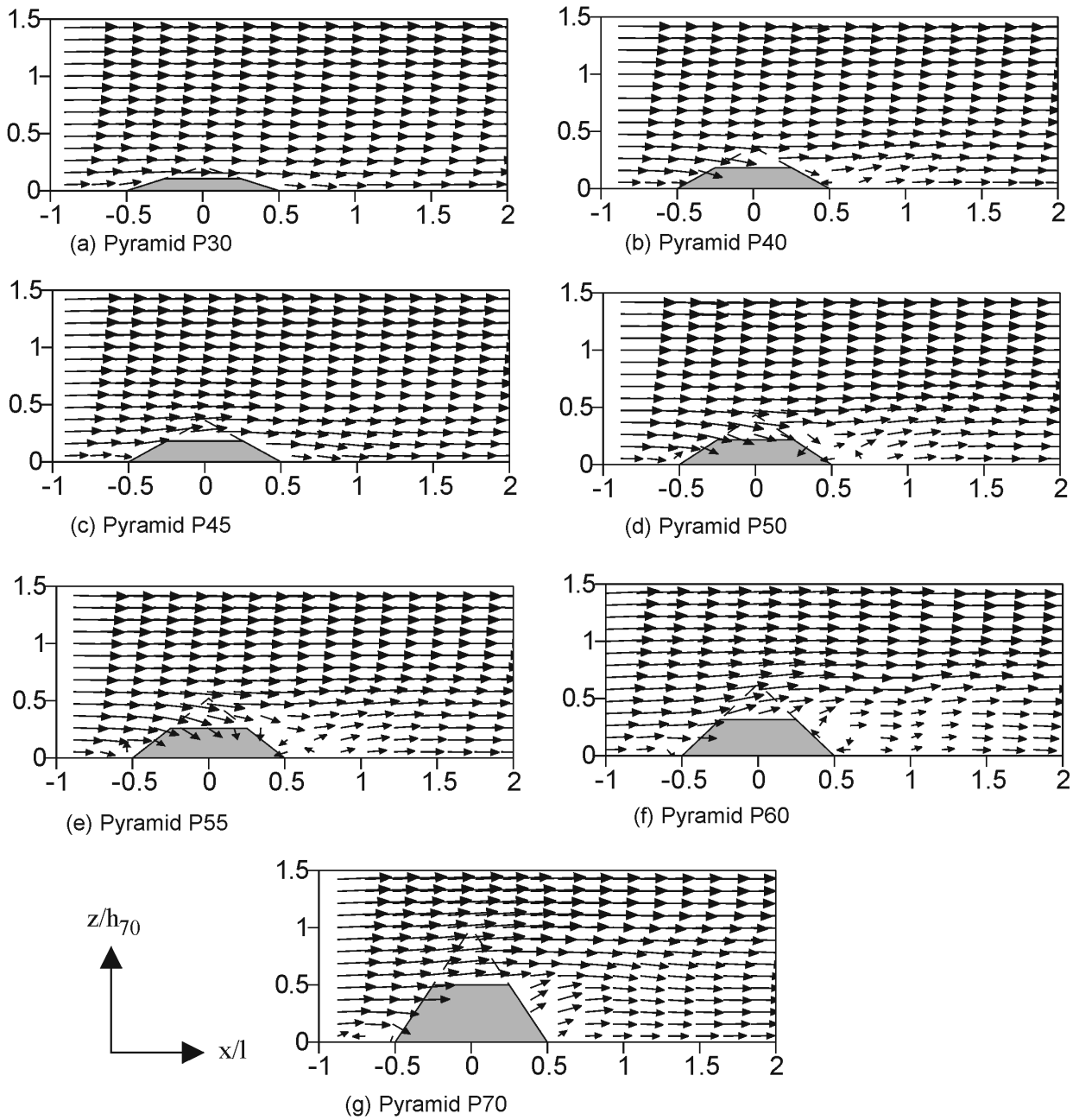


Fig. 5.6. Vector field in a 2D-plane at  $y/l = 0.25$  for investigated pyramids ( $\alpha' = 0^\circ$ ,  $u_0 = 5$  m/s,  $h_{70} = 274.7$  mm)

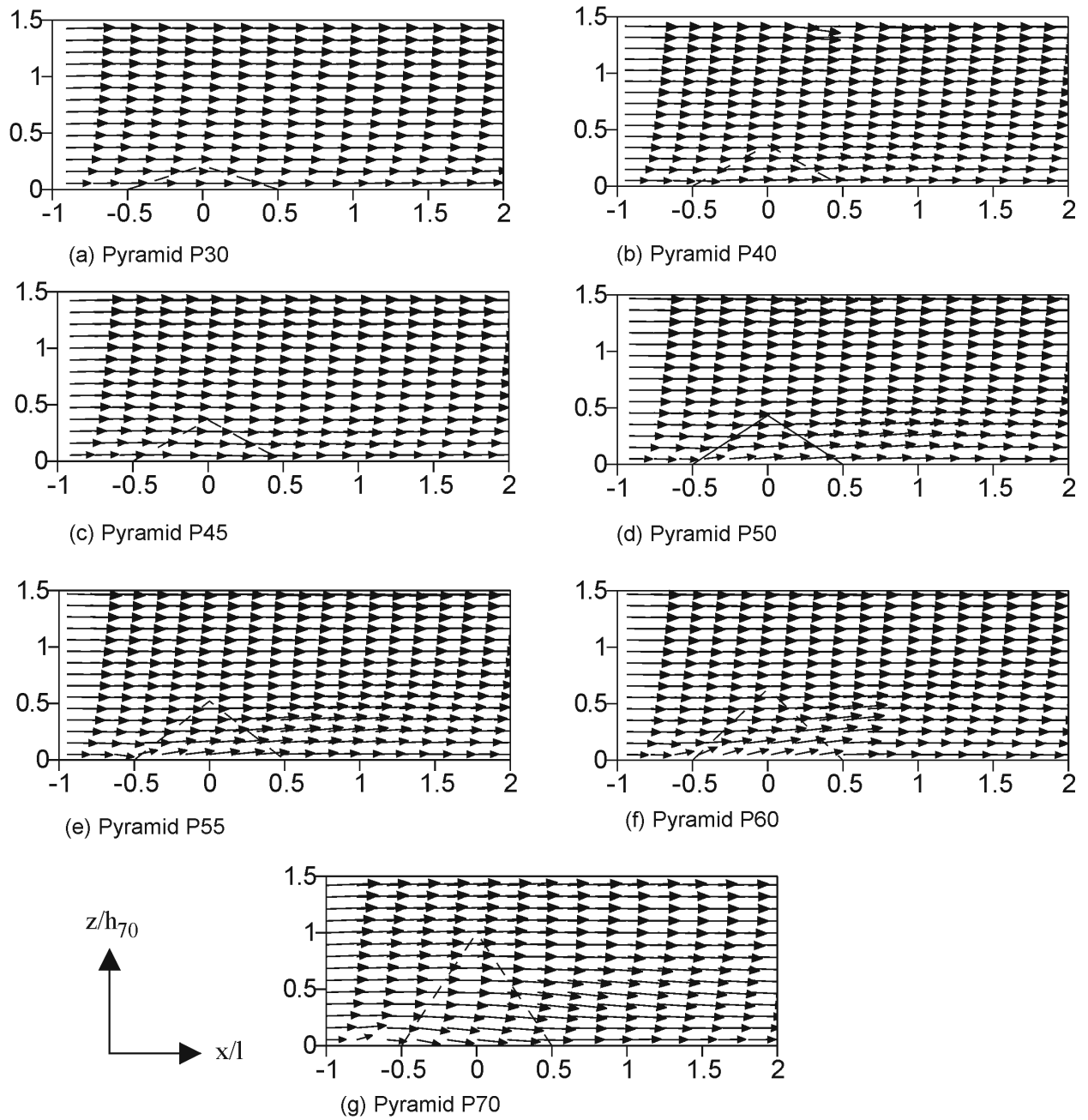


Fig. 5.7. Vector field in a 2D-plane at  $y/l=0.50$  for investigated pyramids ( $\alpha' = 0^\circ$ ,  $u_0 = 5$  m/s,  $h_{70} = 274.7$  mm)

### 5.1.3. Recirculation Zone

The vector plots in Section 5.1.2 show qualitatively the characteristics of the recirculation zone at the leeward side of the pyramids. In this section, the quantitative results are presented. The recirculation zone is defined as the zero streamline ( $\psi=0$ ), which is calculated by integrating the velocity profiles  $u$ . In mathematical form, it can be described as:

$$\psi(z) = \int_0^z u(z) dz \tag{5.1}$$

where  $u(z)$  is the velocity in the main stream direction (longitudinal) at different height  $z$ . One important characteristic of the recirculation zone is the area of recirculation, which has a significant impact to the environment as it affects the dispersion characteristics, especially in the leeward side of the pyramids. Another important characteristic is the reattachment length, which is defined as the point where the zero streamline reaches the ground. Fig. 5.8 shows the recirculation zone in the windward side and leeward side of the pyramids at  $y/l = 0$ . The figure shows that the recirculation zones increase proportional with the height and the base angle of the pyramids in both the windward side and the leeward side of the pyramids.

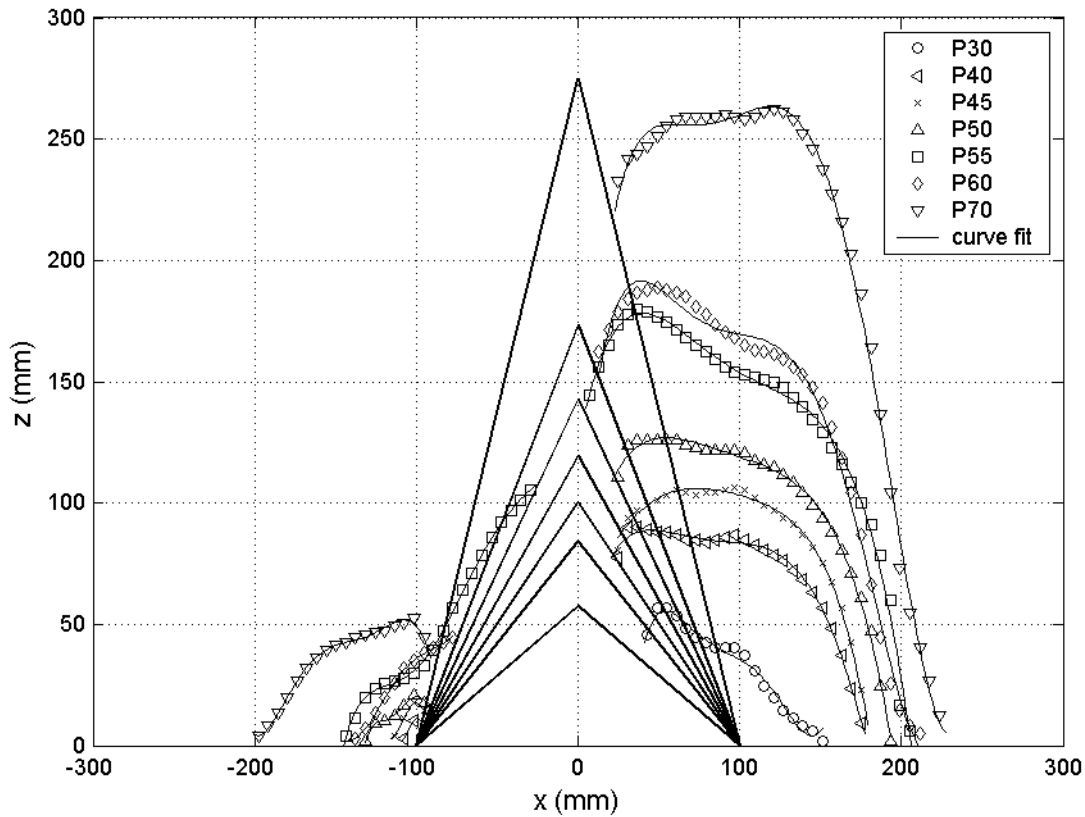


Fig. 5.8. Presentation of zero streamlines which illustrate the recirculation zone in the windward side and leeward side of the pyramids at  $y/l = 0.0$  ( $\alpha' = 0^\circ$ ,  $u_0 = 5$  m/s)

The zero streamlines at the leeward side of the pyramids are presented more clearly in non-dimensional form in Fig. 5.9. In this figure, the length of the pyramid is taken to scale the longitudinal ( $x$ ) and vertical ( $z$ ) distance. Thus, the proportionality of the recirculation zone increment to base angle can be observed. Generally, the curves in Fig. 5.9 clearly show the tendency that the recirculation zone increases with increasing base angle, except between Pyramid P55 and Pyramid P60. The increases of the recirculation zone from pyramid P50 to pyramid P55 are relatively greater as compared to the increases of pyramid P55 to pyramid P60. This causes the zero streamline of pyramid 55 almost coincides with the one of Pyramid P60. At  $x/l = 0.8$ , it is higher than Pyramid P60 and increases slightly when the zero streamline reaches the ground. Despite this phenomenon, the recirculation area of pyramid P55 is still smaller than pyramid P60, as shown in Fig. 5.10.

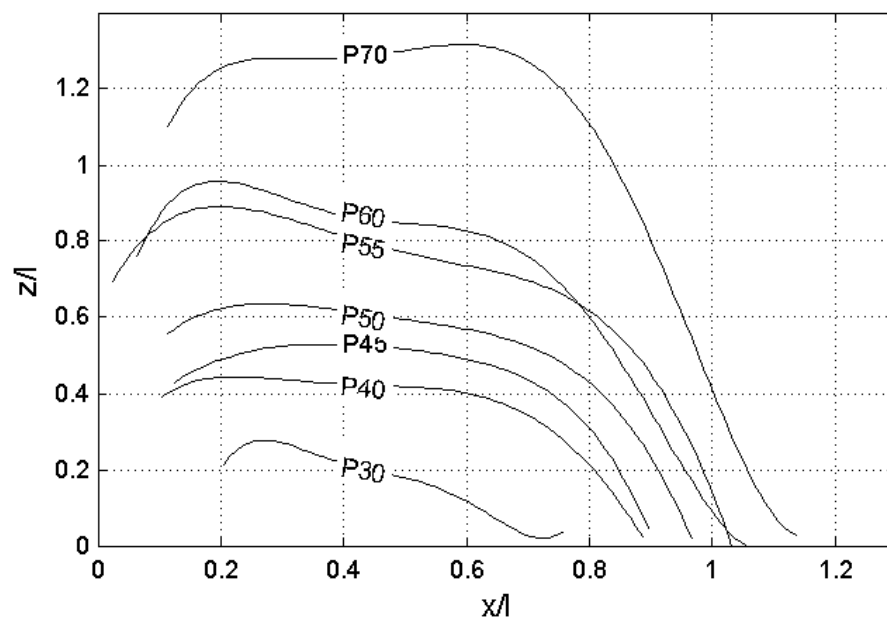


Fig. 5.9. Presentation of non-dimensional zero streamline diagram at the leeward side of the pyramids

Fig. 5.10 shows the non-dimensional area of recirculation zone, which is calculated by integrating the area under the zero streamline from the surface of the pyramid up to the reattachment length and scaled by the base area of the pyramid ( $l^2$ ). The figure clearly shows that the recirculation area at the leeward side of the pyramid increases when the base angle increases. This non-dimensional recirculation area can be approximated by single curve and an equation for estimating the recirculation area as a function of the pyramid base angle for pyramid with base angle  $30^\circ$  to  $70^\circ$  can be generated. The fitted equation is:

$$\frac{A}{l^2} = 0.00029 \cdot \theta^2 - 0.0053 \cdot \theta + 0.0041 \quad (5.2)$$

where  $l$  is the pyramid base length and  $\theta$  is the pyramid base angle.

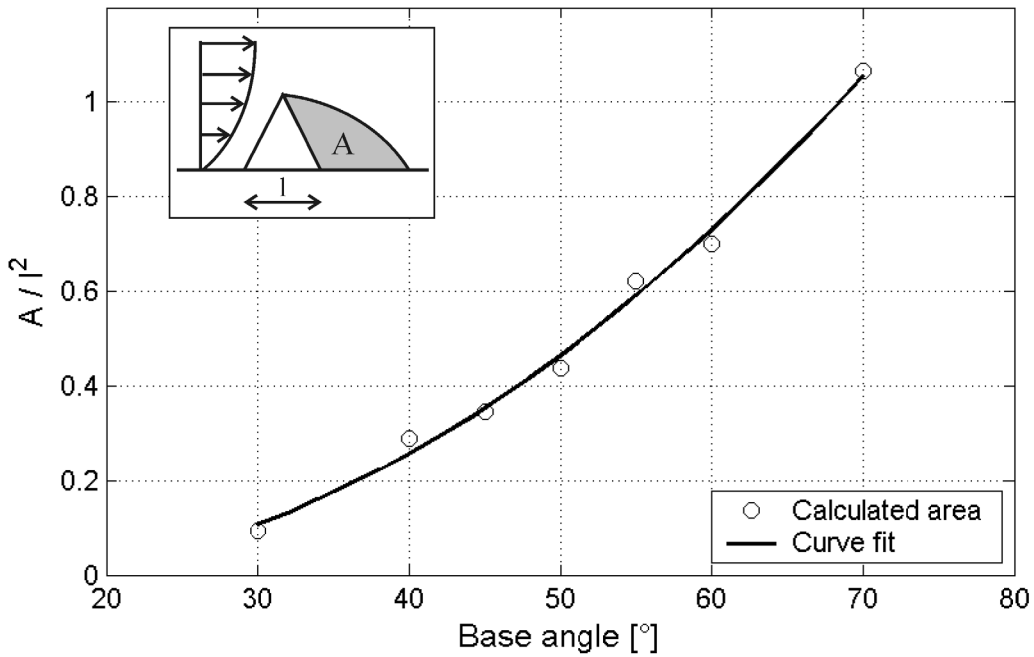


Fig. 5.10. Area of the recirculation zone at  $y/l = 0.0$  in non-dimensional form as a function of base angle for investigated pyramids

The recirculation zone is characterized by the reattachment length in the leeward side of the pyramid, which is regarded as the most important parameter characterizing separated and reattaching flows [Eaton et.al., 1981]. Heist et.al., 1997 estimated the reattachment length by extrapolating to the wall the locus of point where the mean stream wise velocity is zero. In the present study, the reattachment length  $x_r$  is measured from the leeward side surface of the pyramid (at the bottom position) to the point where the zero streamline reaches the ground, and it is normalized with the pyramids height  $h$ . Fig. 5.11 shows the schematic illustrations of the reattachment lengths definition in the leeward side of the cuboidal and pyramidal buildings.

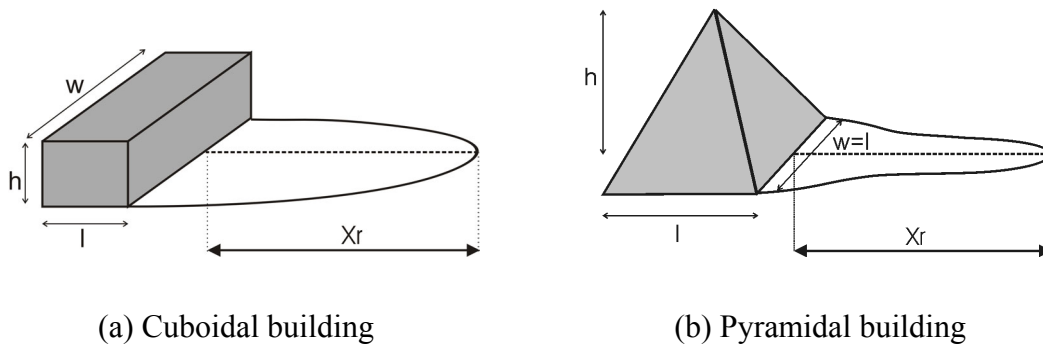


Fig. 5.11. Sketch of reattachment length ( $x_r$ )

Fig. 5.12 shows the reattachment length ( $x_r$ ) of the pyramids in dimensional form at different  $y$  positions. The figure shows that the reattachment lengths are influenced by the steepness and the height of the pyramids. At the centre plane of the pyramid ( $y = 0$  mm), the reattachment lengths increase proportional with the base angle and heights, except for pyramid P55 and P60 where the reattachment lengths almost coincide into one point. When the location of observation is moved to the middle plane ( $y = 50$  mm), a relatively short reattachment length occurs in the leeward side of pyramid P30. Then, the reattachment length increases for pyramid P40, and remains constant as the base angle and height increase to pyramid P45. Afterwards, as the base angle and height increase to pyramid P50, the reattachment length suddenly increases from 36 mm (pyramid P45) to 58 mm (pyramid P50) and after pyramid P50, the reattachment lengths remain relatively constant. This shows that at a certain degree the reattachment lengths are relatively sensitive to the variation of base angle and height.

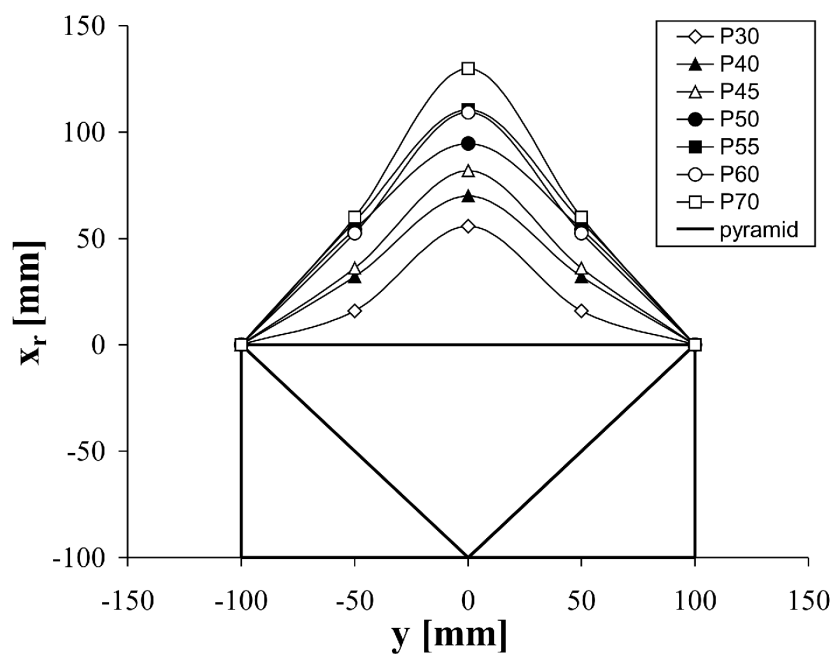


Fig. 5.12. Reattachment length ( $x_r$ ) for different pyramids at different lateral position ( $y$ ) in dimensional form, with wind direction  $\alpha' = 0^\circ$ .

The next figure, Fig. 5.13, shows the reattachment lengths in a non-dimensional form, both axes are normalized with the height of the pyramids. It is clear that with these ratios ( $x_r/h$  and  $y/h$ ), the shallower pyramids are schematically wider than the steeper pyramids. As a consequence, pyramid P30 has the longest dimensionless reattachment length since the wide (broad) geometry of the pyramid creates a larger dimension in comparison to the other pyramids. In general, when the base angle increases, the reattachment length decreases. At the center plane ( $y/h = 0$ ), the reattachment length for pyramid P40, P45, P50, and P55 are relatively similar. The reattachment length decreases again when the base angle increases to pyramid P60 and P70. In Fig. 5.13, two different trends of curve for the reattachment length can be observed. The first trend is

observed for pyramids P30, P40 and P45 and the second for pyramids P50 to pyramid P70. In general, the investigations of a wide range base angle variation ( $30^\circ < \theta < 70^\circ$ ) at various lateral (y) locations shows that the variation of base angles affects significantly the reattachment lengths at the leeward side of the pyramid, despite for certain base angle degrees at some locations, the reattachment lengths coincide at similar length.

Based on the curves of reattachment length, pyramid P30, P40 and P45 can be categorized as shallow pyramids and pyramid P50, P55, P60 and P70 can be categorized as steep pyramids. This classification is in good agreement with the results from Abuomar [2000], who categorized the pyramid into broad pyramids ( $\theta < 52.5$ ) and slender pyramids ( $52.5 < \theta < 82.5$ ). In the present study, so far, the base angle that categorizes the pyramids lies approximately at  $50^\circ \pm 5^\circ$ .

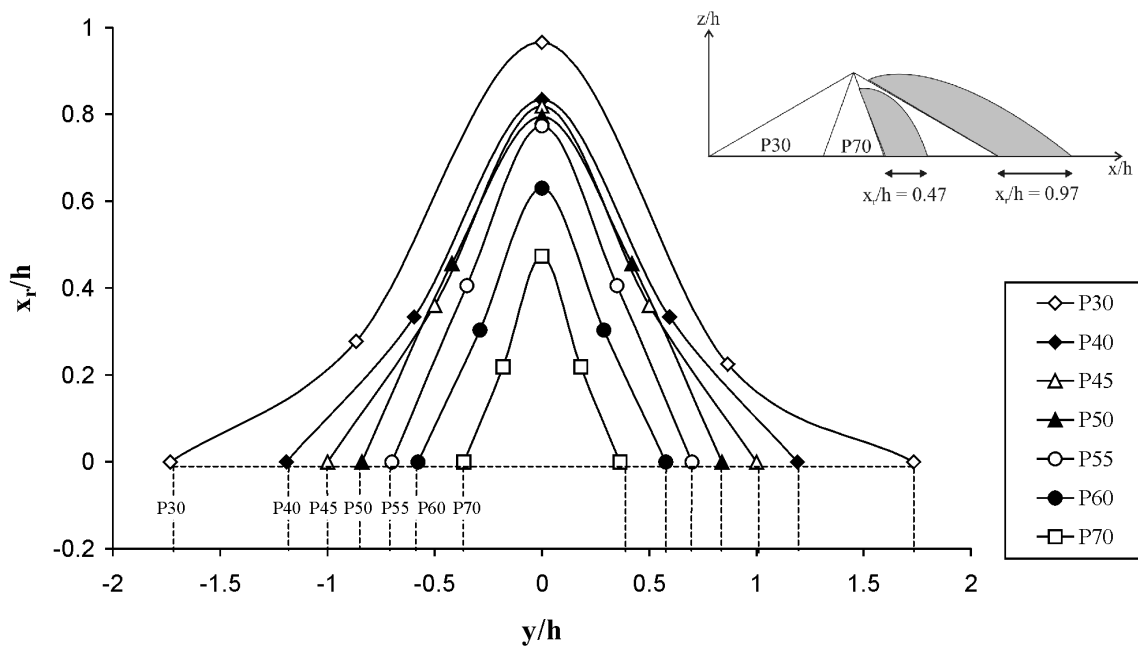


Fig. 5.13. Reattachment length for different pyramids at different lateral position in non-dimensional form ( $x_r/h$  and  $y/h$ ), measured from the pyramid edges with wind direction  $\alpha' = 0^\circ$ .

Evans, 1957 introduced an equation to calculate the reattachment length for rectangular buildings (i.e. cuboidal), which is normalized to the height of the building ( $x_r/h$ ). The geometry of the buildings were characterized by length (l), height (h) and width (w), see Fig. 5.11. The equation can be applied for buildings with  $l/h < 2$ , and later, in 1979, Hosker introduced another equation for  $l/h > 2$  [Hosker, 1984]. Both equations are:

$$\text{Evans } (l/h < 2): \quad \frac{x_r}{h} = \frac{1}{h} + \frac{A \cdot (w/h)}{1.0 + B \cdot (w/h)} \quad (5.3)$$

$$\text{Where } A = -2.0 + 3.7 \cdot (l/h)^{-1/3}$$

$$B = -0.15 + 0.305 \cdot (l/h)^{-1/3}$$



$$\text{Hosker } (l/h > 2): \quad \frac{x_r}{h} = \frac{1.75 \cdot (w/h)}{1.0 + 0.25 \cdot (w/h)} \quad (5.4)$$

Fig. 5.14 shows the comparison of the reattachment lengths between pyramidal and cuboidal buildings. In order to compare the reattachment lengths, a square base cuboidal building was chosen, which has the length ( $l$ ) equal to the width ( $w$ ), see Fig. 5.11. Fig. 5.14 shows that the recirculation length in the leeward side of a pyramid at  $y/l = 0.0$  and  $y/l = 0.25$  are much shorter than that of a cuboidal bluff body with a similar length to height ratio. These phenomena are of interest not only in the area of building aerodynamics or in architecture but also in other technical fields and processes, where the mixing or heat transfer above technical surfaces covered with arrays of small pyramids can be increased significantly.

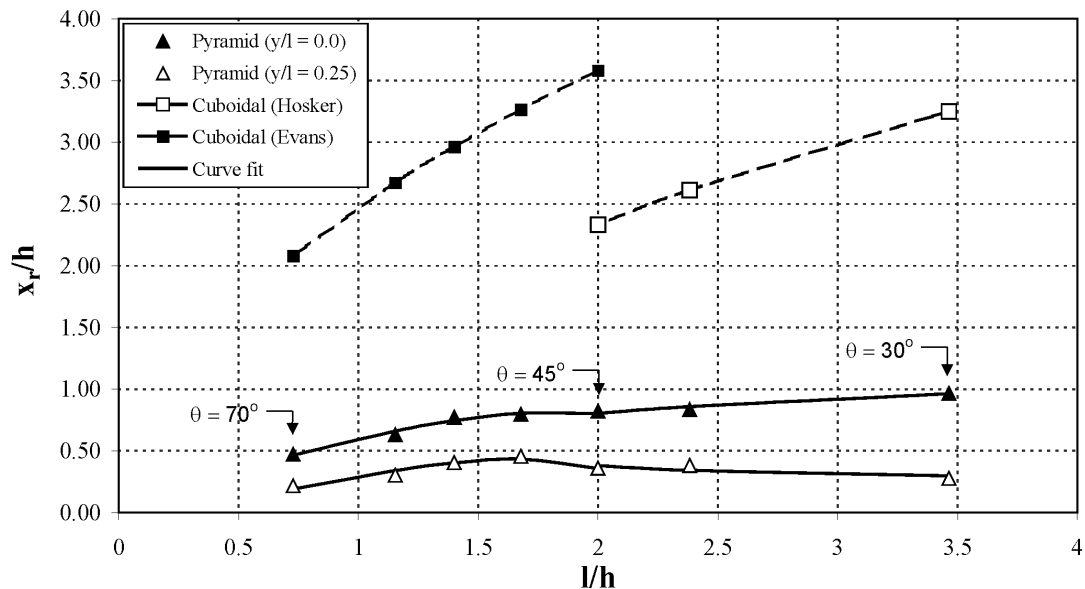


Fig. 5.14. Comparison of the reattachment lengths ( $x_r$ ) between pyramidal and cuboidal buildings ( $w = l$ ) as a function of length to height ratio.

From the presented results in Fig. 5.14, it is clear that for both planes ( $y/l = 0$  and  $y/l = 0.25$ ), there are two types of dependency for the reattachment lengths ( $x_r/h$ ) to  $l/h$ . First, for pyramids with base angles ranging from  $45^\circ$  to  $70^\circ$  and second ranging from  $30^\circ$  to  $45^\circ$ . The length to height ratio of the pyramid with base angle  $45^\circ$  is 2. This ratio ( $l/h = 2$ ) is also the ratio where Evans and Hosker used to differentiate Eq. 5.3 and Eq. 5.4 for cuboidal buildings. Based on the equations from Evans and Hosker, the present results can be approximated by two curves and a set of equations for estimating the reattachment length as a function of the pyramid length and height can be generated. It should be noted that the ratio of the length and height represents also the base angle of the pyramid. The fitted equations (indicated by the solid lines in Fig. 5.14) are:

## 5. Experimental Results

For the center plane ( $y/l = 0.0$ )

$$30^\circ < \theta < 45^\circ \quad \frac{x_r}{h} = \frac{1.044 \cdot (l/h)}{1.0 + 0.799 \cdot (l/h)} \quad (5.5)$$

$$45^\circ < \theta < 70^\circ \quad \frac{x_r}{h} = \frac{1}{h} + \frac{A \cdot (l/h)}{1.0 + B \cdot (l/h)} \quad (5.6)$$

$$\text{Where} \quad A = -2.303 + 1.195 \cdot (l/h)^{-1/3}$$

$$B = -3.628 + 5.366 \cdot (l/h)^{-1/3}$$

For the middle plane ( $y/l = 0.25$ )

$$30^\circ < \theta < 45^\circ \quad \frac{x_r}{h} = \frac{0.257 \cdot (l/h)}{-0.895 + 1.125 \cdot (l/h)} \quad (5.7)$$

$$45^\circ < \theta < 70^\circ \quad \frac{x_r}{h} = \frac{1}{h} + \frac{A \cdot (l/h)}{1.0 + B \cdot (l/h)} \quad (5.8)$$

$$\text{Where} \quad A = 0.479 - 0.713 \cdot (l/h)^{-1/3}$$

$$B = 0.409 - 1.078 \cdot (l/h)^{-1/3}$$

These equations are applied for following conditions:

- Solid (i.e. no ventilation) and sharp edges pyramid
- Flow conditions: urban / city centre area
- Wind direction,  $\alpha' = 0^\circ$

Table 5.1 shows the comparison of the normalized reattachment length obtained from the experiments and obtained from the estimation using the equations above. The error percentage of each available point can be calculated using:

$$\text{Error} = \frac{\left| (x_r/h)_{\text{exp.}} - (x_r/h)_{\text{calc.}} \right|}{(x_r/h)_{\text{exp.}}} \times 100 \% \quad (5.9)$$

and it is found that the possible maximum error is 3.84 %.

Table 5.1. Comparison of reattachment length to height ratio ( $x_r/h$ ) at the leeward side of the pyramid between the experimental results and calculation.

Position	Range of base angle	Base angle	Experiment	Calculated	Error
		(°)	$(x_r/h)_{exp.}$	$(x_r/h)_{calc.}$	(%)
$y/l = 0.0$	$30^\circ < \theta < 45^\circ$	30	0.9661	0.9617	0.45
		40	0.8342	0.8584	2.42
		45	0.8195	0.8052	1.43
	$45^\circ < \theta < 70^\circ$	45	0.8195	0.8024	1.72
		50	0.7950	0.8035	0.86
		55	0.7739	0.7444	2.95
		60	0.6305	0.6600	2.95
	70	0.4732	0.4653	0.79	
$y/l = 0.25$	$30^\circ < \theta < 45^\circ$	30	0.2771	0.2966	1.95
		40	0.3814	0.3430	3.84
		45	0.3600	0.3795	1.95
	$45^\circ < \theta < 70^\circ$	45	0.3600	0.3574	0.26
		50	0.4563	0.4318	2.45
		55	0.4054	0.4027	0.28
		60	0.3032	0.3402	3.70
	70	0.2184	0.1894	2.90	

The zero streamlines at the centre of the pyramids shown in Fig. 5.8 indicate that the curves have a similar shape. The similarities of the curves are examined by plotting the measured zero streamline curves in a non-dimensional form as shown in Fig. 5.15. The reattachment length at  $y/l = 0$  is taken to scale the longitudinal distance ( $x$ ) and the height of the pyramids to scale  $z$ . For pyramids with base angles ranging from  $40^\circ$  to  $60^\circ$ , Fig. 5.15 shows that their non-dimensional zero streamline curves can be approximated by one similar curve. A fifth degree polynomial equation is here proposed for the similarity curve (indicated by the solid line in Fig. 5.15). For practical purposes, the proposed equation can be used to estimate the zero streamline or to illustrate the recirculation area at the centre plane of the pyramids ( $y/l = 0$ ). The proposed equation can be written as:

$$\frac{z}{h} = 15.37x_*^5 - 46.03x_*^4 + 48.32x_*^3 - 23.30x_*^2 + 5.12x_* + 0.63 \quad (5.10)$$

$$\text{where } x_* = \frac{x}{x_r + 0.5 \cdot l}$$

with,  $x$  is the distance measured from the centre of the pyramid,  $x_r$  is the reattachment length,  $l$  is the pyramid base length,  $z$  is the height measured from the ground and  $h$  is the pyramid height.

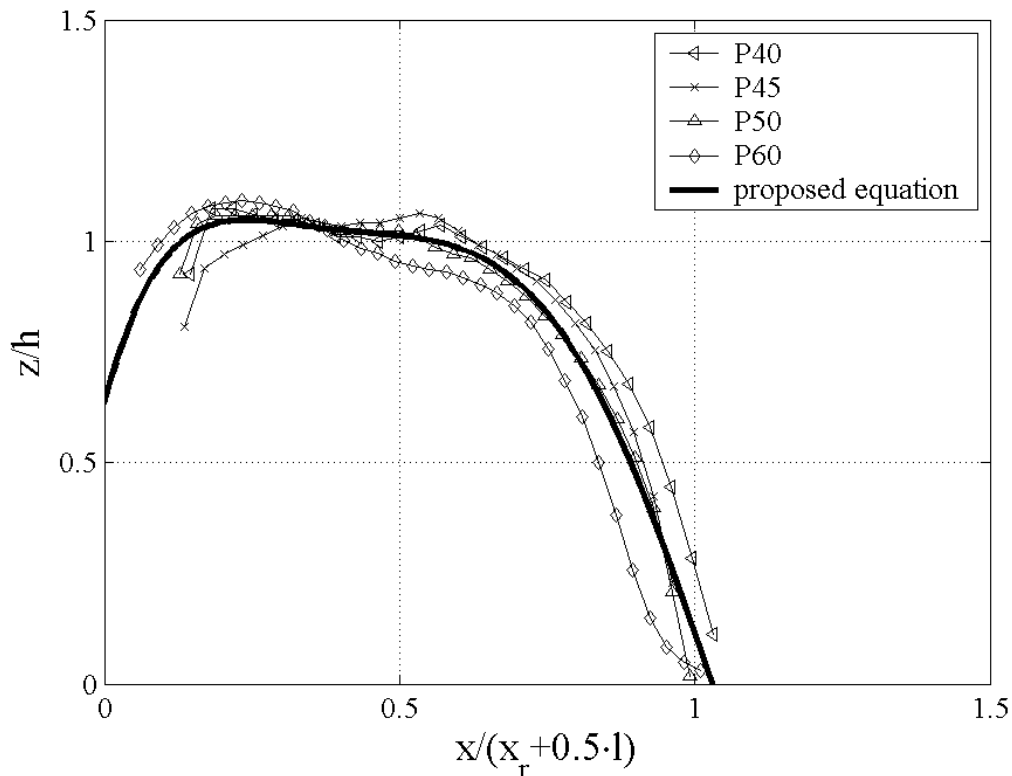


Fig. 5.15. Zero streamline at the leeward side of the centre pyramid ( $y/l = 0$ ), normalized with the height and the reattachment length.

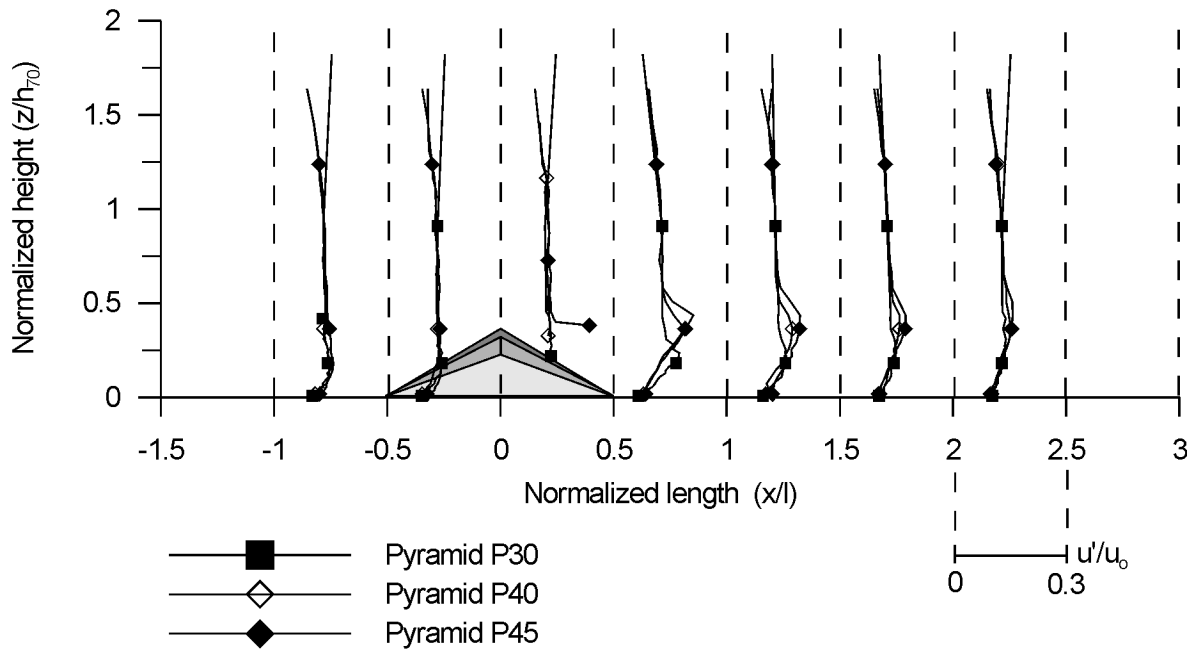
#### 5.1.4. Turbulence Intensity

One of the interesting quantities that characterize a flow is the turbulence intensity, which reflects e.g. the turbulent mixing processes. The turbulence intensities are defined as the fluctuation rate  $u'$  and  $w'$ . Fig. 5.16 and Fig. 5.18 show the profile of turbulence intensities in longitudinal ( $I_u$ ) and vertical direction ( $I_w$ ) at the centre plane,  $y/l = 0.0$ , of the pyramids. In the figures, the turbulence intensities are normalized by the mean velocity at the boundary,  $u_0 = 5$  m/s. The figures clearly show that the turbulence intensities increase as the base angle and height increase.

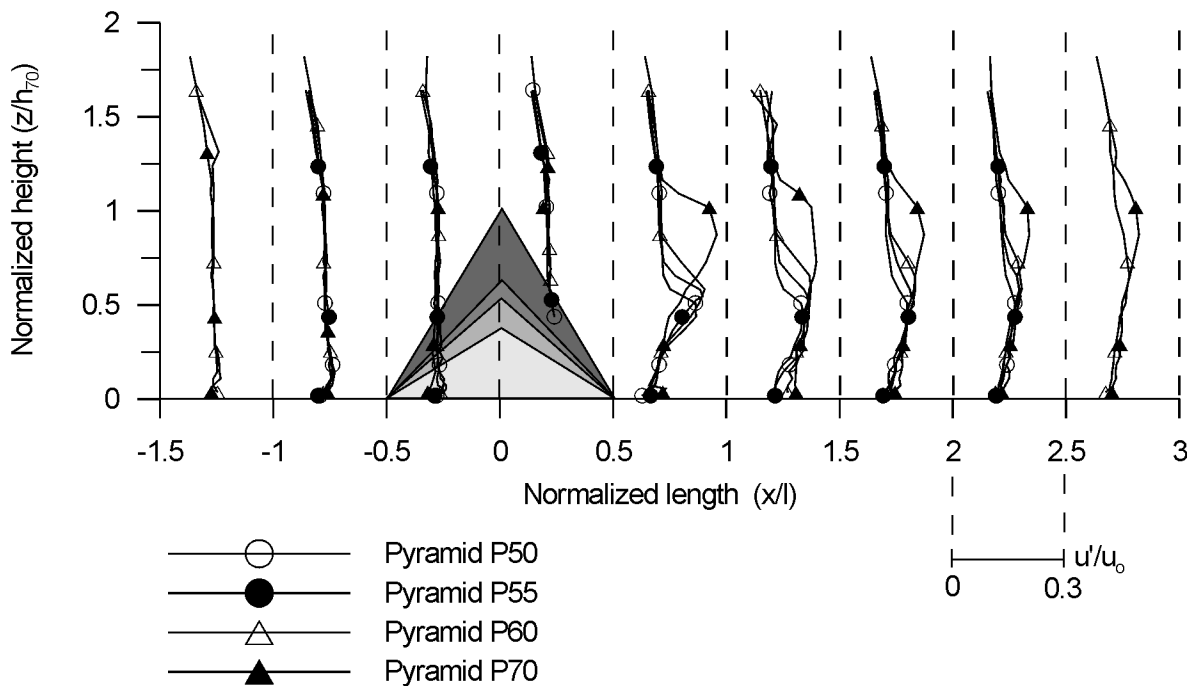
The level of longitudinal turbulent intensity in the stationary incoming flow is in the range of 10 % to 15%. From Fig. 5.16, the disturbances of the stationary condition appear at  $x/l = 0.5$ . For pyramid P30, P40 and P45, the level of maximum longitudinal turbulence intensities are 18 %, 20 %, and 21 %, respectively. The levels are increasing when the base angles of the pyramids increase. The maximum longitudinal turbulence intensity at  $x/l = 0$  occur for pyramid P70 at a level of 28 %.

Fig. 5.16 shows several turbulence intensities profiles at selected locations. In order to gain a better resolution, several profiles near the pyramid were also measured. From the measured points, it is found that the highest level of turbulent intensity actually occurs at a distance of  $x/l = 0.15$  and height of  $z/h = 1$ , i.e. immediately after the tip of the pyramids, as presented in Fig.

5.17. The maximum turbulent intensity for pyramid P30 is found to be 20 %, which is 2 % higher as the turbulence intensity at  $x/l = 0.5$ . The turbulent intensity increases when the base angles increase and reach a maximum when the base angle reaches  $70^\circ$ , which is 32 %.



(a) Pyramids P30 – P45



(b) Pyramids P50 – P70

Fig. 5.16. Longitudinal turbulent intensity at  $y/l = 0.0$  for investigated pyramids ( $\alpha' = 0^\circ$ ,  $u_0 = 5 \text{ m/s}$ ,  $h_{70} = 274.7 \text{ mm}$ )

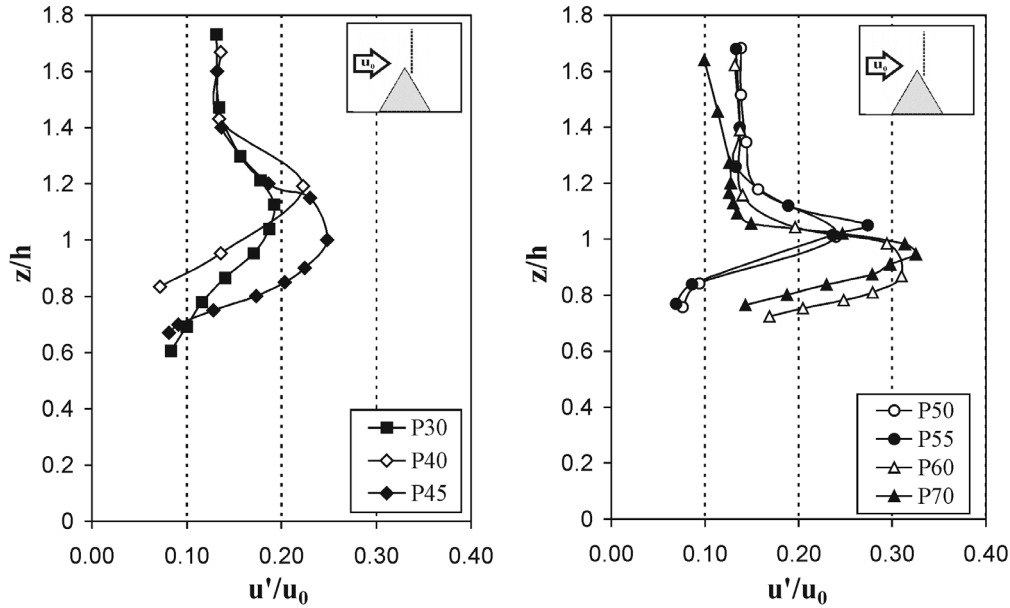
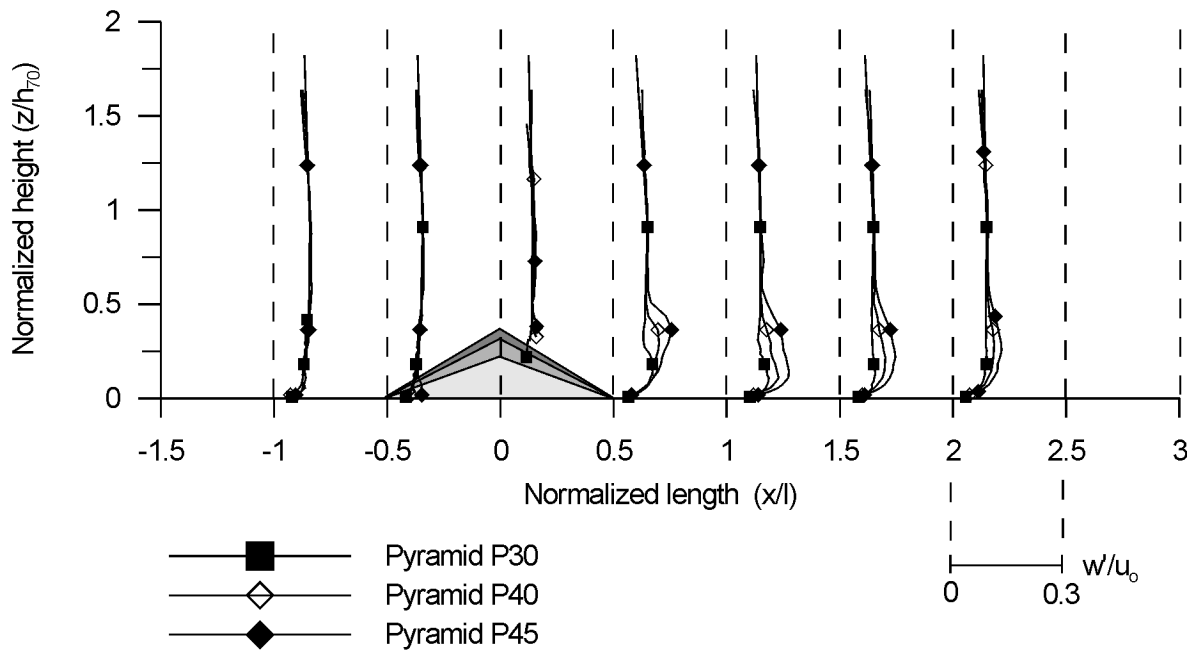


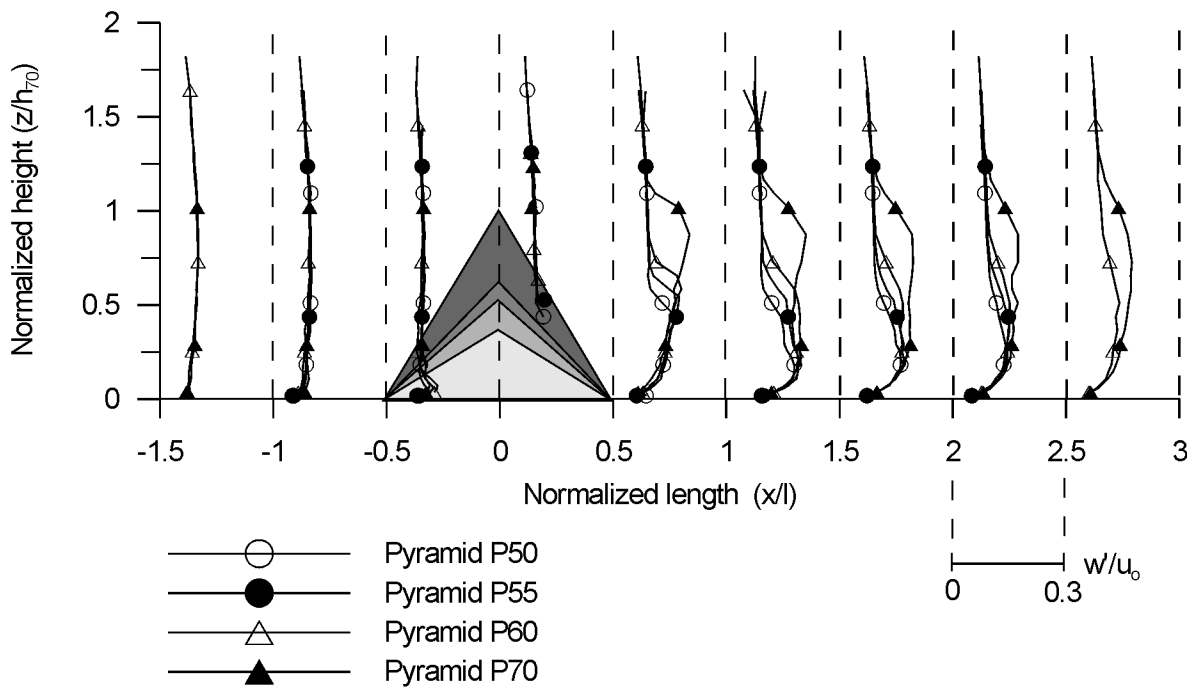
Fig. 5.17. Turbulence intensity profiles for the pyramids at  $y/l = 0.0$  and  $x/l = 0.15$  ( $\alpha' = 0^\circ$ ,  $u_0 = 5$  m/s)

Fig. 5.18 shows the vertical turbulence intensity ( $I_w$ ) profiles at  $y/l = 0.0$ . The undisturbed vertical turbulent intensities level in the approach flow is in the range of 5 % to 10 %. The figures show  $I_w$  increases both at windward and leeward side of the pyramids. At the windward side, the turbulence intensities increase at  $x/l = -0.5$  near the bottom of the pyramids. This is the location where the horseshoe vortices are detected. At the leeward side,  $I_w$  increases up to the tip of the pyramid where the maximum levels are identified. As the base angle increases, the turbulence intensities also increase.

At the upstream side when the base angle reaches  $45^\circ$ , the vertical turbulent intensity near the bottom slightly increases from 5% to 9%. When the base angle increases, the level of turbulence also increases and reaches the maximum for pyramid P70 at 11 %. This is the area where the horseshoe vortices are detected. In the near leeward side of the pyramid, the turbulence intensity level reaches its maximum after the tip of the pyramids. At  $x/l = 0.5$ , the maximum turbulent intensity for pyramid 30 is 10% and it increases to 21 % as the base angle reaches  $70^\circ$ .



(a) Pyramids P30 – P45



(b) Pyramids P50 – P70

Fig. 5.18. Vertical turbulent intensity at  $y/l = 0$  for investigated pyramids ( $\alpha' = 0^\circ$ ,  $u_0 = 5$  m/s,  $h_{70} = 274.7$  mm)

### 5.1.5. Reynolds Shear Stress

The Reynolds shear stresses are estimated based on the changes of the momentum, which are caused by the rate of velocity fluctuations in the flow fields. The values represent a descriptive turbulent rate in the flow fields. It can be formulated as described in Eq. 2.15 [see, e.g. Rotta, J.C., 1972]:

$$\tau'_{xz} = -\rho \overline{u'w'} \quad (5.11)$$

In this study, the Reynolds shear stresses are normalized by the free stream velocity  $u_0$  as formulated below, and then presented in isolines form

$$\tau' = -\frac{\overline{u'w'}}{u_0^2} \quad (5.12)$$

where  $u'$  and  $w'$  are the flow fluctuations in the longitudinal and vertical directions, respectively and  $u_0$  is the free stream velocity at the boundary.

Fig. 5.19 presents the Reynolds shear stresses at  $y/l = 0$  (centre plane) for different pyramids. The dark and light grey colour scaling in the images corresponds to the regions with normalized high and low Reynolds shear stress, respectively. In general, the figure shows that the Reynolds shear stress reaches a peak value at  $x/l = 0.3$ , near the tip of the pyramids. Around these peaks, the lower shear stress extends in the horizontal and in vertical direction. It is shown that the peak value and the extension of shear stress increase as the base angles and the heights of the pyramids increase. For the shallowest pyramid P30, the shear stress increases only slightly to  $-0.008$ . Area with Reynolds shear stress  $-0.008$  extends to the downstream of the pyramid up to  $x/l = 1$ . When the base angle of the pyramid increases to  $40^\circ$  (pyramid P40), the peak shear stress increases to  $-0.009$  and the lower shear extends until  $x/l = 1.2$ . Nevertheless, the increase of the shear stresses for pyramid P30 and P40 is relatively small when compared to the normal conditions (i.e. without model), which is found in the range of  $-0.001$  to  $-0.004$ . This is due to the fact that the base angle and the height of both pyramids are considerably small.

A significant increase of the peak shear stress occurs when the base angle increases from  $40^\circ$  to  $45^\circ$ . The negative peak Reynolds shear stress is found to be  $-0.014$  and occurs at a distance of  $x/l = 0.3$ . The peak is relatively short in length but the area with lower value extends to  $x/l = 1.8$ . For pyramid P50, a negative peak value of  $-0.017$  was found and the area with lower value extends more than  $x/l = 2$ . The Reynolds stress continue to increase until the highest pyramid P70. The negative peak shear stress for pyramid P70 is  $-0.019$  and the area with lower value extends in  $x$  direction. From the figures, it is clear that the base angle and the height of the pyramid significantly change the value and the area of shear stress in the leeward side of the pyramid.



When the observed plane is moved to  $y/l = 0.25$ , the magnitude of the Reynolds shear stress slightly increases as compared to the magnitude at the tip of pyramid at  $y/l = 0.0$ , which is indicated by the darker grey colour near the pyramid edges. High Reynolds shear stress in these areas indicates that the separation flow occurs over the side of the pyramids.

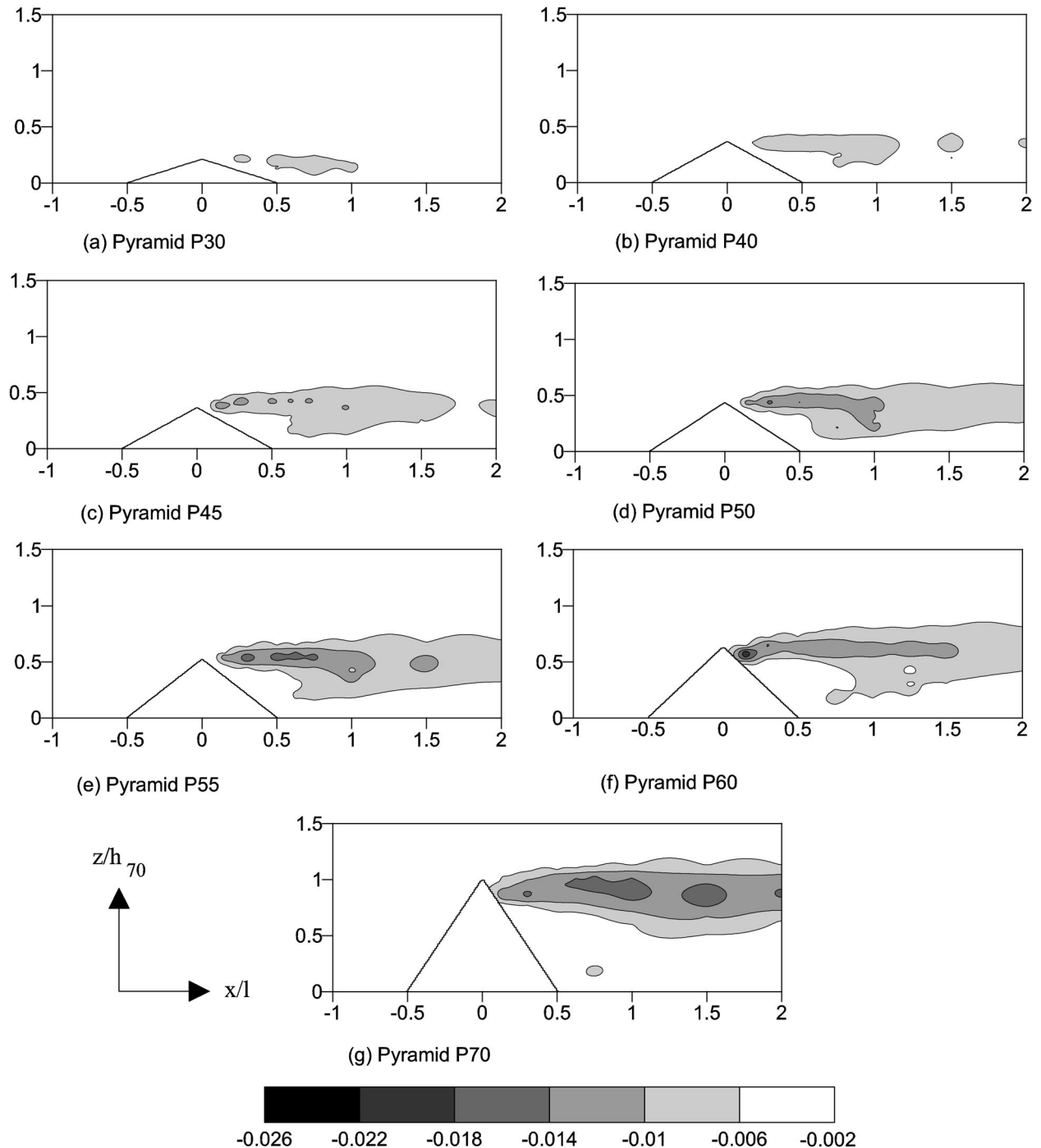


Fig. 5.19. Reynolds shear stress at  $y/l = 0.0$  for investigated pyramids, normalized by the free stream mean velocity ( $\alpha' = 0^\circ$ ,  $u_0 = 5$  m/s,  $h_{70} = 274.7$  mm)

5. Experimental Results

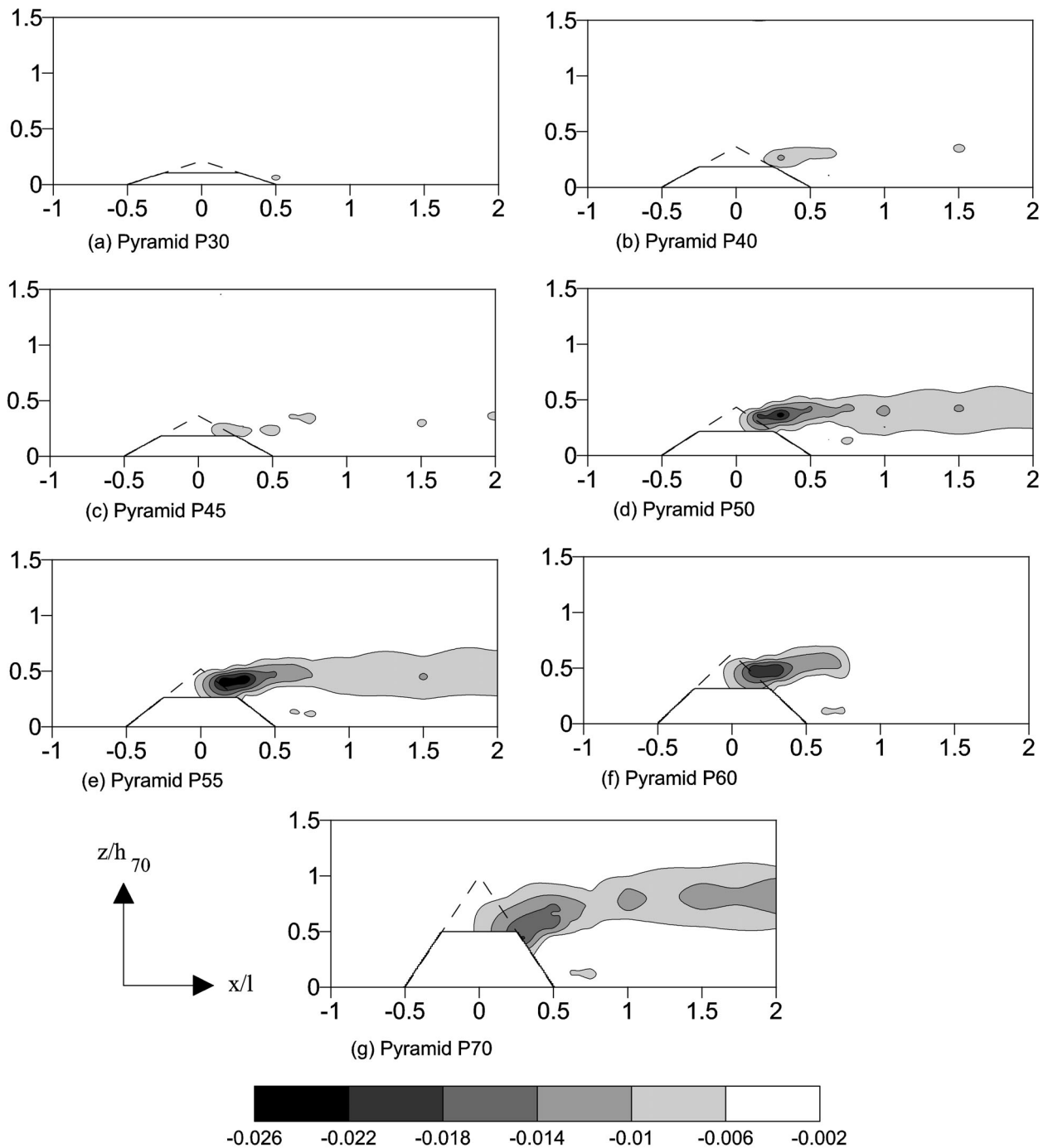


Fig. 5.20. Reynolds shear stress at  $y/l = 0.25$  for investigated pyramids, normalized by the free stream mean velocity ( $\alpha' = 0^\circ$ ,  $u_0 = 5$  m/s,  $h_{70} = 274.7$  mm)

### 5.1.6. Turbulent Kinetic Energy

From the results of the two measured components (i.e. x- and z- directions), the dimensionless turbulent kinetic energy (TKE) can be calculated as:

$$\text{TKE} = \frac{0.75(u'^2 + w'^2)}{u_0^2} \quad (5.13)$$

where,  $u'$  and  $w'$  are the fluctuations of the velocity in the x- and z- direction, respectively, and  $u_0$  is the free stream velocity ( $u_0 = 5$  m/s).

Fig. 5.21 shows the turbulent kinetic energy (TKE) in the centre plane of the pyramids. Similar to the shear stress, the TKE in the leeward side of the pyramids also increases when the base angle and pyramid height increases. In line with the location of the peak shear stress, the high level of TKE also occurs after the tip of the pyramid at a distance of  $x/l = 0.3$ . For pyramid P30, the level of TKE in the leeward side of the pyramid increases as compared to the TKE in the undisturbed wind field. The maximum TKE level in the leeward side of the pyramid P30 is found to be 0.05. This maximum value of TKE is almost two times the TKE in the undisturbed wind field but the affected area is relatively small. When the base angle and height of the pyramid increase, the level of turbulent also increases. The maximum level of TKE is found to be 0.14 when the base angle reaches  $70^\circ$ . This value is almost six times of the TKE in the undisturbed wind fields.

The level of TKE increases with increasing base angles not only in the leeward side of the pyramid but also in the upstream side near the bottom of the pyramid. It is identified when the base angle reaches  $55^\circ$  and increases as the base angle reaches  $70^\circ$ . For Pyramid P55, the TKE is found to be 0.06, which is two times the TKE in the undisturbed wind field and for pyramid P70 the TKE is found to be 0.10, which is four times the TKE in the undisturbed wind field. The increase of the TKE shows that for pyramids with base angles from  $55^\circ$  and greater, the separation occurs in the upstream side of the pyramid and from the separation point to the pyramid surface, recirculation zones are formed.

When the observed plane is shifted to  $y/l = 0.25$ , the maximum TKE do not experience much changes in magnitude and it is no longer coupled directly to the contour of the downstream edge of the pyramid (see Fig. 5.22). It is shown that the flow separation occurs over the side walls. At the back side of the pyramid, the isolines of the turbulent kinetic energy are followed basically by the form of the pyramid, showing high gradients of the turbulent kinetic energy perpendicular to the surface. This might explain why the leeward regions of the pyramids are not filled up with flow-suspended material which is in contrast to cuboidal bluff bodies whose recirculation zone is usually filled up very quickly.

5. Experimental Results

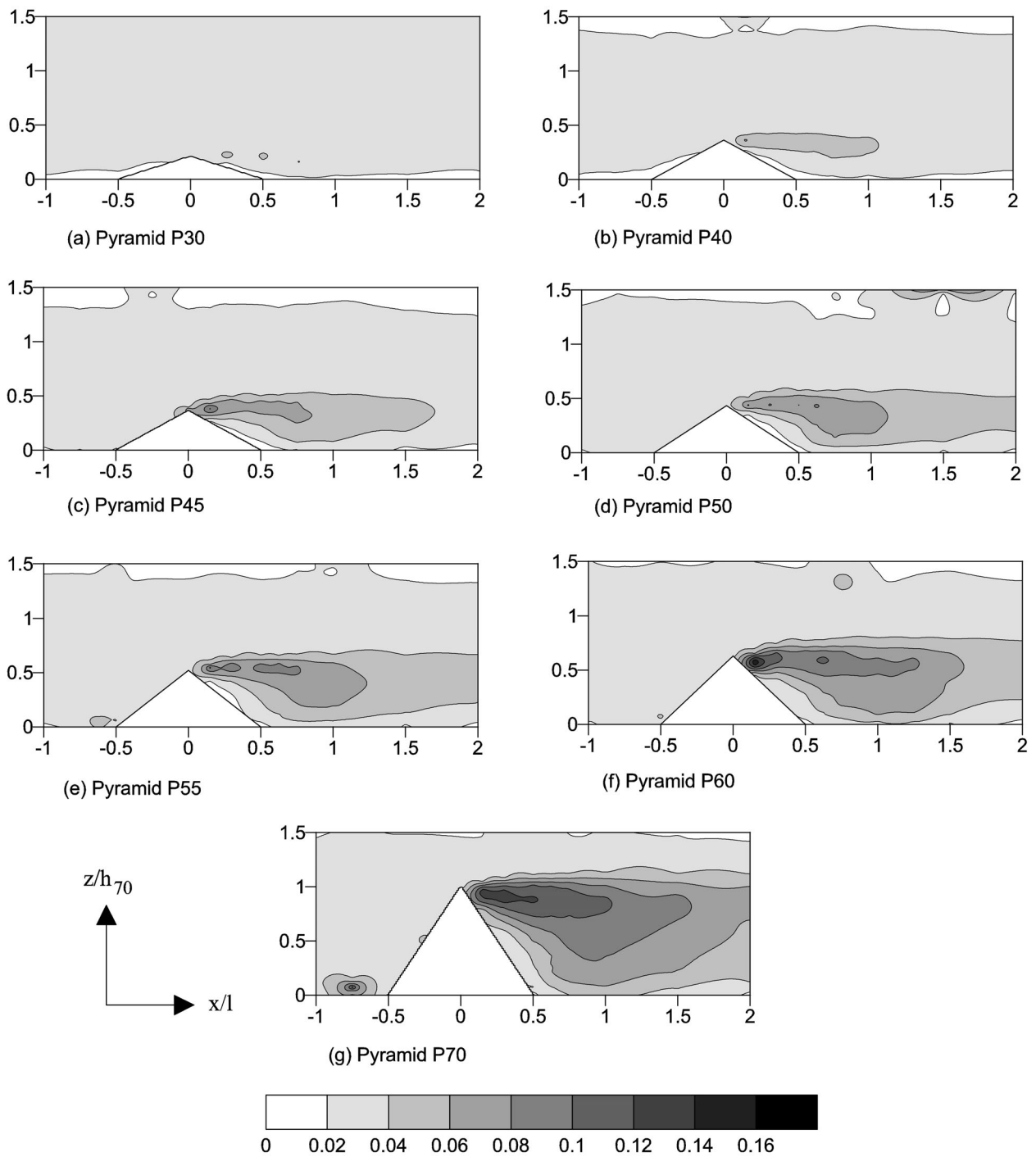


Fig. 5.21. Turbulent kinetic energy at  $y/l = 0$  for investigated pyramids, normalized by free stream velocity ( $\alpha' = 0^\circ$ ,  $u_0 = 5$  m/s,  $h_{70} = 274.7$  mm)

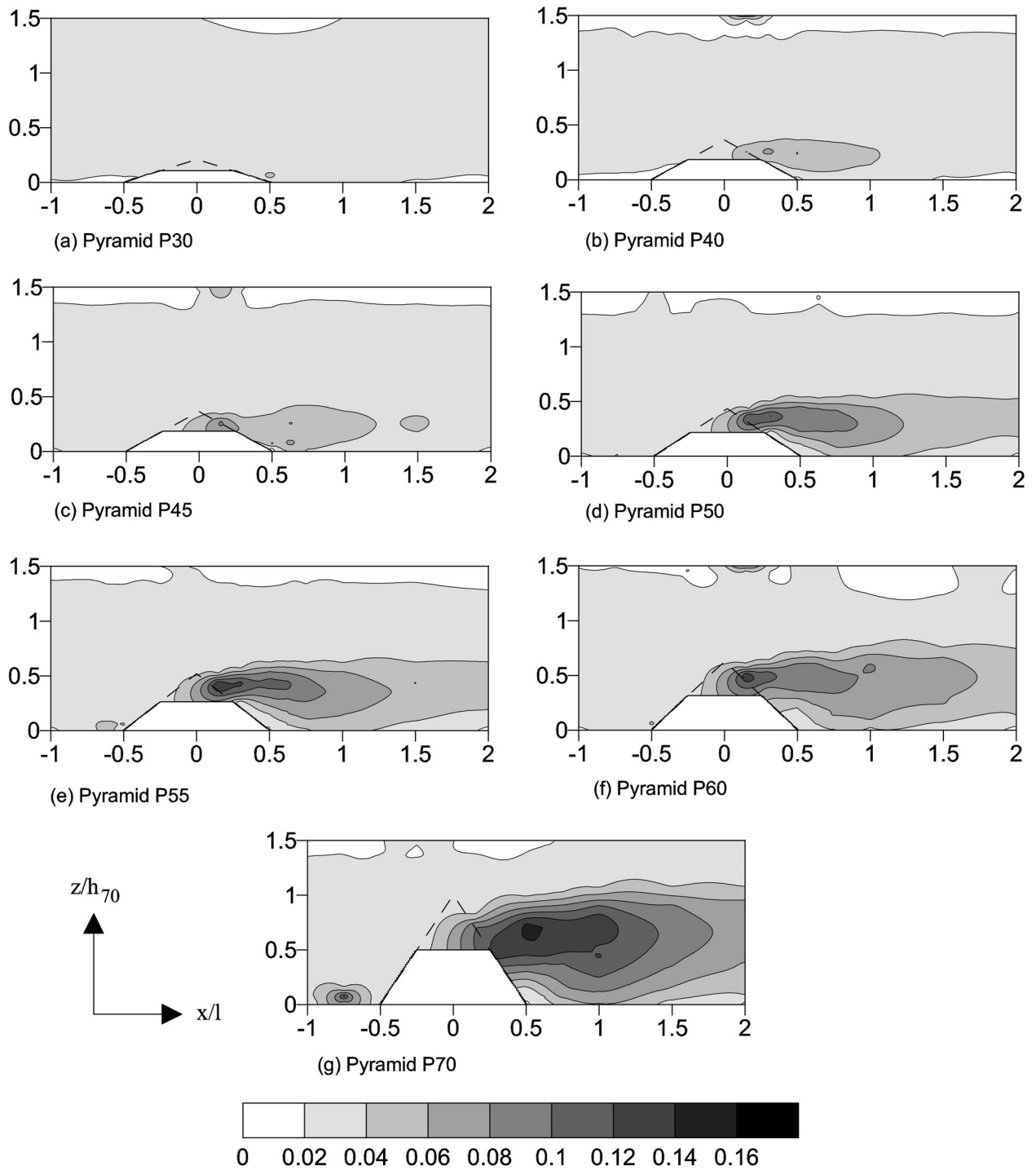


Fig. 5.22. Turbulent kinetic energy at  $y/l = 0.25$  for investigated pyramids, normalized by free stream velocity ( $\alpha' = 0^\circ$ ,  $u_0 = 5$  m/s,  $h_{70} = 274.7$  mm)

## 5. Experimental Results

For the plane at  $y/l = 0.50$ , significant changes of TKE are not found for pyramid P30, P40, PP45 and P50. When the base angle reaches P55, the TKE slightly increases at the upstream and in the leeward side of the pyramid. The magnitude of TKE grows with an increase of the base angle and height.

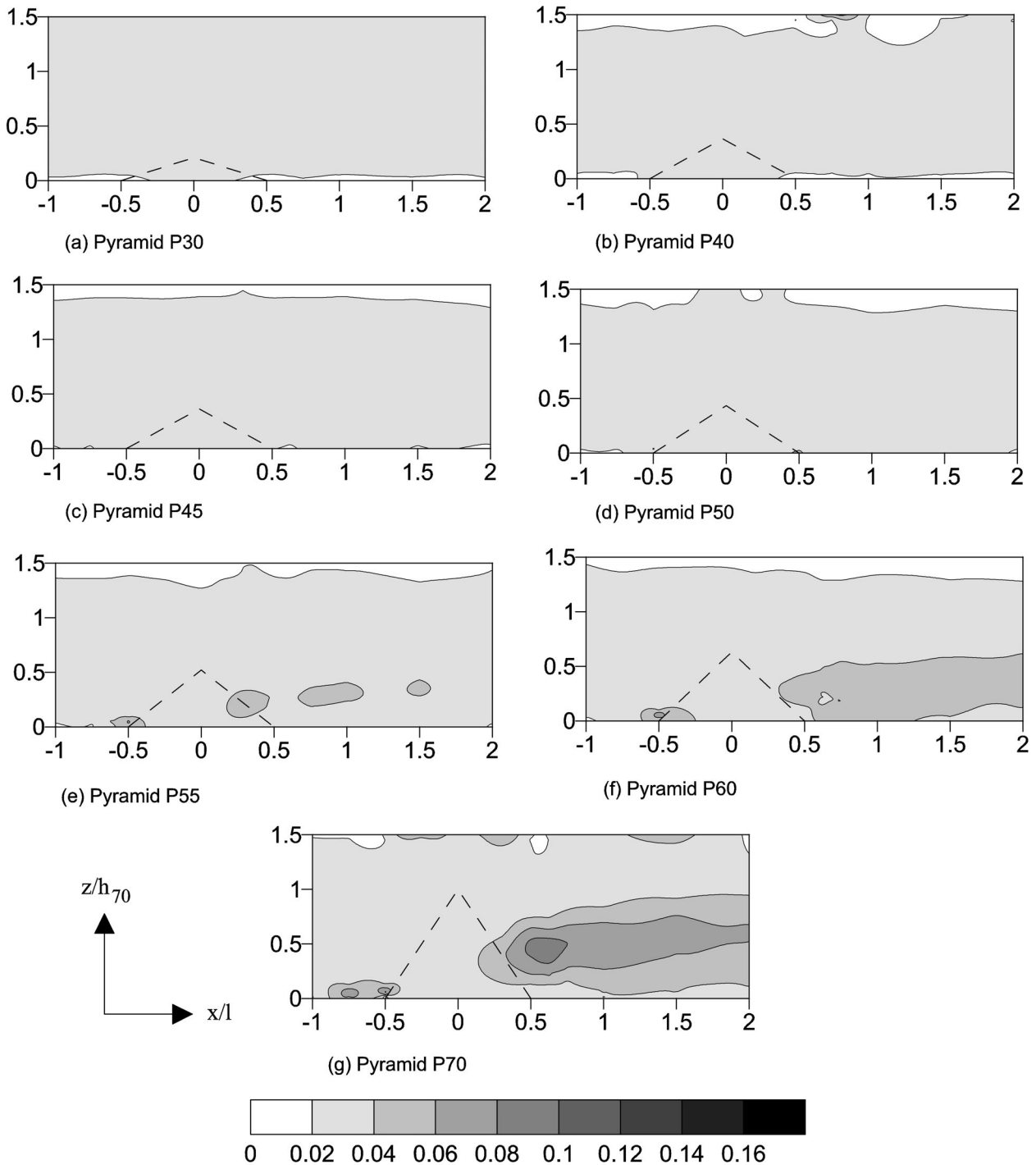


Fig. 5.23. Turbulent kinetic energy at  $y/l = 0.50$  for investigated pyramids, normalized by free stream velocity ( $\alpha' = 0^\circ$ ,  $u_0 = 5$  m/s,  $h_{70} = 274.7$  mm)

Basically, the changes of TKE around the pyramids are one of the evidence that vortices are formed. The results show that significant changes of TKE take place when the base angles are equal or greater than  $55^\circ$ . Therefore, different flow structures between pyramids with base angles smaller than  $55^\circ$  and pyramids with base angle greater than  $55^\circ$  are expected. In other words, the flow structures around pyramids can be categorized as flow structures for shallow pyramids ( $\theta < 45^\circ$ ) and for steep pyramids ( $\theta > 55^\circ$ ). This expectation is in good agreement with the results from Martinuzzi [2003], who categorized pyramids as slender and board pyramids.

## 5.2. Pressure Characteristics of Pyramids

As described in Chapter 4, the pressure measurements were carried out with an incoming flow velocity of 12 m/s (velocity at  $z = 500$  mm) in order to obtain measurable and reliable pressure differences. Four different wind directions,  $\alpha' = 0^\circ, 15^\circ, 30^\circ$  and  $45^\circ$ , were measured (see Fig. 4.4 for wind direction arrangements). Based on these four measurement results, the pressure distribution for further wind direction  $\alpha'$  with  $15^\circ$  step can be generated due to the symmetrical geometry of the pyramid. Thus, thirteen different wind directions ( $\alpha'$ ) ranging from  $0^\circ$  to  $180^\circ$  with  $15^\circ$  step can be investigated. The distribution of pressures and suctions over a building depends largely on how it disturbs the air flow. In this discussion, the datum (reference) from which all pressures and suctions are measured is the ambient pressure in the undisturbed air flow at the top (height) of the building (see Chapter 4, experimental set up). Three important parameters that affect the pressure distribution on the pyramid surfaces are investigated, namely the pyramid base angle, the wind direction and the pyramid height.

### 5.2.1. Influence of the Pyramid Base Angle on the Surface Pressure Distribution

In this section, the influence of pyramid base angles on the distribution of pressure coefficient ( $c_p$ ) in the pyramid surfaces will be discussed. Fig. 5.24 shows the contour plot of the variation of the measured pressure distributions on the pyramid surfaces with varying base angles at a wind direction  $\alpha' = 0^\circ$ . In the figure, the greyscale indicates the mean pressure coefficient ( $c_p$ ) on the pyramid surfaces. When the value of mean  $c_p$  decrease to negative then it indicates suction on the pyramid surface. For all pyramids, the maximum pressure occurs on the windward side surface A. The  $c_p$ -mean distributions indicate that the maximum pressure increases with increasing base angle. For pyramid P30, the maximum value of  $c_p$  is 0.42 and it increases to 0.77 as the base angle reaches  $70^\circ$ . As can be observed in Fig. 5.25. (a), the increase of the pressure with the base angle is not linear. The maximum value of  $c_p$  increases when the base angle increases from  $30^\circ$  to  $40^\circ$ . Then, it slightly decreases as the base angle increases from  $40^\circ$  to  $60^\circ$ . However, the decrease of  $c_p$  within this range does not exceed 5%, which is the margin of error estimated for the present measurement technique (see Chapter 4). Therefore, it seems that the base angle does not significantly affect the maximum pressure for pyramids having base angles between  $40^\circ$  and  $60^\circ$ . An increase of  $c_p$  maximum can be observed again clearly as the base angle increases from  $60^\circ$  to  $70^\circ$ . Similar trends were found for all other wind directions.

The maximum suction (i.e. the minimum value of  $c_p$ ) at wind direction  $\alpha' = 0^\circ$  occurs on the upstream edge of side B and D. At these sides, vertical vortices systems are found (see Fig. 5.1). These vortices systems increase the turbulence intensity in this region. Tieleman (1993) investigated the pressure distribution on surface-mounted prisms. He concluded that the magnitude of  $c_p$  decreases when the turbulence intensities around the bluff body increase. These characteristics are similar to the characteristics of “Delta-wing” vortices in cuboidal building, as described in Chapter 2. However for cuboidal buildings, the delta-wings vortices are formed on the top of the building and creates maximum suction in the corner of the building

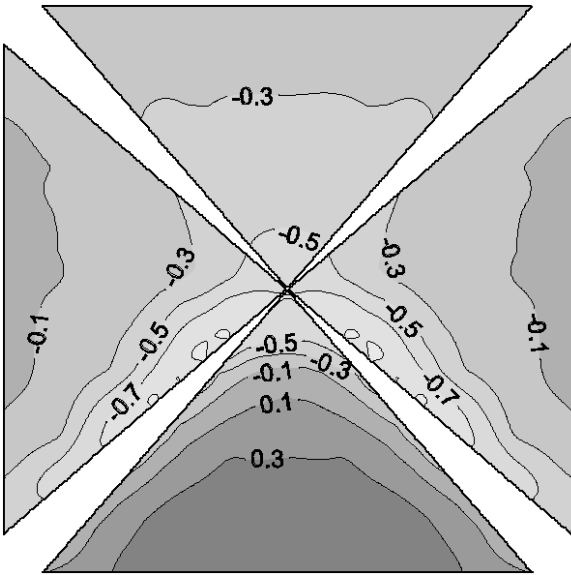


Fig. 5.24(a) Pyramid P30

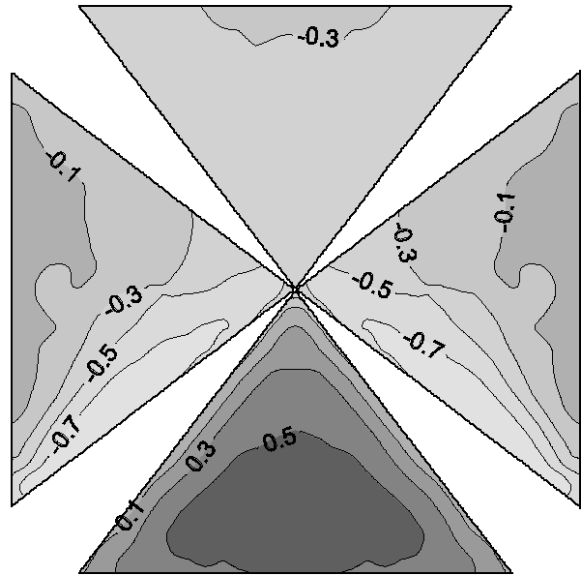


Fig. 5.24(b) Pyramid P40

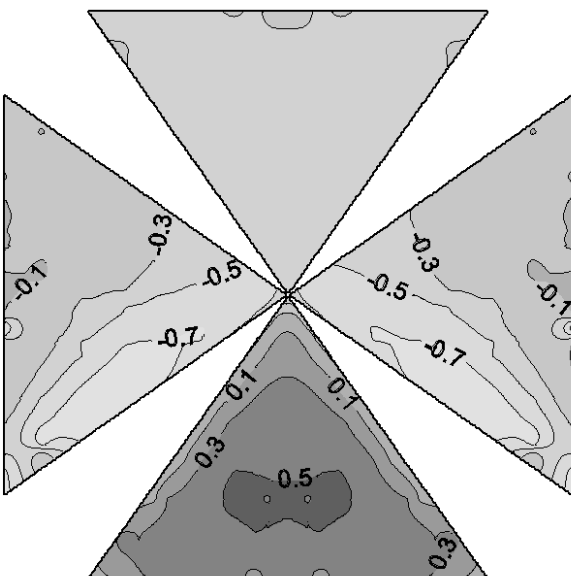


Fig. 5.24(c) Pyramid P45

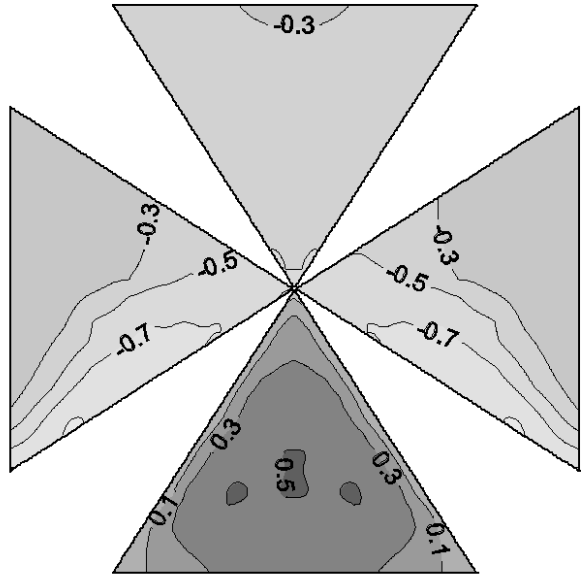


Fig. 5.24(d) Pyramid P50



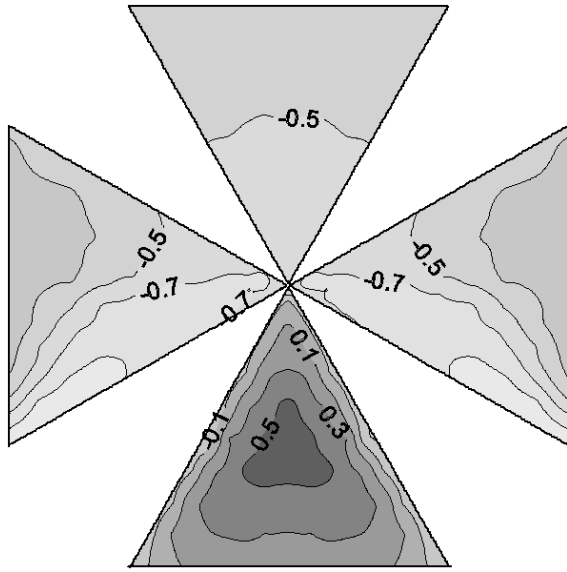


Fig. 5.24(e) Pyramid P55

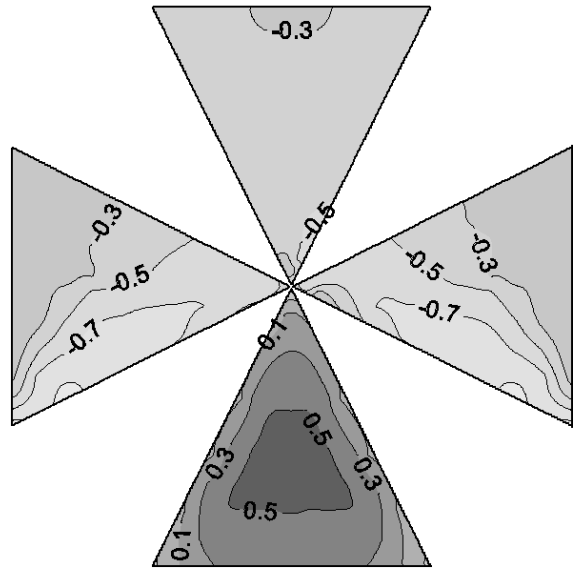


Fig. 5.24(f) Pyramid P60

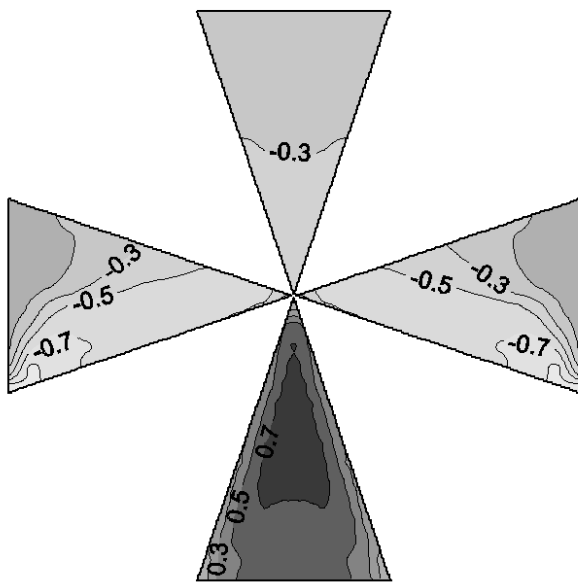


Fig. 5.24(g) Pyramid P70

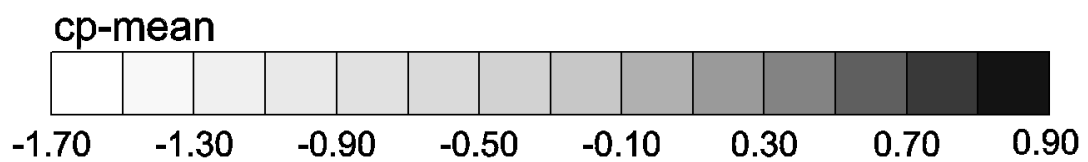
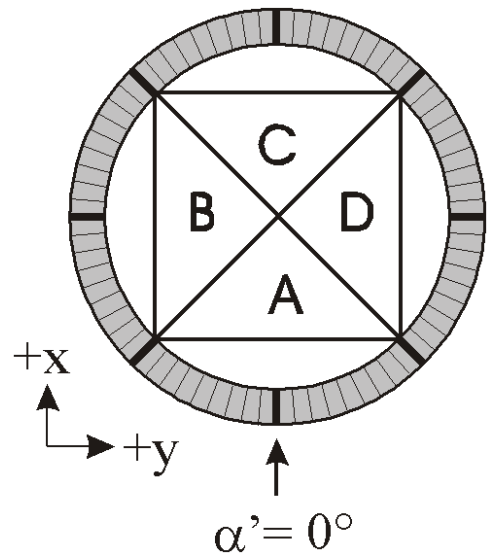


Fig. 5.24. Distribution of mean pressure coefficient ( $c_p$  mean) in the surfaces of the investigated pyramids ( $\alpha' = 0^\circ$ ,  $u_0 = 12\text{m/s}$ )

5. Experimental Results

For pyramid P30, the maximum suction reaches  $-1.1$ . The maximum suction decreases to  $-0.81$  when the pyramid base angle increases to  $40^\circ$  and increases again to  $-1.2$  when the base angle reaches  $70^\circ$ . These values show that the suction on the pyramid surfaces do not increase linearly with the base angle variations, see Fig. 5.25. (b). In contrast to the maximum pressure, the trend of the curves for the minimum pressure is not similar for the different wind directions ( $\alpha'$ ). This is due to the fact that the minimum pressure is closely related to the building-induced turbulence that generates a complex flow structure. Nevertheless, in general it shows two types of similar curve. First, between wind directions  $0^\circ$  to  $60^\circ$ , a similar trend of curve is observed and for wind directions  $75^\circ$  and  $90^\circ$  another type of curve is observed. The difference occur after pyramid P50, where the first curve ( $\alpha' = 0^\circ$  to  $60^\circ$ ) shows the maximum suction decrease, on the other hand, for the second type of curve ( $\alpha' = 75^\circ$  and  $90^\circ$ ), the maximum suction increases when the base angle ( $\theta$ ) increase from  $50^\circ$  to  $70^\circ$ . The results of the measured pressure distributions show that a base angle variation exerts a significant influence on the pressure coefficient ( $c_p$ ) in the surface of a pyramidal building.

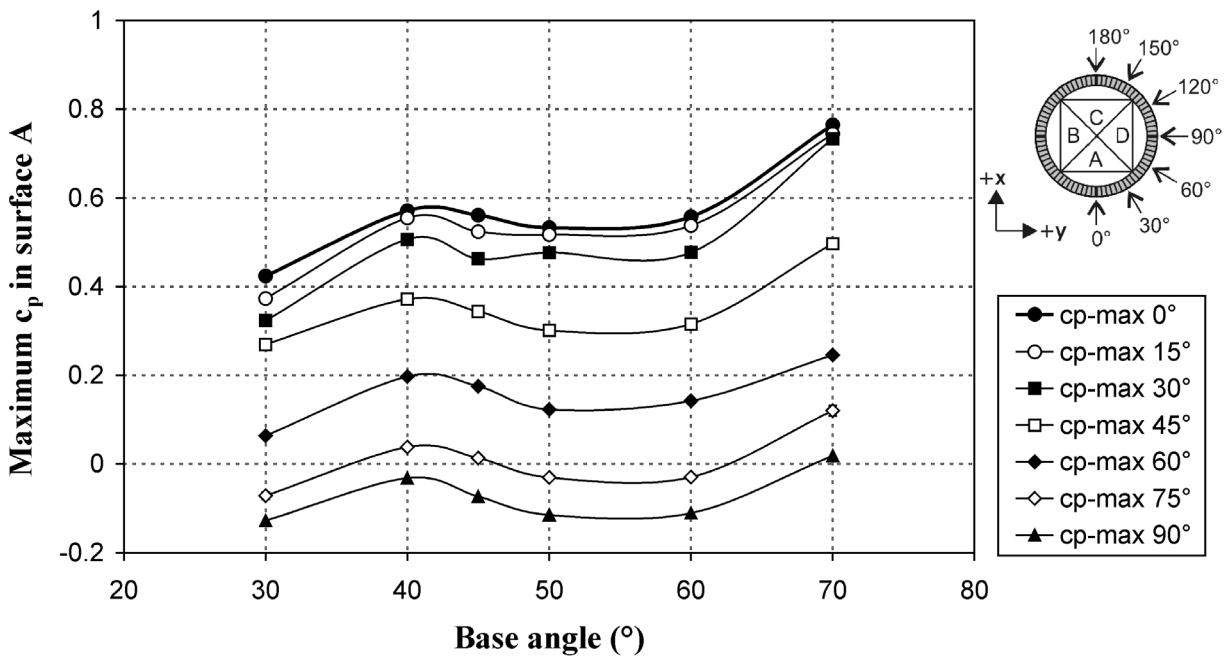


Fig. 5.25(a)  $c_p$ -maximum on surface A as a function of base angle

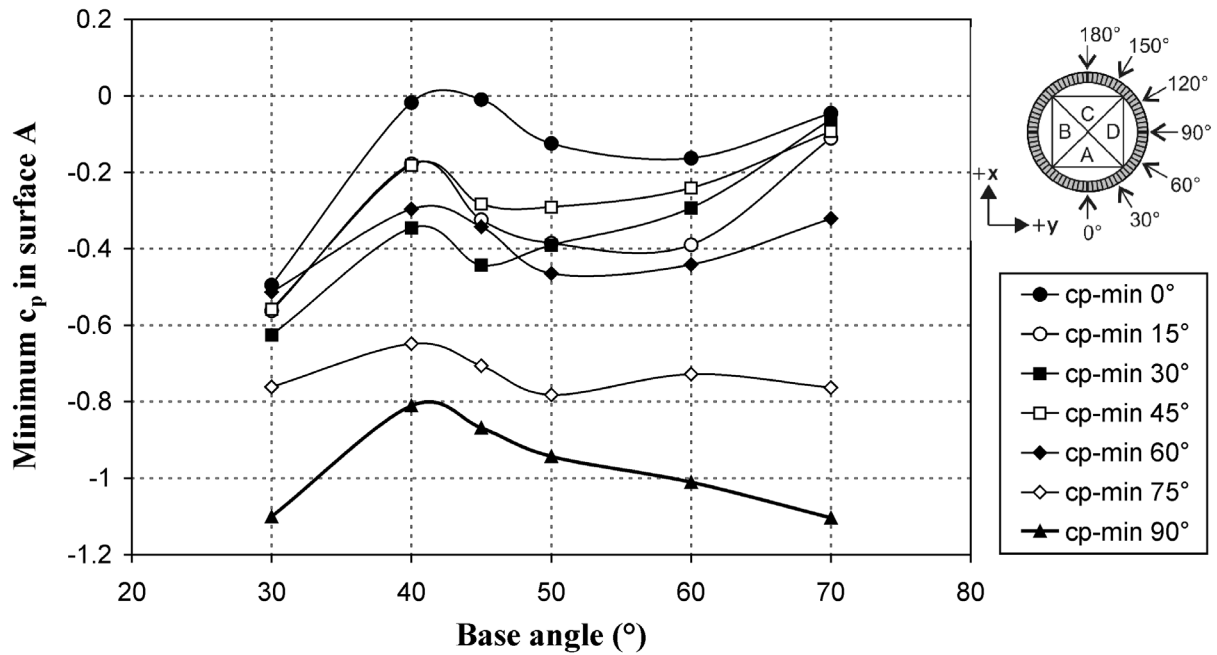


Fig 5.25(b)  $c_{p\text{-minimum}}$  on surface A as a function of base angle

Fig. 5.25. Mean pressure coefficient on surface A as a function of base angle for investigated wind directions

The variation of the base angles also affects the distribution of pressure fluctuations (i.e. the root mean squared values  $c_p'$ ). It can be observed in Fig. 5.26 that the distribution of the pressure fluctuations on the surface of the pyramids is significantly affected by the vortices around the pyramids (see Fig. 5.1). The maximum fluctuations on the surfaces of the pyramid at wind direction 0° are found at the side surfaces B and D at the upstream edge. These are the locations where the flow generates vertical vortex systems. The maximum fluctuations on the side surfaces B and D increase when the base angle increases.

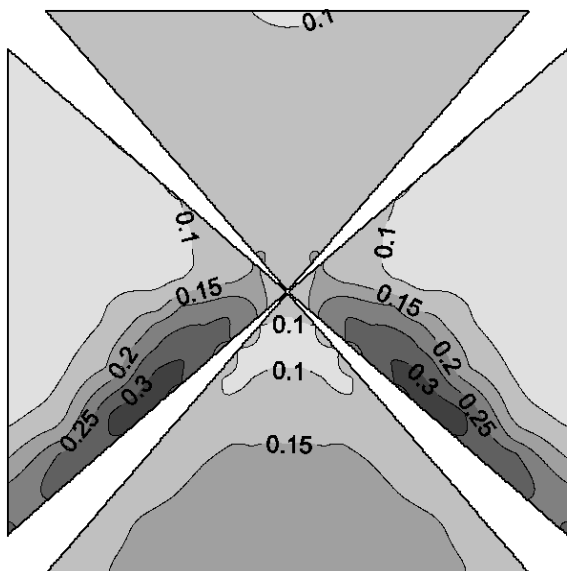


Fig. 5.26(a) Pyramid P30

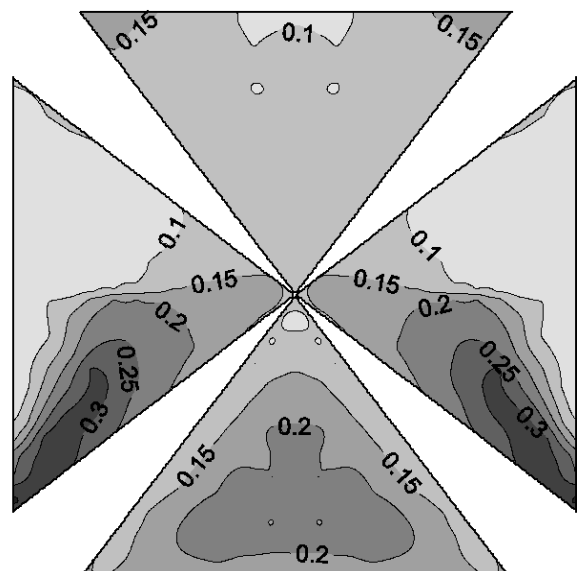


Fig. 5.26(b) Pyramid P40

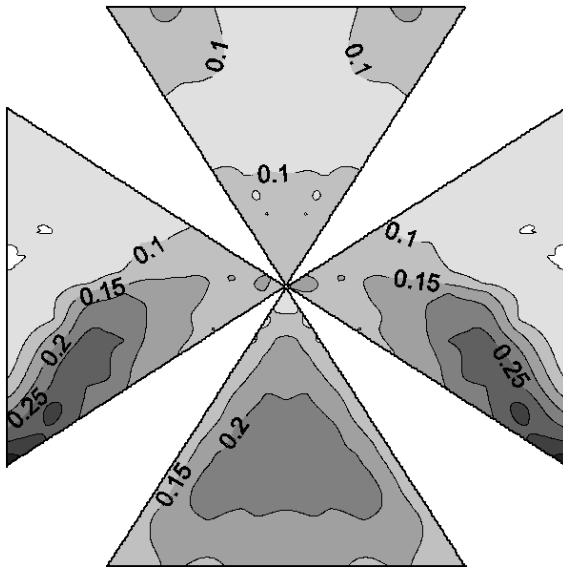


Fig. 5.26(c) Pyramid P45

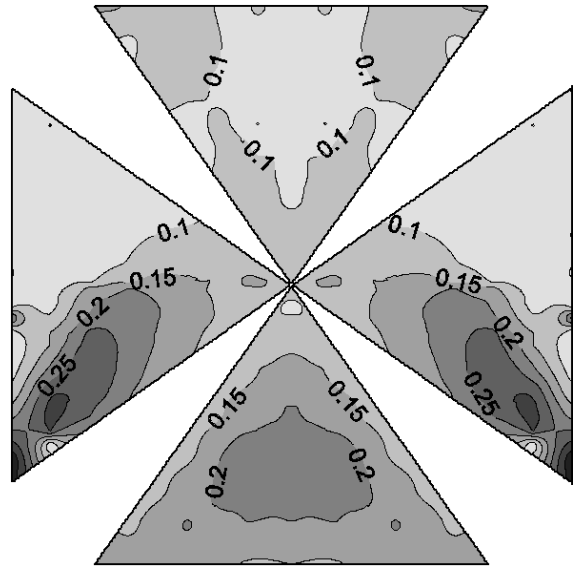


Fig. 5.26(d) Pyramid P50

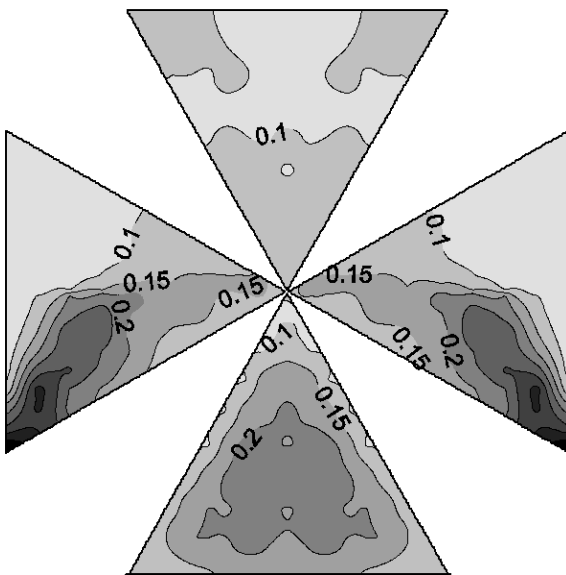


Fig. 5.26(e) Pyramid P55

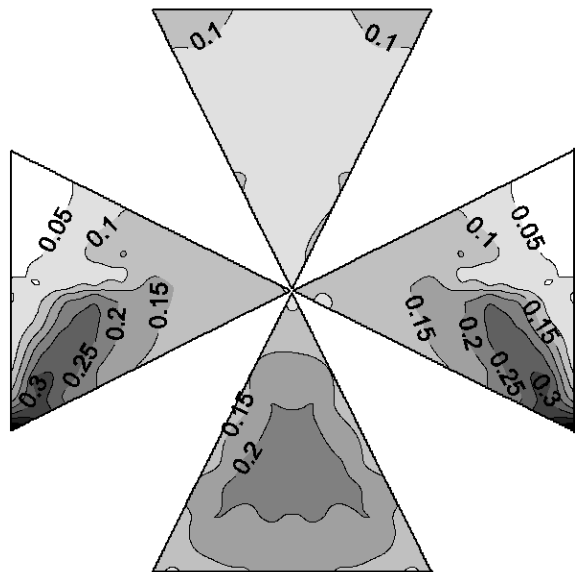


Fig. 5.26(f) Pyramid P60

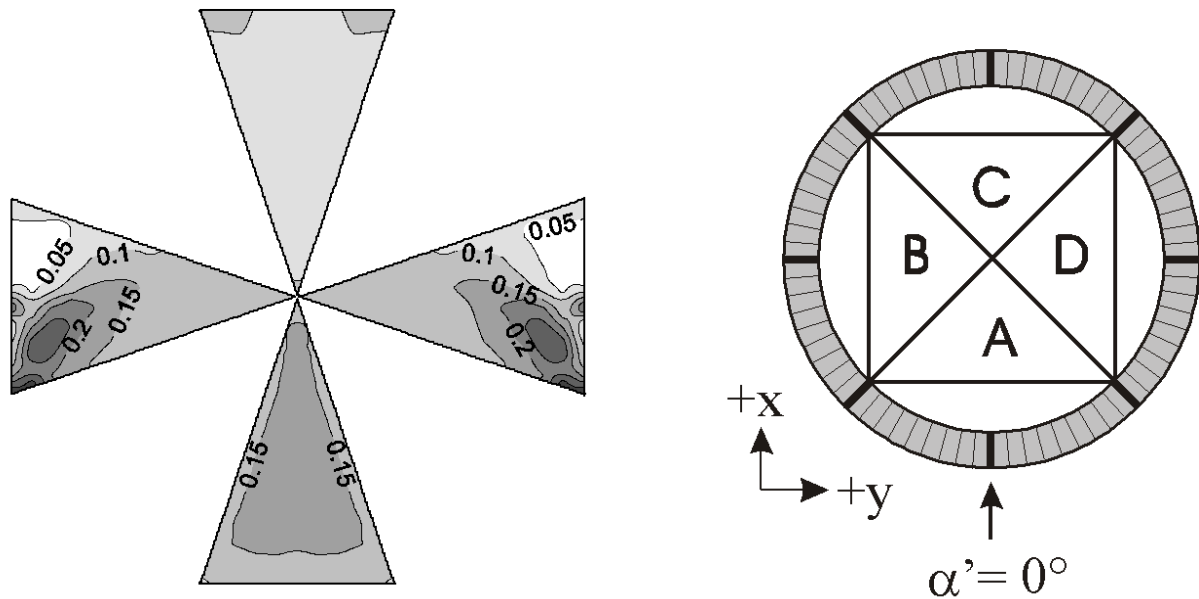
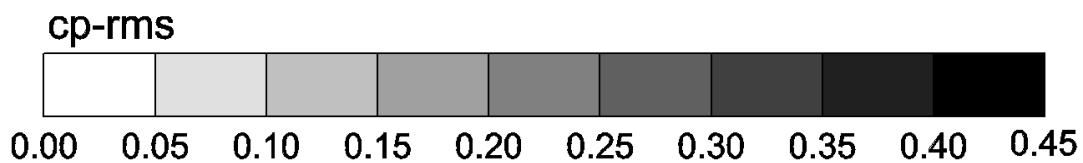


Fig. 5.26(g) Pyramid P70

Fig. 5.26 Distribution of standard deviation of pressure coefficient fluctuations ( $c_p'$ ) on the surfaces of the investigated pyramids ( $\alpha' = 0^\circ$ ,  $u_0 = 12\text{m/s}$ )

Besides affecting the pressure and fluctuation characteristics on the surface of the pyramids, the base angle variation also has an influence on the locations of maximum and minimum pressure and maximum fluctuations in the pyramid surfaces as can be seen in Fig. 5.27. For the shallowest pyramid (pyramid P30), the maximum  $c_p$  was found near the bottom of the windward side surface A. When the base angle of the pyramid increases, the locations of the maximum pressure are shifted toward the centre of the windward side surface A. There are three areas in which the maximum pressures take place depending on the steepness of the base angles. The first area is at a height of  $0h$  to  $0.15h$  ( $h$ : pyramid height) for pyramid P30 and P40. For pyramid P45 to pyramid P60, the maximum pressure occurs at a height of  $0.28h$  to  $0.30h$  and for the pyramids with base angles greater than  $60^\circ$  at a height of more than  $0.5h$ .

In Fig. 5.27, the data points indicated by P70a and P70b represent the pyramids having the same base angle  $70^\circ$  with different height (height of pyramid P70 = 274.75 mm, P70a = 142.81 mm and P70b = 100 mm). It is interesting to observe that the location of the maximum  $c_p$  is relatively constant for these pyramids with the same basis angle but with different heights. This indicates that the distributions of pressure on the pyramid surfaces are more affected by the base angle rather than the profile of wind velocity.

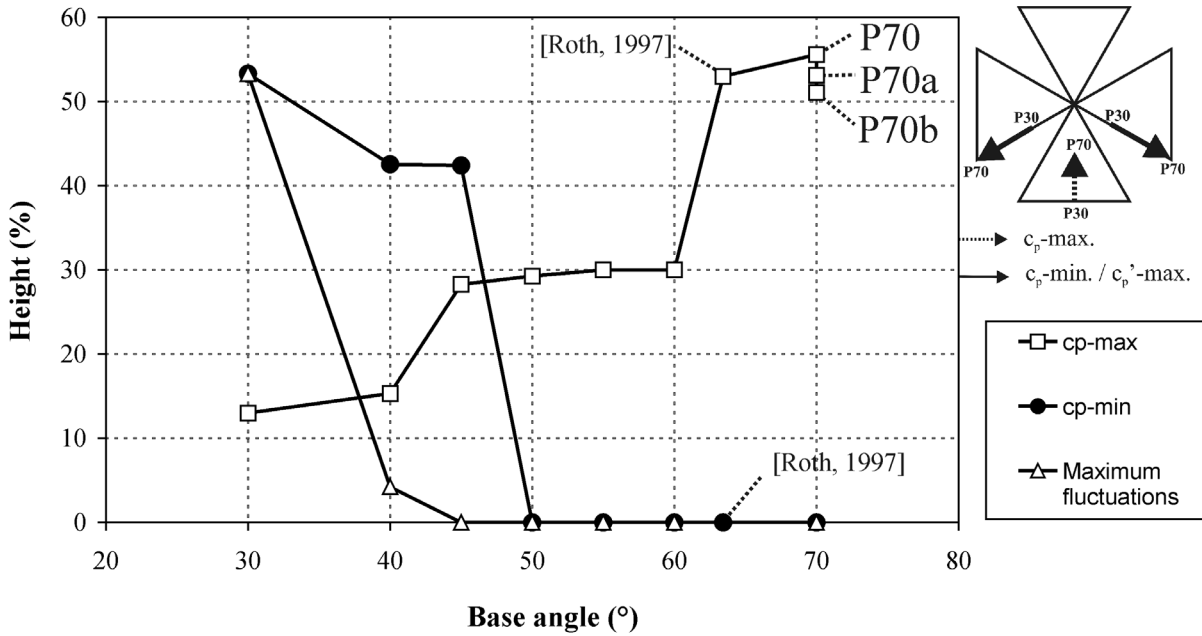


Fig. 5.27. Location of the maximum and the minimum values of mean pressure coefficients ( $c_{p-max}$  and  $c_{p-min}$ ), and the maximum fluctuations as a function of pyramid base angles ( $\alpha' = 0^\circ$ ,  $u_0 = 12\text{m/s}$ )

The maximum suction for the pyramid P30 is detected at the upstream edges above 0.5 h on the side surfaces B and D and move down towards the bottom when the base angles increase. The location of maximum suctions are relatively constant at the near bottom in the corner of the pyramids when the base angles are greater than  $50^\circ$ . A sudden change of the maximum suction location occurs between pyramid P45 and P50.

For the pyramid case with base angle greater than  $60^\circ$ , the results of pressure characteristics with regard to the location of maximum and minimum pressure can be compared to the previous pyramid studies, since their study involves pyramids that can be categorized as steep pyramid [Abuomar et.al 2000, Roth 1997, Ruck et.al. 1997]. For example in Fig. 5.27, the results from Roth [1997], which studied a pyramid with base angle of  $63^\circ$ , were incorporated. These previous studies show that the location of maximum  $c_p$  was found above 50 % of the total pyramid height, and the maximum suction is measured in the bottom corner of the pyramid. In this study the maximum  $c_p$  is found at 53 % of the total pyramid height, and the maximum suction is measured also in the corner of the pyramid.

### 5.2.2. Influence of the Wind Direction on the Surface Pressure Distribution

The next parameter of interest is the wind direction. Fig. 5.28 shows contour maps of the mean pressure distributions on the surfaces of pyramid P70. Similar to the previous section, the greyscale indicates the mean pressure coefficient ( $c_p$ ) on the pyramid surfaces and the negative  $c_p$  values indicate suction on the pyramid surfaces. The contour maps clearly show how the wind direction affects the distribution of the pressure on the pyramid surfaces. Maximum pressure ( $c_p$ )

distribution occur when the wind blows from an angle of  $0^\circ$  and decrease to a minimum with an incoming wind direction of  $45^\circ$ . Similar trends were found for all other pyramids. Despite the different wind directions, the vertical location of the maximum pressure stays relatively constant at approximately 0.53 of the pyramid height for the steep pyramids and near the bottom of the pyramids for the shallow pyramid P30.

Fig. 5.29 shows the fluctuations of pressure coefficient on the surfaces of pyramid P70 for different wind directions. It is clear that for all wind directions, the maximum fluctuations occur at the edge of the pyramids side surfaces. This is always the area where complex vortices arise. For pyramid P70, the maximum fluctuations take place when the wind blows with an angle of  $15^\circ$  on surface C. As the angle of the incoming wind direction increases, the maximum fluctuation decreases again and reaches a minimum when the incoming wind direction is at  $45^\circ$ . Due to the mirror effects, the fluctuations will again increase and reach a maximum when the wind blows at  $75^\circ$  only it occurs on surface A. The influence of the wind direction to the fluctuation distributions is relatively similar for the other pyramids.

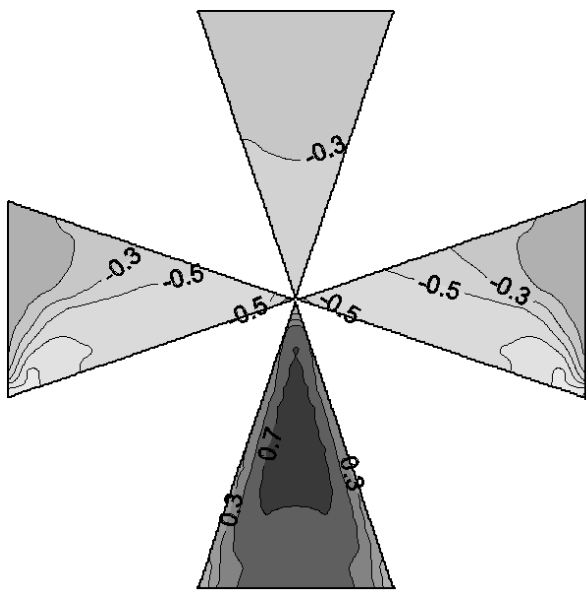


Fig. 5.28(a) Pyramid P70,  $\alpha' = 0^\circ$

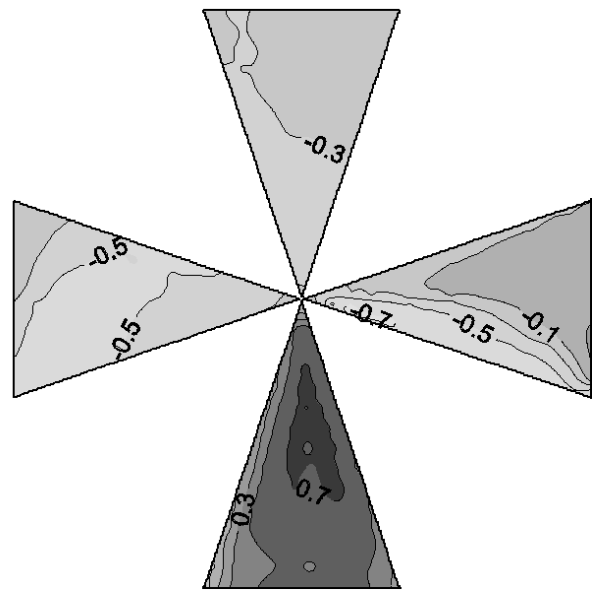


Fig. 5.28(b) Pyramid P70,  $\alpha' = 15^\circ$

5. Experimental Results

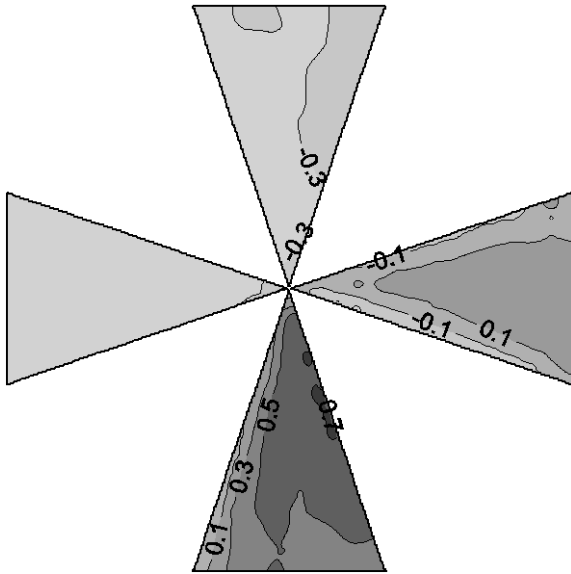


Fig. 5.28(c) Pyramid P70,  $\alpha' = 30^\circ$

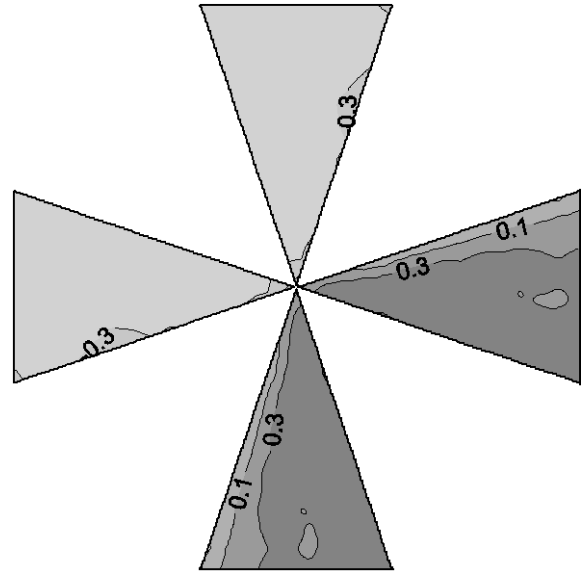


Fig. 5.28(d) Pyramid P70,  $\alpha' = 45^\circ$

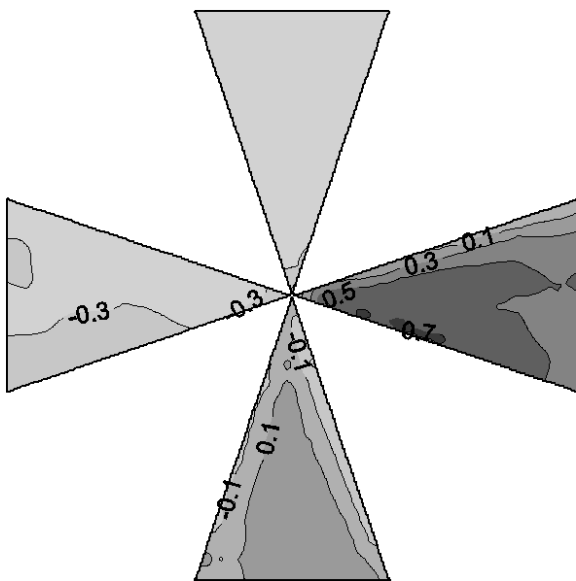


Fig. 5.28(e) Pyramid P70,  $\alpha' = 60^\circ$

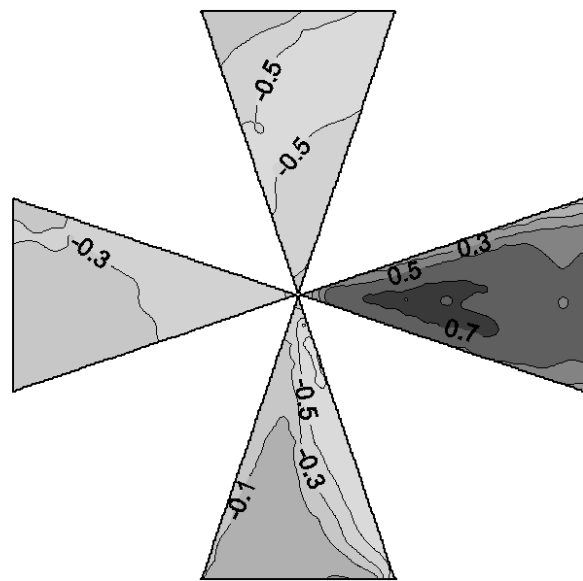


Fig. 5.28(f) Pyramid P70,  $\alpha' = 75^\circ$



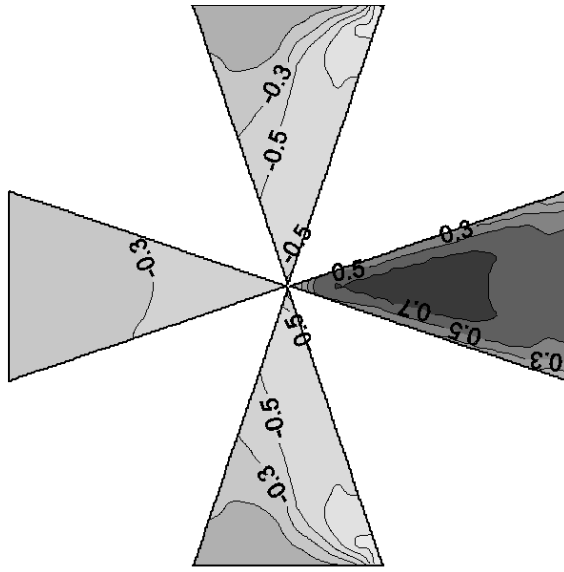


Fig. 5.28(g) Pyramid P70,  $\alpha' = 90^\circ$

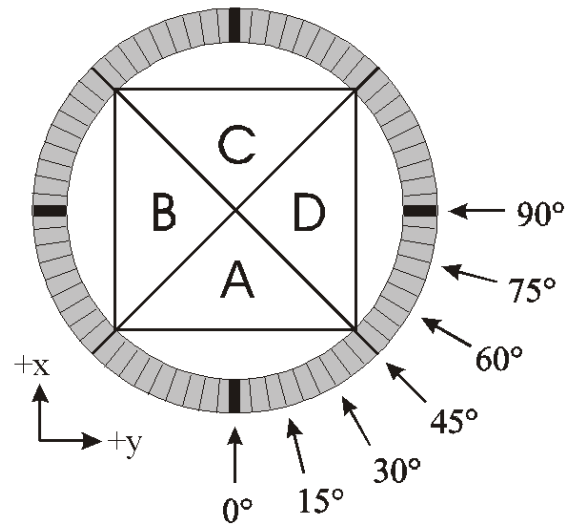


Fig. 5.28. Distribution of mean pressure coefficient on the surface of the pyramid P70 at different wind directions ( $\alpha' = 0^\circ$  to  $\alpha' = 90^\circ$ )

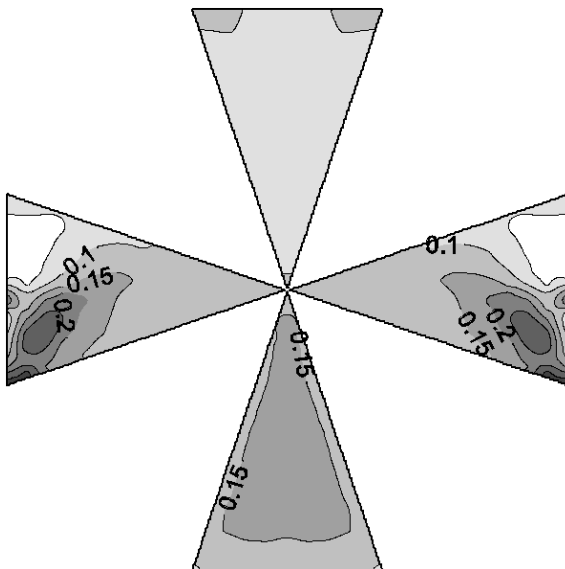


Fig. 5.29(a) Pyramid P70,  $\alpha' = 0^\circ$

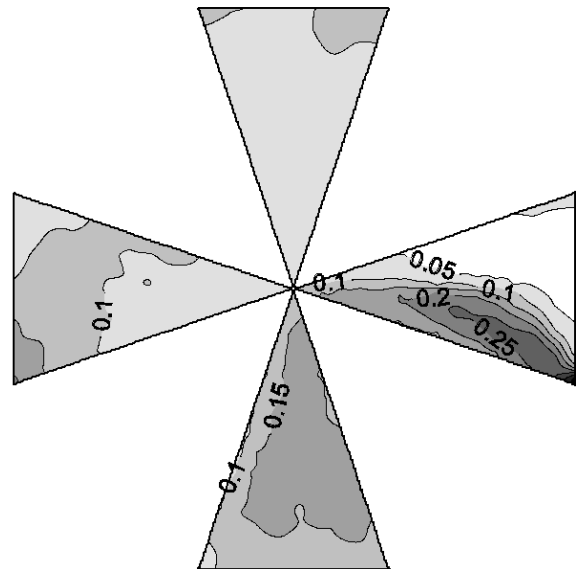


Fig. 5.29(b) Pyramid P70,  $\alpha' = 15^\circ$

5. Experimental Results

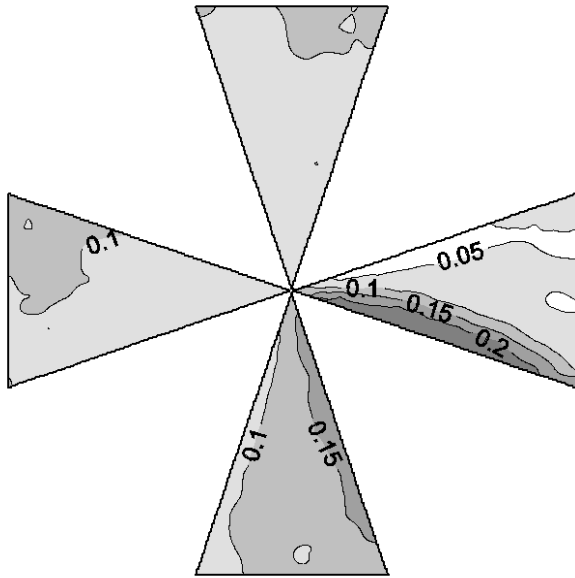


Fig. 5.29(c) Pyramid P70,  $\alpha' = 30^\circ$

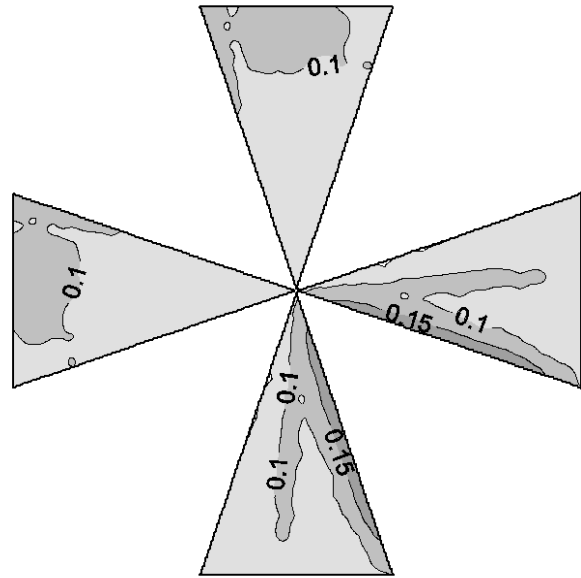


Fig. 5.29(d) Pyramid P70,  $\alpha' = 45^\circ$

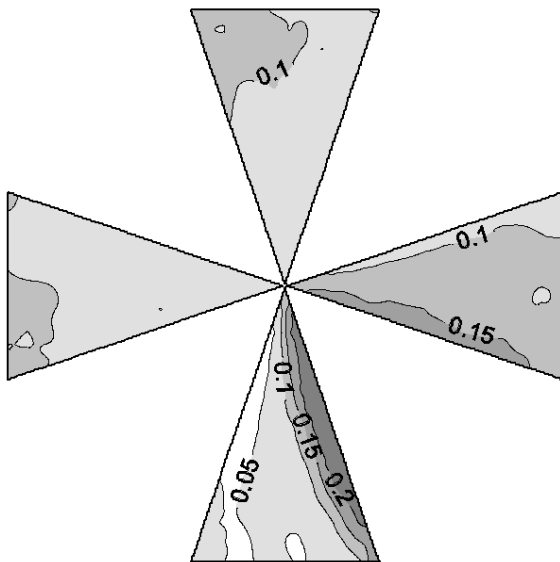


Fig. 5.29(e) Pyramid P70,  $\alpha' = 60^\circ$

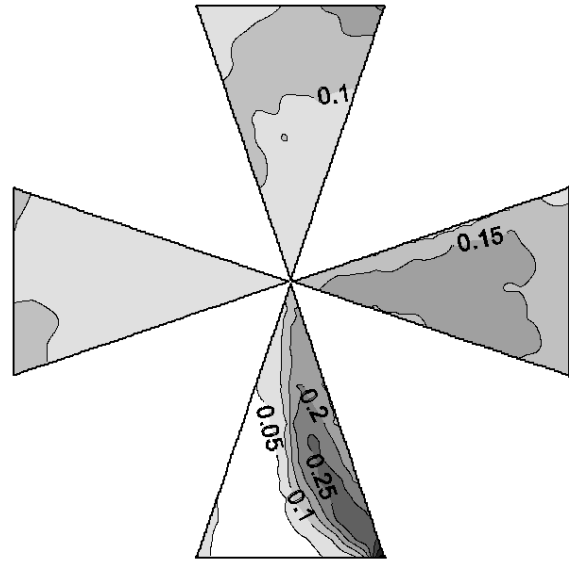


Fig. 5.29(f) Pyramid P70,  $\alpha' = 75^\circ$

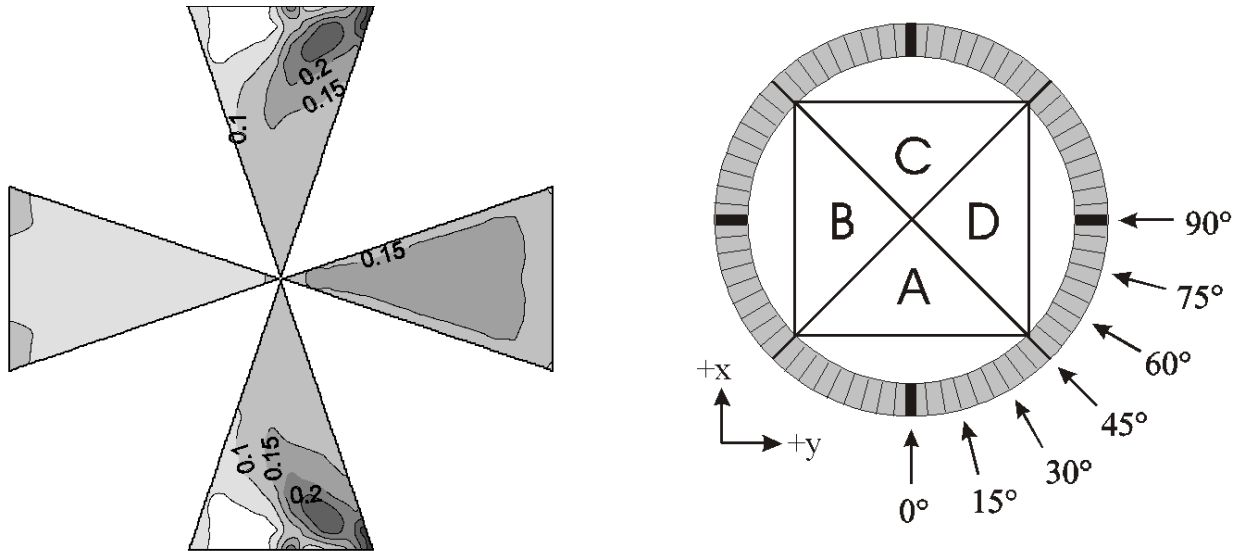


Fig. 5.29 (g) Pyramid P70,  $\alpha' = 90^\circ$

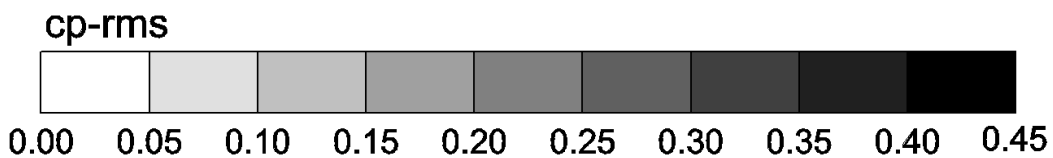


Fig. 5.29. Distribution of standard deviation of pressure coefficient fluctuations on the surface of the pyramid P70 at different wind directions ( $\alpha' = 0^\circ$  to  $\alpha' = 90^\circ$ )

Fig. 5.30 depicts the maximum and minimum pressure coefficients on the selected pyramid surface A as a function of incident wind direction (irrespective of the location of the extreme values on the surface). Obviously, a maximum pressure on this selected surface A is associated with the  $0^\circ$  wind direction, and the symmetric geometry of the pyramid creates a mirror effect to other surfaces. For  $c_p$  maximum, similar trends are observed for almost all pyramids. The pressure on surface A decreases when the wind direction increases from  $0^\circ$  to  $120^\circ$ . For wind directions above  $90^\circ$ , only suction can be found on surface A of the pyramids. The maximum pressure slightly increases when the wind direction is greater than  $120^\circ$ . As the wind directions exceed  $180^\circ$ , the maximum pressure creates a mirror image on surface A.

The minimum pressure (maximum suction) occurs when the wind blows from directions between  $60^\circ$ - $120^\circ$ . The maximum fluctuations on the surface of the pyramids are presented in Fig. 5.30 (c). Similar to the minimum pressure, the maximum fluctuations also occur when the wind blows from a direction between  $60^\circ - 120^\circ$ .

5. Experimental Results

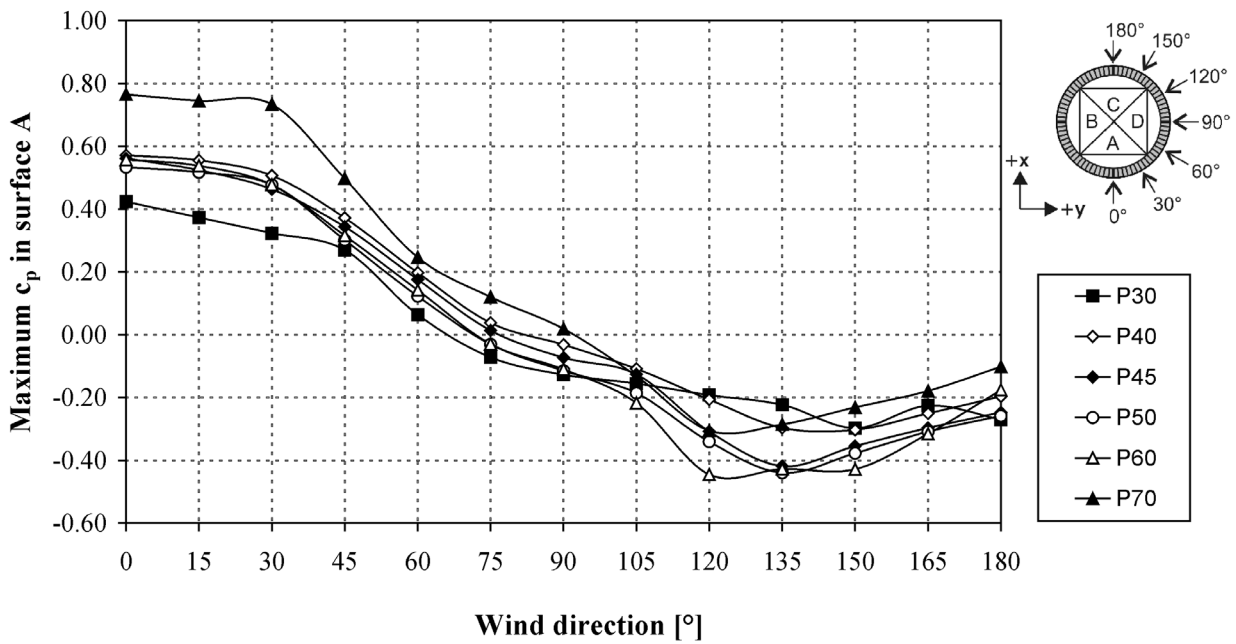


Fig. 5.30(a). Maximum mean pressure coefficients ( $c_p$ ) in surface A

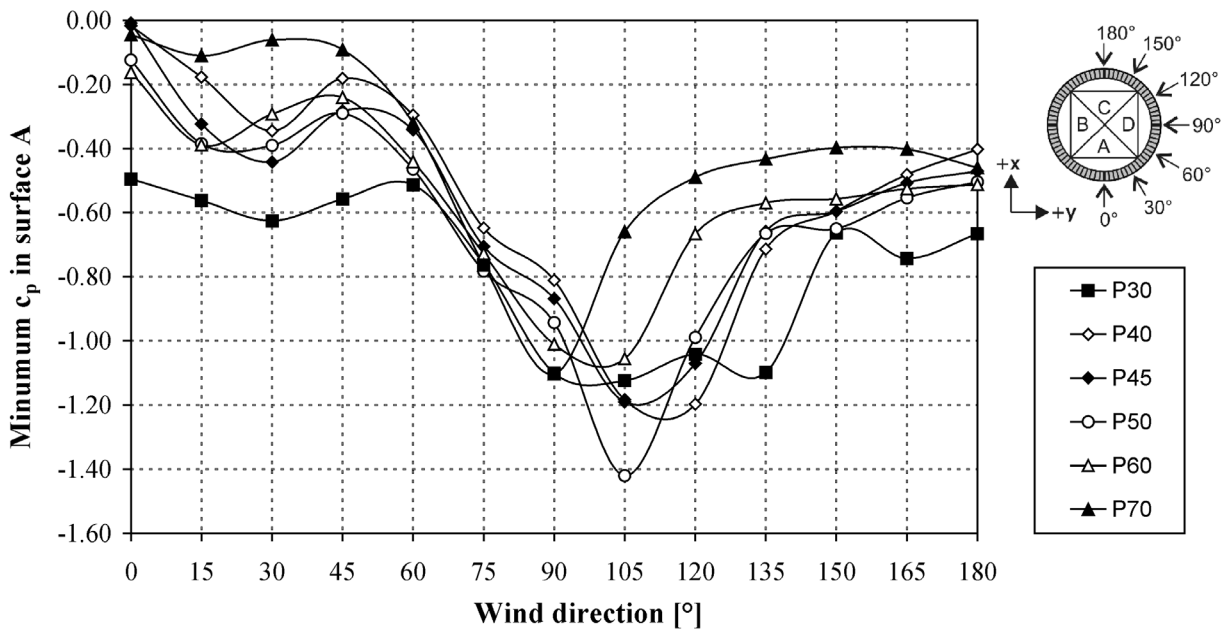


Fig. 5.30(b). Minimum mean pressure coefficients ( $c_p$ ) in surface A

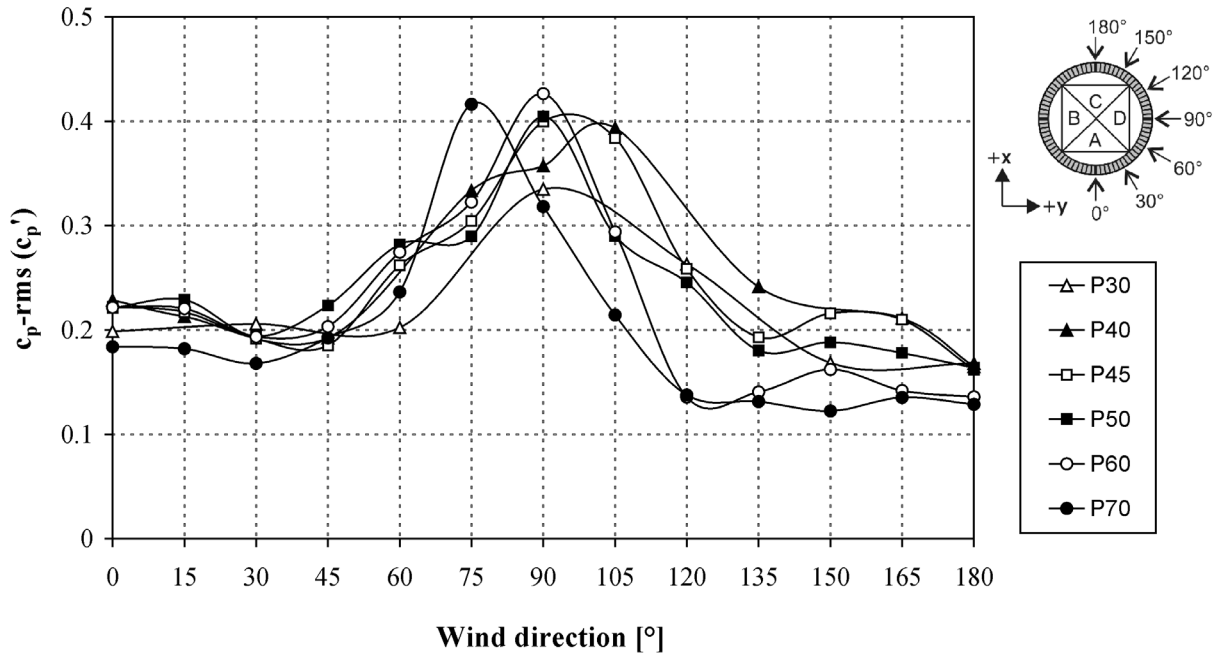


Fig. 5.30(c). Standard deviation of pressure coefficient fluctuations in surface A

Fig. 5.30. Mean pressure coefficients and standard deviation of pressure coefficient fluctuations in surface A of the investigated pyramids as a function of wind directions

### 5.2.3. Influence of the Pyramid Height on the Surface Pressure Distribution

The third investigated parameter is the height with respect to a characteristic length of the problem. As characteristic length, the boundary layer thickness or the roughness length can be chosen. In this study, the height is presented as the Jensen-number. This parameter expresses the height of the body divided by the roughness length ( $z_0=2.49$  mm) of the surface,  $h/z_0$ . As suggested by BRE, a Jensen-number in the range of 20~1000 will cover the range of real buildings [Cook 1990]. For this investigation, three different pyramids with base angle of  $70^\circ$  are investigated, namely pyramid P70, P70a and P70b. The height of pyramid P70, P70a and P70b are 274.75 mm ( $Je=110$ ), 142.81 mm ( $Je=57$ ) and 100.00 mm ( $Je=40$ ), respectively. For comparison the height of pyramid P70a is equal to pyramid P55 and pyramid P70b is equal to pyramid P45.

Fig. 5.31 shows the pressure distribution on the surfaces of pyramid P70, P70a and P70b. In general, the variations of Jensen-number do not significantly change the distribution patterns of pressure and suction on the pyramid surfaces. As stated in Section 5.2.1, the distribution patterns of pressure on the pyramid surfaces are more sensitive to the variation of the base angle rather than to the ratio of height to characteristics length (i.e. Jensen-number). The pressure distribution patterns observed in Fig. 5.31 support this statement. The distribution patterns of the pressure on the pyramid surfaces for the three pyramids with different height are relatively similar. This similarity also occurs for other wind directions. For wind direction  $0^\circ$ , the maximum pressure occurs on surface A (front surface), approximately at  $0.5h$ . The minimum pressure (maximum suction) occurs at the bottom corner of surface B and D (side surface).

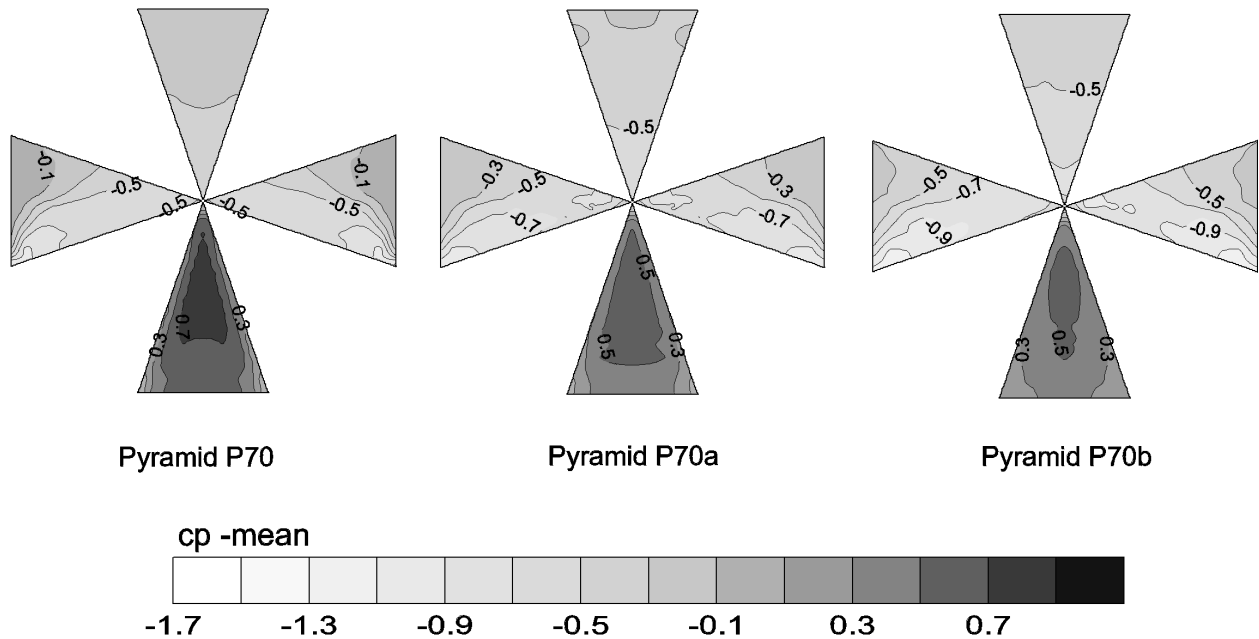


Fig. 5.31. Pressure distribution on the surfaces of pyramid P70 ( $h = 274.75$  mm), P70a ( $h = 142.81$  mm) and P70b ( $h = 100$  mm), at wind direction  $\alpha' = 0^\circ$

However, despite the similar pressure distribution patterns, the magnitude of the pressure on the surfaces shows a variation. For pyramid P70 ( $h = 274.75$  mm), the maximum pressure  $c_p$ -value is 0.78, and decreases to 0.66 and 0.58 for pyramid P70a ( $h = 142.81$  mm) and P70b ( $h = 100$  mm), respectively. Thus, in contrast to the pattern of the pressure distributions, the magnitude of the pressure is sensitive to the variations of base angle and Jensen-number. Fig. 5.32 (a) and (b) show the maximum mean pressure coefficient ( $c_{p-max}$ ) on A surface as a function of wind direction and Jensen-number, respectively. The figures show more clearly that when the height of the pyramids increases with constant velocity profile array and roughness length than the maximum  $c_p$ -value in the surface irrespective of its location also increases. The pressure seems to increase linearly with the height for almost all wind directions.

The maximum suction value in the surface also changes with the variation of Jensen-number even though the differences are relatively small. The variations of the minimum pressure on surface A as a function of wind direction and Jensen-number are presented in Fig. 5.33 (a) and (b), respectively. A general trend for all pyramids can be observed. The suction increases when the wind direction increases from  $0^\circ$  to  $90^\circ$ . At wind direction  $90^\circ$ , maximum suction values are registered in the surface, and after  $90^\circ$  the suction decreases. At wind direction  $0^\circ$  to  $90^\circ$ , the maximum suction is almost independent of the height of the pyramids. Beyond  $90^\circ$ , the maximum suction shows some dependency on the pyramid height. As can be seen in Fig. 5.33(b), the minimum pressure coefficient value in the considered surface is almost no function of the Jensen-number.

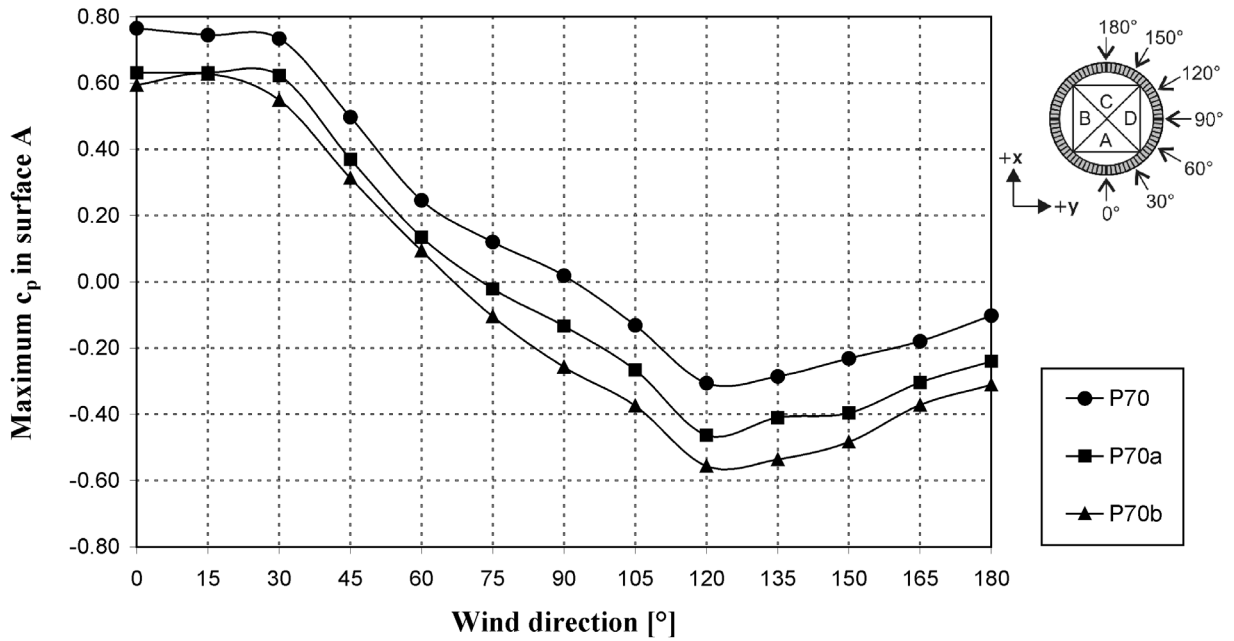


Fig. 5.32(a).  $c_p$ -maximum as a function of wind direction

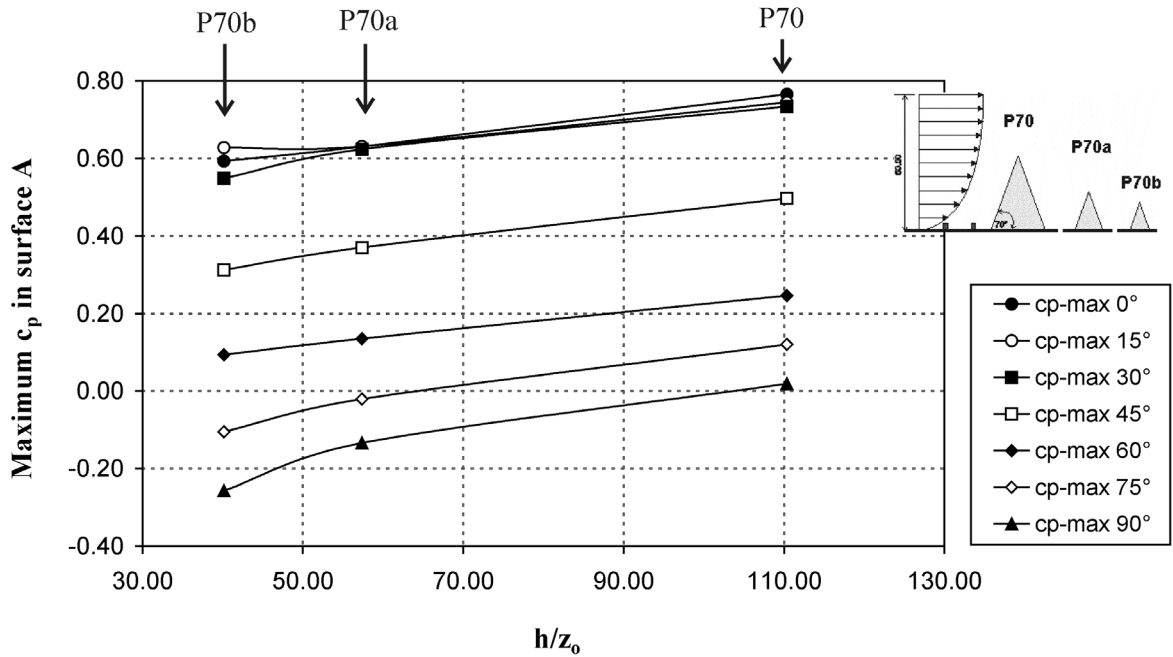


Fig. 5.32(b).  $c_p$ -maximum as a function of Jensen-number, P70 ( $h/z_0 = 110$ ), P70a ( $h/z_0 = 57$ ) and P70b ( $h/z_0 = 40$ )

Fig. 5.32. Maximum pressure coefficient (time-mean) in the surface A as a function of wind direction and Jensen-number for pyramid P70 ( $h = 274.75$  mm), P70a ( $h = 142.81$  mm) and P70b ( $h = 100$  mm).

5. Experimental Results

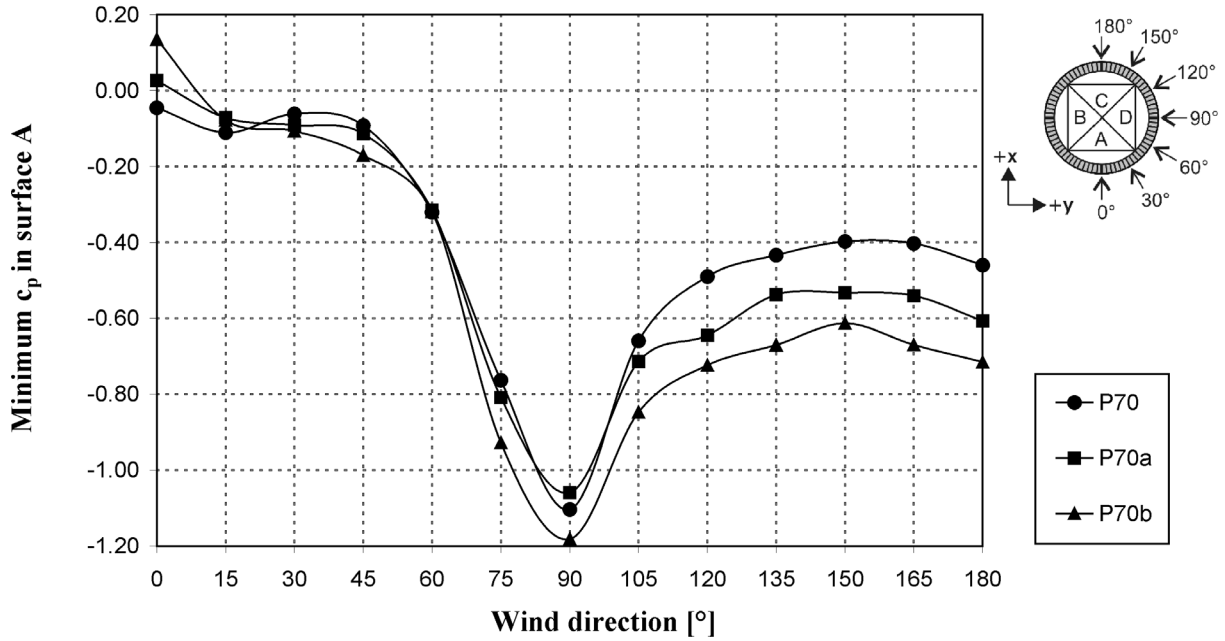


Fig. 5.33(a).  $c_p$ -minimum (maximum suction) as a function of wind direction

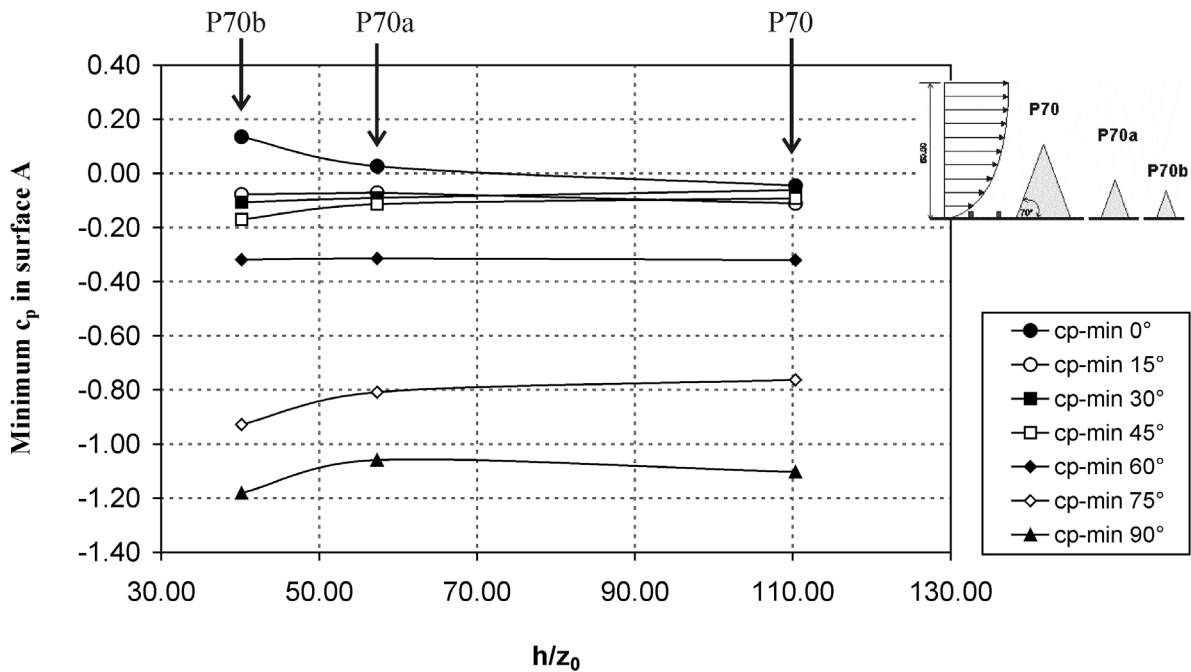


Fig. 5.33(b).  $c_p$ -minimum (maximum suction) as a function of Jensen-number, P70 ( $h/z_0 = 110$ ), P70a ( $h/z_0 = 57$ ) and P70b ( $h/z_0 = 40$ )

Fig. 5.33. Minimum pressure coefficient (time-mean) in surface A as a function of wind direction and Jensen-number for pyramid P70 ( $h = 274.75$  mm), P70a ( $h = 142.81$  mm) and P70b ( $h = 100$  mm).



The distribution patterns of the pressure fluctuations on the surfaces of pyramid P70, P70a and P70b do not differ significantly, as can be seen in Fig. 5.34. Similar to the location of the maximum suction, the maximum fluctuations also occur at the bottom corner of surface B and D. Fig. 5.35 shows the maximum fluctuations on surface A of the pyramids. The maximum fluctuation occurs at wind directions between 60° to 90°. The figures show that the pressure fluctuations on the pyramid surfaces are independent of the Jensen-number.

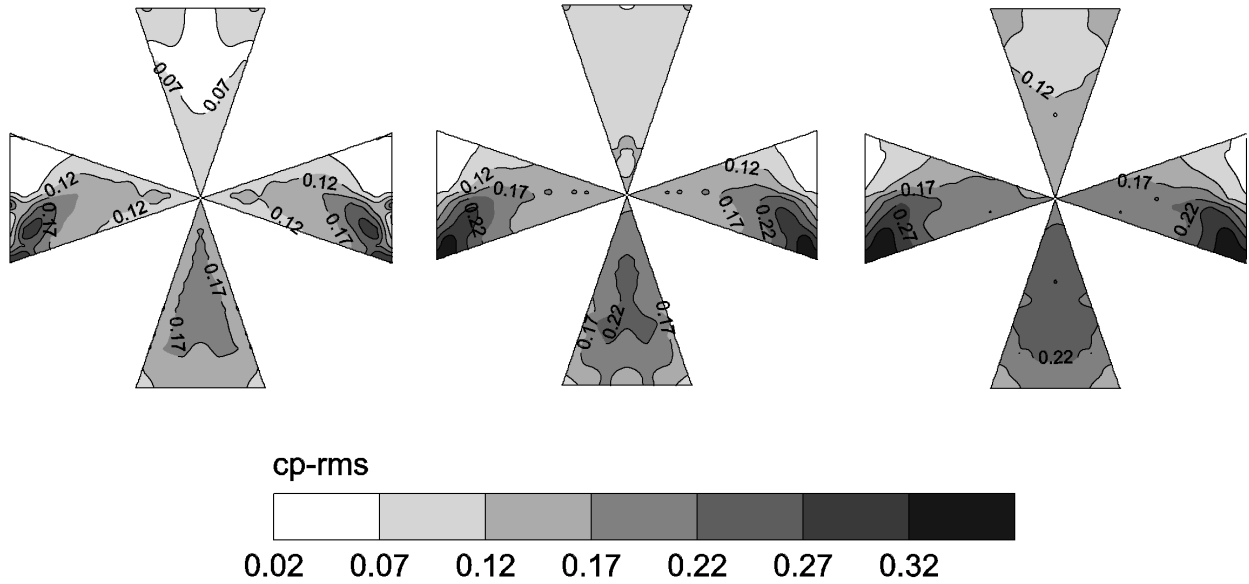


Fig. 5.34. Distribution of the standard deviation of pressure coefficient fluctuations in the surfaces of pyramid P70 ( $h = 274.75$  mm), P70a ( $h = 142.81$  mm) and P70b ( $h = 100$  mm), at wind direction  $\alpha' = 0$

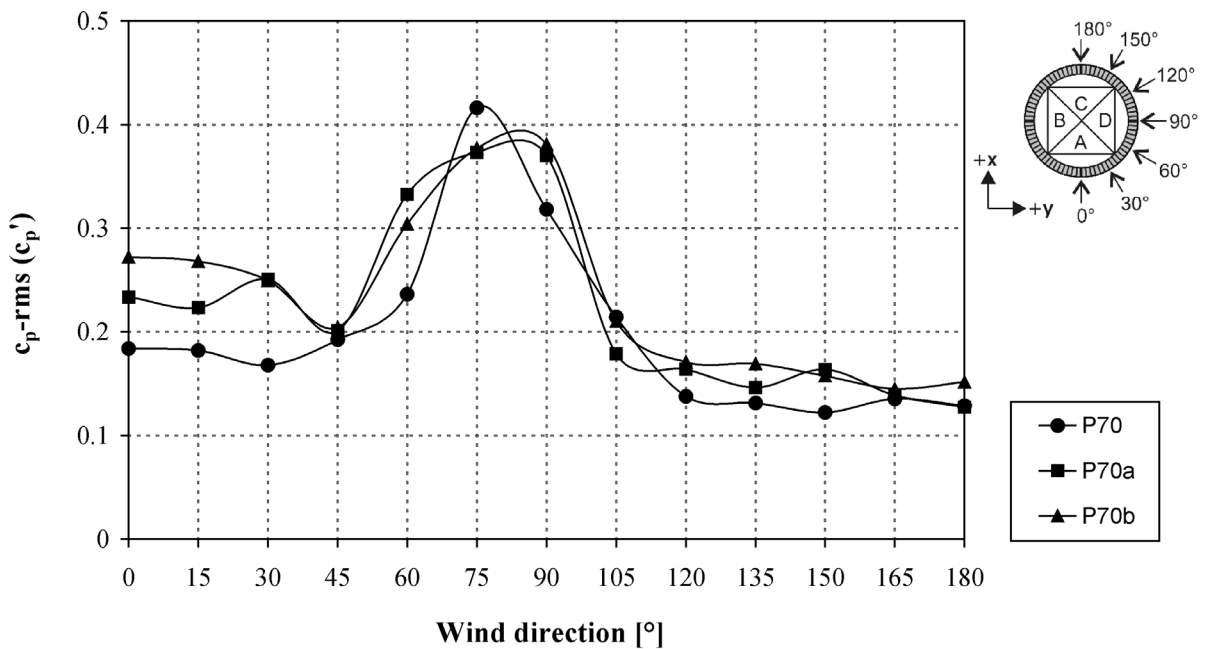


Fig. 5.35. Maximum standard deviation of pressure coefficient fluctuations in surface A as a function of wind direction for pyramid P70 ( $h = 274.75$  mm), P70a ( $h = 142.81$  mm) and P70b ( $h = 100$  mm).

### 5.3. Aerodynamic Coefficients of Pyramids

In this section, the results of the wind-induced forces are presented. As already described in Section 2.5.2, forces are deduced from an integration of local measured pressure values over the pyramid surfaces and introduced to the form of non-dimensional parameters, namely force coefficient and moment coefficient. These two coefficients are also known as aerodynamic coefficients, see also Ikhwan et.al., [2004].

Since force is a vector quantity having magnitude, direction and point of application in the three dimensional space, it is necessary to define a coordinate axes convention. There are two standard axes conventions, namely the body axes and the wind axes. In the present study, the wind axes convention is used. This means, the longitudinal axes (x) is aligned with the incoming-wind direction, the transversal axes (y) is aligned with horizontal cross wind direction and the vertical axes (z) is perpendicular to the longitudinal axes in vertical direction, see Fig. 2.8 for the wind axes conventions.

Based on the axes convention, the force coefficient can be divided into two different coefficients. The force induced by the incoming wind (longitudinal axes) is called the drag and the force induced by the cross wind is called the lift. Respectively, the corresponding force coefficients are called drag coefficient  $c_d$  and lift coefficient  $c_l$ . As far as the moments are concerned, there are three moments, each of them works on different axes. In the present study, only the moment working along the z-axes is discussed ( $c_{m-z}$ ). The calculation methods of these three coefficients are already described in Section 2.5.2 and in Table 5.2 a summary of the aerodynamic coefficients definitions and functions are presented.

Table 5.2. Aerodynamic coefficients

	Drag coefficient	$c_d = \frac{F_d}{\frac{1}{2} \rho u_{ref}^2 A_{proj}} \quad (5.14)$
	Lift coefficient	$c_l = \frac{F_l}{\frac{1}{2} \rho u_{ref}^2 A_{proj}} \quad (5.15)$
	Moment coefficient	$c_{m-z} = \frac{M_z}{\frac{1}{2} \rho u_{ref}^2 A_{proj} l} \quad (5.16)$
$\frac{1}{2} \rho u_{ref}^2$ = reference dynamic pressure at the tip of pyramid, $F_d$ is the drag force, $F_l$ is the lift force, $M_z$ is the moment working at z-axes, $A$ is the projection area of the pyramid in wind direction, and $l$ is the base length of the pyramid		

Three different parameters that affect the aerodynamic coefficients for the investigated pyramidal buildings are again the base angle, the wind direction and the height of the pyramids. The height parameter will be presented in the form of the Jensen-number ( $h/z_0$ ).

### 5.3.1. Drag Coefficient

Fig. 5.36 shows the drag coefficient as a function of base angle. When the wind blows from a direction of  $0^\circ$ , the magnitudes of the drag coefficient for all pyramid are relatively similar, except for pyramid P30, which is considered as an extreme shallow pyramid. When the wind blows from a direction of  $15^\circ$ , the drag coefficient reaches its maximum. The magnitude of the drag coefficients is found to be in the range of 1.4 – 2.2. For wind direction  $30^\circ$  and  $45^\circ$ , the variations of the drag coefficients with the base angle are again relatively small except for pyramid P30 at wind direction  $30^\circ$ . Looking at the figure, it seems that the drag coefficient is not significantly influenced by the base angle variations, except for extremely shallow pyramid.

The drag coefficient is shown as a function of the wind direction in Fig. 5.37. The curves of the drag coefficients for all pyramids show the same trend or pattern. The minimum  $c_d$  occurs with wind direction ( $\alpha'$ )  $0^\circ$  and reaches a maximum when  $\alpha' = 15^\circ$ . With further increase of  $\alpha'$ , the drag coefficients decrease. As can be seen from Fig. 5.36 the drag coefficient of pyramids exposed to tilted, non-frontal wind directions can amount to 4 times the  $c_d$ -value of the frontal wind direction. For angles greater than  $45^\circ$ , a mirror effect is expected due to the symmetrical shape of the pyramids. It is interesting to see that the pyramids experience the highest drag when the wind blows from a direction of  $15^\circ$ . This is caused by the larger area of higher suction on surface B of the pyramids, as shown in Fig. 5.28 which depicts the mean pressure distribution on the pyramid surfaces.

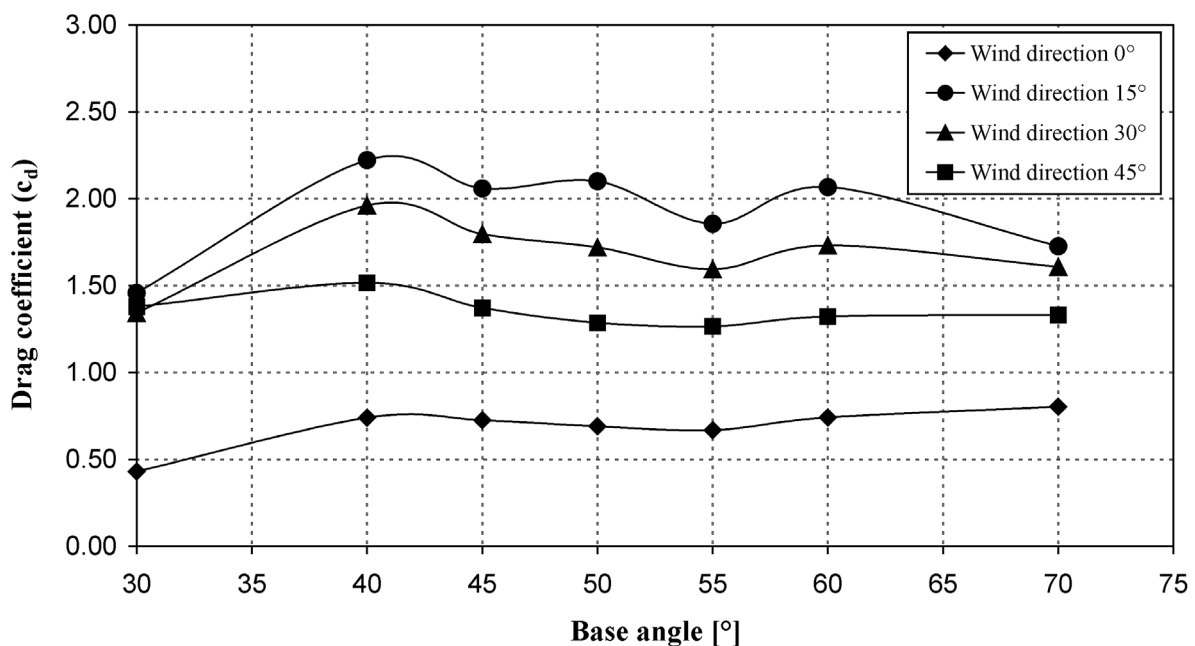


Fig. 5.36. Drag coefficients of pyramids as a function of pyramid base angle

5. Experimental Results

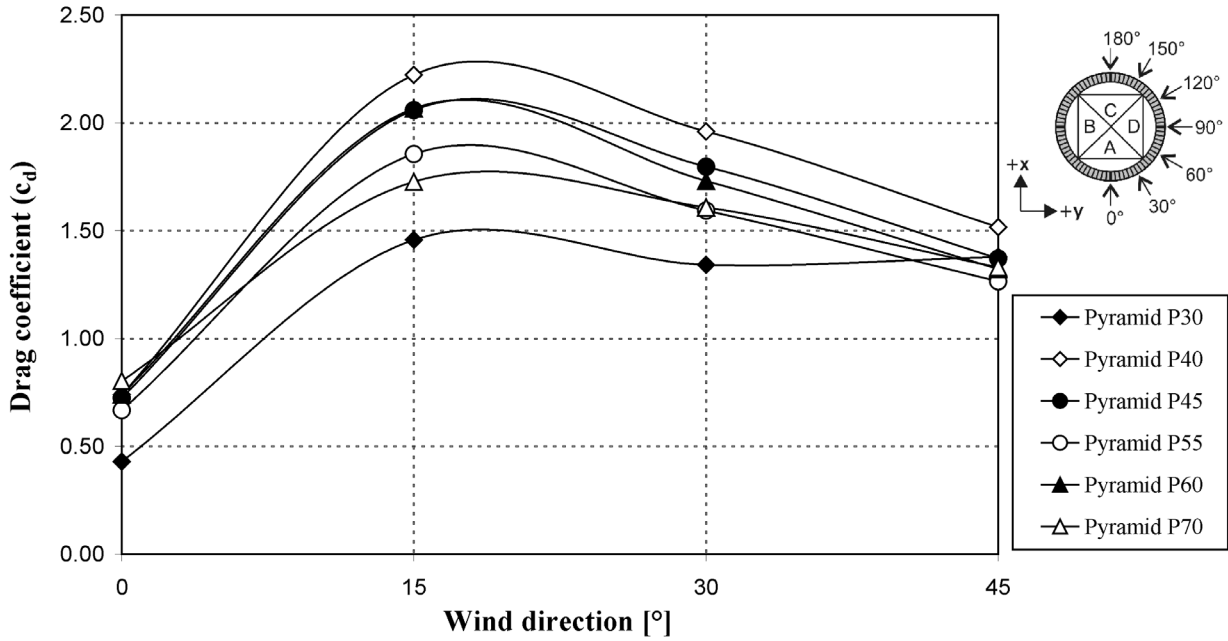


Fig. 5.37. Drag coefficient of pyramids as a function of wind direction

The next parameter of interest is the Jensen-number of the pyramid. The result is presented in Fig. 5.38. From the figure, it can be inferred that the drag decreases as the Jensen-number increases. However, the variation is relatively small. This indicates that the dependency of drag coefficient on the height for pyramid with base angle  $70^\circ$  is relatively small.

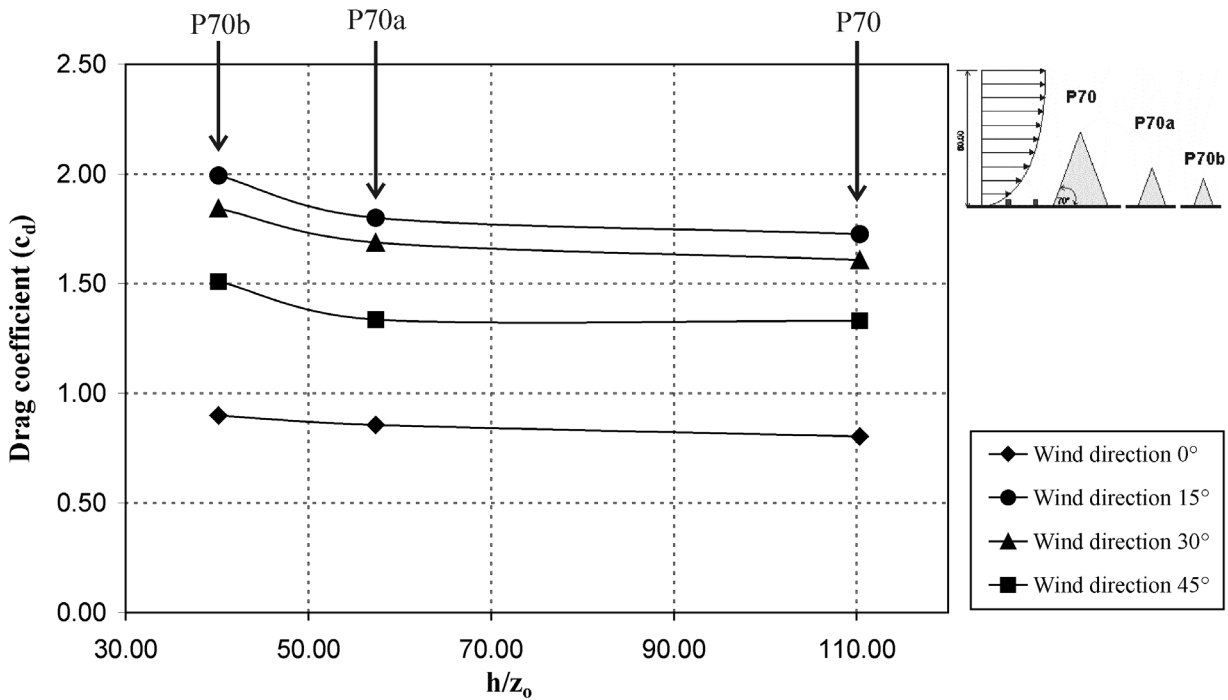


Fig. 5.38. Drag coefficient of pyramids as a function of Jensen-number, P70 ( $h/z_0 = 110$ ), P70a ( $h/z_0 = 57$ ) and P70b ( $h/z_0 = 40$ )

From the three parameters (i.e. base angle, wind direction and height), the present results show that the incoming wind directions give the most significant effect to the drag coefficient for pyramidal buildings. However, for shallow pyramids, the base angle still give a significant effect to the magnitude of drag coefficient when compared to the steep pyramid.

### 5.3.2. Lift Coefficient

Fig. 5.39 shows the influence of base angle variations on the lift coefficients for different wind directions. A similar trend of the lift coefficients curves can be found for all wind directions. When the base angle increases from  $30^\circ$  to  $40^\circ$ , the lift coefficient decreases. Between  $40^\circ$  and  $55^\circ$ , the lift coefficient experiences an increase. Then, the lift coefficient decreases again until a minimum lift occurs when the base angle reaches  $70^\circ$ . In Section 5.1, it has been stated that at the side of pyramids vertical vortex system are occurred. Theoretically, these flow structures should increase the lift coefficient of bluff bodies since it produces suction in the side surfaces of the pyramid. The present results of lift coefficient show that this is not the case for pyramidal structures, which should be addressed carefully. It is obvious that the wall taper for pyramid with base angle greater than  $55^\circ$  inhibits the growth of the lift force at the pyramids.

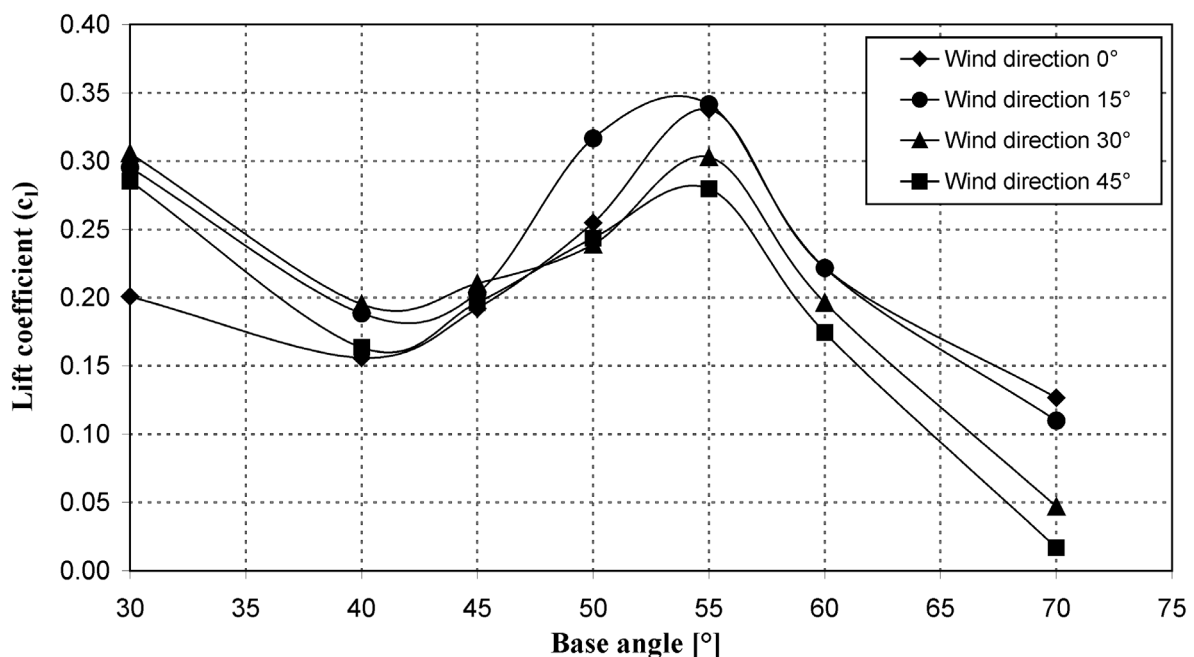


Fig. 5.39. Lift coefficient of pyramids as a function of pyramid base angle

The influence of the incoming wind directions on the lift coefficient is presented in Fig. 5.40. It can be inferred from the figure that two different types of curve exist. Pyramid P30, P40 and P45 show a relatively similar type of curve, whereas pyramid P55, P60 and P70 deliver another type of curve. For the first type of curve (P30, P40 and P45), the lift coefficient increases when the wind direction changes from  $0^\circ$  to  $30^\circ$  and decreases again when wind blows at  $45^\circ$ . Beyond  $45^\circ$ , the lift coefficient value will create a mirror effects due to the symmetrical geome-

try of pyramids. The lift coefficient for the second type of curve (P55, P60 and P70) shows the lift coefficient decrease when the wind direction changes from 0° to 45°. When the wind blows at wind direction of 45°, the lift coefficient reaches it minimum value.

Fig. 5.41 shows the lift coefficient as a function of the Jensen-number (i.e dimensionless height). The figure shows clearly that the Jensen-number has a measurable influence on the lift coefficient of the pyramids. The lift coefficient decreases when the height of the pyramids increases. The relation is likely to be an exponential function. This result is another interesting fact for pyramidal buildings. Not only an increase of the base angle inhibits the growth of the lift force but also an increase of the height gives a similar effect to the lift coefficients. From the results discussed in this section, it can be concluded that the lift coefficient of pyramids depends on the parameters base angle, wind direction and Jensen-number.

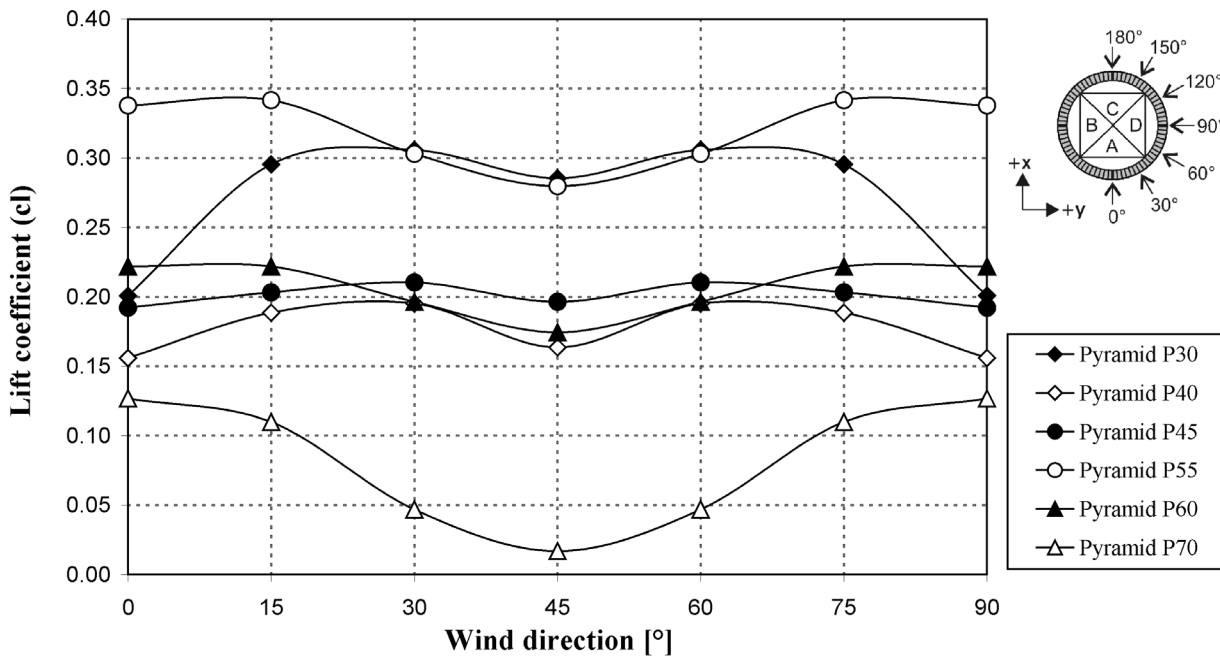


Fig. 5.40. Lift coefficient of pyramids as a function of wind direction

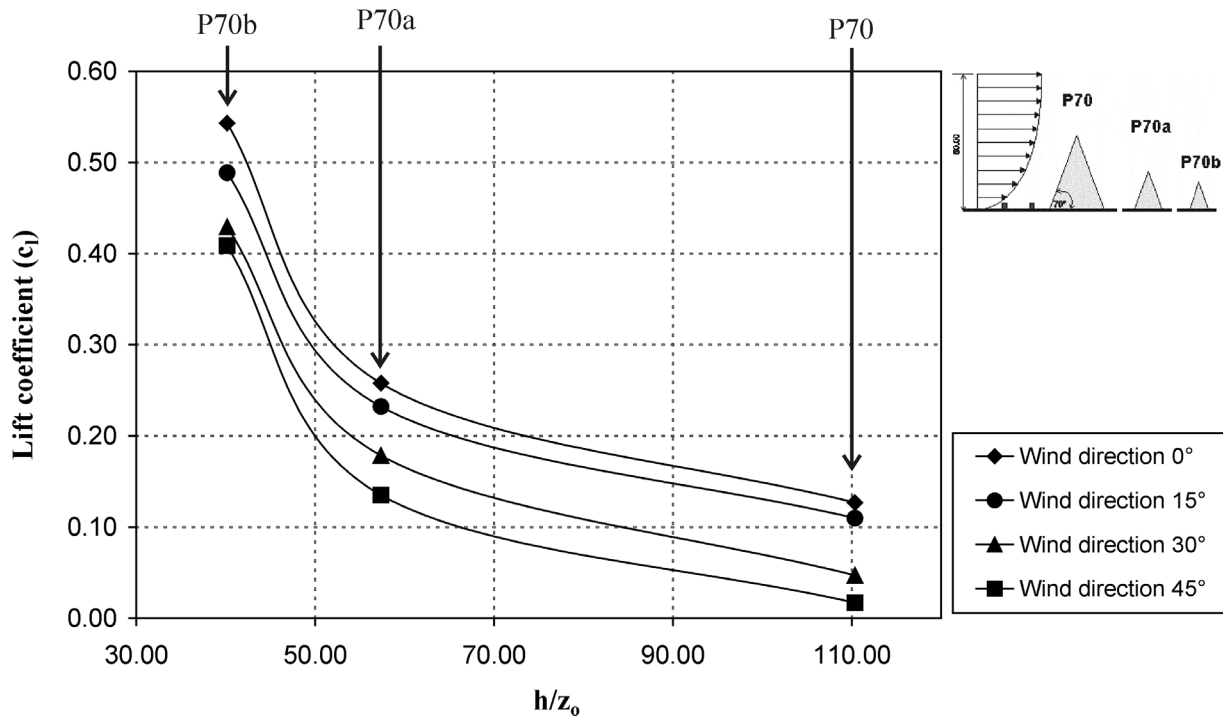


Fig. 5.41. Lift coefficient of pyramids as a function of Jensen-number, P70 ( $h/z_0 = 110$ ), P70a ( $h/z_0 = 57$ ) and P70b ( $h/z_0 = 40$ )

### 5.3.3. Moment coefficient

Fig. 5.42 to Fig. 5.44 show the moment coefficients accounting for moments working at the z-axes as a function of pyramid base angles, wind direction and the height of the pyramid, respectively. The results show that the values of the moment coefficients are relatively small. Typical values are in the range of  $-0.025$  to  $0.025$ . This range is also a typical range found for most of ordinary buildings [Akins et.al., 1997]. Due to the symmetrical shape of the pyramid, the moments fall to almost zero ( $\sim 0$ ) when the wind blows from a direction of  $0^\circ$  and  $45^\circ$ . An interesting fact that can be observed is that variations of the base angles can generate different direction of rotation. From pyramid P30, the moments rotate in one direction and increase as the base angle increase to  $40^\circ$ . After pyramid P40, the moment reduces and when the base angle reaches  $60^\circ$ , the moments rotate in another direction than those with base angles below  $60^\circ$ . This reversal of moment direction was never detected by any previous studies in the area of building aerodynamics. It can be seen more clearly in Fig. 5.43, which shows the moment coefficient for different pyramids as a function of wind directions.

5. Experimental Results

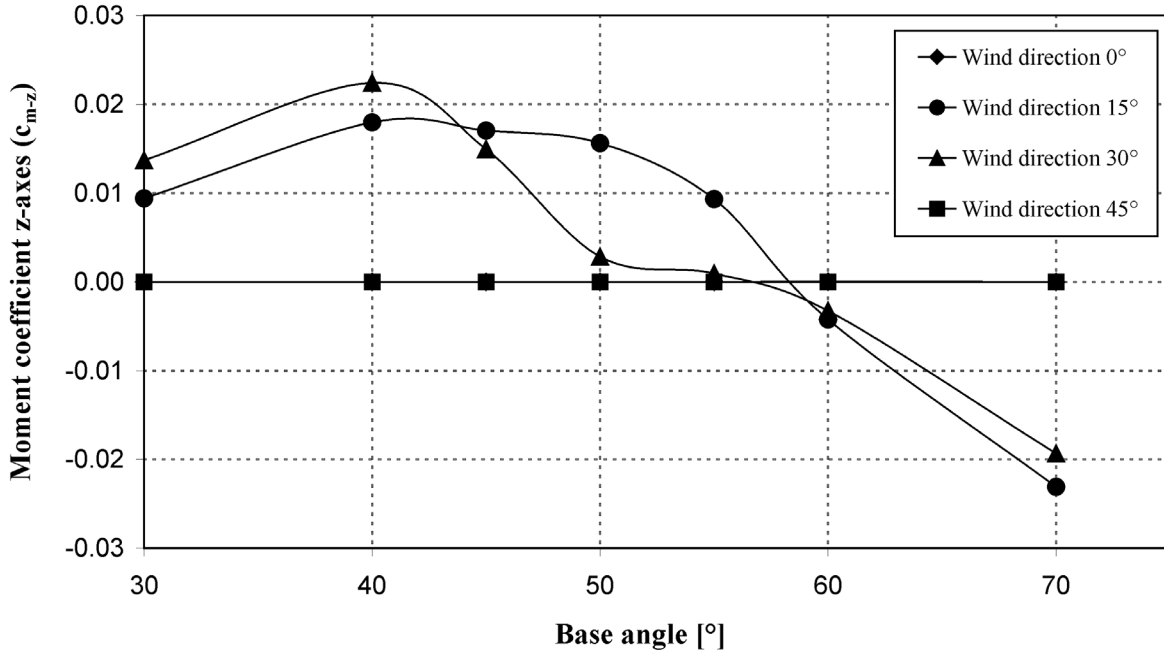


Fig. 5.42. Moment coefficient as a function of pyramid base angle

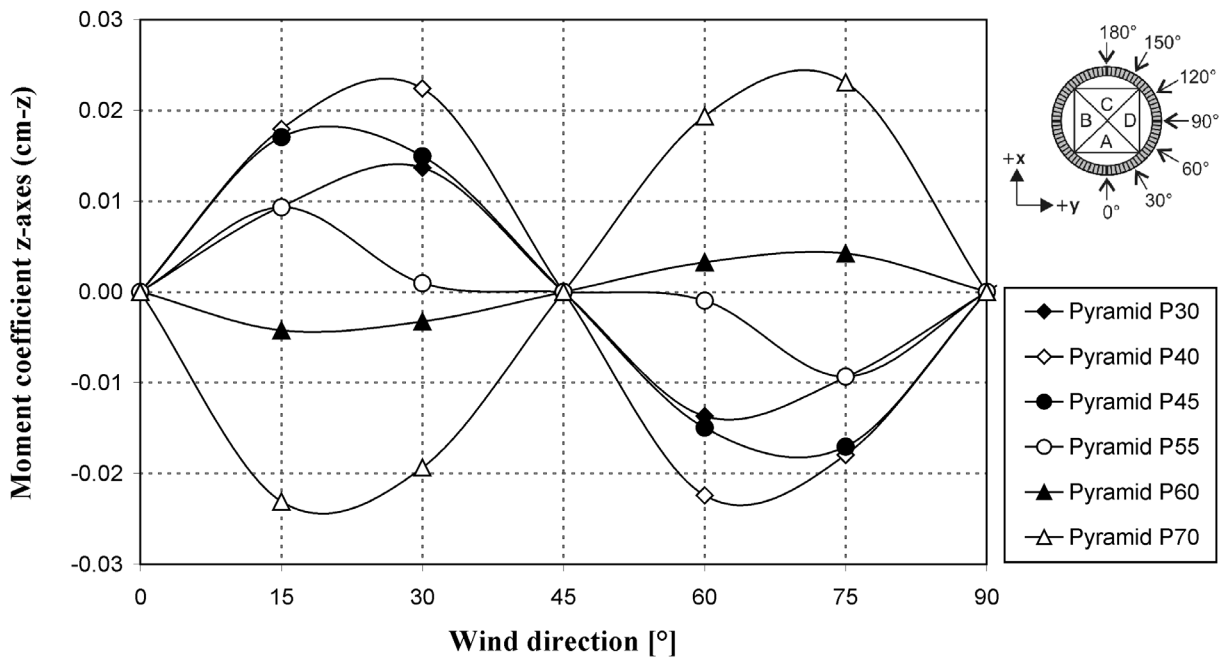


Fig. 5.43. Moment coefficient as a function of wind direction

The symmetrical shape of the pyramid causes a mirror effect at wind direction of 90° and a change of direction of the moment in every 45° of wind direction. For pyramid P30 and P40, the maximum moment occurs when the wind blows from a direction of 30°. For the other pyramids, the maximum occurs when the wind blows from a direction of 15°. For pyramid P55 (medium step pyramid), a different curve reveal. The moment suddenly decreases when the wind direction change from 15° to 30°.



The variations of the moment coefficients as a function of the Jensen-number for pyramids P70, P70a and P70b are depicted in Fig. 5.44. Again, it is clear that there is no effect for the moment when the wind blows from a direction of  $0^\circ$  and  $45^\circ$ . For other wind directions, the height introduces a measurable influence on the magnitude of the moment coefficients. The magnitudes increase when the heights of the pyramid increase from pyramid P70b to pyramid P70a afterwards the moment coefficients decrease. The direction of the moment, however, remains the same at all heights. With these results, it can be concluded that the base angle and the wind direction are the parameters which control the direction of the moment.

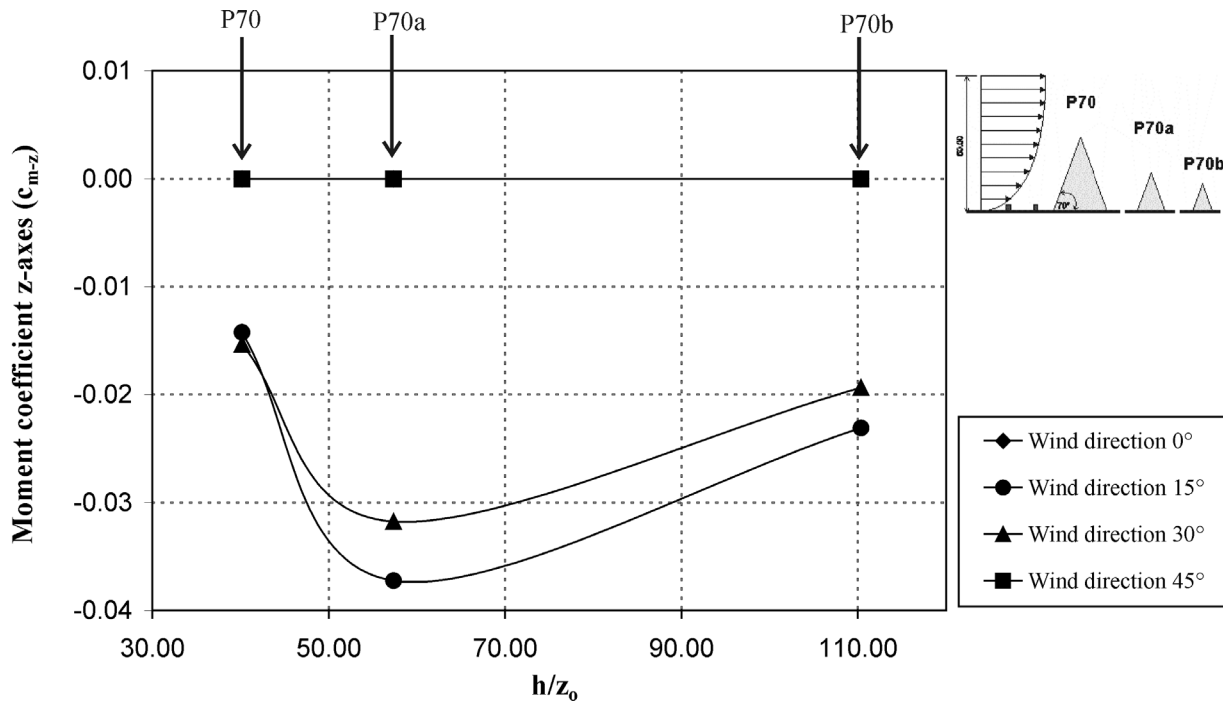


Fig. 5.44. Moment coefficient as a function of Jensen-number, P70 ( $h/z_0 = 110$ ), P70a ( $h/z_0 = 57$ ) and P70b ( $h/z_0 = 40$ )

## 5.4. Summary of Experimental Results

The experimental results were able to show both qualitatively and quantitatively the effects of the investigated parameters (wind direction, base angle and height of the pyramid) on the flow and pressure characteristics. The results obtained from the flow measurements show that variation of the base angle affects significantly the flow characteristics around pyramids.

For the pressure characteristics, a qualitative summary of the effects of the investigated parameters is presented in Table 5.3. The pyramids are classified into shallow pyramids ( $\theta = 30^\circ - 45^\circ$ ) and steep pyramids ( $\theta = 55^\circ - 70^\circ$ ) and the effects of each parameter are categorized as “Significant”, “Less significant” or “Not significant”. The category “Significant” indicates that the pressure characteristics are sensitive to the variation of the parameters. “Less significant” indicates that the sensitivity of the parameter variations are not as strong as the “Significant” cate-

gory. The last category, “Not significant”, indicates that there are no significant changes of the pressure characteristics although the parameters are varied.

For practical purposes, the pressure measurement results would be very important in the area of building design. Despite the fact that more considerations on wind load design are required, in general the results from the present study are able to deliver a contribution for the design of a pyramidal buildings. A summary of the pressure and aerodynamic coefficients for pyramid buildings is presented in Table 5.4. The minimum and maximum values are shown.

Table 5.3. Qualitative summary of the effects of the investigated parameters to the pressure characteristics.

Pressure characteristics	Pyramid categories*	Parameters		
		Wind direction	Base angle	Height
Magnitude of Pressure coefficients	Shallow			X
	Steep			Significant
Magnitude of pressure fluctuations	Shallow		Significant	X
	Steep			Less Significant
Location of $c_{p,max.}$ , $c_{p,min.}$ and $c_{p,max.}$	Shallow	Significant		X
	Steep		Less significant	Not significant
Drag coefficient	Shallow		Significant	X
	Steep		Less significant	Less significant
Lift coefficient	Shallow			X
	Steep		Significant	Significant
Moment coefficient	Shallow			X
	Steep			Less significant

\* Shallow pyramid  $\theta = 30^\circ - 45^\circ$ , Steep pyramid  $\theta = 55^\circ - 70^\circ$

X = not investigated

Table 5.4. Typical value of mean pressure coefficient ( $c_p$ ) on the pyramid surfaces and aerodynamic coefficients (drag, lift and moment coefficient) in minimum and maximum range.

Pyramid types	Pressure coefficient ( $c_p$ )*		Drag coefficient ( $c_d$ )	Lift coefficient ( $c_l$ )	Moment coefficient ( $c_{m-z}$ )
	Min. / Max.	Maximum fluctuations			
Pyramid P30	-1.10 / 0.42	0.34	0.43 / 1.46	0.20 / 0.30	0 / 0.01
Pyramid P40	-1.19 / 0.57	0.40	0.74 / 2.22	0.16 / 0.20	0 / 0.02
Pyramid P45	-1.19 / 0.57	0.40	0.72 / 2.05	0.19 / 0.20	0 / 0.02
Pyramid P50	-1.52 / 0.53	0.40	0.69 / 2.10	0.24 / 0.32	0 / 0.02
Pyramid P55	-1.48 / 0.53	0.41	0.67 / 2.00	0.28 / 0.34	0 / 0.01
Pyramid P60	-1.05 / 0.57	0.42	0.74 / 2.00	0.17 / 0.22	0 / 0.01
Pyramid P70	-1.10 / 0.77	0.42	0.80 / 2.00	0.02 / 0.54	0 / 0.04

- Minus (-) indicate suction

## 6. Additional Numerical Investigations

The main purpose of this thesis was to investigate experimentally the flow and pressure field around pyramids. Numerical studies were performed additionally with a standard Computational Fluid Dynamics (CFD) tool in order to prove whether experimental and numerical studies deliver the same results. Before performing the numerical calculations, it is necessary to ensure that the numerical results deliver reliable results. Therefore, comparison of the experimental results with the numerical results must be first performed. The results from the numerical investigations are presented and discussed in this chapter after a brief description of the applied numerical software.

The numerical simulations were performed using the commercial software package FLOVENT Version 3.2 developed by Flomerics, which is a special software for numerical calculation in the area of building- and environmental aerodynamics. The software is described as an airflow modelling software, designed to calculate airflow, heat transfer and contamination distribution for built environments. It uses techniques of Computational Fluid Dynamics (CFD) and includes the revised  $k$ - $\epsilon$  model for turbulence modelling.

### 6.1. Mathematical Background

In this section, the mathematical backgrounds of FLOVENT that are relevant to the numerical simulations conducted in the present study are briefly described. More detailed specification of the mathematical models can be seen in Flomerics [2000] and a general description of computational method for fluid dynamics can be found among others in Ferziger [1999].

#### Equation of motion

As stated before, the solution procedures in FLOVENT are based on CFD techniques. The three basic governing equations used are the conservation of mass, conservation of momentum and conservation of energy. The derivations of these equations are not detailed here but can be found in many textbooks such as Schlichting, [1965] and Stull [1988].

The present study focuses on the flow in a neutral atmospheric boundary layer. For such condition, the following assumptions are taken:

## 6. Additional Numerical Investigations

- The flow is steady ( $\partial/\partial t = 0$ )
- The flow is incompressible
- Thermal processes are negligible
- Coriolis-effects are negligible
- The flow behaves like a Newtonian-fluid

As already described in Section 2.2, the conservation of mass for incompressible fluids can be written as

$$\frac{\partial u_i}{\partial x_i} = 0 \quad (6.1)$$

and the conservation of momentum (Navier-Stokes equations)

$$\frac{\partial u_i}{\partial t} + u_k \frac{\partial u_i}{\partial x_k} = -g\delta_{3i} - \frac{1}{\rho} \frac{\partial p}{\partial x_i} + \nu \frac{\partial^2 u_i}{\partial x_k \partial x_k} \quad (6.2)$$

In FLOVENT, the modelled equations are discretized using the finite-volume-method. Hereby, the total volume to be calculated is divided into small elements known as grid cells. The partial differential equations are assigned to each grid cell and solved iteratively. The iteration procedure will be interrupted as soon as the solution converges, i.e. the error of the system is under an acceptable value.

### Turbulence Viscosity Model

To simulate a turbulent flow accurately, the temporal terms of the conservation equations must have a time interval or time step ( $dt$ ) sufficiently small to ensure that all turbulent fluctuations even on the smallest time scale are captured. The same applies to all physical dimension of the control volume cells  $dx_i$ . It must be as small as the Kolmogorov length scale, which decreases non-linearly with an increase in Reynolds numbers. An exact numerical modelling is thus impossible due to the enormous calculation efforts. Therefore, the instantaneous terms are split into a mean and a fluctuating part. Incorporating these terms into the instantaneous Navier-Stokes equations and time-averaging the resulting equations leads to the following Reynolds equations (see also Section 2.2).

$$\rho u_j \frac{\partial u_i}{\partial x_j} = -\delta_{i3} \rho g - \frac{\partial p}{\partial x_i} + \mu \frac{\partial^2 u_i}{\partial x_j^2} - \rho \frac{\partial}{\partial x_j} \overline{u'_j u'_i} \quad (6.3)$$

The last term is referred as the Reynolds shear stress which results from time-averaging the instantaneous equation. In a turbulent boundary layer, the Reynolds shear stress comprises turbulent and viscous components. The turbulent components are significantly larger than the viscous components, except in the region extremely close to the wall. The Reynolds shear stress term

introduces a new unknown variable that must be solved. Thus, an additional turbulence closure model is required in order to solve the problem.

Here, a revised k- $\varepsilon$  model is chosen as the turbulence closure model. This turbulence model calculates two variables, namely the kinetic energy of turbulence (k) and the dissipation rate of k (denoted as  $\varepsilon$ ), see Rodi [2000] for a description of k- $\varepsilon$  model. In order to calculate the Reynolds shear stress, the principle of eddy viscosity is applied. Analogue to laminar flows, the shear stresses in turbulent flows are assumed to be proportional to the velocity gradients

$$-\overline{\rho u_i u_j} = \mu_T \left( \frac{\partial \overline{u_i}}{\partial x_j} + \frac{\partial \overline{u_j}}{\partial x_i} \right) - \frac{2}{3} \rho k \delta_{ij} \quad (6.4)$$

in which  $\mu_T$  is the eddy viscosity and defined from dimensional analysis as:

$$\mu_T = C_\mu \rho \frac{k^2}{\varepsilon} \quad (6.5)$$

The transport equations for k and  $\varepsilon$  are:

$$\frac{\partial \rho \overline{U_i k}}{\partial x_i} = \frac{\partial}{\partial x_i} \left[ \left( \mu + \frac{\mu_T}{\sigma_k} \right) \frac{\partial k}{\partial x_i} \right] + P + G - \rho \varepsilon \quad (6.6)$$

$$\frac{\partial \rho \overline{U_i \varepsilon}}{\partial x_i} = \frac{\partial}{\partial x_i} \left[ \left( \mu + \frac{\mu_T}{\sigma_k} \right) \frac{\partial \varepsilon}{\partial x_i} \right] + C_1 \frac{\varepsilon}{k} (P + C_3 G) - C_2 \rho \frac{\varepsilon^2}{k} \quad (6.7)$$

where P is the shear production defined as

$$P = \mu_{\text{eff}} \frac{\partial \overline{U_i}}{\partial x_j} \left( \frac{\partial \overline{U_i}}{\partial x_j} + \frac{\partial \overline{U_j}}{\partial x_i} \right) \quad (6.8)$$

G is the production of turbulence kinetic energy due to buoyancy, given by

$$G = \frac{\mu_{\text{eff}}}{\sigma_T} \beta g_i \frac{\partial T}{\partial x_i} \quad (6.9)$$

## 6. Additional Numerical Investigations

and the empirical constants are:

$$\begin{aligned}C_m &= 0.09 \\C_1 &= 1.44 \\C_2 &= 1.92 \\C_3 &= 1.0 \\\sigma_k &= 1.0 \\\sigma_\varepsilon &= 1.217\end{aligned}$$

One can see that the values of the two variables  $k$  and  $\varepsilon$  are determined using only two extra differential equations. This model has been tried and tested for a whole range of engineering applications and is proven to be stable [Flomerics 2000].

### Near Wall Treatment

The velocity of a flowing fluid directly at the wall is zero, which is known as the non-slip boundary condition. The type of flow between the wall and the bulk flow is known as a wall boundary layer, in which high velocity gradients dominate the flow. To model it accurately, extremely fine grid cells would be needed. Therefore, in Flovent, an empirical relationship is used to describe the shape of the boundary layer near the wall.

A roughness Reynolds number  $Re_R$  is determined based on the height of the roughness elements  $h_r$ , and can be written as:

$$Re_{R,N} = \frac{h_r u_* \rho}{\mu} \quad (6.10)$$

For rough walls ( $Re_R > 3.3$ ), the shear velocity  $u_*$  is estimated based on the velocity  $u$  at the centre of a grid cell and the distance  $y$  from the wall using

$$\frac{u}{u_*} = \frac{1}{0.435} \ln\left(\frac{29.7y}{h_r}\right) \quad (6.11)$$

For smooth walls ( $Re_R < 3.3$ ), the shear velocity  $u_*$  is estimated using the following universal relationships:

$$\frac{u}{u_*} = \frac{1}{0.435} \ln(9y^+) \quad \text{for } y^+ > 11.5 \text{ (turbulent flow)} \quad (6.12)$$

$$\frac{u}{u_*} = y^+ \quad \text{for } y^+ \leq 11.5 \text{ (laminar flow)} \quad (6.13)$$

$$\text{with } y^+ = \frac{y u_* \rho}{\mu}$$

Finally, the wall shear stress  $\tau_o$  can be obtained

$$\tau_o = u_*^2 \rho \quad (6.14)$$

and its value is assigned as a sink of momentum for the grid cells near the wall.

## 6.2. Boundary Conditions

In order to compare the results of numerical and experimental investigations, the wind tunnel was modelled using the FLOVENT software. A schematic illustration of the solution domain for the numerical computation representing the simulated wind tunnel (“numerical wind tunnel”) is given in Fig. 6.1. The “numerical wind tunnel” extends in the main flow direction from  $-2.5 \cdot l < x < 2.5 \cdot l$  ( $l =$  pyramid length), in the lateral direction from  $-3 \cdot l < y < 3 \cdot l$  and in the vertical direction from  $0 \cdot l < z < 2.5 \cdot l$ . The “numerical wind tunnel” acts as the solution domain for the numerical computation and each surface acts as a boundary surface.

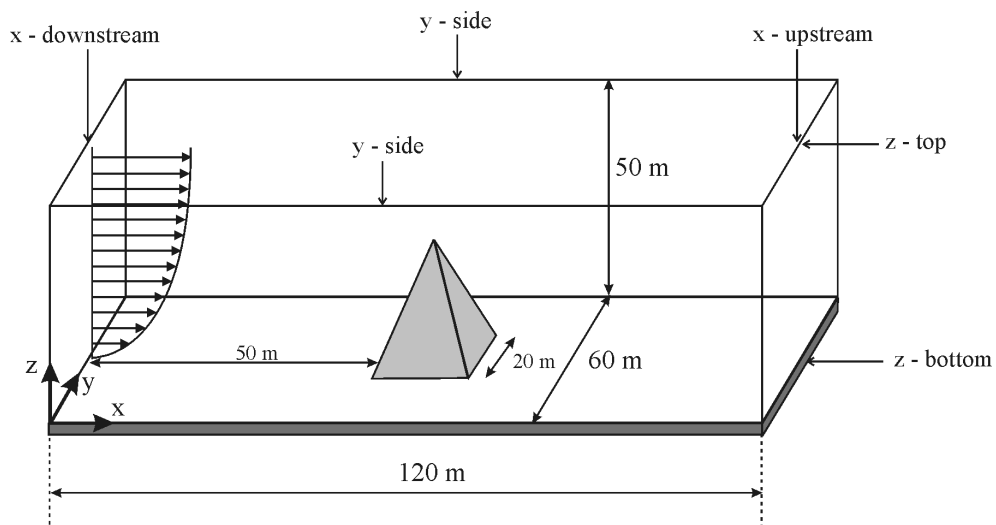


Fig. 6.1. Solution domain for the numerical computation representing the simulated wind tunnel (“numerical wind tunnel”).

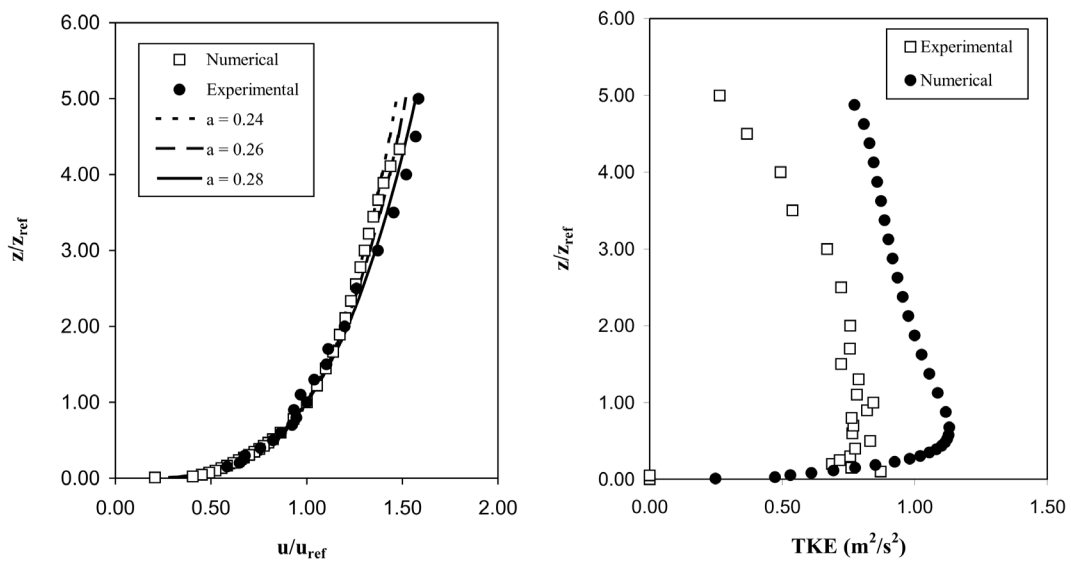
For the bottom boundary surface, the terrain was simulated by introducing a roughness height on the surface. In order to obtain a comparable results between the experimental results and the numerical simulation, the roughness height for the numerical simulation was so chosen that it corresponds to the height of the roughness elements in the wind tunnel. For the downstream and upstream surfaces in the flow direction  $x$  ( $x$  –downstream and  $x$ -upstream) and top surfaces in the  $z$  direction ( $z$ -top), open surfaces were assigned as boundary conditions. This means that a free boundary of constant pressure through which air can flow is applied. In the lat-

eral direction (y direction), a symmetrical boundary of the solution domain was chosen at both sides. These boundaries are frictionless, impermeable and adiabatic planar surfaces.

At the beginning of the solution domain (i.e.  $x=0$ ), the simulated atmospheric boundary layer flow was generated by 20 “Fixed Flow Devices” which are distributed uniformly in height. For each “Fixed Flow Device”, certain values of mean longitudinal velocity and turbulence kinetic energy are assigned which produce an incoming velocity profile and an incoming turbulent kinetic energy profile as shown in Fig. 6.2. It is shown that the incoming flow conditions of the numerical model is similar as the experimental model.

Despite the advantages owned by FLOVENT, a critical limitation arises when applying FLOVENT for the investigation of pyramidal buildings. The main problem is to generate accurately the shape of the pyramid in the solution domain. In order to build a model, FLOVENT introduces what is called “smart part”, which is defined as a parametrically defined object that is made up of basic building block objects. This “smart part” consists of three building block objects that include cuboidal, prism and cylinder. In order to create a pyramid, the optimal combination consists of cuboidal and prism building blocks. However, the combination of these two still leaves gaps at the edges of the pyramid model as presented in Fig. 6.3. The gaps at the edges of the pyramids should have no significant effects when studying macro-scale and two-dimensional phenomena. However, for micro-scale and three-dimensional phenomena, the influence of these sharp edges are obviously significant since the effect of every single gap is taken into account by the program. Each gap introduces small vortices, which affects the whole vortices that are expected to be found at the side surfaces of the pyramids. In order to minimize the effects of this gap to the overall flow structures around the buildings, the pyramid models should be constructed with a higher resolution. However, the higher resolution affects the number of grids that are generated in the solution domain since each of the individual building blocks creates grids in each direction. When the number of grids exceeds one million, the computation efforts will be enormous or in other words not effective anymore. Therefore, an optimal arrangement between the shape of the pyramid and the number of grids must be found by conducting several preliminary investigations.





(a) Mean longitudinal velocity profiles ( $u/u_{ref}$ )      (b) Turbulent Kinetic Energy TKE

Fig. 6.2. Comparison of experimental and numerical simulation of the atmospheric boundary layer flow in the wind tunnel,

In the present numerical study, five different pyramids were investigated, namely pyramid P45n, P50n, P55n, P60n and P70n (n denotes for numeric). Similar to the experimental studies, each pyramid has the same base area which is  $l = 20 \text{ m} \times 20 \text{ m}$ , and the height varies depending on the base angle.

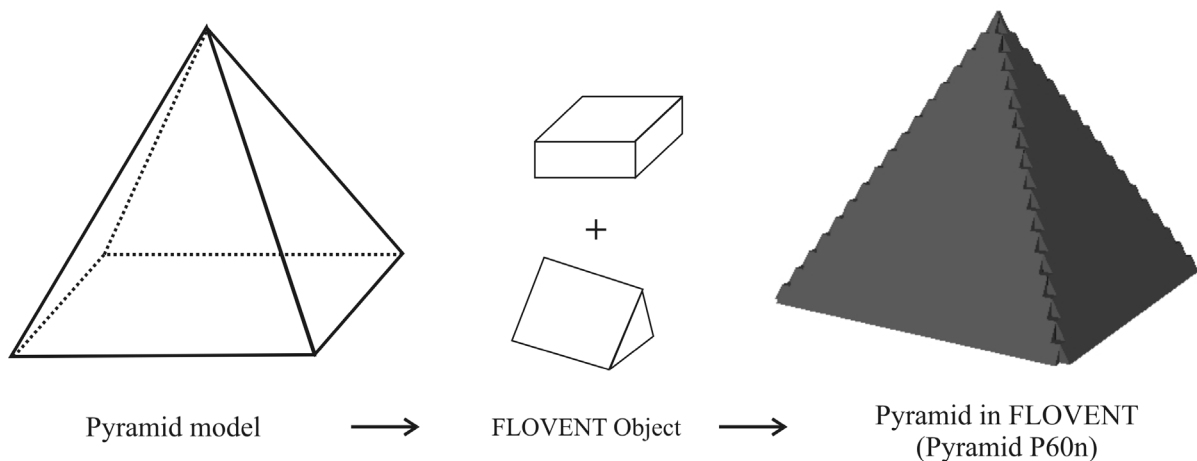


Fig. 6.3. Representation of the pyramid geometry in the numerical model

### 6.3. Numerical Results

Based on the limitation described in the previous section, the same results between experimental and numerical investigations cannot be expected in any case. However, qualitative comparison is still possible, especially at the plane  $y/l = 0$  where the effect from the gaps of the pyramid edges is relatively smaller as compared to the other planes. In this section, selected results from the various numerical investigation attempts are presented. The results are compared with the experimental results and the differences are discussed.

Before comparing the numerical results with the experimental results, several typical visual results obtained from the numerical program are presented. Fig. 6.4 presents flow structures in the cavity at the lee of the pyramid P60n. Quantitatively, the flow structures in the lee of the pyramid from the numerical investigations are similar to the visual observations presented in Fig. 5.1. The flow structures in the lee of the pyramid is characterized by two vorticity concentrations and a rotor vortex at the centre of the pyramids. At the side of the pyramid, the vertical vortex system which is found in the experiment does not occur in the numerical results. At the windward side of the pyramid, for the case of pyramid P60n, no recirculation zone is detected and small recirculation zone is found when the base angle increases to pyramid P70n. However, this area is much smaller than the results obtained in the experiment. This will be shown more clearly in the next section.

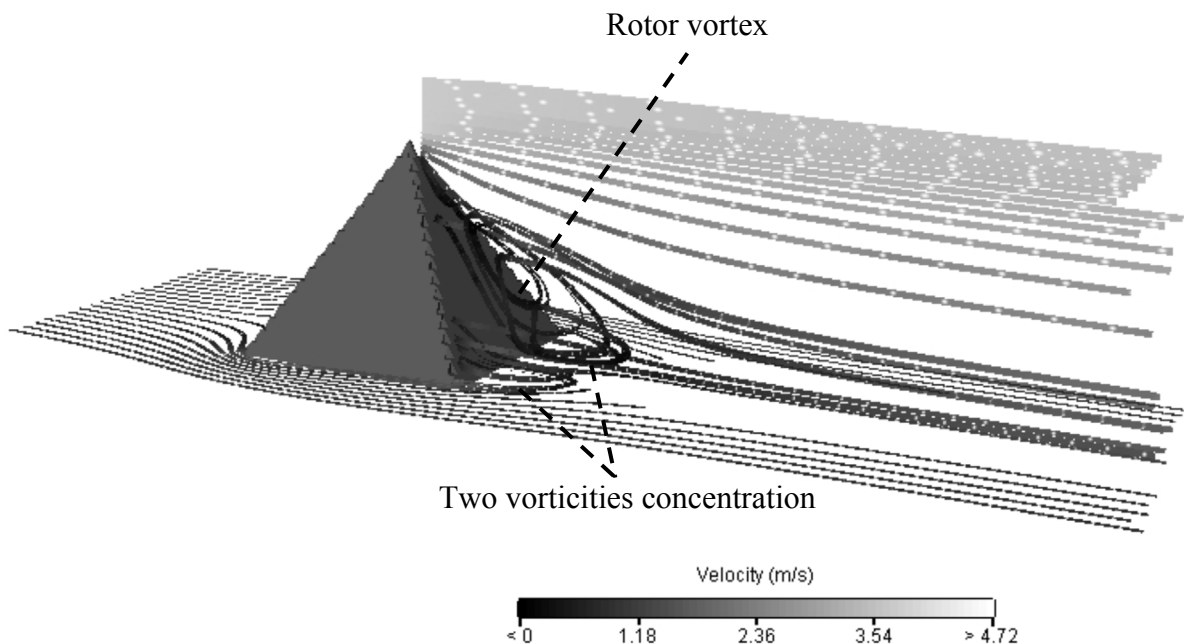


Fig. 6.4. Visualization of flow structure in the lee of the pyramid P60, from FLOVENT visualization program

Fig. 6.5 shows the vector plots at  $y/l = 0$  for pyramid P70n. The overall wake structure of the pyramid is similar to the experimental result, as shown in Fig. 5.5. However, high velocities are detected at the tip of the pyramid which is not found in the experimental results. This is likely

caused by the small gaps at the pyramid edges which create flow structures similar to the thin wall flow structure where high velocities are detected on the top of the wall.

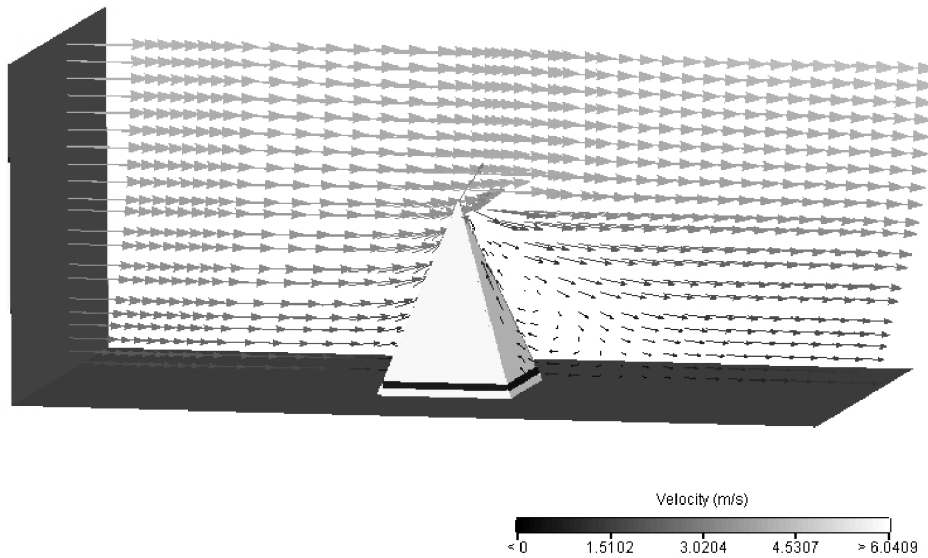


Fig. 6.5. Vector plots at  $y/l = 0$  for pyramid P70n, from FLOVENT visualization program

Fig. 6.6 shows the vector field of the longitudinal velocity near the ground. The grey colour scale shows the scale of the longitudinal velocities which are normalized with the velocity at the boundary ( $u_0 = 5$  m/s). The negative value shows that the velocities move in the opposite direction from the main stream (showed by the vectors). The figure is able to reveal the recirculation zones in the windward and leeward side of the pyramid, which is indicated by the dark coloured area. In the lee of the pyramid, the figure is also able to show the two vorticity concentrations.

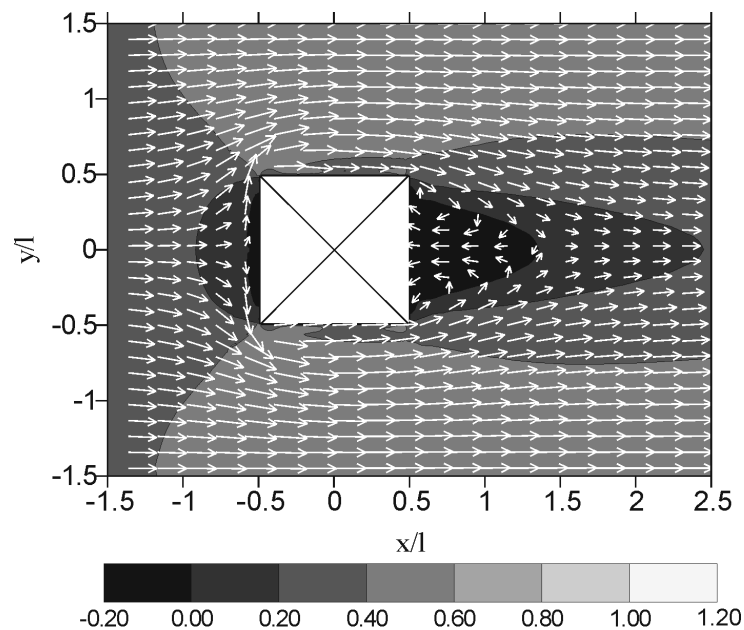


Fig. 6.6. Vector velocity field at the near bottom of pyramid P70n ( $u/u_0$ )

The recirculation zone in the lee of the pyramid from the numerical results can be seen in three-dimensional form in Fig. 6.7. The figure shows the cavity zone, which is created in the lee of the pyramid. The reattachment length at the centre of the pyramid is  $x/l = 1.37$ .

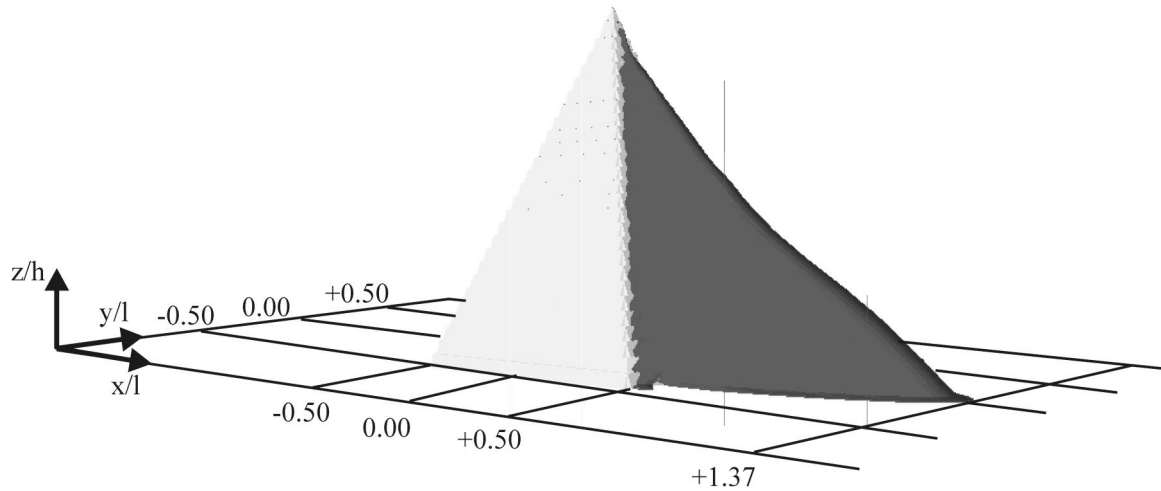
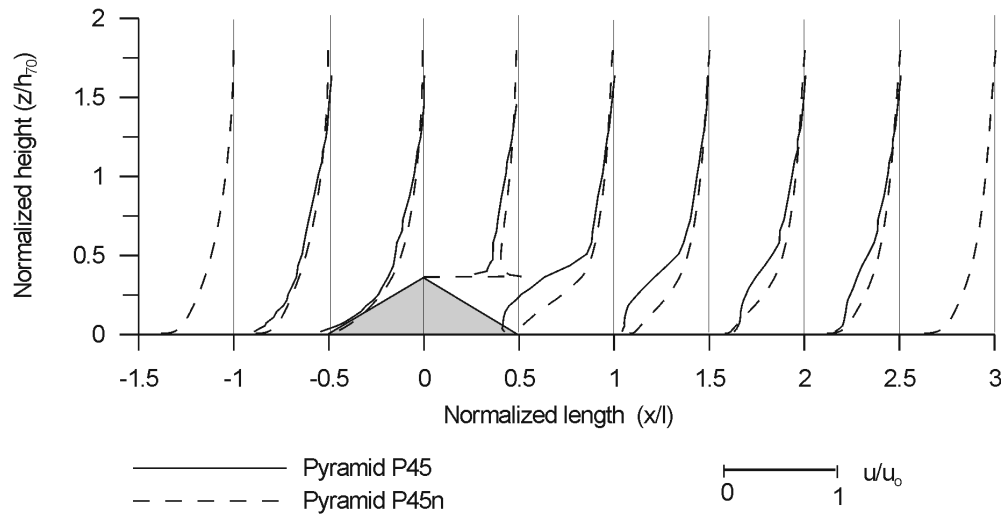
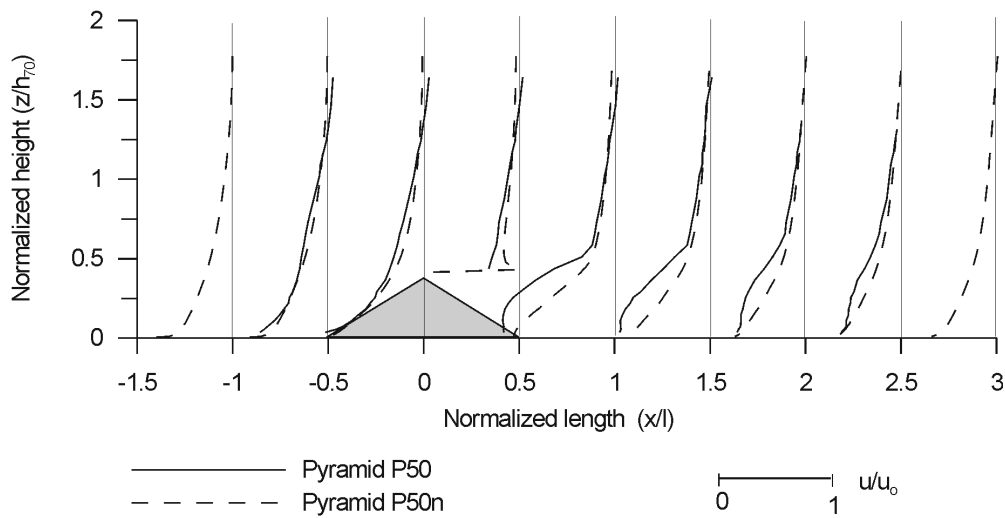
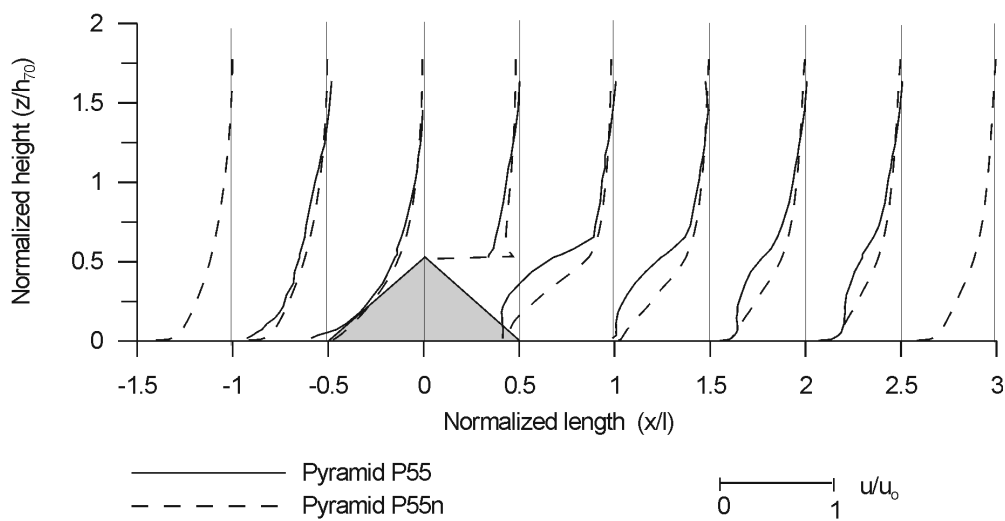


Fig. 6.7. Cavity at the lee of the pyramid P70n, depicted from FLOVENT visualization program

### 6.3.1. Mean Velocity Profiles

In Section 5.1.1, the longitudinal velocity profiles at selected locations ( $x/l$ ) from the experiments were presented. In this section, the numerical results at the same locations are presented and compared with the experimental results. Fig. 6.8 shows a comparison of the longitudinal velocity profiles at the centre plane ( $y/l = 0$ ) of the pyramids. The velocities are normalized by the free stream velocity  $u_0 = 5$  m/s. The  $x$ -axes are normalized by the pyramid lengths and the heights are normalized by the height of pyramid P70 ( $h_{70} = 274.75$  mm). Fig. 6.8 (a) shows the profiles for pyramid P45n. In general, the profiles at the upstream of the pyramid show very good agreement with the experimental results. However, at  $x/l = -0.5$ , the experimental result shows negative velocities at the near bottom which is not identified by the numerical result. Larger differences are detected in the lee of the pyramid. Especially, at a distance of  $x/l = 0.5$ . At this distance, the velocity profile of experimental result shows a point of inflection, where negative velocities are clearly identified. On the other hand, the numerical results show different results. In Fig. 6.8, the negative velocities at the lee of pyramid P45n is not clearly visualized because it is extremely low near the bottom. For higher pyramids, negative velocities are eventually visualized by the numerical calculations as shown in Fig. 6.8 (b) until (e). However, the profiles still show discrepancies between the experimental and numerical results. These large discrepancies are found in almost all results for different pyramids.

(a) Base angle  $45^\circ$ (b) Base angle  $50^\circ$ (c) Base angle  $55^\circ$ Fig. 6.8. Longitudinal mean velocity profiles at  $y/l=0$

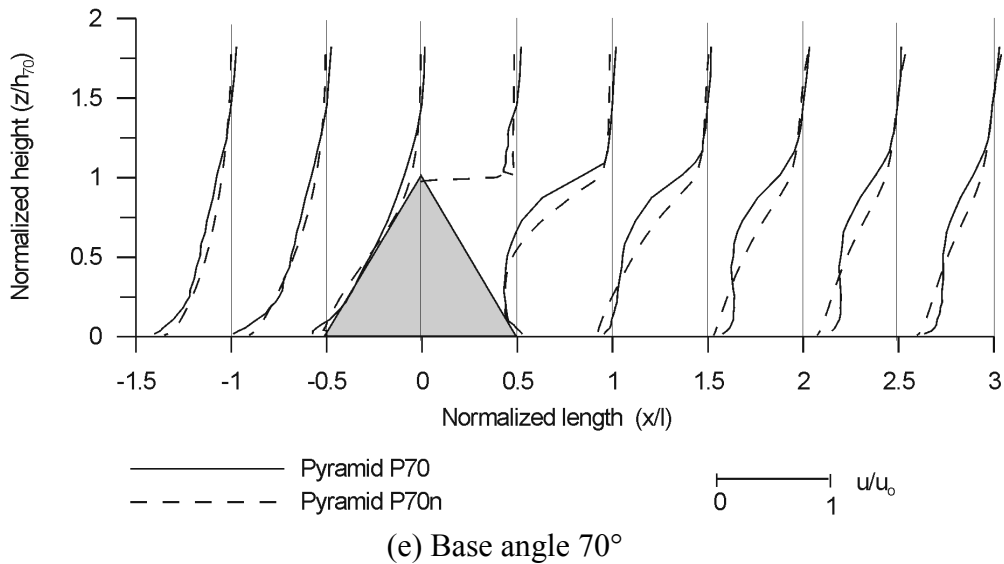
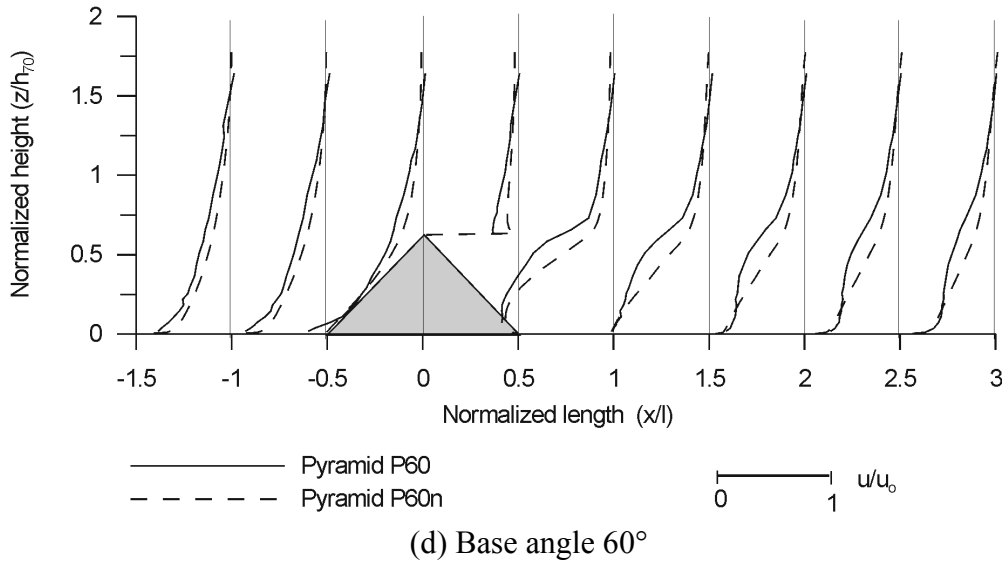


Fig. 6.8. Longitudinal mean velocity profiles at  $y/l=0$

Fig. 6.9 shows a comparison of the longitudinal velocity profiles between the experimental and numerical results at plane  $y/l = 0.25$ . For the pyramid with an base angle of  $\theta = 45^\circ$  (Fig. 6.9.(a)), the discrepancy between the experimental measurements and the numerical computations is not significant. When the base angle increases to  $50^\circ$ (Fig. 6.9.(b)), the experimental and numerical results show some discrepancies. In the windward side of the pyramid, a small recirculation zone is detected by the experimental results but not by the numerical results. The same is also observed in the lee of the pyramid, especially at  $x/l = 0.5$ . The shear stresses obtained from the numerical computations are not as large as the ones obtained from the experimental measurements. The differences becomes significant especially when the area of recirculation zones are calculated (see Chapter 6.3.2). When the flow goes further downstream, the numerical results show that the incoming flow profile is already generated at  $x/l = 1$ . This indicates that besides smaller recirculation zone, the numerical results also deliver smaller wakes. Similar obser-

variations are found for the pyramids with  $\theta = 55^\circ$  and  $60^\circ$ . As described in Chapter 5, the experimental results are likely to detect secondary recirculation zones in the lee of the pyramid as the base angle increases to  $70^\circ$ . In contrast, these structures are not detected in the numerical results. In general, the recirculation zones obtained from the numerical results are always smaller than those obtained from the experimental results.

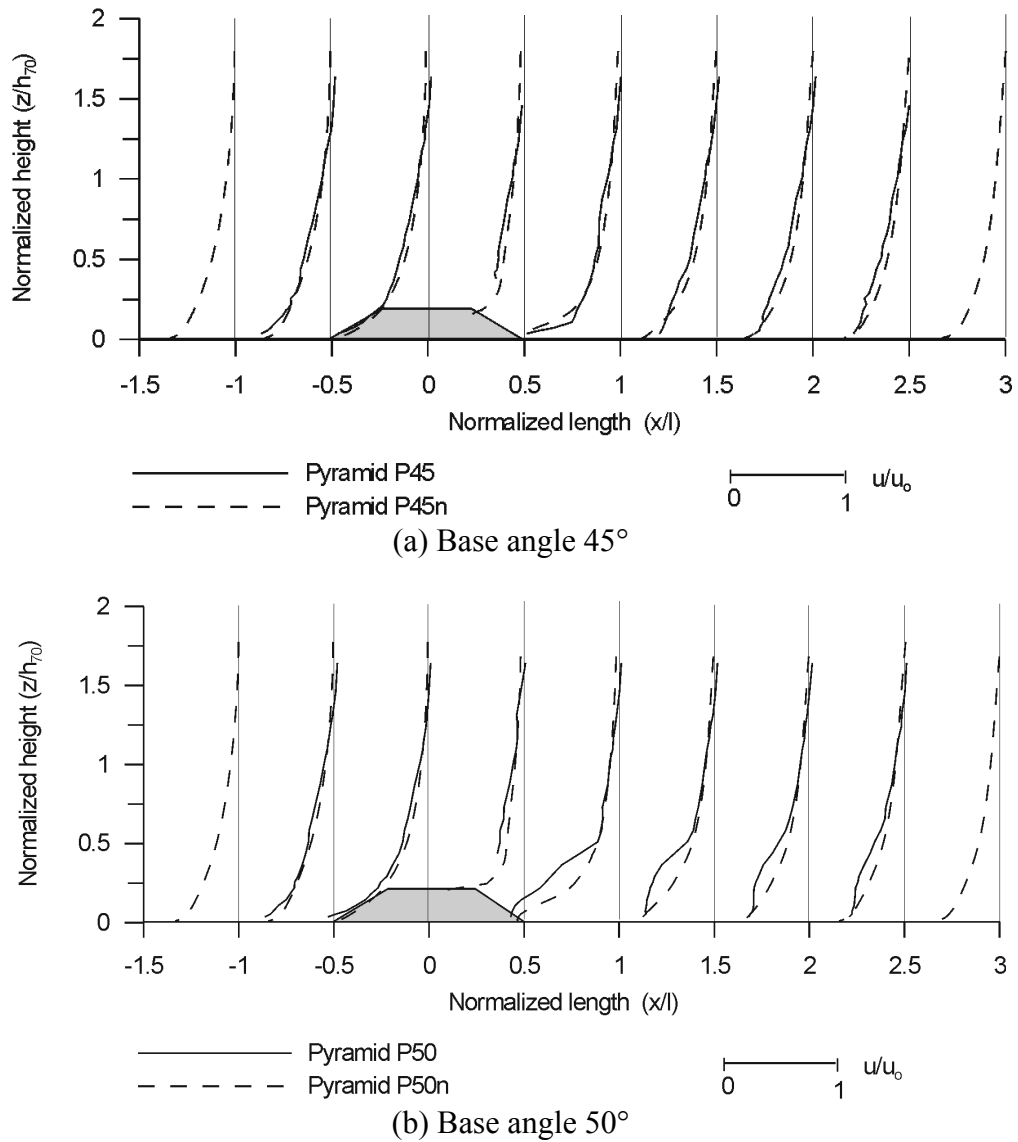
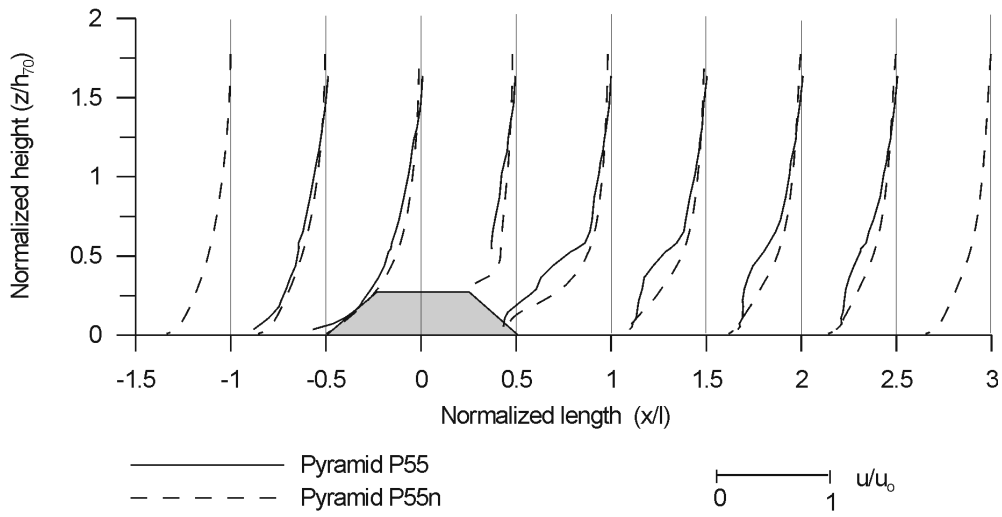
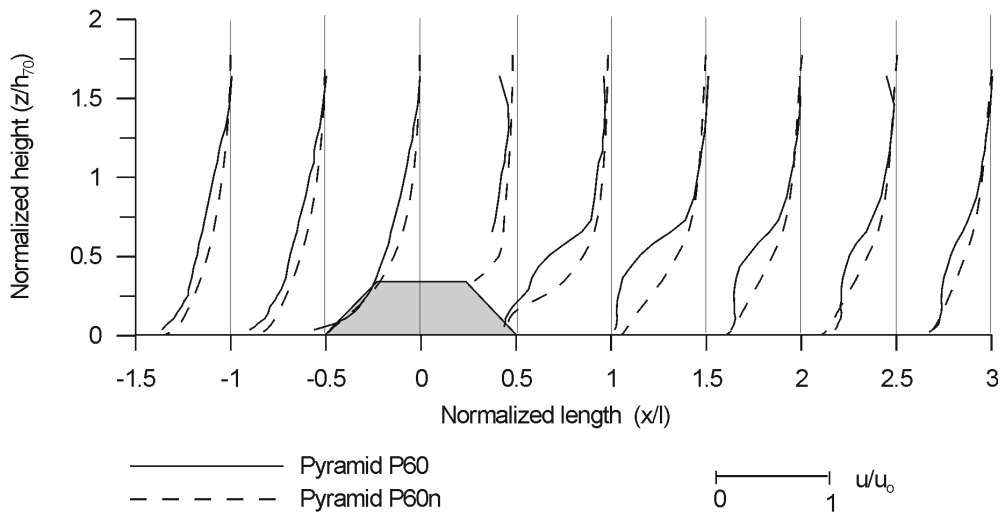


Fig 6.9. Longitudinal mean velocity profiles at  $y/l=0.25$

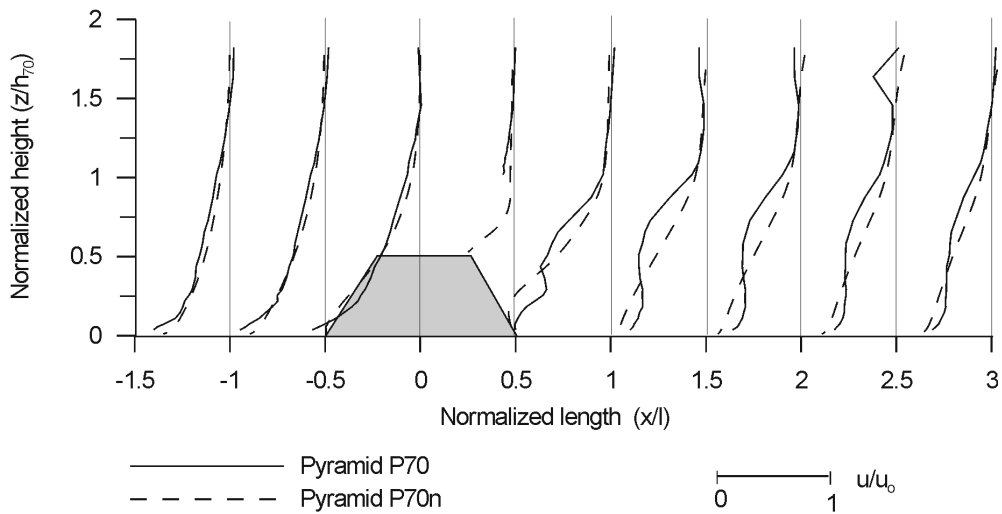
6. Additional Numerical Investigations



(c) Base angle  $55^\circ$



(d) Base angle  $60^\circ$



(e) Base angle  $70^\circ$

Fig. 6.9. Longitudinal mean velocity profiles at  $y/l=0.25$



Fig. 6.10 shows the longitudinal mean velocity profiles at  $y/l=0.50$  obtained from the numerical simulations and the experimental measurements. In general, the numerical and experimental velocity profiles at this plane are in good agreement, except for pyramid P70n (Fig. 6.10 (c)). The velocities in the lower region at  $x/l = 0.5$  and  $x/l = 1.0$  for the numerical profiles are slower than the experimental profiles. Again, it is likely that the small gaps at the edges of the numerical pyramids significantly affect the velocity by inhibiting the incoming flow profiles to be created.

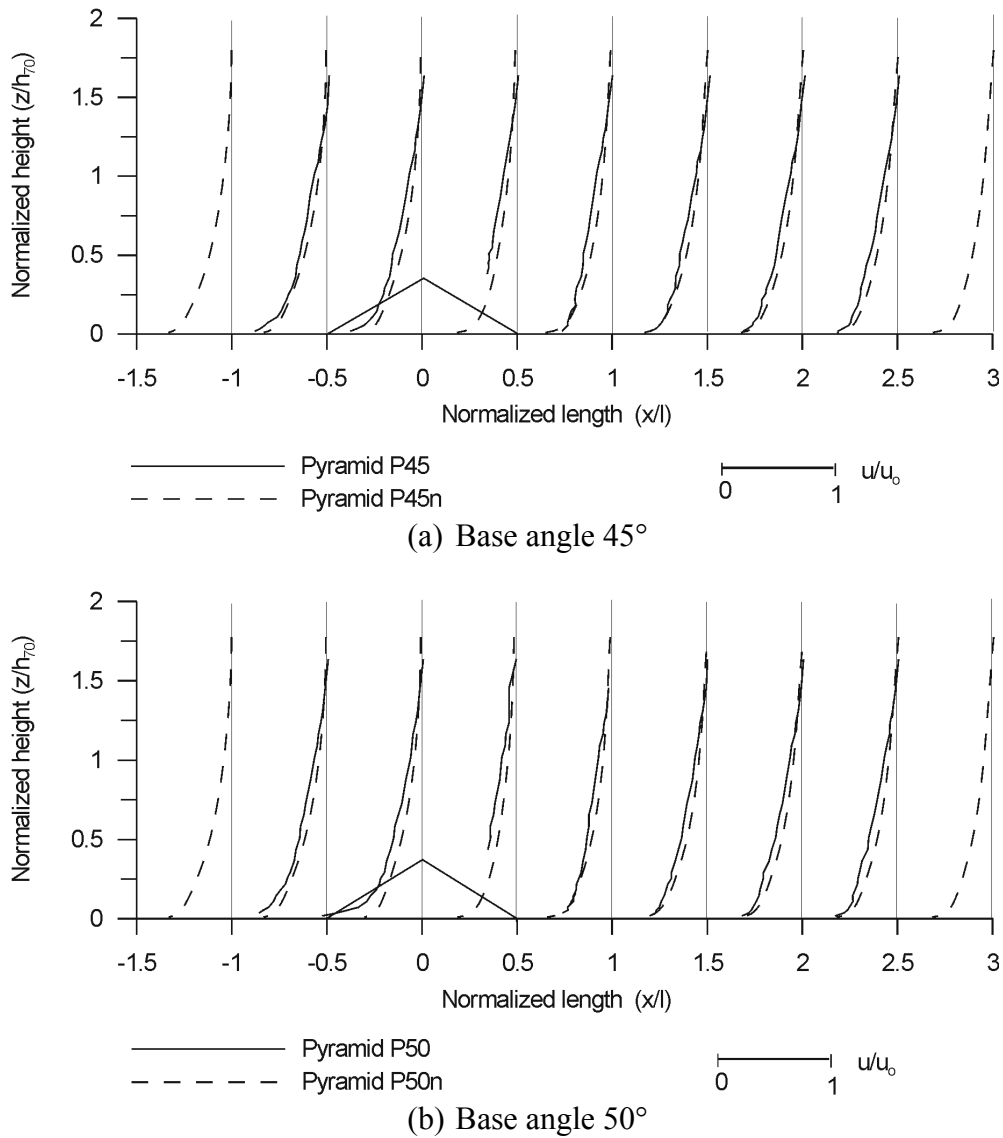
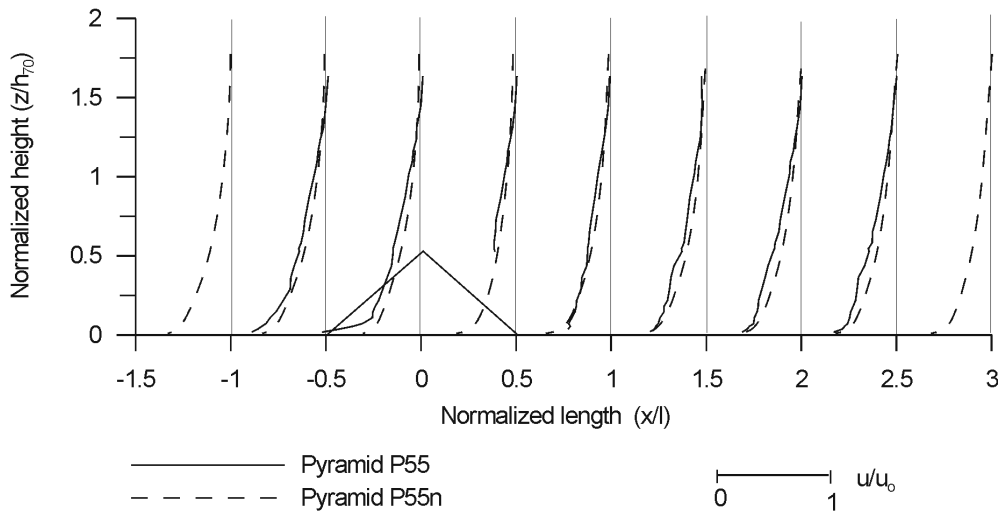
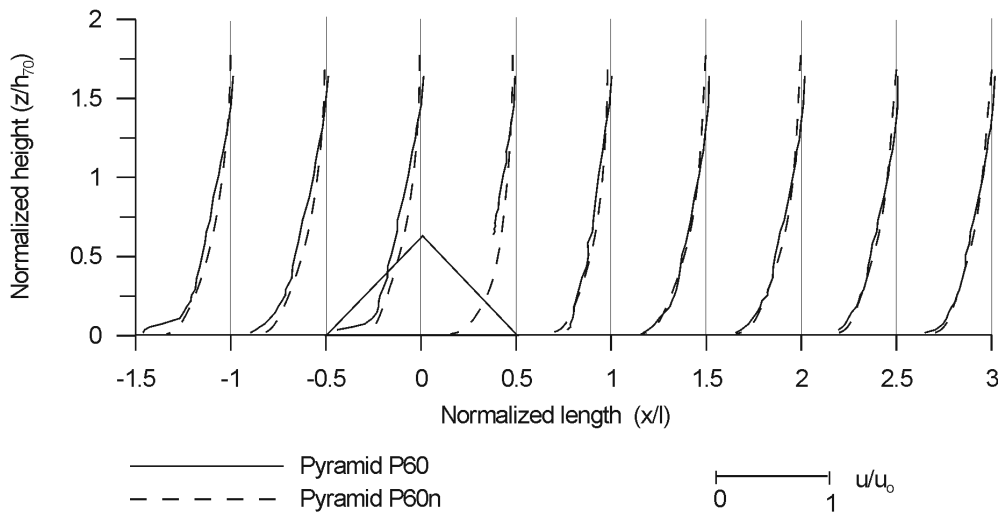


Fig. 6.10. Longitudinal mean velocity profiles at  $y/l=0.50$ .

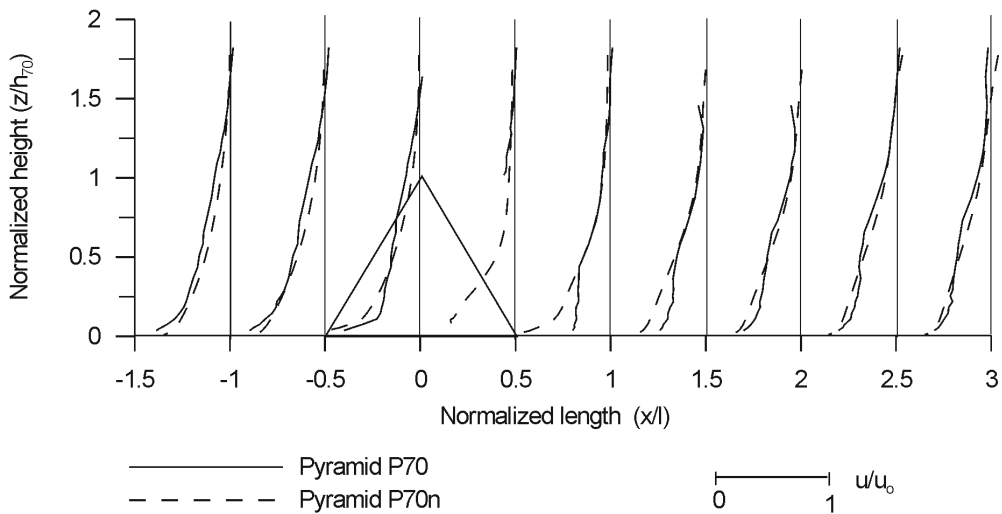
6. Additional Numerical Investigations



(c) Base angle  $55^\circ$



(d) Base angle  $60^\circ$



(e) Base angle  $70^\circ$

Fig. 6.10. Longitudinal mean velocity profiles at  $y/l=0.50$ .

### 6.3.2. Velocity Fields

The next parameter to be compared is the vector fields of the velocities, which is a combination of the longitudinal and vertical velocities. If present, the vector fields should be able to visualize or reveal the recirculation zones in the windward and leeward side of the pyramids. The vector fields obtained from the experimental measurements can be seen in Section 5.1.2. Fig. 6.11 shows the vector fields obtained from the numerical results for different pyramids at  $y/l = 0$ , which can be compared to the experimental results (see Fig. 5.5). The vector fields in Fig. 6.11 indicate that the recirculation zone in the windward side of the pyramids are only detected for pyramid P70n. On the other hand, the experimental results show that small recirculation zones are already detected from pyramid P45 and the area of the recirculation zones increase with an increase of the base angles. In the lee of the pyramids, the recirculation zones can be observed from pyramid P55n and increase when the base angle increases, whereas the experimental results show that the shallowest pyramid (i.e. pyramid P30) already induces a recirculation zone.

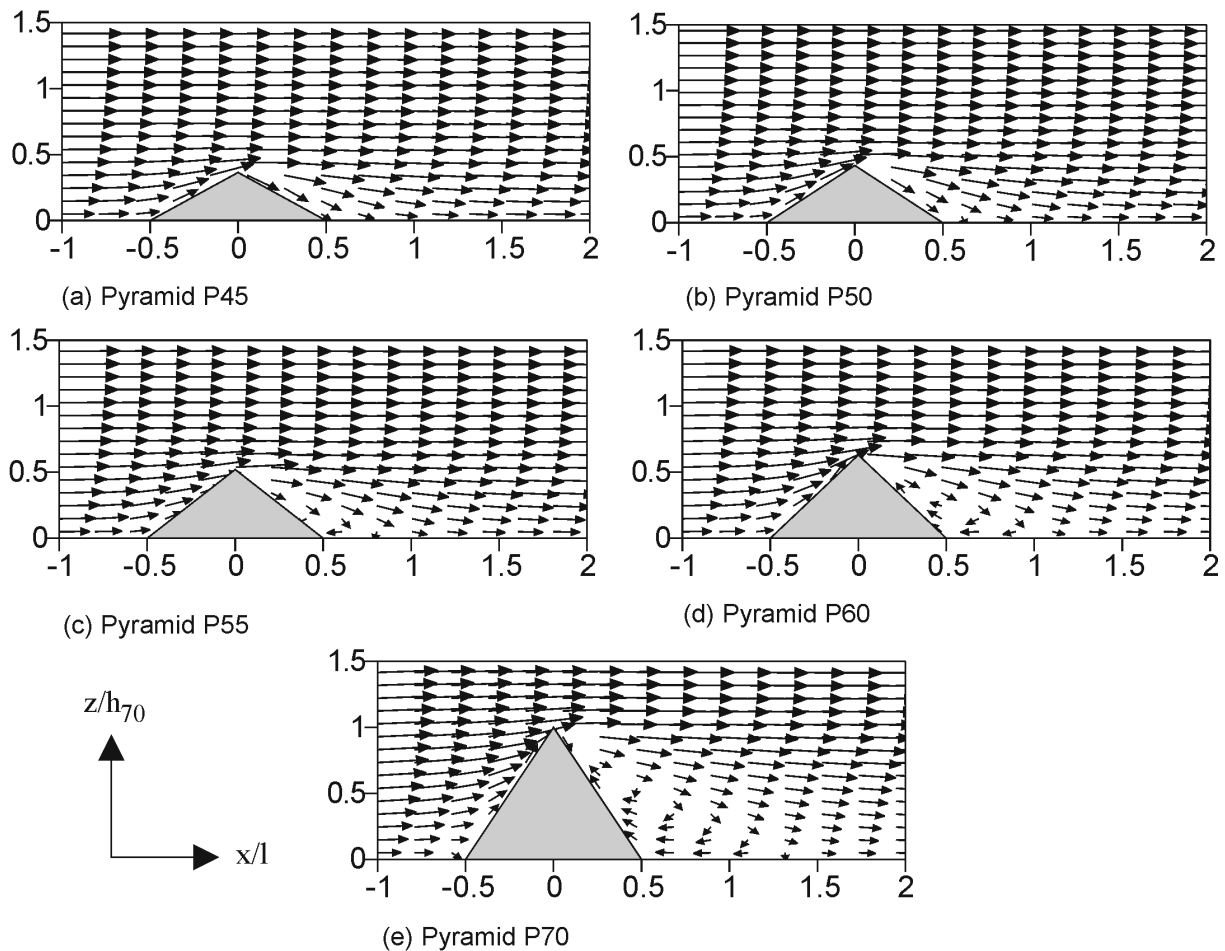


Fig. 6.11. Vector velocity fields at the  $y/l = 0$  for different pyramids

6. Additional Numerical Investigations

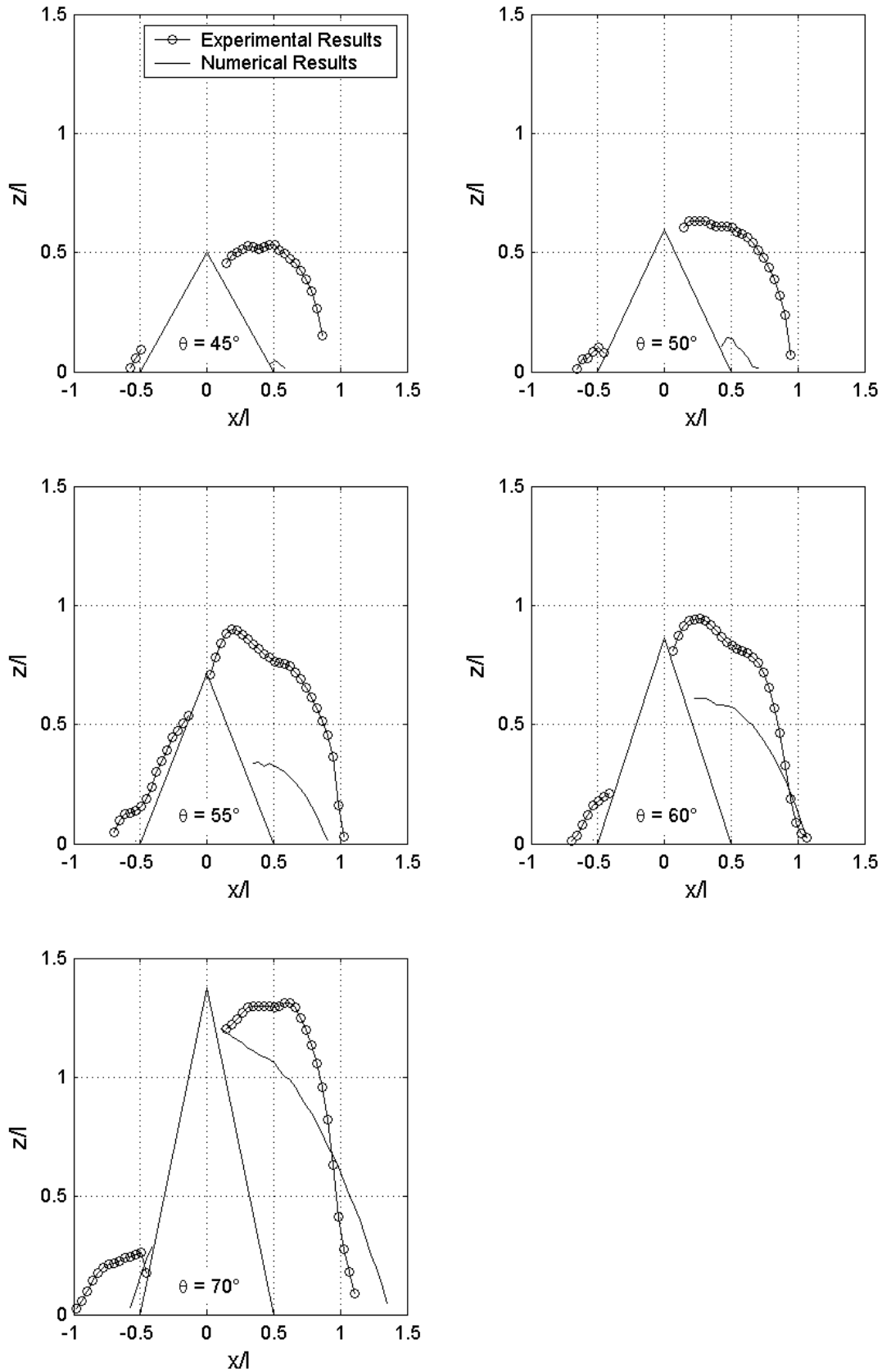


Fig. 6.12. Comparison of recirculation zone between numerical and experimental results, in the windward and leeward side of the pyramid

Quantitatively, the recirculation zone in the windward and leeward side of the pyramid at  $y/l = 0$  is presented in Fig. 6.12. As already described in Chapter 5, the recirculation zone is characterized by the zero streamline (see Eq. 5.1). In Fig. 6.12, the experimental results are also incorporated for comparison. It is clear that the recirculation zone for the numerical results in the windward side of the pyramids only occur for pyramid P70n. On the other hand, a small recirculation zone is already detected for pyramid P45n in the leeward side of the pyramid. Both the experimental and numerical results show that when the base angle and height increase, the recirculation zone also increases. However, the recirculation zone from the numerical results are much smaller than that from the experimental results. The calculated area of the recirculation zones can be seen in Fig. 6.13. The figure shows that despite the area differences, qualitatively both results give similar trends.

In Section 6.2, the boundary conditions of the numerical simulations have been described. It has been shown that the initial conditions between the numerical and experimental wind tunnel are simulated as similar as possible. Therefore, the most possible explanation of the different results here is the representation of the pyramid. Thus, it is important to make the gap at the pyramid edges as small as possible in order to improve the accuracy of the numerical simulations. However, smaller gaps will increase the number of grids of the solution domain and hence require more time for the solution to converge.

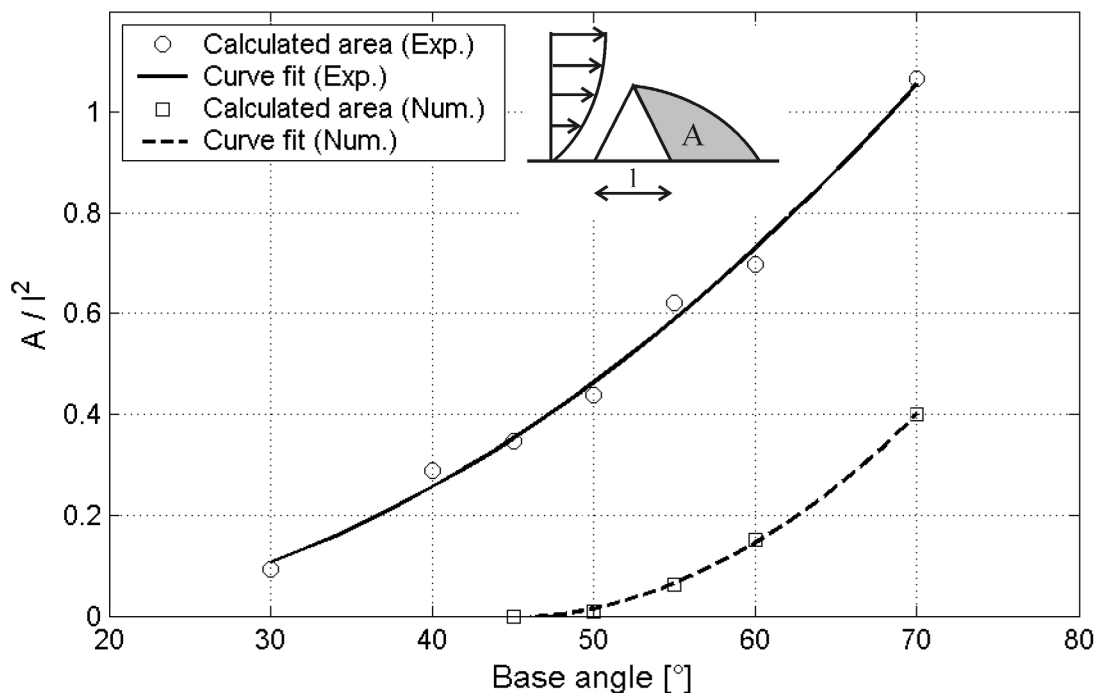


Fig. 6.13. Comparison of the recirculation zone area at  $y/l = 0$  for numerical and experimental results.

### 6.3.3. Reattachment Lengths

As already described in Section 5.1.3., the recirculation zone is characterized by the reattachment length in the lee of the pyramid, which is regarded as the most important parameter characterizing separated and reattaching flows [Eaton et al., 1981]. The reattachment length  $x_r$  is measured from the leeward side surface of the pyramid (at bottom position) to the point where the zero streamline reaches the ground.

Fig. 6.14 shows the reattachment lengths normalised with the pyramid height obtained from the numerical calculations. The experimental results are also incorporated in the figure for comparison. Quantitatively, large discrepancies are observed between the experimental and numerical results. At  $y/l = 0.0$ , the reattachment length for pyramid P45n (n indicates numerical results) is much shorter in comparison to pyramid P45. When the base angle increases, the experimental results show that the reattachment lengths are decreasing. On the other hand, the numerical results show that when the base angle increases, the reattachment length significantly increases. As the base angle reaches  $60^\circ$ , the reattachment length of numerical pyramids are longer than the experimental results. When the plane of observation is moved to the middle ( $y/l = 0.25$ ), the numerical results show similar trend as the centre plane. Pyramid P45n has the shortest reattachment length and it increases significantly as the base angle increases. Then, the reattachment length decreases as the base angle increases from  $55^\circ$  to  $70^\circ$ .

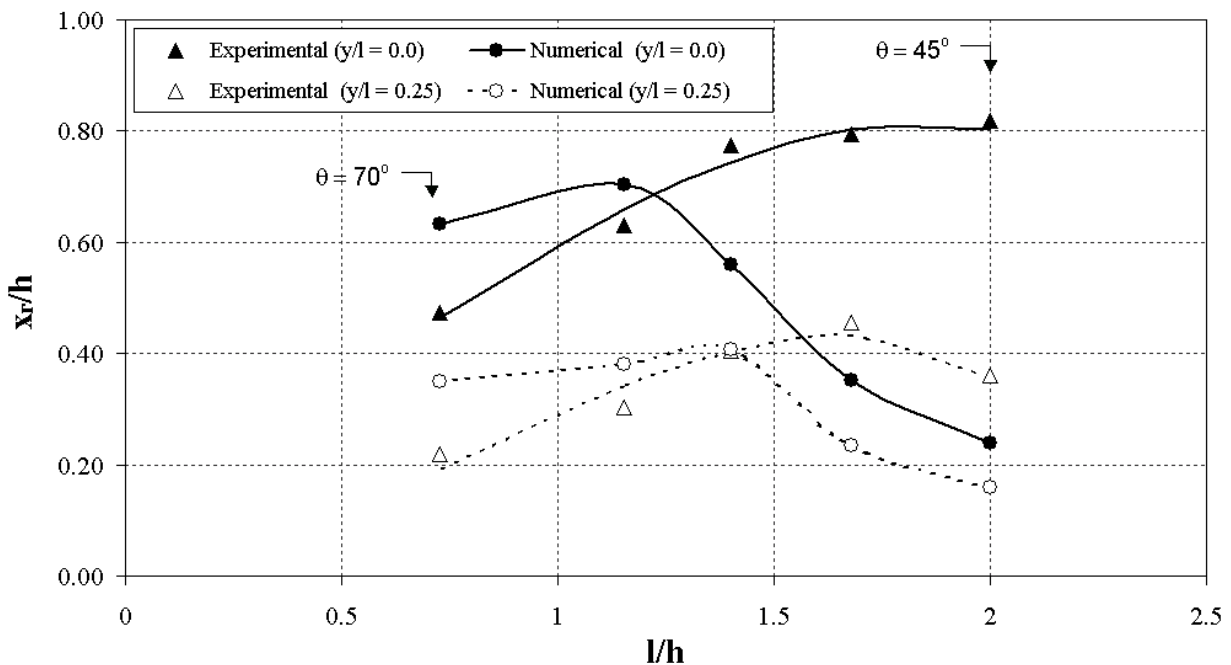


Fig. 6.14 Comparison of experimental and numerical results for the reattachment length ( $x_r/h$ ) at the lee of the pyramids as a function of the pyramid length and height ratio.

As stated at the beginning of this chapter, the initial objective of the numerical study was to simulate the experimental investigations with further variations of the influencing parameters. Unfortunately, at this stage of study, quantitative comparison between the numerical and experimental results could not be performed yet. The results in

Fig. 6.14 shows that the simplification of the pyramid geometry in the numerical investigation affects significantly the computational results and these effects are not negligible. Therefore, before conducting numerical investigations with further variation of pyramids, it is necessary to overcome the limitation of the software in generating the perfect shape of a pyramid (i.e. to build sharp edges pyramids without gaps in the solution domain).

## 7. Conclusions

The objective of this study was to investigate the flow and pressure characteristics around pyramidal structures or buildings in order to gain an improved and detailed understanding of the aerodynamics involved. Currently, the technical layout with respect to wind load assumption of pyramidal buildings is usually not listed in standard tables. Therefore, the specific objective of this study is to provide the typical values of pressure and aerodynamic coefficients specifically for pyramidal buildings. For practical purposes, this study is meant to fill the gap of standard tables for wind load design of pyramids.

In order to achieve the objective of this study, the flow characteristics around pyramidal buildings and the pressure distributions on the pyramid surfaces were investigated through detailed and accurate laboratory experiments. The experiments were conducted in the atmospheric boundary layer wind tunnel of the Laboratory of Building- and Environmental Aerodynamics, Institute for Hydromechanics, at the University of Karlsruhe.

The flow measurements were performed using a 2-D Laser Doppler anemometry (LDA). Seven different pyramids having the same base length with varying base angles ( $\theta = 30^\circ, 40^\circ, 45^\circ, 50^\circ, 55^\circ, 60^\circ, 70^\circ$ ) were investigated. The incoming flow in the wind tunnel was simulated with a wind direction of  $\alpha' = 0^\circ$  (normal to the windward surface) and a free stream velocity,  $u_0 = 5$  m/s corresponding to Reynolds numbers (Re) ranging from 12.000 to 90.000 depending on the pyramid heights (h). The incoming flow can be categorized as a flow between suburban and city center areas (Wind Technology Association, *Windtechnologische Gesellschaft, WTG* and EUROCODE 1). The results for the flow characteristics investigation around pyramids can be summarized as follows:

- The flow around a pyramid gives rise to a discrete horseshoe vortex system which is not so uniform as the system of e.g. cuboidal bluff body. When the wind blows from a direction of  $0^\circ$ , the wall taper induces a vortex system consisting of two conical vortices rotating near the outer edges of the leeward side and a rotor vortex in the vertical middle plane.
- Two separation lines are identified near the bottom at the side surface and at the lee of the pyramid which is suggested to come from the resulting horseshoe vortex that occurs at the upstream side and extends to the sides of the pyramid.



- It was found that for flows around a pyramid the length of the recirculation zone in the lee of the pyramids are much shorter and smaller as compared to cuboidal buildings. A set of equations to calculate the reattachment length and area of recirculation zone at the lee of pyramids as a function of pyramid base angle were delivered. To illustrate the recirculation zone at the lee of a pyramid, an equation to estimate the zero streamline as a function of reattachment length were proposed.
- Another important characteristic was the turbulent kinetic energy. At the lee side of the pyramids, the isolines of the turbulent kinetic energy show high gradients of turbulent kinetic energy perpendicular to the surface. This fact is considered important since it might be one explanation, why the wake regions of pyramids, especially in the desert, do not fill up with flow-suspended material.

The pressure measurements were carried out using a standard pressure tapping technique. The incoming flow was simulated with a velocity of 12 m/s in order to obtain measurable and reliable pressure differences. Seven pyramids having a constant base length ( $l = 200$  mm) with varying base angles and two pyramids having a constant base angle ( $\theta = 70^\circ$ ) with varying heights ( $h = 142.81$  mm and 100 mm) were investigated. Four different wind directions ( $\alpha' = 0^\circ, 15^\circ, 30^\circ$  and  $45^\circ$ ) were measured. Due to the symmetrical geometry of the pyramid, the pressure distribution on the pyramid surfaces for further wind directions ( $\alpha' > 45^\circ$  with  $15^\circ$  step) could be generated. The investigation of pressure coefficient ( $c_p$ ) in the pyramid surfaces can be concluded as follows:

- All investigated parameters (base angle, wind direction and Jensen-number) affect the magnitude of pressure, suction and fluctuation in the pyramid surfaces. Besides the magnitude, the pressure distribution pattern (the location of the local maximum and minimum pressure including the maximum suction) is also affected by these parameters (see qualitative summary in Table 5.2).
- Generally, the maximum pressure was found to increase as the base angle of the pyramid increases. An exception was observed for base angle ranging between  $40^\circ$  to  $60^\circ$ , where the maximum pressure remains relatively constant. The maximum local suction occurs for pyramids with base angle in the range of  $50^\circ$  to  $55^\circ$ . Suction occurs mainly in areas with high turbulence intensities. The maximum fluctuations on the side surfaces were found to increase as the base angle increases.

## 7. Conclusions

- At the front surface, it was found that the maximum of local pressure occurs when the wind blows from  $0^\circ$  ( $\alpha' = 0^\circ$ ) and decreases to a minimum at  $\alpha' = 45^\circ$ . The maximum suction occurs in the side surface when the wind blows from  $15^\circ$  direction. The maximum pressure fluctuations occur on the pyramid side surface when the wind blows in a range of  $\alpha' = 0^\circ$  to  $15^\circ$ .
- An increase of the pyramid height (Jensen-number) increases slightly the pressure in the pyramid surfaces. However, the distribution patterns (i.e. location of maximum local pressure and suction) are not much affected by the Jensen-number.

Furthermore, from an integration of the local measured pressure values, results of wind-induced forces could be deduced. The forces were presented in the form of aerodynamics coefficients, namely the drag coefficient ( $c_d$ ), lift coefficient ( $c_l$ ) and moment coefficient working at z-axes (cm-z). The investigations of aerodynamic coefficients for a pyramidal structure can be summarized as follow:

- The incoming wind directions have the most influence on the drag coefficient. The drag coefficient of pyramids exposed to tilted, non-frontal wind directions ( $\alpha' = 15^\circ$ ) can amount to 4 times the  $c_d$ -value of the frontal wind direction ( $\alpha' = 0^\circ$ ). For shallow pyramids, the variation of base angle also affects more the magnitude of drag coefficient as compared to steep pyramids. The maximum drag coefficient for a pyramidal building was found for pyramid with base angle  $40^\circ$  and wind blows from  $15^\circ$  direction.
- The lift coefficient was found to be influenced also by all three parameters (base angle, wind direction, Jensen-number). The results show that an increase of pyramid base angle and height, especially for steep pyramid case inhibits the growth of the lift force. The maximum lift coefficient for a pyramidal building was found for pyramid with base angle  $70^\circ$  with Jensen-number of 40 and wind blows from  $0^\circ$  direction.
- For the moment coefficients, the most important result was the detection of a reversal moment direction for different pyramids. The results indicate that the parameters controlling the direction of the moment are the base angle and the wind direction. The point where the reversal of the moment direction occurs is at  $\theta = 55^\circ$ . The reversal of the moments also takes place with a change of the wind direction for every  $45^\circ$ . This is obviously caused by the symmetrical shape of the pyramid. The maximum moment for a pyramidal building was found for pyramid with base angle  $70^\circ$  with Jensen-number  $Je = 57$  and wind direction  $15^\circ$ .

The specific objective of this study was to provide the typical values of pressure and aerodynamic coefficients for pyramidal buildings which can be used for structural calculations. The values that are given in this study can be used to fill in the gap of the unavailable design values for pyramidal buildings in standard tables. A summary of the pressure and aerodynamic coefficients for pyramidal buildings was presented in Table 5.3.

Besides the experimental investigations in the laboratory, numerical investigations were also additionally performed in order to prove, whether experimental and numerical studies deliver the same results. The numerical study were performed with the aid of a software package called FLOVENT version 3.2 from Flomerics Ltd., which is a special software for numerical calculations in the area of building- and environmental aerodynamics. The numerical investigation can be concluded as follows:

- Despite some excellent features owned by this program, limitations arise when applying the program to simulate pyramidal buildings. The main limitation of the program is that it failed to generate the perfect shape of a pyramid (see Fig. 6.3). Attempts to minimize this limitation were already performed.
- Qualitatively, the numerical results showed the same tendency or trend with the experimental results. However, quantitatively, the numerical results showed discrepancies with the experimental results. It is obvious that the limitation of the program in generating pyramidal structure was the main reason for the discrepancies.

## References

- Abuomar, M.M., Martinuzzi, R.J., 2000, An Experimental Investigation of the flow around a Surface Mounted Pyramid, 6th Triennial International symposium on Fluid Control, Measurement and Visualization, August 13-17, Sherbrooke, Canada.
- Acarlar, M.S., Smith, C.R., 1987, A Study of Hairpin Vortices in a Laminar Boundary Layer. Part 1. Hairpin Vortices Generated by a Hemisphere Protuberance, *J. Fluid Mech.*, Vol. 175, p. 1-41.
- Akins, R.E., Peterka, J.A., 1997, Mean Force and Moment Coefficients for Buildings in Turbulent Boundary Layer, *Journal of Industrial Aerodynamics*, 2, pp.195-209.
- Albrecht, H.E., Borys, M., Damaschke, N., Tropea, C., 2003, *Laser Doppler and Phase Doppler Measurement Techniques*, Springer – Verlag, Berlin, Germany.
- ASCE, 1987, *Wind Loading and Wind-Induced Structural Response*, ASCE Structural Division, New York.
- ASCE, 1996, *Wind Tunnel Studies of Buildings and Structures*, *Journal of Aerospace Engineering*, January, pp. 19-37.
- Baals, D.D. and Corliss W.R., 1981, *Wind Tunnel of NASA*, NASA History office, Online publication at <http://www.hq.nasa.gov> in november 2004, Washington, D.C.
- Becker, G., 1993, Vermessung des Strömungsfeldes um beheizte Bauwerke mit Hilfe Laser-Doppler Anemometrie, implomarbeit, Institut for Hydromechanics, University of Karlsruhe.
- Cermak, J.E., 1971, Laboratory Simulation of the Atmospheric Boundary Layer, *AIAA Journal*, Vol. 9, No. 9, pp. 1743-1754
- Cermak, J.E., 1975. Application of Fluid Mechanics to Wind Engineering Problems – a Freeman Scholar Lecture, *Journal of fluids Engineering*, ASME, March, pp. 9-38.
- Chyu, M.K., Natarajan, V., 1996, Heat transfer on the base of three-dimensional Protruding Elements, *Int. J. Heat Mass Transfer* 29, pp. 2925 – 2935.
- Cochran, L.S., 2004, Wind effects on Lowrise Buildings, Proceedings of the Conference to Honor Professor Prem Krishna, Indian Society for Wind Engineering, Nagpur, India, February.
- Cook, N., 1985, *The Designer's Guide to Wind Loading of Building Structures*, Part 1. Building Research Establishment Report, London, Butterworths.
- Cook, N.J., 1990, *The Designer's Guide to Wind Loading of Building Structures*, Part 2: Static Structures, Building Research Establishment Report, London, Butterworths.

- Counihan, J., 1969, An Improved Method of Simulation an Atmospheric Boundary Layer in a Wind Tunnel, Atmospheric Environment Pergamon Press, Vol. 3, pp. 197-214.
- Counihan, J., 1975, Adiabatic Atmospheric Boundary Layers: A Review and Analysis of Data from the Period 1880-1972, Atmospheric Environment 9, pp. 871-905.
- Davenport, A.G., Isyumov, N., 1967, The Application of the Boundary Layer Wind Tunnel to the Prediction of Wind Loading, Proceedings Wind Effects on Buildings and Structures, Ottawa, Canada.
- Donohoe S.R., Bannink W.J., 1997, Surface Reflection Visualizations of Shock-Wave/Vortex Interactions Above a Delta Wing, AIAA J. 35, pp. 1569 – 1573
- Drain, L.E., 1980, The Laser Doppler Technique, Wiley-Interscience Publication, John Wiley & Sons, Chichester.
- Durst, F., Melling, A., Whitelaw, J.H., 1981, Principles and Practice of Laser-Doppler Anemometry, Academic Press, New-York, USA.
- Eaton, J.K, Johnston, J.P., 1981, A Review of Research on Subsonic Turbulent Flow Reattachment, AIAA J., 19, pp. 1093-1100
- Ekman, V.W., 1905, On the influence of the Earth's Rotation on Ocean Currents, Arkiv för matematik, astronomi och fysik, 2(11), pp. 1-53.
- Elliasson, B., Dänliker, R., 1974, A theoretical Analysis of Laser Doppler Flowmeters, Optica Acta., Vol. 21, No. 2, pp. 119-149.
- Elsäßer, B., 1999, *Windkanaluntersuchung zur Wechselwirkung zwieschen Sockelwällen und Windschutzflanzungen in einer bodennahen atmosphärischen Grenzschicht, Diplom-arbeit*, Institut for Hydromechanics, University of Karlsruhe.
- Ermshaus, R., Naudascher, E., 1997. *Der Niedergeschwindigkeitwindkanal des Institut für Hydromechanik, Universität Karlsruhe*, Internal Report Nr. 548, 1977
- EUROCODE 1: Basis of Design and Actions on Structure, 1991, Part 2.4: Wind Actions,.
- Farmer, W.M., 1972, Measurement of Particles Size, Number Density and Velocity using a Laser Interferometer, Journal of Applied Optics, Vol. 1, pp. 2603-2609
- Ferziger, J.H., Peric, M., 1999, Computational fo Fluid Dynamics, Springer-Verlag Berlin Heidelberg New York..
- Flomerics Ltd., 2000, Guide to defining the Mathematical Model, Document Number: FLOVENT/MM/1000/1/0.
- Garrat, J.R., 1994, The Atmospheric Boundary Layer, Cambrige University Press.
- Heist, D.K., Gouldin, F.C., 1997, Turbulent Flow Normal to Triangular Cylinder. Journal of Fluid Mechanics, vol.331, pp. 107-125.
- Heneka, P. und Ruck, B, 2004, Development of a storm damage risk map of Germany - A review of storm damage functions, Proceedings of the International Conference for Disasters and Society, Karlsruhe.
- Hosker Jr., R.P., 1984, Flow and Diffusion Near Obstacles. Atmospheric Science and Power Production, United States Department of Energy, Randerson, D. (editor), pp. 241-326.
- Houghton, E.L., Carruthers, N.B., 1976, Wind forces on Buildings and Structures: an Introduction, Edward Arnold (publisher) Ltd.

## References

- Hoydysh, W. G., Griffiths, R. A., Ogawa, Y.: 1974, A Scale Model Study of the Dispersion of Pollution in Street Canyons, 67th Annual Meeting of the Air Pollution
- Hunt, J.C.R., 1972, A Theory of Turbulent Flows Round Two-Dimensional Bodies, *J. Fluid Mech.*, (61), part 4, pp. 625-706.
- Hunt, J.C.R., Abell, C.J., Peterka, J.A., Woo, H., 1978, Kinematical Studies of the Flow around Free a Surface-Mounted Obstacles; Applying Topology to Flow Visualization, *J. Fluid Mech.*, Vol. 86, part 1, p. 179-200.
- Ikhwan, M., Ruck, B., 2002, Investigation of Flow and Pressure Characteristic Around Pyramidal Shape Buildings, 10. GALA-Tagung, Lasermethoden in Der Strömungstechnik, , B. Ruck, A. Leder, D. Dopheide (Ed.), Rostock, 10. bis 12. September 2002,
- Ikhwan, M., Ruck, B., 2003, "Investigation of Flow and Pressure Phenomena around Pyramidal Structure". Proc. Physmod 2003 – International Workshop on Physical Modelling of Flow and Dispersion Phenomena, University of Florence, CRIACIV, Prato, Italy.
- Ikhwan, M., Ruck, B. 2003, „Instationarität des Strömungs- und Druckfeldes bei der Pyramidenumströmung“. Proc. 11. GALA-Tagung Lasermethoden in der Strömungstechnik, , B. Ruck, A. Leder, D. Dopheide (Ed.), Physikalisch-Technische Bundesanstalt Braunschweig, Deutschland.
- Ikhwan, M., Ruck, B. 2004, „Wind Load Coefficients for Pyramidal Buildings “. Proc. 12. GALA-Tagung Lasermethoden in der Strömungstechnik, B. Ruck, A. Leder, D. Dopheide (Ed.), Karlsruhe, Deutschland.
- Ikhwan, M., Ruck, B. 2005, "Flow and Pressure Field Characteristics around Pyramidal Buildings", Submitted to *Journal of Wind and Environmental Engineering*.
- Irwin, H.P.A.H., 1981, The design of Spires for Wind Simulation, *J. Wind Eng. Ind. Aerodyn.*, 7, pp. 361-366.
- Irwin, H.P.A.H., 1981, The design of Spires for Wind Simulation, *J. Wind Eng. Ind. Aerodyn.*, 7, pp. 361-366.
- Isyumov, N. 1999. Overview of Wind Action on Tall Building and Structures. *Wind Engineering into 21<sup>st</sup> Century*, Rotterdam, ISBN 90-5809-059-0, pp. 15-28.
- Kaimal J.C., Finnigan, J.J., 1994, *Atmospheric Boundary Layer Flows, Their Structure and Measurement*, Oxford Univ. Press.
- Knoll, F., 1989, La Pyramide du Grand Louvre. Die Pyramide des Grand Louvre. The Pyramid to the Grand Louvre, *IABSE Proceedings*, Nr. P131/89, pp. 1-12.
- Lawson, T. 2001, *Building Aerodynamics*, Imperial College Press.
- Martinuzzi, R.J., Abuomar, M., 2003, Study of the Flow around Surface-mounted Pyramids, *Experiments in Fluids* 34, pp. 379 – 389.
- Martinuzzi, R.J., Tropea, C., 1993, The Flow around surface-mounted Prismatic Obstacles Placed in a Fully Developed Channel Flow, *J. Fluids Eng.*, 115, pp. 85-92.
- Mehler, S., 1997. The Origin of the Word "Pyramid", Research Article, [www.gizapyramid.com](http://www.gizapyramid.com).
- Meroney, R.N., 1982, Turbulent Diffusion near Buildings, *Engineering Meteorology*, Editor Plate, E.J., Elsevier scientific Publishing, pp. 481-525.
- Neimann, H.J., 1993. The boundary layer wind tunnel: an experimental tool in building aerodynamics and environmental engineering, *J. Wind Eng. Ind. Aerodyn.*, 48, pp. 145-161.

- Pasquill, F., 1972, Some Aspect of Boundary Layer description, J. Royal Meteorol. Soc., 98, pp. 469-456.
- Peterka, J.A., Meroney, R.N., Kothari, K.M., 1985, Wind Flow Patterns About Buildings. J. Wind Eng. Ind. Aerodyn. 21, p. 21-38.
- Plate, E.J., (ed.), 1982. Engineering Meteorology, Elsevier Scientific Publishing Company, 1982.
- Plate, E.J., 1995. Windprobleme in dichtbesiedelten Gebieten, WTG-Berichte Nr. 3, Hrsg. E. Plate, Windtechnologische Gesellschaft, Aachen.
- Richards, P.J., Hoxey, R.P., Short, L.J., 2001, Wind pressure on a 6 m cube, J. Wind Eng. Ind. Aerodyn., 89, pp. 1553-1564.
- Robertson, A.P., Hoxey, R.P., Short, J.L., Ferguson, W.A., Blackmore, P.A., 1998, Prediction of structural loads from fluctuating wind pressures: Validation from full-scale force and pressure measurements, J. Wind Eng. Ind. Aerodyn., 74-76, pp. 631-640.
- Rodi, W., 2000, Turbulence Models and Their Application in Hydraulics, 3<sup>rd</sup>. edition, IAHR, AIRH, A.A. Balkema, Rotterdam.
- Roth, M. 1997, Analyse der Umströmung pyramidenförmiger Hindernisse, Diplomarbeit, Institute for Hydromechanics, University of Karlsruhe.
- Roth, M., 2000, Review of Atmospheric Turbulence over Cities, Quart. J. Roy. Meteorol. Soc., 126, pp. 941-990.
- Roth, M., 1997, *Analyse der Umströmung pyramidenförmiger Hindernisse*, Diplomarbeit, IfH, Forschungsgruppe Stömungsmesstechnik, Univ. Karlsruhe (TH).
- Rotta, J.C., 1972, Turbulente Strömungen, B.G. Teubner, Stuttgart.
- Ruck, B., Schmitt, T., Loy, T., 1986, Signalbewertung in der Laser-Doppler-anemometrie durch Periodenlängenvergleich, Tech. Mess. 6, pp. 185 – 191.
- Ruck, B., 1987, Laser Doppler Anemometry – a Non-Intrusive Optical Measuring Technique for Fluid Velocity, Particle Characterization, 4 , pp.26-37.
- Ruck, B., 1987, Laser-Doppler-Anemometrie, AT-Verlag, Stuttgart, Germany.
- Ruck, B. (Ed.), 1990, Laser Methoden in der Stromungmesstechnik, AT-Verlag, Stuttgart, Germany.
- Ruck, B., Roth, M., 1997. The Flow and Pressure Distribution Around Pyramids. Laser Anemometry Advances and Applications, Proceedings of the 7<sup>th</sup> International Conference, September 8-11, pp.761-769.
- Ruck, B., 2001. *Strömungstechnische Bemessung pyramidenförmiger Bauwerke*, Project proposal submitted to DFG.
- Rudd, M.J., 1969, A new Theoretical Model for the Laser Doppler Meter, Journal of Physics E: Scientific Instruments, Vol. 2, pp. 723-726
- Sachs, P., 1972, Wind Forces in Engineering, International Series of Monograph in Civil Engineering, Vol. 3, Pergamon Press, Oxford, New York, Toronto, Sydney, Braunschweig.
- Sacré, C., 2002, Extreme wind speed in France: the '99 storms and their consequences. *Journal of Wind Engineering and Industrial Aerodynamics* 90, pp.1763-1771
- Sakamoto, H., Arie, M., Vortex Shedding from a Rectangular Prism and a Circular Cylinder Placed Vertically in a Turbulent Boundary Layer, J. Fluid Mech. (1983), Vol. 126, p. 147-165.

- Savory E., Toy N., 1988, The Separated Shear Layers Associated with Hemispherical Bodies in Turbulent Boundary Layers. *J Wind Eng Ind Aerodyn* 28:291–300
- Schilling, S., 1994, Die Pyramide von Las Vegas, *Bauingenieur*, Jg. 69, Nr. 2, pp.90.
- Schlichting H., Gersten, K., 2000, *Boundary Layer Theory*, 8<sup>th</sup> Rev. and enl. Ed., Springer-Verlag Berlin Heidelberg New York.
- Schüssler, K., 1983, *Die ägyptischen Pyramiden: Erforschung, Baugeschichte u. Bedeutung*, Du Mont, Köln.
- Simiu, E., Scanlan, H.R., 1996, *Wind Effects on Structures*, John Wiley and Sons, Canada.
- Snyder, W. H.: 1972, 'Similarity Criteria for the Application of Fluid Models to the Study of Air Pollution Meteorology', *Boundary-Layer Meteorol.* 3, 113–134.
- Socket, H., 1984, *Aerodynamik der Bauwerke*, Vierweg, Braunschweig.
- Stull, R.B., 1988, *An introduction to boundary layer meteorology*, Kluwer, XII, 666 S., Atmospheric sciences library ; 13.
- Sullivan, R., Greeley, R., 1993, Comparison of aerodynamic roughness measured in a field experiment and in a wind tunnel simulation, *J. Wind Eng. Ind. Aerodyn.*, 48 (93), pp. 25-30.
- Taylor, T.J., 1991, Wind Pressure on Hemispherical Dome, *J. Wind Eng. Ind. Aerodyn.*, 40, pp. 199-213.
- Tennekes, H., Lumley, J.L., 1972, *A First Course in Turbulence*, The MIT Press.
- Tennekes, H. 1973, The Logarithmic Wind Profile, *J. Atmospheric Science*, 30, pp. 234-238.
- Tieleman, H.W., 1993, Pressure on Surface-Mounted Prism: The Effects of Incident Turbulence, *J. Wind Eng. Ind. Aerodyn.*, 49 (1993), pp. 289-300.
- Tielman, H.W., Surry, D., Lin, J.X., 1994, Characteristics of Mean and Fluctuating Pressure Coefficients under Corner (Delta Wing) Vortices, *J. Win. Eng. Ind. Aerodyn.*, 52, pp. 263-275.
- Tieleman, H.W., 1995, Universality of Velocity Spectra, *J. Wind. Eng. Ind. Aerodyn.*, 56, p. 55-69.
- Tieleman, H.W., 1998, Wind Tunnel Simulation of Wind Loading on Low-rise Structures, *J. Wind Eng. Ind. Aerodyn.*, 74-76, pp. 675 – 685.
- Tieleman, H.W., Hajj, M.R., 1999, Pressure Characteristics for Separated Flows, *Wind Engineering in to 21st Century*, Balkema, Rotterdam, pp. 1731-1738.
- Tieleman, H.W., 2003, Wind Tunnel Simulation of Wind Loading on Low-rise Structures : a Review, *J. Wind Eng. Ind. Aerodyn.*, 91, pp. 1627-1649.
- Tuchmann, J.L., 1993, Egypt Hits Las Vegas at a Breathtaking Pace, *ENR*, 231, pp. 26-32.
- Uehara, K., Wakamatsu, S., Ooka, R., 2003, Studies on Critical Reynolds Number Indices for Wind Tunnel Experiments on Flow within Urban Areas, *Boundary-Layer Meteorol.* 107, 353-370.
- Uematsu, Y., Yamada, M., Karasu, A., 1997, Design Wind Loads for Structural Frames on Flat Long-span Roofs: Gust Loading Factor for the Bemas Supporting Roofs, *J. Wind Eng. Ind. Aerodyn.*, 66, pp. 35-50.
- Wieghart, K., Übertragungsvorgängen in turbulenten Reibungsschichten, *ZAMM Bd. 27 (11/12) (1948)*, p. 346-355.



- Wieringa, J., 1993, Representative Roughness Parameters for Homogeneous Terrain, *Boundary Layer Meteorology*, 63 (1993), p. 323-363.
- Wolfseher, U., Gertis, K., 1978, Bodennahe Aerodynamik, *Gesundheitsingenieur*, Jg. 99 (9), pp. 259 – 274.
- Wolfseher, U., Gertis, K., 1978, Bodennahe Aerodynamik, *Gesundheitsingenieur*, Jg. 99 (9), pp. 259 – 274.
- Woo, H.G.C., Peterka, J.A., Cermak, J.E., 1977, Wind Tunnel Measurements in the Wakes of Structures, NASA Contract, Rep. No. 2086.

Pyramid pictures online source (July 2004)

Euromed. Clinic	<a href="http://www.fag-neustadt-aisch.de">www.fag-neustadt-aisch.de</a> / <a href="http://www.euromedclinic.de">www.euromedclinic.de</a>
Faisaliah Tower	<a href="http://www.saudi-us-relations.org/photos/faisaliah-tower.html">www.saudi-us-relations.org/photos/faisaliah-tower.html</a>
Hard Rock Café	<a href="http://www.hardrock.com">www.hardrock.com</a>
High Altitude Pyramid	<a href="http://www.geocities.com/CapeCanaveral/6280/pyramid1.html">www.geocities.com/CapeCanaveral/6280/pyramid1.html</a>
London Int. Exhibition Centre	<a href="http://www.moxley.co.uk">www.moxley.co.uk</a>
Luxor Hotel	<a href="http://www.vegas.com">www.vegas.com</a>
Pyramid Arena	<a href="http://www.davidicke.net">www.davidicke.net</a>
Pyramid Green House	<a href="http://hem.passagen.se/andervad/blood.html">hem.passagen.se/andervad/blood.html</a>
Pyramid House	<a href="http://queenami.tripod.com">queenami.tripod.com</a>
Pyramid House	<a href="http://www.sips.org/news/pyramid_house.htm">www.sips.org/news/pyramid_house.htm</a>
Pyramid House	<a href="http://www.windsongproductions.com">www.windsongproductions.com</a>
Pyramid Louvre	<a href="http://www.louvre.fr">www.louvre.fr</a>
Pyramid Office-building	<a href="http://www.aidan.co.uk">www.aidan.co.uk</a> , by Aidan O'Rourke
Pyramid San Francisco:	<a href="http://david.dupplaw.me.uk">david.dupplaw.me.uk</a>
Summum Pyramid	<a href="http://www.summum.us/pyramid">www.summum.us/pyramid</a>

## References

# Lebenslauf

## Persönliche Daten

Name: Muhammad Ikhwan  
Geboren am: 20. März 1975 in Jakarta, Indonesien  
Nationalität: Indonesisch  
Familienstand: verheiratet, ein Sohn und eine Tochter

## Schulbildung

1981 – 1987 Grundschule SDN Menteng 02 Pagi, Jakarta, Indonesien  
1987 – 1990 Mittelschule SMP Kanisius, Jakarta, Indonesien  
1990 – 1993 Oberschule SMA Kanisius, Jakarta, Indonesien

## Studium und Promotion

1993 – 1998 B.Eng, Bachelor of Engineering for Civil Engineering at the University of Indonesia, Jakarta, Indonesien  
1999 – 2000 M.Sc. (Master of Science) for Water and Environmental Engineering at the University of Surrey, UK  
08/01 – 06/05 Wissenschaftlicher Angestellter am Institut für Hydromechanik, Laboratorium für Gebäude- und Umweltaerodynamik, Universität Karlsruhe

## Berufliche Tätigkeit

Seit Oktober 1998 Lehrbeauftragter am Civil Engineering Department, University of Indonesia, Jakarta, Indonesien